

CONTACTLESS MAGNETIC BRAKE
FOR AUTOMOTIVE APPLICATIONS

A Dissertation
by
SEBASTIEN EMMANUEL GAY

Submitted to the Office of Graduate Studies of
Texas A&M University
in partial fulfillment of the requirements for the degree of

DOCTOR OF PHILOSOPHY

May 2005

Major Subject: Electrical Engineering

CONTACTLESS MAGNETIC BRAKE
FOR AUTOMOTIVE APPLICATIONS

A Dissertation
by
SEBASTIEN EMMANUEL GAY

Submitted to Texas A&M University
in partial fulfillment of the requirements
for the degree of

DOCTOR OF PHILOSOPHY

Approved as to style and content by:

Mehrdad Ehsani
(Chair of Committee)

Hamid Toliyat
(Member)

Shankar Bhattacharyya
(Member)

Mark Holtzapple
(Member)

Chanan Singh
(Head of Department)

May 2005

Major Subject: Electrical Engineering

ABSTRACT

Contactless Magnetic Brake for
Automotive Applications. (May 2005)

Sebastien Emmanuel Gay, Dipl. of Eng., Institut National Polytechnique de Grenoble;

M.S., Texas A&M University

Chair of Advisory Committee: Dr. Mehrdad Ehsani

Road and rail vehicles and aircraft rely mainly or solely on friction brakes. These brakes pose several problems, especially in hybrid vehicles: significant wear, fading, complex and slow actuation, lack of fail-safe features, increased fuel consumption due to power assistance, and requirement for anti-lock controls.

To solve these problems, a contactless magnetic brake has been developed. This concept includes a novel flux-shunting structure to control the excitation flux generated by permanent magnets. This brake is wear-free, less-sensitive to temperature than friction brakes, has fast and simple actuation, and has a reduced sensitivity to wheel-lock.

The present dissertation includes an introduction to friction braking, a theory of eddy-current braking, analytical and numerical models of the eddy-current brake, its excitation and power generation, record of experimental validation, investigation and simulation of the integration of the brake in conventional and hybrid vehicles.

To my parents, my family, my friends, my many professors and my few mentors.

ACKNOWLEDGMENTS

Thanks go to Mr. Philippe Wendling of Magsoft Corporation for his patience and diligence to answer my questions about Flux 3D. Many problems were solved and much time was saved thanks to his help.

TABLE OF CONTENTS

	Page
ABSTRACT	iii
DEDICATION	iv
ACKNOWLEDGMENTS.....	v
TABLE OF CONTENTS	vi
LIST OF FIGURES.....	x
LIST OF TABLES	xx
 CHAPTER	
I INTRODUCTION.....	1
1 Friction braking of vehicles and its disadvantages.....	1
2 The concept of an integrated brake	5
3 Fundamental physics of eddy-current braking	8
4 Review of existing eddy-current brake concepts	9
5 Novel eddy-current brake concepts.....	14
6 Research plan	19
II THEORETICAL ANALYSIS OF EDDY-CURRENT BRAKING	21
1 Method of theoretical analysis of the eddy-current brake.....	21
2 Theoretical analysis derivations	22
2.1 Modeling of the excitation field	25
2.2 Distribution of the excitation flux	28
2.3 Distribution of eddy-currents and associated fields	34
2.4 Computation of the braking force	40
3 Investigation of eddy-current braking using the analytical model	43
3.1 Implementation of the analytical model.....	43
3.2 Fundamental physics of eddy-current brakes.....	45
3.2.1 Eddy-current brake torque-speed curve	45
3.2.2 Distribution of the flux and current densities.....	47
3.3 Impact of design parameters on the brake's performance.....	53
3.3.1 Impact of mean disc radius.....	53

CHAPTER		Page
	3.3.2 Impact of disc area	57
	3.3.3 Impact of disc thickness	60
	3.3.4 Impact of airgap width	63
	3.3.5 Impact of stator pole width.....	66
	3.3.6 Impact of stator pole number	68
	3.3.7 Impact of electrical conductivity	71
	3.3.8 Impact of magnetic permeability.....	73
	3.3.9 Impact of permanent magnet properties.....	75
	4 Limitations of theoretical analysis	78
III	FINITE ELEMENT ANALYSIS OF EDDY-CURRENT BRAKING ..	81
	1 Fundamentals of finite element analysis	81
	2 Selection of finite-element analysis method	82
	3 Comparison of analytical and finite-element results.....	90
	4 Analysis of the impact of design parameters on performance	95
	4.1 Similarities with theoretical analysis.....	95
	4.2 Impact of disc area	96
	4.3 Impact of disc thickness	99
	4.4 Impact of airgap width	103
	4.5 Impact of electrical conductivity.....	106
	4.6 Impact of ferromagnetic properties	114
	4.7 Impact of permanent magnet properties.....	123
	5 Conclusions on numerical analysis	124
IV	EXPERIMENTAL VALIDATION	125
	1 Objective and experimental procedure	125
	2 Test-bed design	127
	3 Measurement of the disc's properties.....	140
	4 Comparison of experimental and finite-element data	145
	5 Conclusions on experimental validation	150
V	INTEGRATION OF THE BRAKE IN VEHICLE SYSTEMS	152
	1 Braking with eddy-current brakes	152
	1.1 Pure eddy-current braking with unlimited force	154
	1.1.1 Brake with constrained critical speed.....	154
	1.1.2 Brake with optimized critical speed	160
	1.2 Integrated braking with limited force.....	163
	1.2.1 Brake with constrained critical speed.....	164

CHAPTER		Page
	1.2.2 Brake with optimized critical speed	167
2	Integrated braking of automobiles.....	176
	2.1 Braking performance requirements	176
	2.2 Conceptual design of an automobile integrated brake	179
	2.3 Integrated braking in conventional drive trains.....	193
	2.3.1 Braking system control strategy	193
	2.3.2 Performance in the FTP 75 Urban drive cycle	194
	2.3.3 Performance in the FTP 75 Highway drive cycle ..	198
	2.4 Integrated braking of series hybrid drive trains	203
	2.4.1 Braking system control strategy	204
	2.4.2 Performance in the FTP 75 Urban drive cycle	210
	2.4.3 Performance in the FTP 75 Highway drive cycle ..	213
	2.4.4 Performance in the NREL drive cycle	215
	2.5 Impact of temperature on braking performance	225
	2.6 Impact of eddy-current braking on friction brake wear	226
	2.7 Power assistance energy consumption of integrated brake ...	229
	2.8 Anti-lock control of the integrated brake	230
	2.9 Traction control with the integrated brake	235
	2.10 Dynamic stability control with the integrated brake	238
3	Integrated braking of heavy duty road vehicles	251
	3.1 The integrated braking of commercial trucks and trailers....	251
	3.1.1 Braking system architecture	252
	3.1.2 Dynamic stability control of commercial trucks	260
	3.1.3 Anti-lock control of commercial trucks	262
	3.1.4 The integrated brake as a backup brake	263
	3.2 Integrated braking of urban buses	263
4	Integrated braking of rail vehicles.....	274
	4.1 Integrated braking of light rail vehicles	274
	4.2 Integrated braking of high-speed trains.....	277
	4.3 Integrated braking of freight trains.....	279
5	Integrated braking of other vehicles.....	281
6	Electric motor emergency braking with an eddy-current brake	282
7	Trepan kinetic energy control by eddy-current braking	288
VI	SUMMARY AND CONCLUSIONS.....	289
	1 Summary	289
	2 Conclusions	294
	REFERENCES	297
	APPENDIX A	302

	Page
VITA	305

LIST OF FIGURES

FIGURE	Page
1 Forces involved in friction braking	2
2 Temperature dependence of friction coefficient	3
3 Integrated brake concept	6
4 Fundamental physics of eddy-current braking	9
5 Telma electromagnetic retarder.....	10
6 Shunted magnet structure, shunting position	16
7 Shunted magnet structure, non-shunting position	17
8 Rotated magnet structure, aligned position	18
9 Rotated magnet structure, quadrature position.....	18
10 Eddy-current brake.....	22
11 Eddy-current paths	24
12 Two-dimensional regions	24
13 Nd-Fe-B permanent magnet magnetization characteristics	25
14 Permanent-magnet / current sheet equivalence.....	25
15 Angular dimensions of a pole pair	26
16 Current sheet density profile of a pole pair	27
17 Implementation algorithm	44
18 Typical torque-speed curve for an eddy-current brake	46
19 Flux density and eddy-current density map for a pole pair at standstill.....	48

FIGURE	Page
20 Flux and current density map for a pole pair at 1% of critical speed.....	49
21 Flux density and current density map for a pole pair at critical speed.....	50
22 Flux density and current density map for a pole pair at 5x critical speed.....	51
23 Elemental braking force distribution at five times the critical speed.....	52
24 Torque-speed curve dependency on the mean disc radius	54
25 Critical speed vs. mean disc radius	55
26 Peak torque vs. mean disc radius	56
27 Torque-speed curve dependency on the disc area	57
28 Peak torque vs. disc area	58
29 Critical speed vs. disc area	59
30 Torque-speed curve dependency on disc thickness.....	60
31 Peak torque vs. disc thickness	61
32 Critical speed vs. disc thickness	62
33 Flux density and current density plots at 5x critical speed, e=5mm	63
34 Torque-speed curve vs. airgap width, e=20mm	64
35 Peak torque vs. airgap width	65
36 Critical speed vs. airgap width	66
37 Peak torque vs. pole width	67
38 Critical speed vs. pole width	68
39 Peak torque vs. number of pole pairs	69
40 Critical speed vs. number of pole pairs	70

FIGURE		Page
41	Torque-speed curve for various materials	72
42	Critical speed vs. disc material conductivity.....	73
43	Torque-speed curve for ferromagnetic material.....	74
44	Torque-speed curves for different permanent magnet materials.....	76
45	Peak torque vs. magnet magnetization.....	77
46	FLUX 3D's infinite box	84
47	Use of periodicities to reduce the size of a model.....	85
48	Normal and tangential flux conditions	86
49	Use of symmetries for the modeling of a finned disc.....	87
50	Use of normal flux conditions	88
51	Two different BH curve models for ferromagnetic materials	89
52	Meshed geometry	91
53	Transient analysis results	92
54	Compared results of 3D finite element and analytical models.....	93
55	Surface current density at critical speed.....	94
56	Peak torque vs. disc area	97
57	Critical speed vs. disc area	98
58	Peak torque vs. disc thickness, nonmagnetic material	99
59	Critical speed vs. disc thickness, nonmagnetic material	100
60	Peak torque vs. disc thickness, ferromagnetic material	101
61	Critical speed vs. disc thickness, ferromagnetic material	102

FIGURE	Page	
62	Peak torque vs. airgap width, non-saturated ferromagnetic disc.....	103
63	Peak torque vs. airgap width, saturated ferromagnetic disc	104
64	Critical speed vs. airgap width, ferromagnetic disc	105
65	Torque-speed curves for nonmagnetic materials of various resistivities	106
66	Peak torque vs. disc material conductivity.....	107
67	Presence of radial flux density due to return current path.....	108
68	Generation of eddy-current braking force by space-shift of eddy-currents ..	109
69	Current return path in a high conductivity material	110
70	Current return path in a low conductivity material	110
71	Critical speed vs. disc material conductivity, nonmagnetic material	111
72	Peak torque vs. disc material conductivity, ferromagnetic	112
73	Critical speed vs. disc material conductivity, ferromagnetic	113
74	Peak torque vs. relative permeability, $J_s=1.8T$	114
75	Critical speed vs. relative permeability, $J_s=1.8T$	116
76	Peak torque vs. saturation magnetization.....	117
77	Relative permeability in saturated disc, $J_s=0.8T$, $B_r=1.4T$	118
78	Flux density in disc, $J_s=0.8T$, $B_r=1.4T$	119
79	Reaction of saturated materials to eddy-currents	120
80	Flux density in non-saturated disc, $J_s=2.2T$ $B_r=1.4T$	121
81	Relative permeability in non-saturated disc, $J_s=2.2T$ $B_r=1.4T$	121
82	Critical speed vs. saturation magnetization.....	122

	FIGURE	Page
83	Test bed architecture	127
84	DC motor and drive	128
85	DC motor and eddy-current brake torque-speed curves.....	129
86	Torquemeter	131
87	Plastic hub	132
88	Cobalt ring.....	133
89	Water box	134
90	NdFeB permanent magnets	135
91	Stator back-iron	136
92	Stator assembly	137
93	Complete stator assembly and mount.....	138
94	Assembled eddy-current brake.....	139
95	Complete test bed.....	140
96	SQUID magnetometer, instrument.....	142
97	SQUID magnetometer, processing electronics	143
98	Initial magnetization BH curve for cobalt sample.....	144
99	Finite element and experimental torque-speed curves	145
100	Microscopic BH curves for cobalt	148
101	Impact of viscous and fluid friction on torque	149
102	Normalized torque-speed curve	153
103	Relative speed vs. relative time, low initial speed	155

FIGURE	Page	
104	Relative speed vs. relative time, high initial speed	157
105	Stopping time vs. initial speed, no significant friction.....	158
106	Stopping time vs. initial speed, significant friction.....	159
107	Stopping time vs. critical speed and initial speed, significant friction.....	161
108	Stopping time vs. critical speed and initial speed, no friction.....	162
109	Stopping time vs. critical and initial speed, no friction, $T_p=240\text{N.m}$	163
110	Stopping time vs. initial speed and peak braking force, tire limited	165
111	Diminishing return in increasing peak force	166
112	Deceleration time vs. maximum peak torque and critical speed.....	167
113	Optimum critical speed vs. peak braking force.....	168
114	Stopping time vs. peak braking force.....	169
115	Eddy-current and friction force, emergency braking	170
116	Eddy-current and friction brake dissipated energy, emergency braking.....	171
117	Fraction of kinetic energy dissipated by eddy-current braking, $\mu=0.8$	172
118	Fraction of kinetic energy dissipated by eddy-current braking, $F_p=8\text{kN}$	173
119	Fraction of kinetic energy dissipated by eddy-current braking, $F_p=40\text{kN}$...	174
120	Fraction of kinetic energy dissipated by eddy-current braking, $F_p=16\text{kN}$...	175
121	Test vehicle maximum braking curves.....	178
122	Integrated brake conceptual design	180
123	View of individual pole configuration	181
124	Conceptual design eddy-current brake torque-speed curve	183

FIGURE	Page	
125	Pole flux pattern in quadrature position	184
126	Pole flux pattern in quadrature position, zoom	184
127	Pole flux pattern in aligned position	185
128	Torque on one magnet vs. magnet angle.....	186
129	Magnet angular position vs. time	187
130	Conceptual design peak torque vs. magnet angle	190
131	Individual eddy-current brake control and actuation system	191
132	Conventional vehicle integrated brake controller	193
133	Braking torque distribution, FTP75 Urban drive cycle.....	194
134	Eddy-current braking force locus against rated braking force curve	195
135	Integrated brake speed and temperature profile, FTP75 Urban cycle	196
136	Critical speed and peak torque locus, FTP75 Urban drive cycle	197
137	Eddy-current braking force locus against warm brake force-speed curve	198
138	Braking torque distribution, FTP75 Highway drive cycle	199
139	Eddy-current braking force locus against maximum braking force curve	200
140	Integrated brake speed and temperature, FTP75 Highway drive cycle.....	201
141	Critical speed and peak torque locus, FTP 75 Highway drive cycle.....	202
142	Eddy-current braking force locus against hot brake force-speed curve	203
143	Braking system control block diagram.....	205
144	Complementarity of regenerative and eddy-current braking	209
145	FTP75 Urban drive cycle braking curves.....	211

	FIGURE	Page
146	FTP75 Urban drive cycle, brake temperature profile.....	212
147	FTP75 Highway drive cycle braking curves	213
148	FTP75 Highway drive cycle, brake temperature.....	214
149	Speed and elevation profiles, NREL drive cycle	215
150	Braking force distribution, NREL drive cycle	216
151	Occurrence of eddy-current braking.....	217
152	Cumulative energy dissipated by eddy-current braking.....	218
153	Speed, elevation and brake temperature profile	219
154	Switching between regenerative and eddy-current braking	221
155	Drift of critical speed and peak torque, NREL drive cycle	222
156	Eddy-current braking force points against maximum braking force curve...	223
157	Eddy-current braking force points against warm brake force-speed curve...	224
158	Wheel and ground speeds, initial speed below critical speed	232
159	Forces on a slipping wheel	233
160	Ground and wheel speeds, initial speed above critical speed	234
161	Ground and wheel speeds after 67ms, initial speed below critical speed	235
162	Dynamic stability control principle.....	239
163	Forces on a vehicle with the front axle on zero-adherence surface.....	240
164	Yaw torque on a vehicle with one axle on a zero adherence surface	241
165	Yaw torque and compensating torque, conceptual design	242
166	Yaw torque and compensating torque, constrained critical speed	243

FIGURE	Page
167 Constrained critical speed and increased peak braking torque.....	244
168 Lateral velocity.....	247
169 Lateral deviation from trajectory after 1s.....	249
170 Lateral deviation from trajectory after 67ms.....	250
171 Braking effort – speed vs. grade.....	252
172 Retarder design.....	254
173 Braking system configurations for a commercial truck	257
174 Design of a constrained-speed retarder for a commercial truck.....	258
175 Braking effort curves vs. braking force – speed curves	259
176 Matching retarder and vehicle braking effort.....	260
177 Dynamic stability balance of forces for a trailer	262
178 Irisbus Agora 18m braking force – speed curves	264
179 Stopping time vs. critical speed and peak force, initial speed = 130km/h ...	266
180 Stopping time vs. critical speed and peak force, initial speed = 60km/h	268
181 New York Bus drive cycle speed profile	269
182 New York Bus braking points vs. eddy-current brake curves.....	270
183 Lateral deviation for the Irisbus Agora 18m after 67ms	272
184 Stopping time vs. critical speed and peak force	274
185 8-hour tramway drive cycle.....	275
186 15-hour tramway drive cycle.....	276
187 Braking points, tramway	277

FIGURE		Page
188	Stopping time for TGV vs. critical speed and peak force	278
189	Eddy-current braking of a winch.....	284
190	Load speed after motor failure at t=0s	285
191	Brake operating points	286
192	Brake operating points for initial speed superior to critical speed.....	287
193	Impact of temperature on electrical conductivity.....	302
194	Normalized saturation magnetization vs. temperature	303

LIST OF TABLES

TABLE		Page
1	Telma retarders performances	11
2	Permanent magnet materials	15
3	Brake design parameters	45
4	Electrical conductivity of various metals at 20°C	71
5	Relative magnetic permeability of various soft magnetic materials at 20°C	74
6	Saturation magnetization of various permanent magnet materials at 20°C...	75
7	DC motor characteristics	128
8	Test eddy-current brake characteristics	130
9	Magnetic data for the cobalt ring	144
10	Curve parameters.....	145
11	Test vehicle parameters	164
12	Vehicle parameters	177
13	Target integrated brake parameters	179
14	Conceptual design geometric and material parameters.....	182
15	Actuator torque and power requirements	188
16	Possible actuator.....	189
17	Hybrid drive train parameters	204
18	Balance of dissipated energy, FTP 75 Urban drive cycle	212
19	Balance of dissipated energy, FTP 75 Highway drive cycle.....	215

	TABLE	Page
20	Kinetic energy balance, NREL drive cycle	225
21	Reduction of friction brake kinetic energy dissipation	227
22	Chassis dimensions	248
23	Renault Magnum commercial truck parameters	252
24	Irisbus Agora 18m parameters	265
25	Kinetic energy dissipation summary	271
26	Crane parameters.....	283

CHAPTER I

INTRODUCTION

1 – Friction braking of vehicles and its disadvantages

Road, rail, and air vehicles all rely mainly or solely on mechanical friction brakes. These brakes are composed of two functional parts: a rotor connected to the wheels and a stator fixed to the chassis of the vehicle. The rotor is either a drum or a disc generally made of cast iron for road and rail vehicles, and carbon fiber for aircraft. The stator comprises shoes (drum brakes) or pads (disc brakes) made of a soft friction material and an actuator, generally a hydraulic piston.

Although the principle is the same for drum and disc brakes, the terminology used from there on refers to disc brakes. The contact between the soft material of the pads and the surface of the rotor is characterized by a high friction coefficient. When braking is commanded by the driver, the actuator presses the pads against the rotor, thus inducing a friction force tangential to the surface of the rotor, which opposes the motion of the vehicle (Fig. 1). The braking force is proportional to the normal force developed by the actuator pressing the pads against the rotor and the coefficient of friction:

$$F_{braking} = f \cdot N_{actuator} \quad (1)$$

This dissertation follows the style and format of the *IEEE Transactions on Magnetics*.

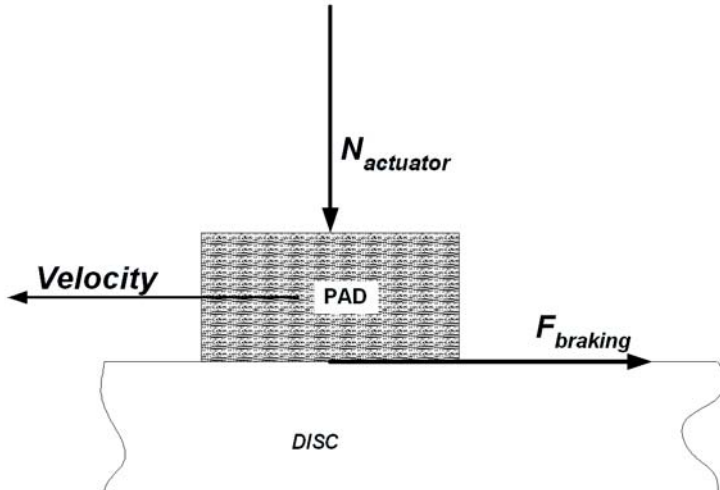


Fig. 1: Forces involved in friction braking

Friction braking is dissipative: the vehicle's kinetic energy is dissipated as heat at the contact surface between the pads and the disc. Kinetic energy dissipation results in a very significant increase of the disc and pads temperatures. Although most of the heat is ultimately dissipated through forced convection by the disc's cooling fins, during a braking phase the temperature of the disc and pads may rise to several hundreds of Celsius degrees. The friction coefficient between the pads and the disc, and therefore the maximum braking force obtainable depends on temperature [1], increasing slightly from room temperature to a maximum, and decreasing rapidly beyond a certain point (Fig. 2). The decrease in braking force at high temperature is a phenomenon called "fading". It is usually encountered when a vehicle is driven downhill because of the supplementary force due to the grade and the weight of the vehicle. In some dramatic cases, the brakes can lose all braking capability and the vehicle is totally brakeless. Another effect of temperature is disc warping, which occurs as a result of very high disc temperature

during heavy braking. This phenomenon is rarely encountered in road or rail vehicles, but has prompted the replacement of cast iron discs by carbon fiber discs on aircraft.

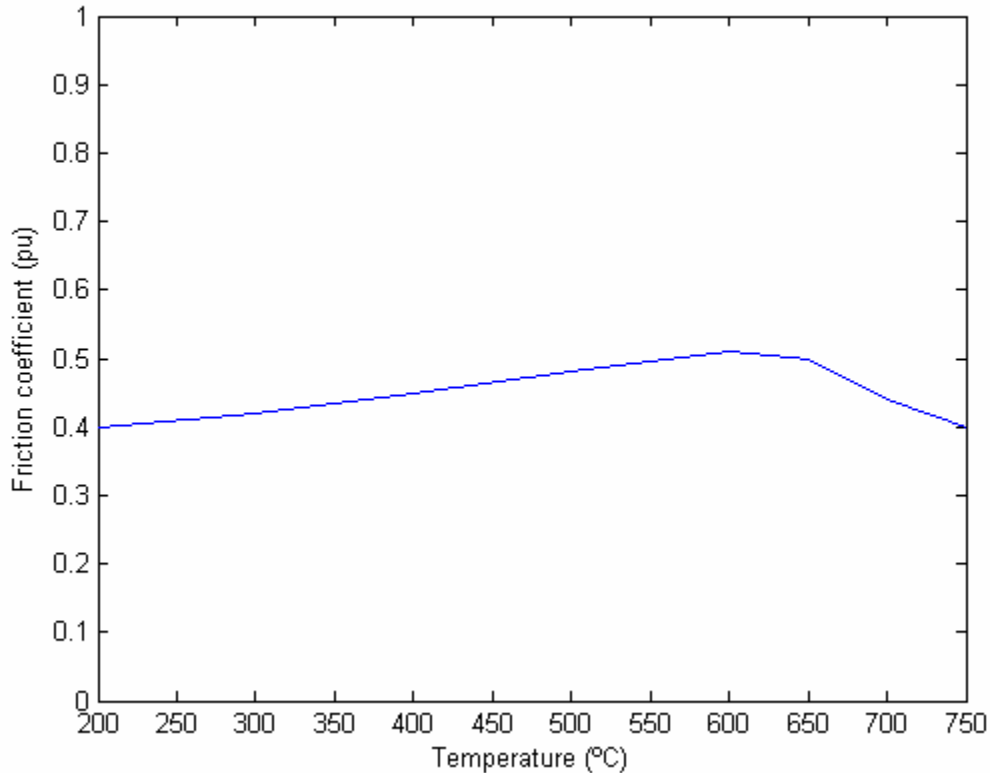


Fig. 2: Temperature dependence of friction coefficient

The combined effects of friction, heat, exposure to water and dirt result in the abrasion of the pads. Consequently, the pads must be changed regularly, whereas the rotors sometimes need to be resurfaced. The cost of new pads and maintenance personnel costs are significant for heavy-duty vehicles (trucks and buses). Furthermore, the dust from the pads may be harmful to the environment and the health of populations.

Heavy and/or fast vehicles require very large braking forces to bring them to a complete stop. Such forces are usually beyond the capabilities of a human operator, which has prompted the installation of power assistance on nearly all road, rail and air vehicles [2]. The assistance mechanism is usually pneumatic for gasoline vehicles and trains or hydraulic for diesel vehicles and aircraft. The assistance mechanism requires many parts, which are often redundant for safety reasons. There is therefore a significant increase in complexity due to this additional hardware. Furthermore, the pumps required on diesel vehicles and aircraft take their toll on the fuel economy of the vehicle. It is worth noting that hybrid vehicles would also require an assistance pump to guarantee assistance even when the engine is shut down.

There is also a propagation time associated with the assistance mechanism, which delays the application of braking from the time the driver pushes the pedals. This delay is significant in buses, trucks, and trains where the brake fluid lines are long. Delays in brake application result in significant increases in braking distances and increased control complexity. Brake controls are required to balance the braking forces between the rear and front axles depending on vehicle load, speed and road conditions, but also to prevent wheel-lock. Anti-lock controls, known as ABS are an important safety feature of modern road vehicles. In addition, the latest generation of automobiles incorporates dynamic stability control systems that correct the driver's mistakes to a certain point and maintain the vehicle on a safe trajectory even under harsh road conditions. The interface between the electronic controls and the hydraulic circuit is ensured by electrically

actuated valves that operate in a switching mode, either open or shut. There are additional nonlinearities in the brake system due to delays in fluid ducts, nonlinear contact between pads and discs, etc..., which render brake control delicate.

In conclusion, although friction brakes are compact and effective, they suffer from several disadvantages, some a mere annoyance and some a real burden on users and owners, whether private or commercial. While these problems are being dealt with currently, it is at a cost, which it would be beneficial to reduce.

2 – The concept of an integrated brake

In order to remedy to the disadvantages of friction brakes, the integrated brake concept was developed as part of the present research (Fig. 3).

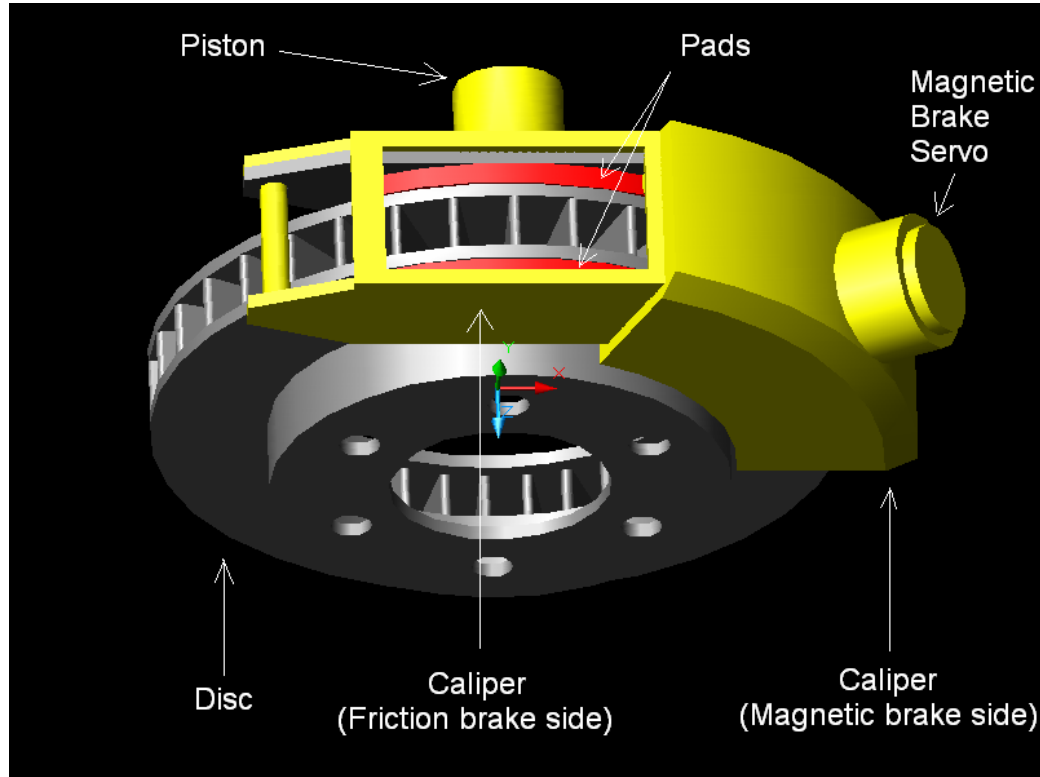


Fig. 3: Integrated brake concept

The integrated brake combines a friction brake with an eddy-current brake on the same caliper. This combination has several advantages:

- Reduced wear of friction pads: the eddy-current brake can provide a large fraction of the braking force, thereby reducing the amount of kinetic energy dissipated at the pads and consequently reducing their wear. The eddy-current brake is contactless and therefore wear-free.
- Reduced sensitivity to fading: the eddy-current brake can assist the friction brake when the rotor is hot. The combination of two sources of braking torque compensates for their respective loss of effectiveness at high temperature.

Furthermore, it is possible to increase the effectiveness of the friction brake by keeping the pads cool. This is achieved by relying as heavily as possible on the eddy-current brake.

- Reduced sensitivity to wheel lock: the eddy-current brake reacts faster to control inputs than a friction brake. Therefore, the brake's control system can prevent wheel-lock more easily than with friction brakes. Furthermore, the friction brake is mostly used at low speeds. The effects of wheel lock are much less severe at low speed than at high speed.
- Faster control dynamics: the eddy-current brake is directly controlled by its excitation magnetic field. The response time of an eddy-current brake is counted in milliseconds, whereas the response time of mechanical systems is counted in tenths of seconds. This is particularly true of power assisted and pneumatic brake systems. [2]
- Easier integration with vehicle electronic driving aids: ABS, traction control and dynamic stability systems require fast response times for more precise and safer vehicle control. The fast response time of eddy-current brakes makes them more suitable for interfacing with these electronic driving aids.
- Reduced fuel consumption of power assistance: the primary reliance on eddy-current braking reduces the maximum braking force required from friction brakes. The power assistance requirement is consequently decreased, making it effective to replace the hydraulic actuation and vacuum assistance by an electric actuation, which drains power only when actuation is needed.

3 – Fundamental physics of eddy-current braking

An eddy-current brake consists of a stationary source of magnetic flux (permanent magnet or electromagnet) in front of which a conductor (metal disc, drum or rail) is moving. Because of the motion, the conductor experiences a time-varying magnetic flux density, which by virtue of Lenz's law results in an electric field:

$$\nabla \times \vec{E} = -\frac{\partial \vec{B}}{\partial t} \quad (2)$$

This electric field results in circulating currents in the conductor by virtue of Ohm's law:

$$\vec{J} = \sigma \cdot \vec{E} \quad (3)$$

These currents are called “eddy-currents”. The interaction of eddy-currents with the flux density results in a force that opposes the motion:

$$\vec{F} = \vec{J} \times \vec{B} \quad (4)$$

Fig. 4 illustrates the fundamental physics of eddy-current braking applied to a disc.

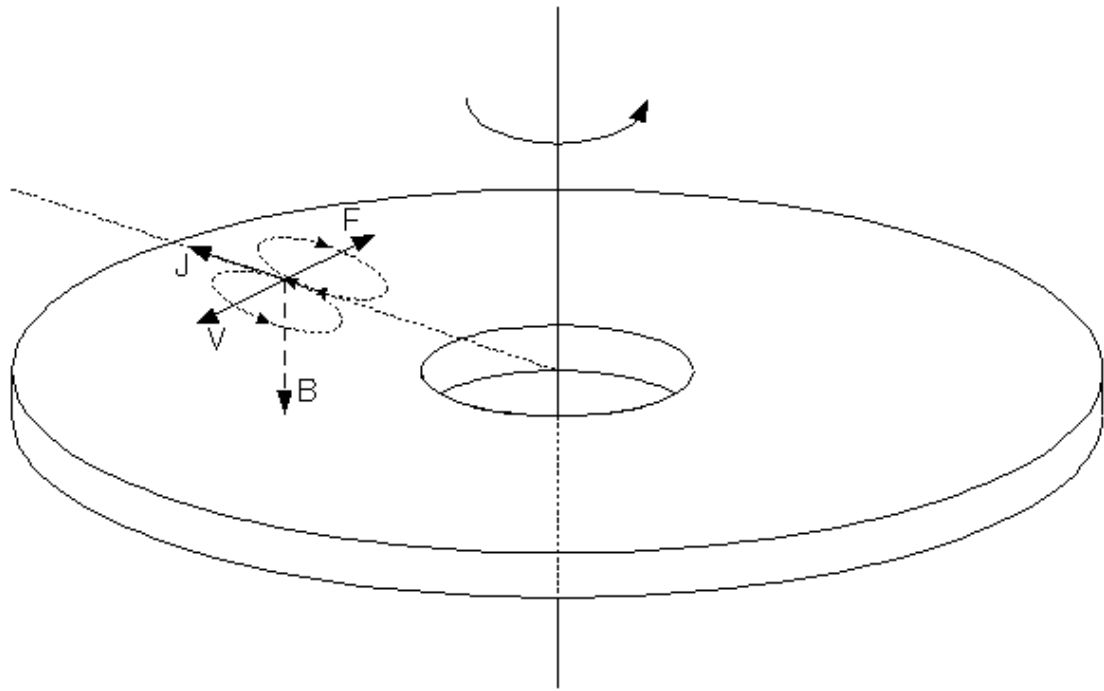


Fig. 4: Fundamental physics of eddy-current braking

Fundamental physics reveal three important characteristics of eddy-current braking:

- A braking force is induced without any mechanical contact between the rotor and the stator. Eddy-current brakes are thus wear-free.
- The braking force is easily controllable by controlling the magnitude of the flux source.

4 – Review of existing eddy-current brake concepts

Eddy-current brakes are currently in use in three types of vehicles: commercial trucks, buses and some passenger trains [3,4]. Eddy-current brakes used in trains are linear and

use the rail as an armature. They are also used in a variety of applications such as oil rigs, textile industry, etc... In trucks and buses, the eddy-current brake is often referred to as an “electromagnetic or electric retarder”. It is a single brake installed on the transmission shaft of the vehicle. It is used as a supplement to the main friction brake system to prevent it from overheating during downhill driving. The world leader in electromagnetic retarders is the French company Telma ®. Fig. 5 shows an electromagnetic retarder manufactured by Telma.

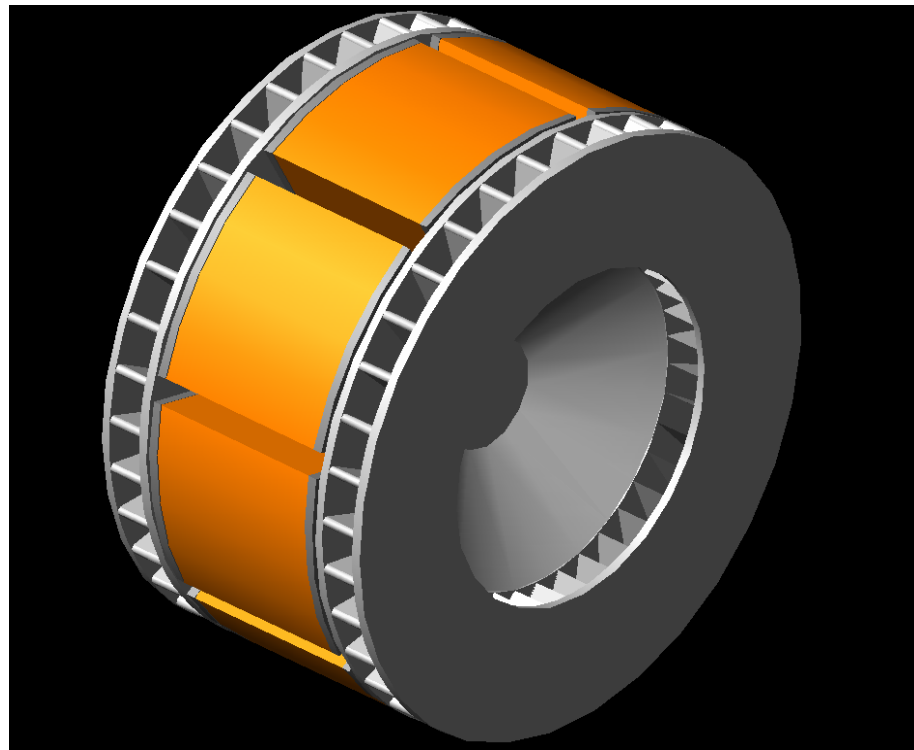


Fig. 5: Telma electromagnetic retarder

The retarder consists of eight alternating-polarity iron-core electromagnets arranged in a circle faced on both side by two cast iron rotors. The rotors have an armature ring facing the electromagnets. The armature has fins on its back side in order to dissipate the braking energy through forced convection. The ring of iron on the outside of the rotor is called a “cheek” and guarantees the mechanical rigidity of the rotor. The performances of Telma’s retarders are listed in TABLE 1.

TABLE 1
Telma retarders performances, [3]

Model	Minimum Peak Torque	Maximum Peak Torque
Axial	350 N.m	3300 N.m
Focal	850 N.m	3300 N.m

These retarders have disc outer diameters ranging from 352mm to 464mm and an airgap of 1mm or 1.4mm. Although the rated excitation current is not disclosed by the manufacturer, users have reported it to be within the 70-90A range.

Electromagnetic retarders have many advantages:

- Contactless braking and absence of maintenance: because the braking torque is induced without contact across an airgap, there is no wear on the parts of the retarder and therefore no need to change them. The no-maintenance requirement is one of the major selling arguments for electromagnetic retarders.

- Reduced sensitivity to high temperatures: while the characteristics of the brake are affected by temperature, the impact is lesser than for the pad-rotor friction coefficient. Electromagnetic retarders can thus operate at higher temperatures than conventional friction brakes.
- Relative ease of control: instead of electromechanical valves controlling a hydraulic or pneumatic circuit, the electromagnetic retarder is controlled solely by its excitation current. Controlling a current proportionally is easily achieved with power electronics.

However, their requirement for a large excitation current is a major disadvantage. The most significant drawback is the lack of failure safety. The excitation current may not be available for a variety of reasons, in which case the retarder is totally useless. Furthermore, the excitation current is necessarily supplied at a low voltage, which induces high ohmic losses in conductors, diminished bus voltage, and renders electronic control challenging. Additional resulting problems include heavy wiring from the battery to the retarder, heating of the coils.

In order to palliate to these disadvantages, it is possible to replace the electromagnets by permanent magnets. However, in gaining a loss-free, powerless permanent source of excitation, controllability is lost. Indeed, permanent magnets cannot be “turned off” or controlled directly. The magnetic flux crossing the airgap to excite the disc must be

controlled by a variable magnetic circuit on the stator. Most patents for permanent magnet retarders revolve around variable magnetic circuit architectures.

One commonly encountered flux control scheme involves a drum brake excited by permanent magnets facing the inner side of the drum and attached to a ring. The ring of magnets is moved in and out of the volume inside the drum to modulate the surface area of magnets facing the drum. Thus, the amount of flux crossing the airgap to excite the rotor can be varied continuously. This scheme has been implemented and tested by Isuzu in Japan [4]. There are several disadvantages to this architecture: the magnets are in the airgap and thus exposed to the heat generated on the drum, the whole stator has to be moved and when completely disengaged, nearly doubles the length of the retarder.

US Patent #6,237,728 relates to a drum brake, using two rows of permanent magnets. Each magnet is included in a horseshoe ferromagnetic circuit. One row is attached to a fixed stator inside the drum. The other row is attached to a stator, which can be rotated slightly. The rotation brings the horseshoes from each row to present the same polarity to the drum or gets the horseshoe of one row to short-circuit the horseshoes of the other row. While this system is compact and does provide the ability to turn-on and off the flux in the airgap, it doesn't provide the ability to control the flux linearly between the two extreme positions. Furthermore, the magnets are only minimally preserved from the heat generated on the rotor.

US Patent #6,209,688 and 5,944,149 relate to a drum brake with two rows of permanent magnets. One row is mounted on a fixed stator, while the other is mounted on a stator that can be rotated slightly. A ferromagnetic plate is between the magnets and the inner surface of the drum brake. If two magnets with different polarities are paired, then the flux shunts through the ferromagnetic plate. If the polarities are similar, the flux is pushed towards the drum and braking is induced. This structure is no more capable of linearly varying the flux between the on and off positions than that claimed in the previous patent. The magnets are also located close to the heated rotor.

5 – Novel eddy-current brake concepts

Existing eddy-current brake concepts all have several disadvantages that make it difficult to integrate them with a friction brake in a same unit. We developed a novel concept of eddy-current brake suitable for integration with friction brakes. The novel eddy-current brake uses rare-earth permanent magnets instead of electromagnets to generate the excitation magnetic field without dissipating energy. Rare-earth permanent magnets are very compact sources of magnetic flux, much more than electromagnets. TABLE 2 shows a comparison of rare-earth permanent magnet materials with conventional permanent magnet materials.

TABLE 2
Permanent magnet materials [5]

Material	B _r (T)	H _{ci} (kA/m)	BH _{max} (kJ/m ³)	T _c (°C)
Ferrite	0.42	242	33.4	450
Alnico9	1.10	145	75.0	850
SmCo ₅	1.00	696	196	700
Nd ₂ Fe ₁₄ B	1.22	1120	280	300

Neodymium-Iron-Boron (NdFeB) magnets have a higher energy product than Samarium-Cobalt (SmCo) magnets. They are also cheaper because neodymium is a much more commonly occurring metal than samarium. NdFeB is thus the preferred permanent magnet material for a low-cost, light, compact and powerful flux source. However, it has a much lower curie temperature than either Alnico or SmCo. Furthermore, neodymium magnets cannot practically be operated without a significant loss of their magnetization beyond 100°C.

There are therefore two challenges in using permanent magnets as flux sources in eddy-current brakes: controlling the magnitude of the flux and preserving the magnets from the high temperatures. Two variable-geometry magnetic circuit structures were developed to control the flux from permanent magnets: the shunted magnet structure and the rotated magnet structure. In the shunted magnet structure, a ferromagnetic bar is used to bypass the airgap and short-circuit the permanent magnet. The flux density in the airgap is varied from zero to a maximum by sliding the bar from a shunting position to a

non-shunting position. Fig. 6 shows the shunted magnet structure in shunting position and Fig. 7 shows the same structure in non-shunting position.

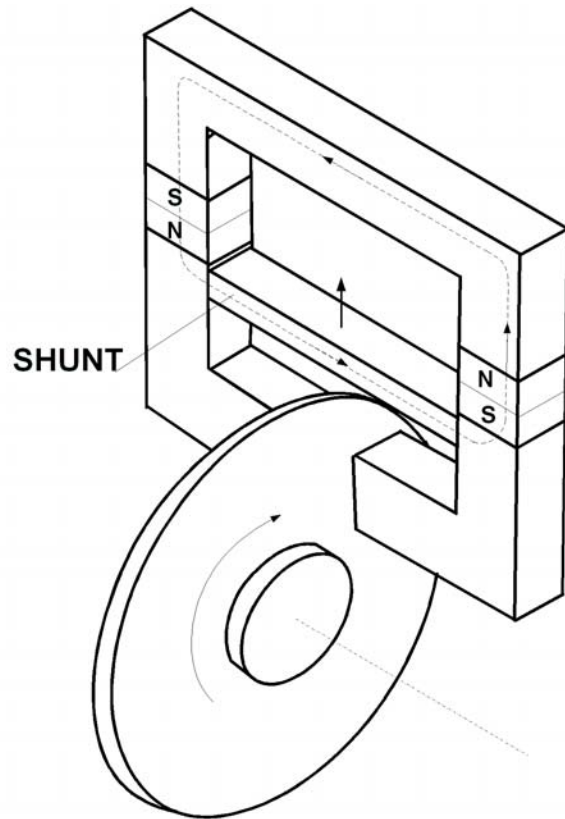


Fig. 6: Shunted magnet structure, shunting position

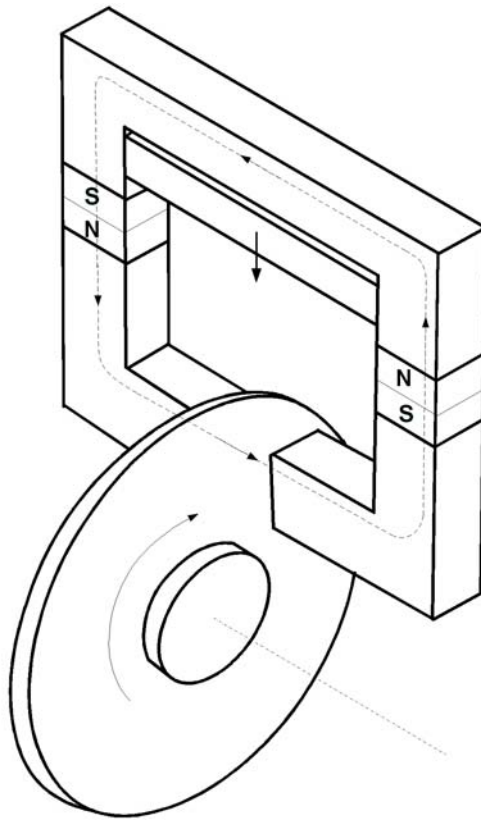


Fig. 7: Shunted magnet structure, non-shunting position

In the rotated magnet structure, the magnet is rotated from a position of alignment with the magnetic circuit to a position in quadrature with the magnetic circuit. When aligned with the magnetic circuit, the permanent magnet delivers all its flux through the airgap. When the permanent magnet is in quadrature, its flux is short-circuited by the magnetic circuit without ever reaching the airgap. Fig. 8 and Fig. 9 show the rotated magnet structure in aligned and quadrature position.

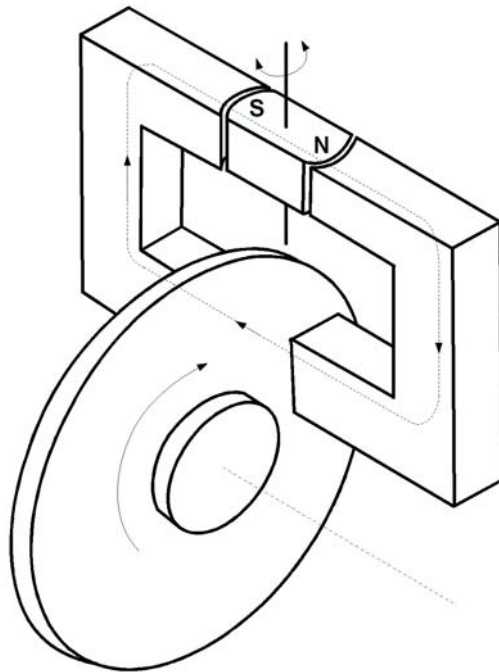


Fig. 8: Rotated magnet structure, aligned position

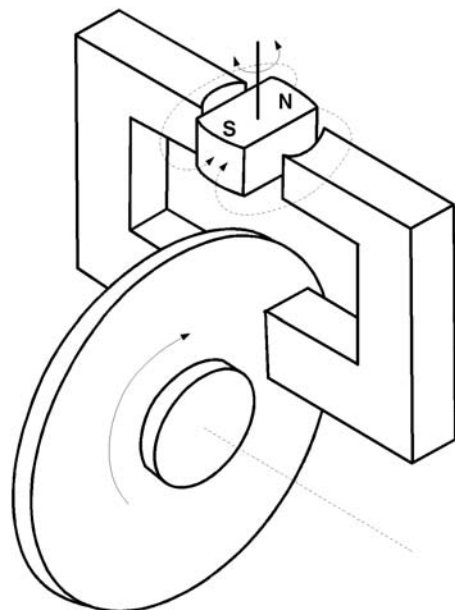


Fig. 9: Rotated magnet structure, quadrature position

Both structures provide thermal protection for the magnets by keeping them away from the airgap and by providing some room to insert a heat shield. Additional thermal protection is required to limit heat conduction from the poles of the magnetic circuit.

Variable-geometry magnetic circuits provide a simple, compact, cost-effective, and fast way of controlling the flux from a permanent magnet over a broad dynamic range. Only a small electric actuator is required to control the geometry of the circuit.

6 – Research plan

The purpose of the present dissertation is to analyze the integrated brake, validate it experimentally, provide a conceptual design, and analyze its integration in automobiles.

The research plan is decomposed as follows:

- Theoretical analysis: An analytical model is derived for the eddy-current brake and its fundamental physics are investigated. The model provides a preliminary sizing of the brake and critical information about the sensitivity to design parameters.
- Numerical analysis: The numerical analysis is used to overcome the limitations of the analytical model. The influence of geometric, electrical and magnetic parameters is investigated to determine the optimum geometry and material

properties for the eddy-current brake. Numerical modeling is also used to design a test bed and provide a conceptual design for automotive applications.

- Experimental validation: A test bed has been built based on specifications from numerical analysis and data has been gathered and compared to the numerical analysis data. The objective is to validate the accuracy of numerical analysis and to explain potential divergences. This validation is necessary to establish the ability of numerical analysis to model eddy-current brakes.
- Expansion of the concept: Several additional innovations are analyzed and incorporated in the integrated brake in order to make the concept more complete and more relevant to real world applications. The investigation is based on numerical analysis.
- Integration study: The use of the integrated brake in conventional and hybrid automobiles is investigated. Specifications for the respective sizing of the friction, regenerative and eddy-current brake are derived through an optimization study and the gains achieved are analyzed.

CHAPTER II

THEORETICAL ANALYSIS OF EDDY-CURRENT BRAKING

1 – Method of theoretical analysis of the eddy-current brake

The purpose of the analytical model is to rapidly provide insight into the fundamental physics of eddy-current braking, and preliminary design data which verifies whether the performance and size are compatible with the envisioned application.

The analytical modeling of eddy-current brakes has been studied previously. The scope and complexity of the models vary greatly. Several publications only aim at providing a simple and restrictive model of eddy-current braking [6-9], others attempt to analyze the fundamental characteristics of the torque-speed curve [10-15].

Several complex analytical models have been proposed using Coulomb's method of images [16,17], while others have solved Maxwell's equations more generally [18-21]. An interesting method has been proposed in several publications [4,22-26]. This method is based on a layer approach and is sometimes referred to as the Rogowski's method. It offers a very rigorous and methodical approach without excessive complexity and unlike most other methods, it allows describing the airgap and the air beyond the disc. It is most extensively described in [23]. The method proposed in the present chapter is derived from this method.

It is worth noting that only one publication [16] reports an attempt to optimize the design of an eddy-current brake and investigate the impact of design parameters on performance.

2 – Theoretical analysis derivations

Fig.10 below shows the basic eddy-current brake considered for the purpose of the analytical model. Only the rotor and the permanent magnets of alternate polarities are represented. The stator back-iron is not represented but is located in the plane immediately on top of the permanent magnets.

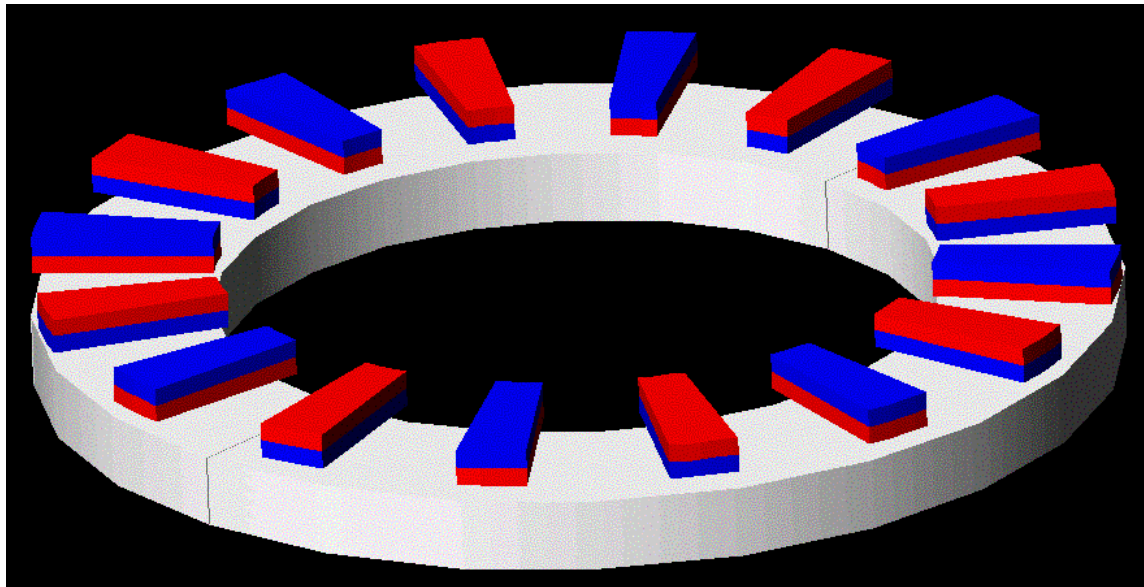


Fig. 10: Eddy-current brake

The problem is most easily described in a cylindrical coordinate system $(\bar{r}, \vec{\theta}, \bar{z})$.

The disc material is considered linear, whether magnetic or not. The problem can then be solved by superposition of two sub-problems: a static problem and an eddy-current problem. In the static problem, only the stator magnetization is considered. There are no eddy-currents. For the eddy-current problem, it is assumed no stator magnetization, only eddy-currents in the disc.

The geometry of the problem is invariant in the radial direction in the region of interest, i.e. from the inner radius to the outer radius. The magnetic field generated by the magnets is strictly confined to the $(\vec{\theta}, \bar{z})$ plane. If the width of the ring is much greater than its thickness, then it may be assumed that the eddy-currents are infinite in the radial direction and that the return paths of the currents have a negligible effect on the overall problem (see Fig. 11). The problem can thus be reduced to a two-dimensional approximation, in the $(\vec{\theta}, \bar{z})$ plane.

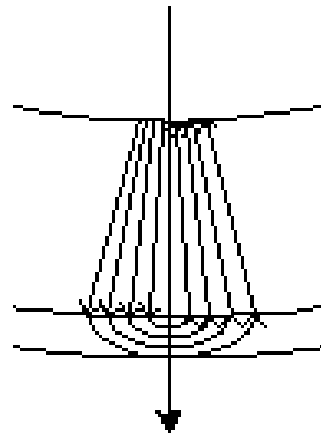


Fig. 11: Eddy-current paths

The geometry is divided into 3 regions: airgap, disc and air beyond the disc. The stator is modeled as a region of infinite permeability by the means of a boundary condition for the airgap. Fig. 12 shows the decomposition of the geometry into regions, where g is the airgap width and e is the thickness of the disc.

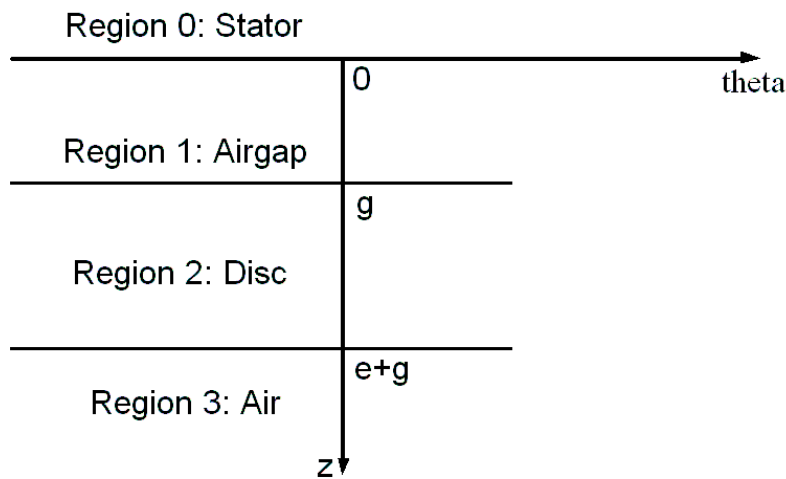


Fig. 12: Two-dimensional regions

2.1 – Modeling of the excitation field

The stator uses permanent magnets to generate the excitation flux. The magnets are defined using two parameters: the saturation magnetization M_{sat} and the coercive field H_{ci} . In the case of NdFeB magnets, the BH curve is linear in the operating quadrant (see Fig. 13), which corresponds to a magnetization of $+M_{sat}$.

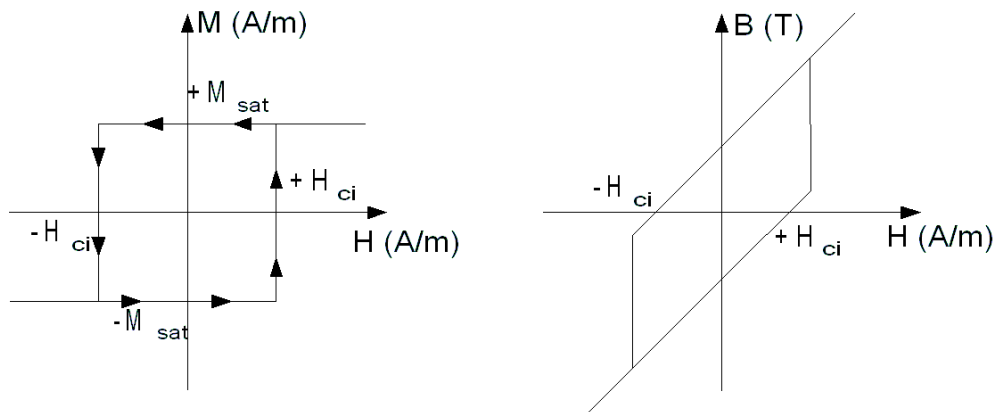


Fig. 13: Nd-Fe-B permanent magnet magnetization characteristics

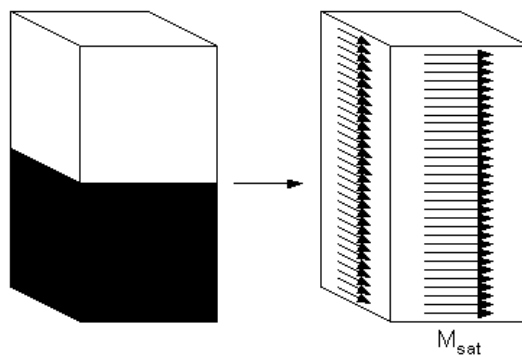


Fig. 14: Permanent-magnet / current sheet equivalence

The magnetization of a permanent magnet results in a surface current sheet, with a surface current density M_{sat} in amperes per meter (Fig. 14). This current sheet is analogous to a one-turn coil carrying a current given by:

$$I_0 = M_{sat} \cdot h_{magnet} \quad (5)$$

h_{magnet} is the height of the magnet in meters. The stator is modeled as a current sheet in the $(\vec{\theta}, \vec{z})$ plane. The current sheet is invariant in the z direction because the poles have an arc shape, therefore the magnetization profile needs only be described along the $\vec{\theta}$ axis. The decomposition of the magnetization profile follows. The stator has $2p$ poles, each with a magnet. Each pole pair spawns an arc of $2\pi/p$. Fig. 15 shows the angular dimensions of a pole pair.

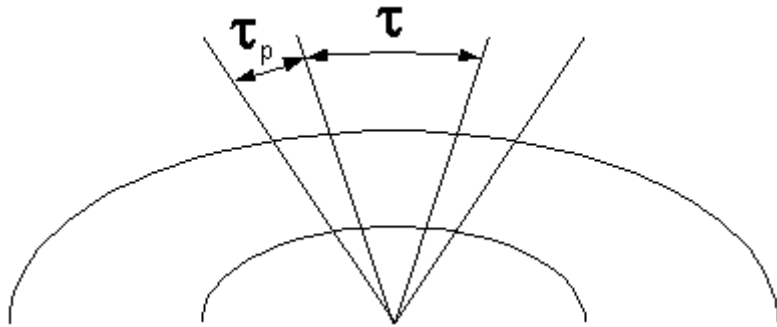


Fig. 15: Angular dimensions of a pole pair

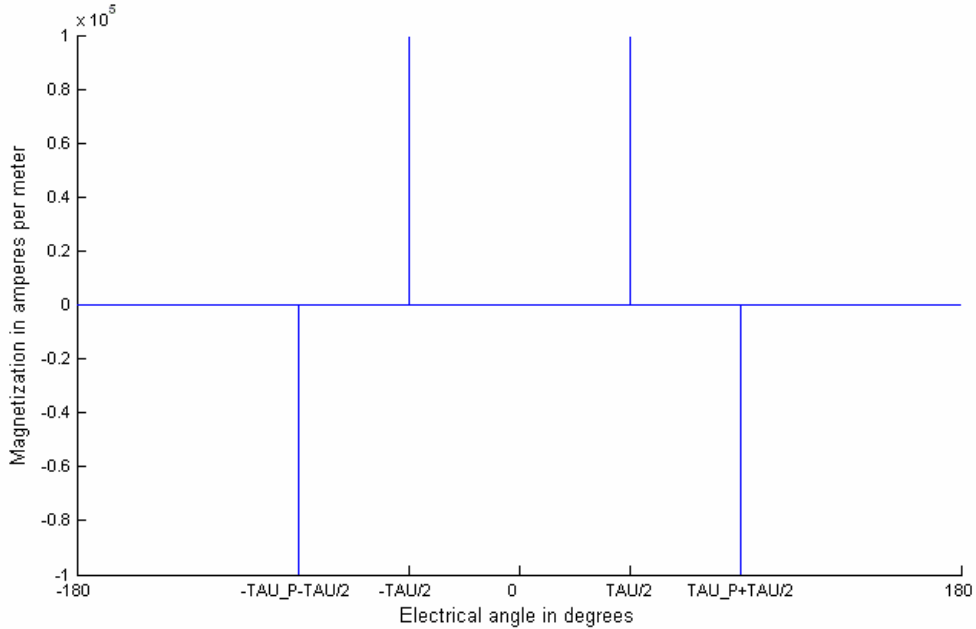


Fig. 16: Current sheet density profile of a pole pair

The magnetization profile is symmetrical about $\theta = 0$ (Fig. 16). Consequently, the decomposition is exclusively in cosine terms.

$$\begin{cases} a_h = \frac{2p}{\pi} \int_0^{\pi/p} M_s(\theta) \cdot \cos(h\theta) \cdot d\theta \\ b_h = 0 \end{cases} \quad (6)$$

While the magnetization profile is composed of impulses of null arc pitch, the modeling starts with impulses of finite width equal to τ_c :

$$a_h = \frac{2p \cdot I_0}{\pi \cdot \tau_c} \left(\int_{\frac{\tau}{2p} - \frac{\tau_p}{2p}}^{\frac{\tau}{2p} - \frac{\tau_p}{2p}} \cos(h\theta) \cdot d\theta - \int_{\frac{\tau}{2p} + \frac{\tau_p}{2p}}^{\frac{\tau}{2p} + \frac{\tau_p}{2p} + \tau_c} \cos(h\theta) \cdot d\theta \right) \quad (7)$$

$$a_h = \frac{2p \cdot I_0}{\pi \cdot h \cdot \tau_c} \left(\left[\sin(h\theta) \right]_{\frac{\tau}{2p} - \frac{\tau_p}{2p}}^{\frac{\tau}{2p} - \frac{\tau_p}{2p}} - \left[\sin(h\theta) \right]_{\frac{\tau}{2p} + \frac{\tau_p}{2p} - \tau_c}^{\frac{\tau}{2p} + \frac{\tau_p}{2p} + \tau_c} \right) \quad (8)$$

After some algebra:

$$a_h = \frac{8pI_0}{\pi h \tau_c} \sin\left(\frac{h\tau_c}{2p}\right) \sin\left(\frac{h\tau}{2p}\right) \sin\left(\frac{h(\tau_c + \tau_p)}{2p}\right) \quad (9)$$

Ideally, the current sheet around a magnet is infinitely thin. The corresponding magnetization profile is the limit of a_h when $\tau_c \rightarrow 0$:

$$a_h = \lim_{\tau_c \rightarrow 0} \left(\frac{8pI_0}{\pi h \tau_c} \sin\left(\frac{h\tau_c}{2p}\right) \sin\left(\frac{h\tau}{2p}\right) \sin\left(\frac{h(\tau_c + \tau_p)}{2p}\right) \right) \quad (10)$$

$$a_h = \frac{4pI_0}{\pi} \sin\left(\frac{h\tau_p}{2p}\right) \sin\left(\frac{h\tau}{2p}\right) \quad (11)$$

Finally, the rotational speed of the disc (ω , in radians per second) is factored in. All things being relative, it is assumed that the stator rotates with respect to a stationary disc. The magnetization profile is then modeled as a current wave traveling above the rotor:

$$M_s(\theta) = \sum_{h=1,2,3,\dots}^{+\infty} a_h \cdot \Re \left\{ e^{jh(\omega t - \theta)} \right\} \quad (12)$$

2.2 – Distribution of the excitation flux

In the static problem, Lorentz's law does not apply and since there are no currents in the airgap, rotor and air, Ampere's law reduces to:

$$\nabla \times \vec{H} = \vec{0} \quad (13)$$

Because the rotor material is considered linear, this law may be rewritten as:

$$\nabla \times \vec{B} = \vec{0} \quad (14)$$

The magnetic vector potential is used to simplify the solving of the problem:

$$\vec{B} = \nabla \times \vec{A} \quad (15)$$

Ampere's law is then written as:

$$\nabla \times \nabla \times \vec{B} = \vec{0} \quad (16)$$

$$\nabla \times \nabla \times \vec{B} = \nabla(\nabla \cdot \vec{A}) - \nabla^2 \vec{A} = \vec{0} \quad (17)$$

A Coulomb gauge is used:

$$\nabla \cdot \vec{A} = 0 \quad (18)$$

The static problem is then described by one single equation over the entire geometry::

$$\nabla^2 \vec{A} = \vec{0} \quad (19)$$

In the cylindrical system of coordinates used for the description of the eddy-current brake, the flux density components derive from the magnetic vector as:

$$\begin{cases} B_r = \frac{1}{r} \frac{\partial A_z}{\partial \theta} - \frac{\partial A_{\bar{\theta}}}{\partial z} \\ B_{\bar{\theta}} = \frac{\partial A_r}{\partial z} - \frac{\partial A_z}{\partial r} \\ B_z = \frac{1}{r} \left(\frac{\partial(rA_{\bar{\theta}})}{\partial r} - \frac{\partial A_r}{\partial \theta} \right) \end{cases} \quad (20)$$

In the 2D approximation of the problem, there is no flux density in the \vec{r} direction.

There are only components in the \vec{z} and $\vec{\theta}$ directions because the flux originates from

and loops back to the source in the $(\bar{z}, \bar{\theta})$ plane. Furthermore, the geometry is constant in the \vec{r} direction. Therefore:

$$\frac{\partial}{\partial r} = 0 \quad (21)$$

The two components of the flux density are thus expressed as:

$$\begin{cases} B_{\bar{r}} = 0 \\ B_{\bar{\theta}} = \frac{\partial A_{\bar{r}}}{\partial z} \\ B_{\bar{z}} = -\frac{1}{r} \frac{\partial A_{\bar{r}}}{\partial \theta} \end{cases} \quad (22)$$

Only the \bar{r} component of the magnetic vector potential needs to be considered. The general equation thus simplifies to:

$$\nabla^2 A_{\bar{r}} = 0 \quad (23)$$

$$\frac{1}{r} \frac{\partial}{\partial r} \left(r \frac{\partial A_{\bar{r}}}{\partial r} \right) + \frac{1}{r^2} \frac{\partial^2 A_{\bar{r}}}{\partial \theta^2} + \frac{\partial^2 A_{\bar{r}}}{\partial z^2} = 0 \quad (24)$$

The equation is further simplified due to the invariance of the problem in the radial direction:

$$\frac{1}{r^2} \frac{\partial^2 A_{\bar{r}}}{\partial \theta^2} + \frac{\partial^2 A_{\bar{r}}}{\partial z^2} = 0 \quad (25)$$

The solution of the equation is periodic in the angular direction with a periodicity defined by the stator. Therefore, the solution has the following form:

$$A_{\bar{r}} = f(z) \cdot \Re \left\{ e^{jh(\omega t - \theta)} \right\} \quad (26)$$

The differential equation thus becomes:

$$\frac{1}{r^2} f(z) \cdot \Re\{-jh)^2 e^{jh(\omega t-\theta)}\} + f''(z) \cdot \Re\{e^{jh(\omega t-\theta)}\} = 0 \quad (27)$$

$$-\frac{h^2}{r^2} f(z) \cdot \Re\{e^{jh(\omega t-\theta)}\} + f''(z) \cdot \Re\{e^{jh(\omega t-\theta)}\} = 0 \quad (28)$$

The diffusion term along the z axis is thus given by:

$$f''(z) - \frac{h^2}{r^2} f(z) = 0 \quad (29)$$

The characteristic equation for this differential equation is:

$$\lambda^2 + 0 \cdot \lambda - \frac{h^2}{r^2} = 0 \quad (30)$$

With the following discriminator:

$$\Delta = 4 \frac{h^2}{r^2} \quad (31)$$

The discriminator is always positive, so the roots of the characteristic equation are:

$$\lambda_{1,2} = \pm \frac{h}{r} \quad (32)$$

For the static problem, the general form of the radial component of the magnetic vector potential is thus:

$$A_{r0} = \left(C e^{\frac{h}{r}z} + D e^{-\frac{h}{r}z} \right) \cdot \Re\{e^{jh(\omega t-\theta)}\} \quad (33)$$

C and D are coefficients determined by boundary conditions. The magnetic vector potential can thus be written for the airgap, the disc and the air beyond the disc:

$$A_{r01} = \left(C_1 e^{\frac{h}{r}z} + D_1 e^{-\frac{h}{r}z} \right) \cdot \Re\{e^{jh(\omega t-\theta)}\} \quad (34)$$

$$A_{\bar{r}02} = \left(C_2 e^{\frac{h}{r}z} + D_2 e^{-\frac{h}{r}z} \right) \cdot \Re \{ e^{jh(\omega t - \theta)} \} \quad (35)$$

$$A_{\bar{r}03} = \left(C_3 e^{\frac{h}{r}z} + D_3 e^{-\frac{h}{r}z} \right) \cdot \Re \{ e^{jh(\omega t - \theta)} \} \quad (36)$$

The tangential magnetic field is defined at the surface of the stator:

$$H_{airgap} - H_{stator} = M_s \quad (37)$$

The permeability of the stator was assumed to be infinite. Therefore, there is no field in the stator, which is modeled as a boundary condition in the airgap:

$$H_{\bar{\theta}01} = M_s(\theta, t) \quad (38)$$

$$B_{\bar{\theta}01} = \mu_0 M_s(\theta, t) \quad (39)$$

$$\frac{\partial A_{\bar{r}01}}{\partial z} = M_{sh} \cdot \Re \{ e^{jh(\omega t - \theta)} \} \quad (40)$$

$$\left(C_1 \frac{h}{r} e^{\frac{h}{r}z} - D_1 \frac{h}{r} e^{-\frac{h}{r}z} \right) \cdot \Re \{ e^{jh(\omega t - \theta)} \} = \mu_0 M_{sh} \cdot \Re \{ e^{jh(\omega t - \theta)} \} \quad (41)$$

μ_0 is the permeability of vacuum. The boundary condition equation at the surface of the stator ($z = 0$) is thus:

$$C_1 - D_1 = \frac{r}{h} \mu_0 M_{sh} \quad (42)$$

The second boundary condition is the conservation of normal flux at the interface between the airgap and the disc ($z = g$):

$$B_{\bar{z}01}(z = g) = B_{\bar{z}02}(z = g) \quad (43)$$

$$-\frac{1}{r} \frac{\partial A_{\bar{r}01}}{\partial \theta} = -\frac{1}{r} \frac{\partial A_{\bar{r}02}}{\partial \theta} \quad (44)$$

$$\left(C_1 e^{\frac{h}{r}z} + D_1 e^{-\frac{h}{r}z} \right) \cdot \Re \left\{ -j \cdot e^{jh(\omega t - \theta)} \right\} = \left(C_2 e^{\frac{h}{r}z} + D_2 e^{-\frac{h}{r}z} \right) \cdot \Re \left\{ -j \cdot e^{jh(\omega t - \theta)} \right\} \quad (45)$$

Thus the second boundary condition equation is:

$$C_1 e^{\frac{h}{r}g} + D_1 e^{-\frac{h}{r}g} - C_2 e^{\frac{h}{r}g} - D_2 e^{-\frac{h}{r}g} = 0 \quad (46)$$

The third boundary condition is the conservation of the tangential field at the airgap-disc interface ($z = g$):

$$H_{\bar{\theta}01}(z = g) = H_{\bar{\theta}02}(z = g) \quad (47)$$

$$\frac{B_{\bar{\theta}01}(z = g)}{\mu_0} = \frac{B_{\bar{\theta}02}(z = g)}{\mu_0 \mu_r} \quad (48)$$

$$\mu_r \frac{\partial A_{\bar{r}01}}{\partial z}(z = g) = \frac{\partial A_{\bar{r}02}}{\partial z}(z = g) \quad (49)$$

$$\mu_r \frac{h}{r} \left(C_1 e^{\frac{h}{r}g} - D_1 e^{-\frac{h}{r}g} \right) = \frac{h}{r} \left(C_2 e^{\frac{h}{r}g} - D_2 e^{-\frac{h}{r}g} \right) \quad (50)$$

μ_r is the relative magnetic permeability of the disc material. The third boundary condition equation is:

$$\mu_r C_1 e^{\frac{h}{r}g} - \mu_r D_1 e^{-\frac{h}{r}g} - C_2 e^{\frac{h}{r}g} + D_2 e^{-\frac{h}{r}g} = 0 \quad (51)$$

The fourth and fifth boundary condition equations are similar to the second and third, and are computed at the disc-air interface ($z = g + e$):

$$C_2 e^{\frac{h(g+e)}{r}} + D_2 e^{-\frac{h(g+e)}{r}} - C_3 e^{\frac{h(g+e)}{r}} - D_3 e^{-\frac{h(g+e)}{r}} = 0 \quad (52)$$

$$C_2 e^{\frac{h}{r}(g+e)} - D_2 e^{-\frac{h}{r}(g+e)} - \mu_r C_3 e^{\frac{h}{r}(g+e)} + \mu_r D_3 e^{-\frac{h}{r}(g+e)} = 0 \quad (53)$$

The sixth boundary condition is the vanishing of the fields at infinity in the air, which results in the sixth boundary condition equation:

$$C_3 = 0 \quad (54)$$

The sixth equations can be reduced to five by inserting the sixth into the fourth and fifth.

The static problem can be written in matrix form:

$$\begin{bmatrix} 1 & -1 & 0 & 0 & 0 \\ e^{\frac{h}{r}g} & e^{-\frac{h}{r}g} & -e^{\frac{h}{r}g} & -e^{-\frac{h}{r}g} & 0 \\ \mu_r e^{\frac{h}{r}g} & -\mu_r e^{-\frac{h}{r}g} & -e^{\frac{h}{r}g} & e^{-\frac{h}{r}g} & 0 \\ 0 & 0 & e^{\frac{h}{r}(g+e)} & e^{-\frac{h}{r}(g+e)} & -e^{-\frac{h}{r}(g+e)} \\ 0 & 0 & e^{\frac{h}{r}(g+e)} & -e^{-\frac{h}{r}(g+e)} & \mu_r e^{-\frac{h}{r}(g+e)} \end{bmatrix} \cdot \begin{bmatrix} C_1 \\ D_1 \\ C_2 \\ D_2 \\ D_3 \end{bmatrix} = \begin{bmatrix} \frac{r}{h} \mu_0 M_{sh} \\ 0 \\ 0 \\ 0 \\ 0 \end{bmatrix} \quad (55)$$

2.3 – Distribution of eddy-currents and associated fields

The differential equations in the airgap and in the air are similar for the eddy-current and static problem because there are no eddy-currents in these two regions. The differential equation describing the eddy-current problem in the disc is derived from Lorentz' law:

$$\nabla \times \vec{E} + \frac{\partial \vec{B}}{\partial t} = \vec{0} \quad (56)$$

$$\nabla \times \sigma \vec{E} + \sigma \frac{\partial \vec{B}}{\partial t} = \vec{0} \quad (57)$$

σ is the conductivity of the disc material expressed in Siemens. The application of Ohm's law yields:

$$\nabla \times \vec{J}_1 + \sigma \frac{\partial \vec{B}}{\partial t} = \vec{0} \quad (58)$$

The current density corresponds to eddy-currents. By Ampere's law, these eddy-currents generate a magnetic field:

$$\nabla \times \nabla \times \vec{H}_1 + \sigma \frac{\partial \vec{B}}{\partial t} = \vec{0} \quad (59)$$

The subscript "1" is necessary to later distinguish the field variables resulting from eddy-currents from the total field variables. The flux density is introduced:

$$\nabla \times \nabla \times \mu_0 \mu_r \vec{H}_1 + \sigma \mu_0 \mu_r \frac{\partial \vec{B}}{\partial t} = \vec{0} \quad (60)$$

$$\nabla \times \nabla \times \vec{B}_1 + \sigma \mu_0 \mu_r \frac{\partial \vec{B}}{\partial t} = \vec{0} \quad (61)$$

The distinction must be clearly made between the flux density resulting from eddy-currents (\vec{B}_1) and the total flux density, which corresponds to the following sum:

$$\vec{B} = \vec{B}_0 + \vec{B}_1 \quad (62)$$

The magnetic vector potential is introduced:

$$\nabla \times \nabla \times \nabla \times \vec{A}_1 + \sigma \mu_0 \mu_r \frac{\partial (\nabla \times (\vec{A}_0 + \vec{A}_1))}{\partial t} = \vec{0} \quad (63)$$

$$\nabla \times \left(\nabla \times \nabla \times \vec{A}_1 + \sigma \mu_0 \mu_r \frac{\partial (\vec{A}_0 + \vec{A}_1)}{\partial t} \right) = \vec{0} \quad (64)$$

$$\nabla \times \nabla \times \vec{A}_1 + \sigma \mu_0 \mu_r \frac{\partial (\vec{A}_0 + \vec{A}_1)}{\partial t} = \vec{0} \quad (65)$$

$$\nabla(\nabla \cdot \vec{A}_1) - \nabla^2 \vec{A}_1 + \sigma \mu_0 \mu_r \frac{\partial (\vec{A}_0 + \vec{A}_1)}{\partial t} = \vec{0} \quad (66)$$

Since a Coulomb gauge is used, the equation reduces to:

$$\nabla^2 \vec{A}_l - \sigma \mu_0 \mu_r \frac{\partial(\vec{A}_0 + \vec{A}_l)}{\partial t} = \vec{0} \quad (67)$$

Only the radial component of the magnetic vector potential is of interest for the problem:

$$\frac{1}{r^2} \frac{\partial^2 A_{\vec{r}12}}{\partial \theta^2} + \frac{\partial^2 A_{\vec{r}12}}{\partial z^2} - \mu_0 \mu_r \sigma \frac{\partial(A_{\vec{r}02} + A_{\vec{r}12})}{\partial t} = 0 \quad (68)$$

The general form of the solution is as follows:

$$A_{\vec{r}12} = \left(R_2 e^{\frac{\alpha}{r}z} + S_2 e^{-\frac{\alpha}{r}z} \right) \cdot \Re \{ e^{jh(\omega t - \theta)} \} \quad (69)$$

It can be demonstrated that $A_{\vec{r}12} = -A_{\vec{r}02}$ is a particular solution of the differential equation:

$$-\frac{1}{r^2} \frac{\partial^2 A_{\vec{r}02}}{\partial \theta^2} - \frac{\partial^2 A_{\vec{r}02}}{\partial z^2} - \mu_0 \mu_r \sigma \frac{\partial(A_{\vec{r}02} - A_{\vec{r}02})}{\partial t} = 0 \quad (70)$$

$$-\frac{1}{r^2} \frac{\partial^2 A_{\vec{r}02}}{\partial \theta^2} - \frac{\partial^2 A_{\vec{r}02}}{\partial z^2} = 0 \quad (71)$$

$$A_{\vec{r}02} = \left(C_2 e^{\frac{h}{r}z} + D_2 e^{-\frac{h}{r}z} \right) \cdot \Re \{ e^{jh(\omega t - \theta)} \} \quad (72)$$

$$\frac{h^2}{r^2} \left(C_2 e^{\frac{h}{r}z} + D_2 e^{-\frac{h}{r}z} \right) \cdot \Re \{ e^{jh(\omega t - \theta)} \} - \frac{h^2}{r^2} \left(C_2 e^{\frac{h}{r}z} + D_2 e^{-\frac{h}{r}z} \right) \cdot \Re \{ e^{jh(\omega t - \theta)} \} = 0 \quad (73)$$

The general and particular forms are inserted in the differential equation, which yields the following after elimination of the periodic terms:

$$\frac{\alpha^2}{r^2} \left(R_2 e^{\frac{\alpha}{r}z} + S_2 e^{-\frac{\alpha}{r}z} \right) - \frac{h^2}{r^2} \left(R_2 e^{\frac{\alpha}{r}z} + S_2 e^{-\frac{\alpha}{r}z} \right) = j \mu_0 \mu_r \alpha h \left(R_2 e^{\frac{\alpha}{r}z} + S_2 e^{-\frac{\alpha}{r}z} \right) \quad (74)$$

Then:

$$-\frac{h^2}{r^2} + \frac{\alpha^2}{r^2} - \mu_0 \mu_r j \omega h = 0 \quad (75)$$

Therefore:

$$\alpha^2 = h^2 + j r^2 \mu_0 \mu_r \sigma \omega \quad (76)$$

The solutions of the eddy-current problem for each region are:

$$A_{\bar{r}11} = \left(R_1 e^{\frac{h}{r}z} + S_1 e^{-\frac{h}{r}z} \right) \cdot \Re \{ e^{jh(\omega t - \theta)} \} \quad (77)$$

$$A_{\bar{r}12} = \left(R_2 e^{\frac{\alpha}{r}z} + S_2 e^{-\frac{\alpha}{r}z} \right) \cdot \Re \{ e^{jh(\omega t - \theta)} \} - \left(C_2 e^{\frac{h}{r}z} + D_2 e^{-\frac{h}{r}z} \right) \cdot \Re \{ e^{jh(\omega t - \theta)} \} \quad (78)$$

$$A_{\bar{r}13} = \left(R_3 e^{\frac{h}{r}z} + S_3 e^{-\frac{h}{r}z} \right) \cdot \Re \{ e^{jh(\omega t - \theta)} \} \quad (79)$$

The coefficients are determined by boundary conditions. At the interface between the stator and the airgap ($z = 0$), the flux density is exclusively normal because of the assumption that the stator has an infinite permeability:

$$B_{\bar{\theta}11} = 0 \quad (80)$$

$$\frac{\partial A_{\bar{r}11}}{\partial z} = 0 \quad (81)$$

$$\frac{h}{r} \left(R_1 e^{\frac{h}{r}z} - S_1 e^{-\frac{h}{r}z} \right) \cdot \Re \{ e^{jh(\omega t - \theta)} \} = 0 \quad (82)$$

$$R_1 e^{\frac{h}{r}z} - S_1 e^{-\frac{h}{r}z} = 0 \quad (83)$$

At $z = 0$:

$$R_1 - S_1 = 0 \quad (84)$$

At the interface airgap-disc, the conservation of normal flux density and tangential field yields the second and third boundary condition equations:

$$B_{\bar{z}11}(z = g) = B_{\bar{z}12}(z = g) \quad (85)$$

$$B_{\bar{\theta}11}(z = g) = B_{\bar{\theta}12}(z = g) \quad (86)$$

The two equations are obtained after elimination of periodic and common terms:

$$R_1 e^{\frac{h}{r}g} + S_1 e^{-\frac{h}{r}g} - R_2 e^{\frac{\alpha}{r}g} - S_2 e^{-\frac{\alpha}{r}g} = - \left(C_2 e^{\frac{h}{r}g} + D_2 e^{-\frac{h}{r}g} \right) \quad (87)$$

$$\mu_r \frac{h}{r} R_1 e^{\frac{h}{r}g} - \mu_r \frac{h}{r} S_1 e^{-\frac{h}{r}g} - \frac{\alpha}{r} R_2 e^{\frac{\alpha}{r}g} + \frac{\alpha}{r} S_2 e^{-\frac{\alpha}{r}g} = - \frac{h}{r} \left(C_2 e^{\frac{h}{r}g} - D_2 e^{-\frac{h}{r}g} \right) \quad (88)$$

The same conditions apply to the disc-air interface and yield:

$$R_2 e^{\frac{\alpha}{r}(g+e)} + S_2 e^{-\frac{\alpha}{r}(g+e)} - S_3 e^{-\frac{h}{r}(g+e)} = C_2 e^{\frac{h}{r}(g+e)} + D_2 e^{-\frac{h}{r}(g+e)} \quad (89)$$

$$\frac{\alpha}{r} R_2 e^{\frac{\alpha}{r}(g+e)} - \frac{\alpha}{r} S_2 e^{-\frac{\alpha}{r}(g+e)} + \mu_r \frac{h}{r} S_3 e^{-\frac{h}{r}(g+e)} = \frac{h}{r} \left(C_2 e^{\frac{h}{r}(g+e)} - D_2 e^{-\frac{h}{r}(g+e)} \right) \quad (90)$$

Finally, the condition that the fields must vanish at infinity yields:

$$R_3 = 0 \quad (91)$$

The equation relative to the eddy-current problem can be written in matrix form:

$$A \cdot X = B \quad (92)$$

$$A = \begin{bmatrix} 1 & -1 & 0 & 0 & 0 \\ e^{\frac{h}{r}g} & e^{-\frac{h}{r}g} & -e^{\frac{h}{r}g} & -e^{-\frac{h}{r}g} & 0 \\ \mu_r \frac{h}{r} e^{\frac{h}{r}g} & -\mu_r \frac{h}{r} e^{-\frac{h}{r}g} & -\frac{\alpha}{r} e^{\frac{\alpha}{r}g} & \frac{\alpha}{r} e^{-\frac{\alpha}{r}g} & 0 \\ 0 & 0 & e^{\frac{\alpha(g+e)}{r}} & e^{-\frac{\alpha(g+e)}{r}} & -e^{-\frac{k(g+e)}{r}} \\ 0 & 0 & \frac{\alpha}{r} e^{\frac{\alpha(g+e)}{r}} & -\frac{\alpha}{r} e^{-\frac{\alpha(g+e)}{r}} & \mu_r \frac{h}{r} e^{-\frac{h}{r}(g+e)} \end{bmatrix} \quad (93)$$

$$X = \begin{bmatrix} R_1 \\ S_1 \\ R_2 \\ S_2 \\ S_3 \end{bmatrix} \quad (94)$$

$$B = \begin{bmatrix} 0 \\ -\left(C_2 e^{\frac{h}{r}g} + D_2 e^{-\frac{h}{r}g} \right) \\ \frac{h}{r} \left(D_2 e^{-\frac{h}{r}g} - C_2 e^{\frac{h}{r}g} \right) \\ C_2 e^{\frac{h}{r}(g+e)} + D_2 e^{-\frac{h}{r}(g+e)} \\ \frac{h}{r} \left(C_2 e^{\frac{h}{r}(g+e)} - D_2 e^{-\frac{h}{r}(g+e)} \right) \end{bmatrix} \quad (95)$$

It is important to notice that the solution of each problem depends on the radius r and on the harmonics order h . It can be demonstrated numerically that a limited number of values of r and a linear extrapolation in between provides sufficient accuracy due to the monotonic character of the solution. Similarly, the computation for a limited number of harmonics is required because the effects on flux density distribution, eddy-current distribution and braking force diminish very rapidly with increasing harmonic order.

2.4 – Computation of the braking force

The braking force can be computed at any depth, radius and angular position:

$$\Delta \vec{F} = \vec{J}_{ec} \times \vec{B}_{total} \quad (96)$$

The use of complex notations allows removing the periodic terms from the solution:

$$J_{ec} = J_m \cdot \cos(\omega t + \phi) \quad (97)$$

$$B_{total} = B_m \cdot \cos(\omega t + \phi) \quad (98)$$

The instantaneous force resulting from their interaction is:

$$F_{\bar{x}}(t) = J_m B_m \cos^2(\omega t + \phi) \quad (99)$$

The average force is then:

$$F_{avg} = \frac{\omega}{2\pi} \int_0^{2\pi} J_m B_m \cos^2(\omega t + \phi) \cdot dt \quad (100)$$

$$F_{avg} = \frac{1}{2} J_m B_m \quad (101)$$

The same result can be obtained by using complex notations:

$$\tilde{J}_{ec} = J_m \cdot e^{j(\omega t + \phi)} \quad (102)$$

$$\tilde{B}_{total} = B_m \cdot e^{j(\omega t + \phi)} \quad (103)$$

The complex conjugate of the flux density is:

$$\tilde{B}_{total}^* = B_m \cdot e^{-j(\omega t + \phi)} \quad (104)$$

The force is thus expressed as:

$$F_{avg} = \frac{1}{2} \tilde{J}_{ec} \cdot \tilde{B}_{total}^* \quad (105)$$

$$F_{avg} = \frac{1}{2} J_m \cdot B_m \quad (106)$$

Consequently:

$$\Delta \vec{F} = \vec{J}_{ec} \times \vec{B}_{total}^* \quad (107)$$

$$\Delta \vec{F} = \begin{vmatrix} J_{\bar{r}} & 0 & 0 \\ 0 & B_{\bar{\theta}}^* & -J_{\bar{r}} \cdot B_{\bar{z}}^* \rightarrow \Delta F_{braking} \\ 0 & B_{\bar{z}}^* & J_{\bar{r}} \cdot B_{\bar{\theta}}^* \rightarrow \Delta F_{lateral} \end{vmatrix} \quad (108)$$

In complex notation, the flux density vector is written as:

$$\vec{B}_{total} = \begin{cases} 0 \\ B_{\bar{\theta}} = \frac{\alpha}{r} \left(R_2 e^{\frac{\alpha z}{r}} - S_2 e^{-\frac{\alpha z}{r}} \right) e^{jh(\omega t - \theta)} \\ B_{\bar{z}} = j \frac{h}{r} \left(R_2 e^{\frac{\alpha z}{r}} + S_2 e^{-\frac{\alpha z}{r}} \right) e^{jh(\omega t - \theta)} \end{cases} \quad (109)$$

The eddy-current density is obtained from Lorentz's law:

$$\nabla \times \vec{E} + \frac{\partial \vec{B}}{\partial t} = \vec{0} \quad (110)$$

$$\vec{B} = \nabla \times \vec{A} \quad (111)$$

$$\nabla \times \vec{E} + \frac{\partial(\nabla \times \vec{A})}{\partial t} = \vec{0} \quad (112)$$

$$\vec{E} + \frac{\partial \vec{A}}{\partial t} = \vec{0} \quad (113)$$

$$\sigma \vec{E} + \sigma \frac{\partial \vec{A}}{\partial t} = \vec{0} \quad (114)$$

$$\vec{J} = -\sigma \frac{\partial \vec{A}}{\partial t} \quad (115)$$

The only component of the current density is thus:

$$J_{\vec{r}} \sim jh\sigma\omega \cdot \left(R_2 e^{\frac{\alpha}{r}z} + S_2 e^{-\frac{\alpha}{r}z} \right) \cdot e^{jh(\omega t - \theta)} \quad (116)$$

Therefore, the braking force is:

$$\begin{aligned} \Delta F_{\bar{\theta}} = & \\ & - jh\sigma\omega \left(R_2 e^{\frac{\alpha}{r}z} + S_2 e^{-\frac{\alpha}{r}z} \right) e^{jh(\omega t - \theta)} \left[j \frac{h}{r} \left(R_2 e^{\frac{\alpha}{r}z} + S_2 e^{-\frac{\alpha}{r}z} \right) e^{jh(\omega t - \theta)} \right]^* \end{aligned} \quad (117)$$

$$\begin{aligned} \Delta F_{\bar{\theta}} = & \\ & - jh\sigma\omega \left(R_2 e^{\frac{\alpha}{r}z} + S_2 e^{-\frac{\alpha}{r}z} \right) \left[j \frac{h}{r} \left(R_2 e^{\frac{\alpha}{r}z} + S_2 e^{-\frac{\alpha}{r}z} \right) \right]^* e^{jh(\omega t - \theta)} \left(e^{jh(\omega t - \theta)} \right)^* \end{aligned} \quad (118)$$

$$\Delta F_{\bar{\theta}} = - jh\sigma\omega \cdot \left[j \frac{h}{r} \right]^* \cdot \left(R_2 e^{\frac{\alpha}{r}z} + S_2 e^{-\frac{\alpha}{r}z} \right) \cdot \left(R_2 e^{\frac{\alpha}{r}z} + S_2 e^{-\frac{\alpha}{r}z} \right)^* \quad (119)$$

$$\Delta F_{\bar{\theta}} = - \frac{h^2}{r} \sigma\omega \cdot \left\| R_2 e^{\frac{\alpha}{r}z} + S_2 e^{-\frac{\alpha}{r}z} \right\|^2 \quad (120)$$

The total braking force is obtained by integration of the elemental force:

$$F_{braking} = \int_g^{g+e} dz \int_0^{2\pi} d\theta \int_{Rinner}^{Router} \Delta F_{\bar{\theta}} \cdot r \cdot dr \quad (121)$$

Because R_2, S_2 are dependant upon the radius, it is very difficult to integrate the braking force by hand along the \vec{z} and \vec{r} axes. Note that the integration along the angular direction is straightforward:

$$\int_0^{2\pi} \Delta F_{\bar{\theta}} \cdot d\theta = -2\pi \frac{h^2}{r} \sigma\omega \cdot \left\| R_2 e^{\frac{\alpha}{r}z} + S_2 e^{-\frac{\alpha}{r}z} \right\|^2 \quad (122)$$

The integration is performed numerically along the \vec{z} and \vec{r} axes. The braking torque is obtained by integrating the elemental torque:

$$T_{braking} = \int_g^{g+e} dz \int_0^{2\pi} d\theta \int_{Rinner}^{Router} r \cdot \Delta F_\theta \cdot r \cdot dr \quad (123)$$

3 – Investigation of eddy-current braking using the analytical model

3.1 – Implementation of the analytical model

Due to their complexity, the results of the analytical derivations are implemented and computed using Matlab ®. The braking torque is computed for a broad speed range. Flux density and current density maps are also computed for each speed. Fig. 17 shows the algorithm used.

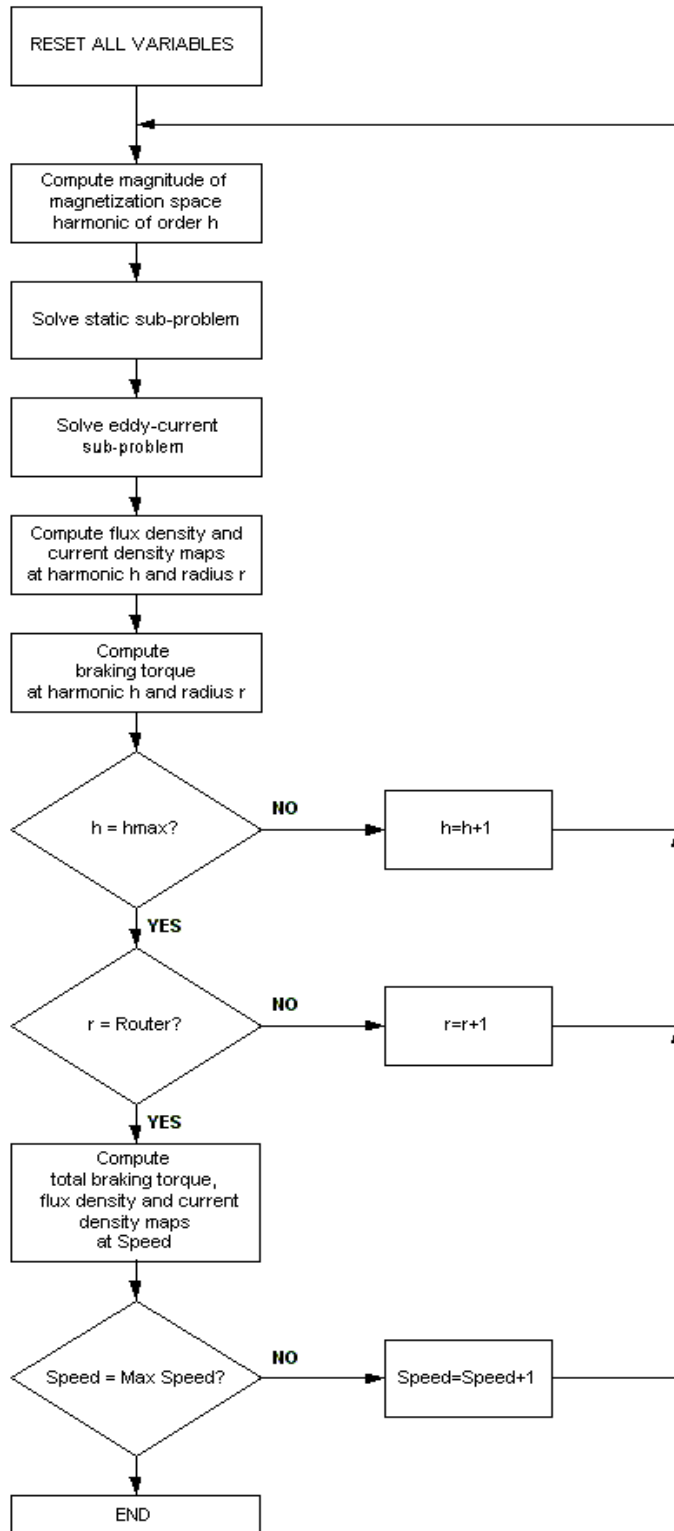


Fig. 17: Implementation algorithm

3.2 – Fundamental physics of eddy-current brakes

3.2.1 – Eddy-current brake torque-speed curve

Fig. 18 shows the torque-speed curve a brake with the design parameters in TABLE 3.

TABLE 3
Brake design parameters

PARAMETER	SYMBOL	VALUE
Permanent magnet remnant flux	B_r	$1.3T$
Height of permanent magnet	h_{magnet}	$10mm$
Relative permeability of disc material	μ_r	1
Conductivity of disc material	σ	$5.8 \times 10^7 \Omega^{-1}$
Number of pole pairs	p	8
Pole width	τ_p	60°
Arc between north and south pole	τ	180°
Airgap width	g	$1mm$
Disc thickness	e	$20mm$
Disc inner radius	R_{inner}	$100mm$
Disc outer radius	R_{outer}	$150mm$

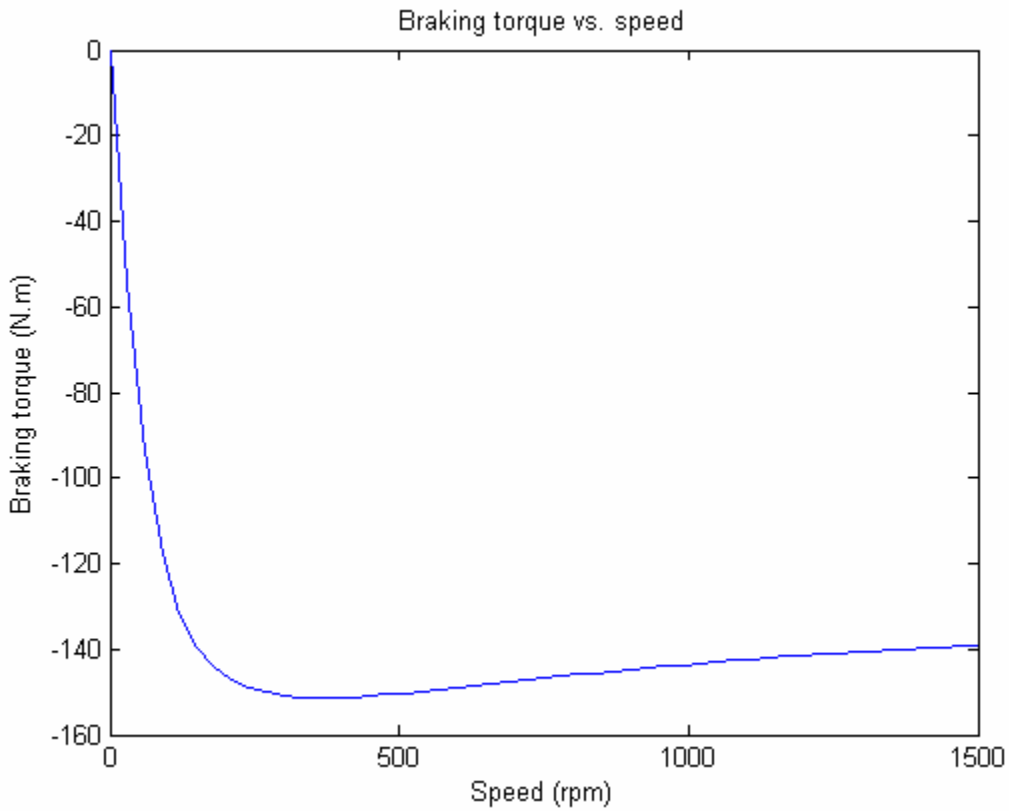


Fig. 18: Typical torque-speed curve for an eddy-current brake

The torque speed curve of an eddy-current brake has four salient characteristics:

- No torque at zero speed: Lenz's law dictates that a time invariant flux density may not result in an electric field. Therefore, at zero speed no eddy-currents are induced in the brake's disc and no torque results.
- Linear torque region: As the disc gathers speed, it sees a time-variant flux density and eddy-currents are induced. Because the currents have a low amplitude, their resulting magnetic field does not oppose significantly the excitation field produced by the magnets. Therefore, the amplitude of the currents is primarily

dictated by Lenz's law and evolves almost linearly with speed. Consequently the braking torque is proportional to the eddy-current magnitude and evolves almost linearly with speed.

- Critical speed: This is the speed at which the braking torque peaks. The reaction field resulting from the eddy-currents is no longer negligible and begins to weaken the field produced by the magnets. The braking force evolves slower than the speed and eventually peaks at critical speed.
- High speed region: Beyond critical speed, the reaction field produced by eddy-currents evolves faster than speed and weakens the net product of total flux density and eddy-currents. The braking force continuously decreases.

It is worth noting that the typical torque-speed characteristic of an eddy-current brake is very similar to that of an induction motor, only with a reversed speed axis. This is due to the similarities in structures between the two machines. In fact, some induction motors are built with a plain rotor rather than a squirrel cage. They are referred to as “smooth-rotor” induction motors [27-31]. An eddy-current brake is an induction motor with stator windings energized by dc currents.

3.2.2 – Distribution of the flux and current densities

Following is a series of contour plots of the two functional variables of the eddy-current brake, i.e. flux density and eddy-current density. These plots have been generated for the four characteristics operating points or regions of the brake.

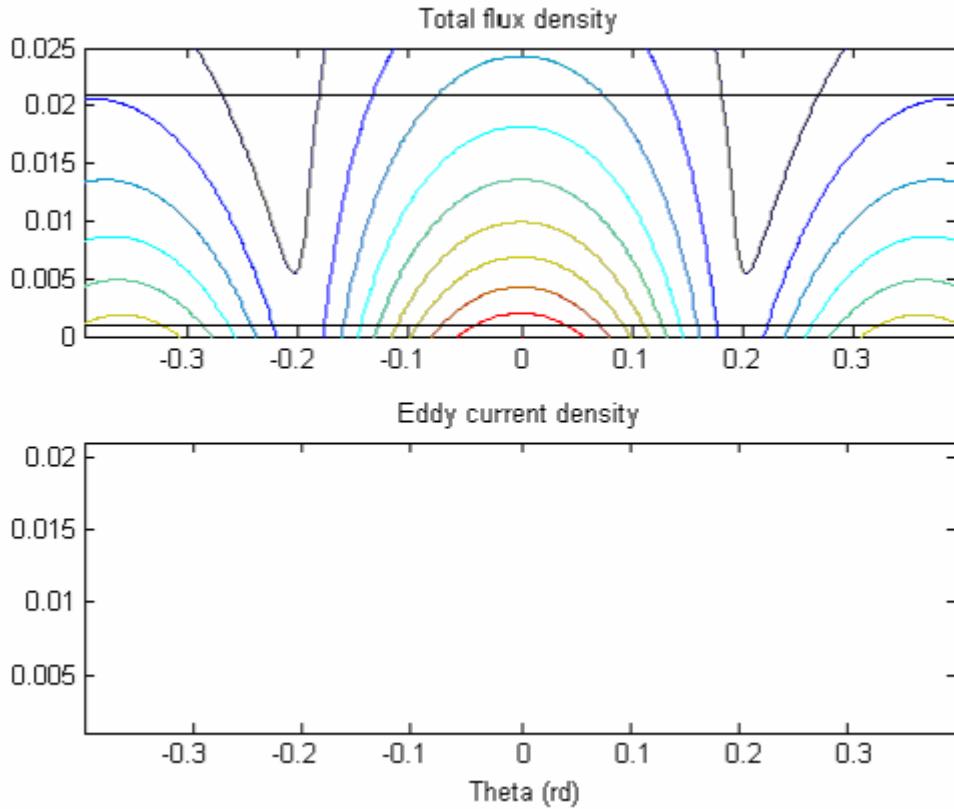


Fig. 19: Flux density and current density map for a pole pair at standstill

Fig. 19 shows the contour maps of flux density and eddy-current density in the airgap and disc of the brake in the $(\vec{\theta}, \vec{z})$ plane at zero speed. The flux density lines conform to theory by looping around the edges of the magnets. Because the disc is made of a non-magnetic material, there is no discontinuity of the flux lines at the interface between the disc and air. Due to the null speed, there are no eddy-currents induced. The flux density loops strictly in the $(\vec{\theta}, \vec{z})$ plane: there is no component in the radial direction.

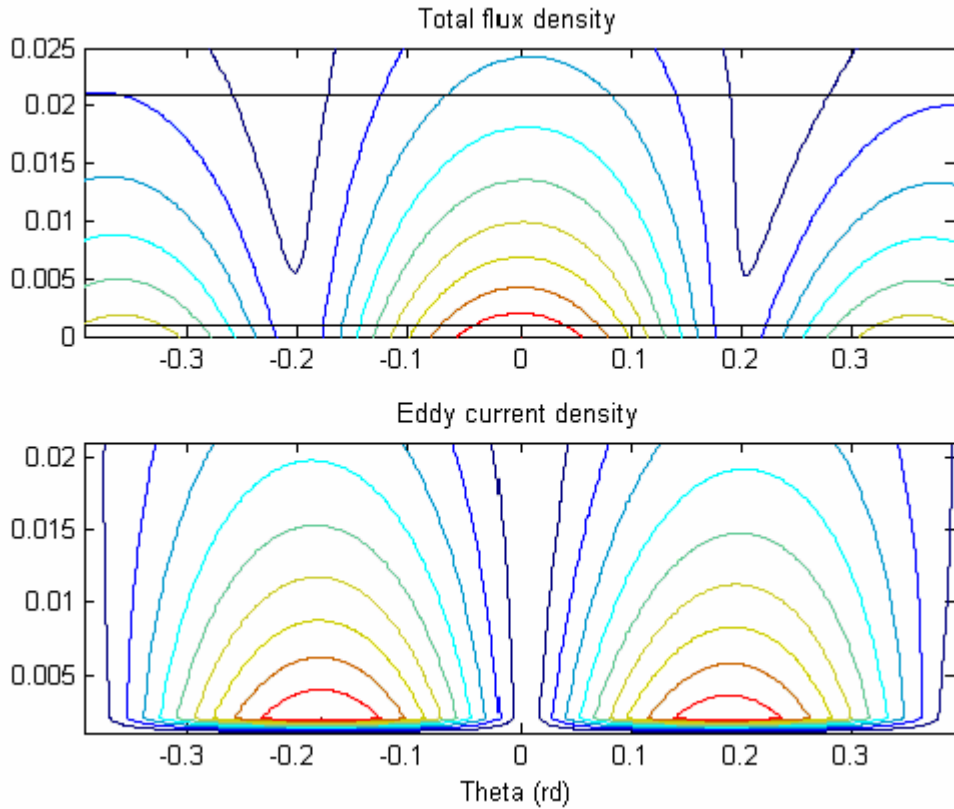


Fig. 20: Flux and current density map for a pole pair at 1% of critical speed

Fig. 20 shows the contour maps of flux density and eddy-current density in the airgap and disc of the brake in the $(\bar{\theta}, \bar{z})$ plane at very low speed (1% of critical speed). The slight motion results in eddy-currents circulating in the disc. The epicenters of current production are at the surface of the disc in the airgap, exactly below the edges of the magnets. The leading edges of the magnets produce currents in direction opposite to the trailing edges. Eddy-currents circulate in the radial direction, perpendicular to the $(\bar{\theta}, \bar{z})$ plane displayed on Fig. 20. The flux density contour is similar to the standstill contour plot, being insignificantly affected by the reaction from eddy-currents. Note that the

contours are symmetrical with respect to the axes of the magnets. They are aligned along lines that are parallel to the magnets' axes.

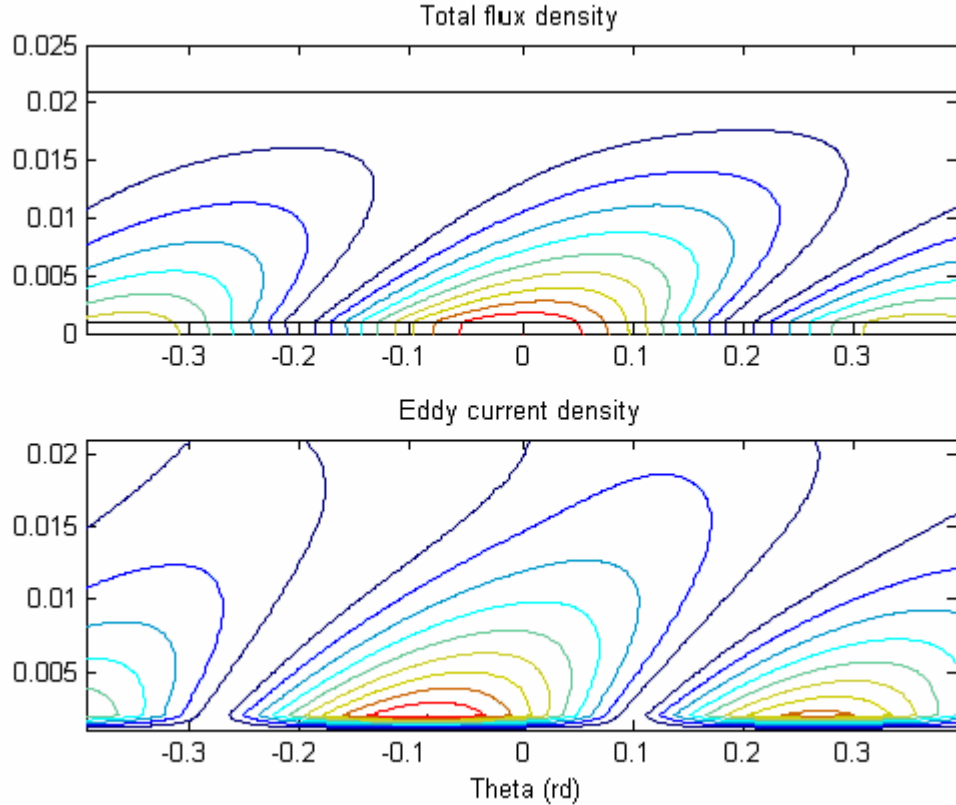


Fig. 21: Flux density and current density map for a pole pair at critical speed

Fig. 21 shows the contour maps of flux density and eddy-current density in the airgap and disc of the brake in the $(\bar{\theta}, \bar{z})$ plane at critical speed. Eddy-currents are now much stronger and their field weakens significantly the field of the magnets. This is the basis of the skin effect, which results in current density and flux density values decreasing exponentially with depth in the disc. The reaction field of eddy-currents also tilts the axis

of the contour plots and shifts the epicenters of eddy-current formation behind the centerlines of the magnets. Both tilt and epicenter shift are function of speed. Note that there is a discontinuity in the flux density contour plot as it crosses the airgap into the disc. This result from eddy-currents in the disc and not from a magnetization of the disc.

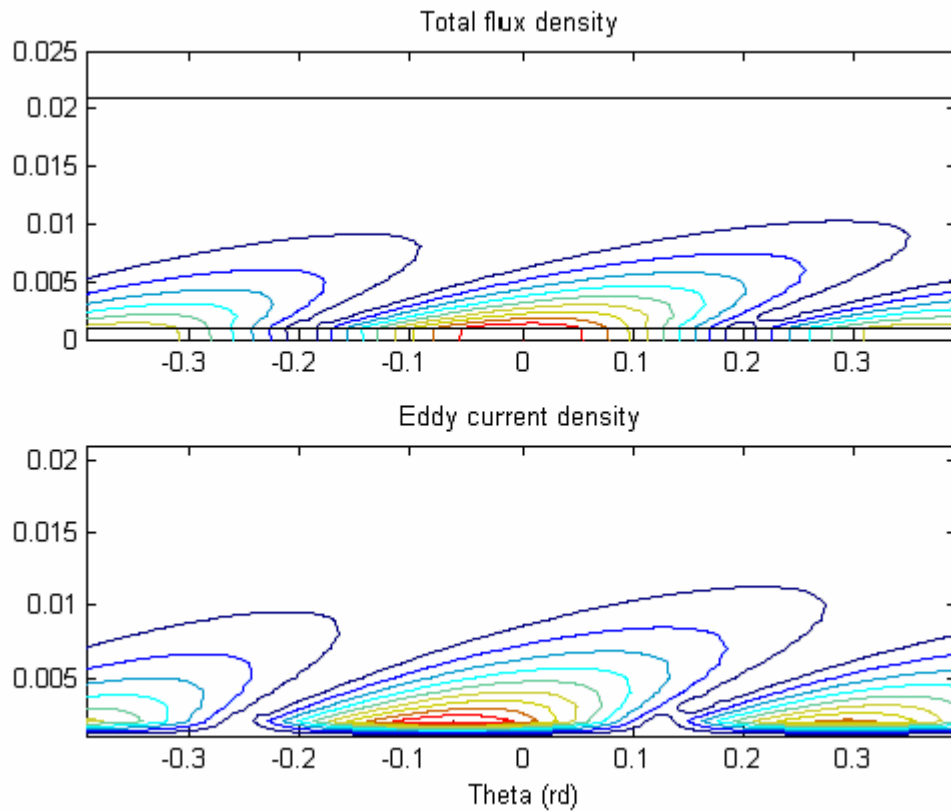


Fig. 22: Flux density and current density map for a pole pair at 5x critical speed

Fig. 22 shows the contour maps of flux density and eddy-current density in the airgap and disc of the brake in the $(\bar{\theta}, \bar{z})$ plane at five times the critical speed. The skin effect, tilt and epicenter shift are much more pronounced than at critical speed. The braking

force is now generated primarily in the immediate vicinity of the airgap surface of the disc. As speed increases, the skin depth decreases very sharply consequently reducing the amount of braking torque generated. At infinite speed, the brake produces no torque at all. Fig. 23 shows the elemental braking force distribution in the disc at five times the critical speed. The outermost line on the contour plot is drawn for 10% of the maximum elemental force. It appears clearly that most of the braking force is generated in a volume located between the airgap and one quarter of the disc's thickness.

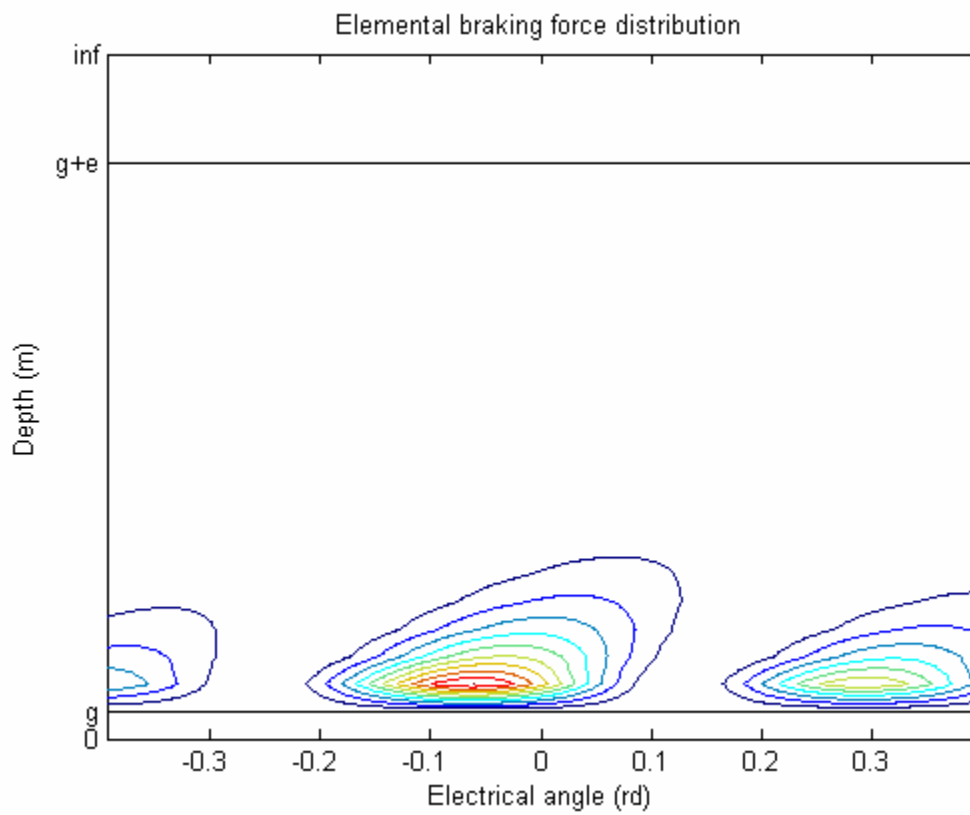


Fig. 23: Elemental braking force distribution at five times the critical speed

3.3 – Impact of design parameters on the brake's performance

Several simulations were run by varying one brake design parameter at a time. All other parameters were kept to their initial value as listed in TABLE 3 unless otherwise noted.

3.3.1 – Impact of mean disc radius

Fig. 24 shows the dependency of the torque-speed characteristic on the mean disc radius. The parameters used for the simulation are the parameters listed in TABLE 3, except for the radii. The mean radius is varied from 10cm to 20cm while the difference between the outer and inner radii is kept at 1cm. The mean radius is expressed as follows:

$$R_{mean} = \frac{(R_{outer} + R_{inner})}{2} \quad (124)$$

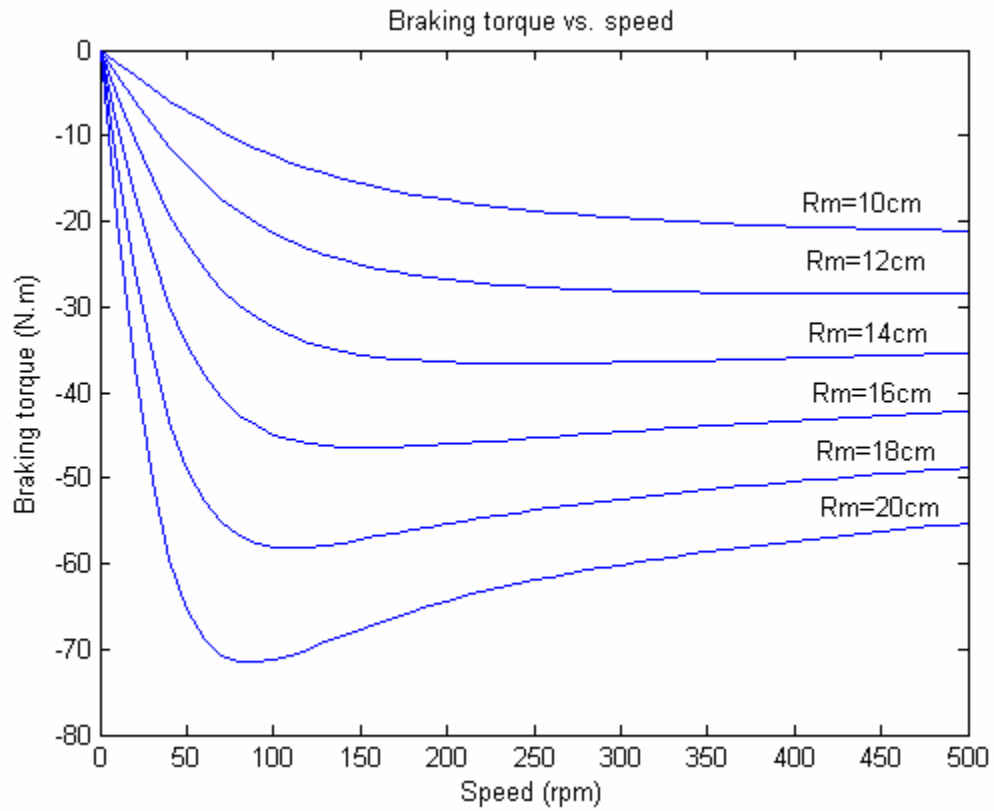


Fig. 24: Torque-speed curve dependency on the mean disc radius

Fig. 25 shows the evolution of critical speed with the disc's mean radius. Fig. 26 shows the respective evolution of the peak torque. The critical speed diminishes rapidly although there are no changes in the stator current sheet harmonic distribution.

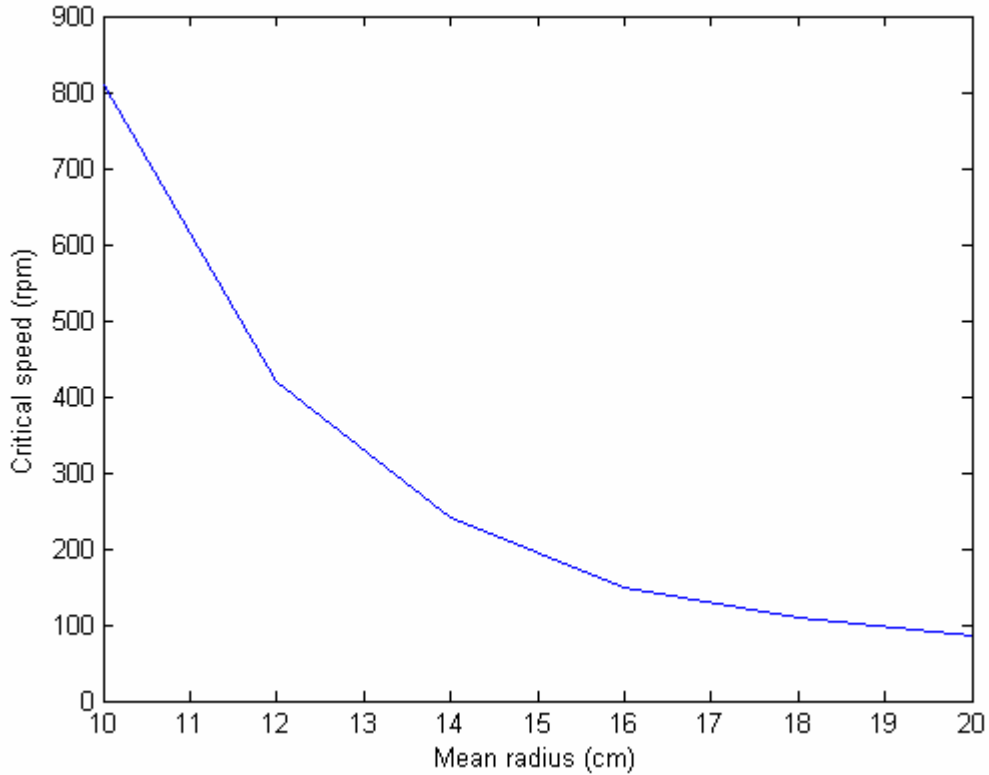


Fig. 25: Critical speed vs. mean disc radius

The peak torque increases with the mean radius (Fig. 26), which is consistent with the fact that the braking force acts on an increasingly longer lever arm. However, the peak torque is increasing faster than linearly and does so at a decreasing critical speed. There is therefore a strong secondary effect that acts on the peak torque. This is due to the fact that when the mean radius increases, the length of the pole arc increases although the angular width remains the same. This has two effects:

- The pole area increases linearly with the mean radius. Therefore, the braking force increases linearly and the braking torque increases with the mean radius

squared. However, since the torque peaks at a lower speed, it increases slightly slower than squared.

- The ratio of the disc's mean radius to its thickness increases, which would tend to increase critical speed (see sub section 3.2.2). However, the linear speed increases with the mean radius, so the eddy-currents intensity increases as well, which results in a stronger skin effect for a same angular speed. The net result is a decrease of the critical speed.

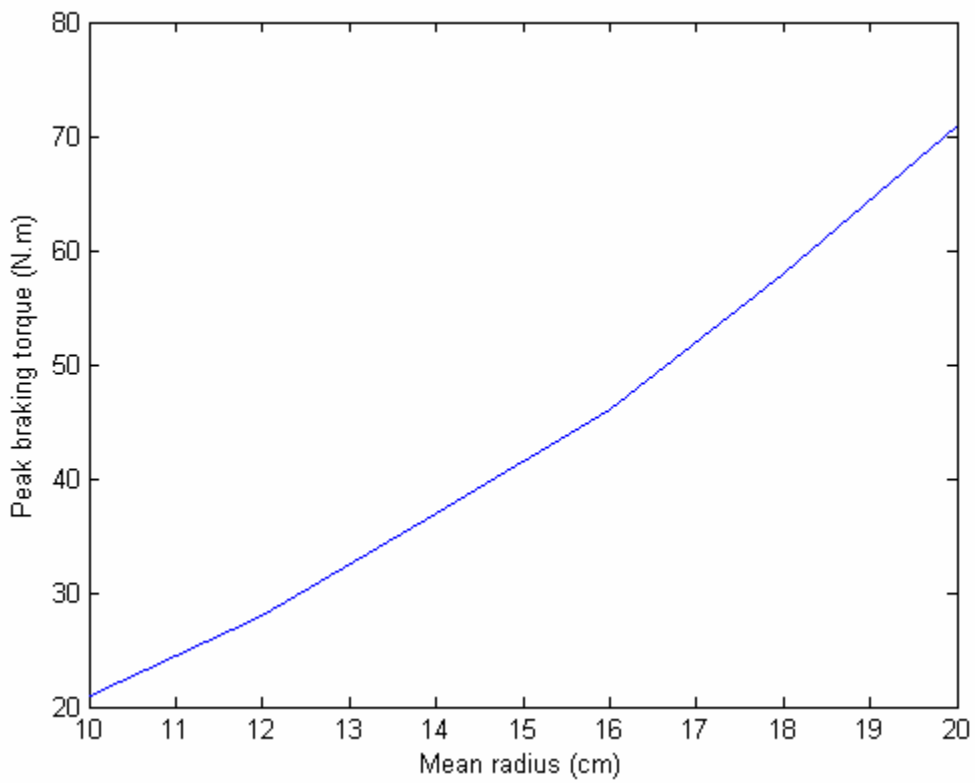


Fig. 26: Peak torque vs. mean disc radius

3.3.2 – Impact of disc area

Fig. 27 shows the dependency of the torque-speed curve dependency on the disc area if the area is increased strictly by the means of the inner and outer radii:

$$A_{disc} = \pi(R_{outer}^2 - R_{inner}^2) \quad (125)$$

The calculations were performed for a mean radius of 20cm, and for a difference between outer and inner radii varying from 1cm to 10cm.

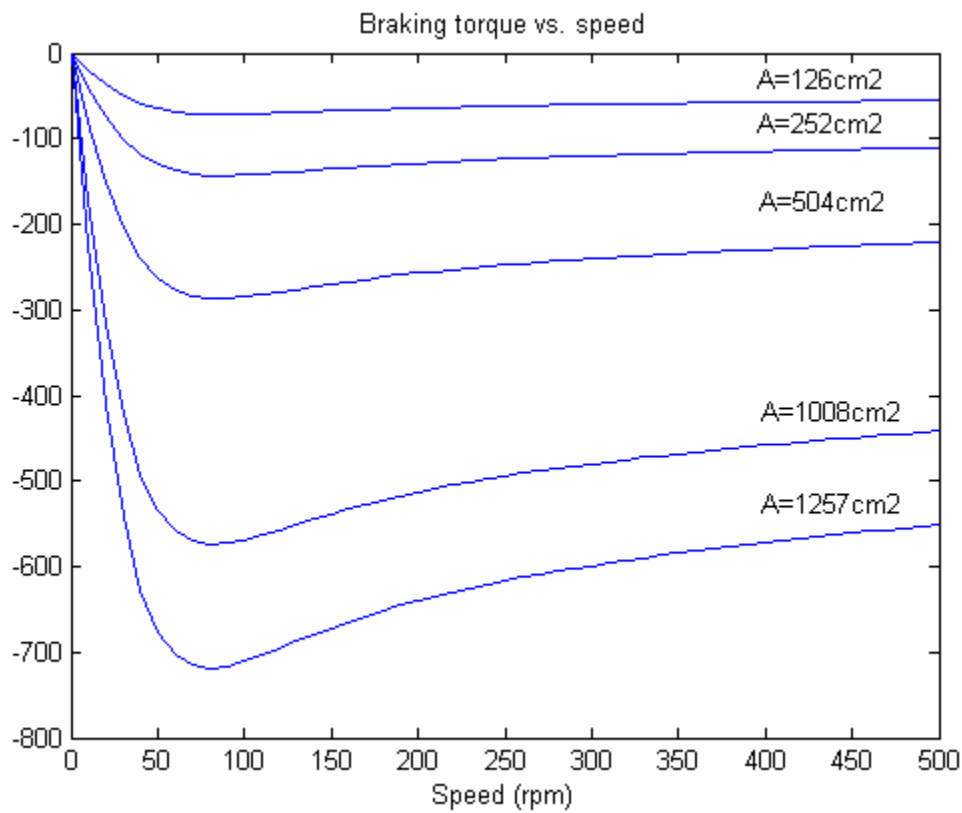


Fig. 27: Torque-speed curve dependency on the disc area

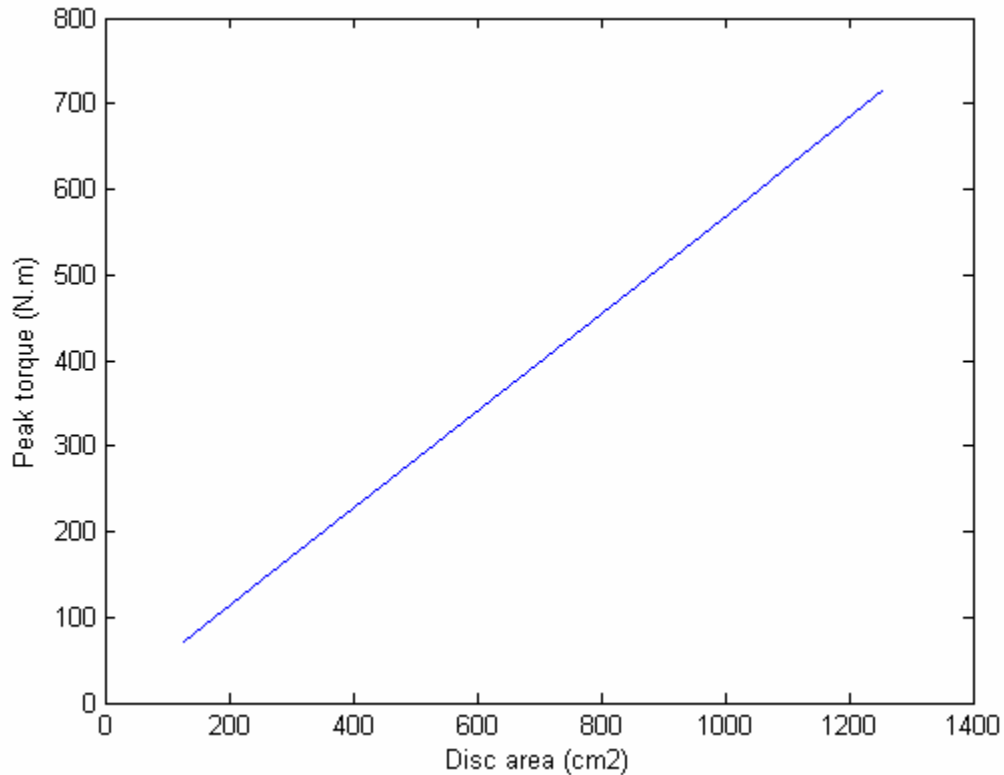


Fig. 28: Peak torque vs. disc area

Fig. 28 shows that the peak torque increases linearly with the disc area, while the critical speed remains constant. Rather than a direct dependency on the disc area, there are two mutually compensating effects at play:

- For a constant mean radius, the outer radius is increasing. This contributes with a torque increase with the radius squared and a critical speed decreasing inversely with the radius.

- The inner radius is increasing. This contributes with a torque decrease proportional to the radius squared and a critical speed increasing inversely with the radius.

The net effect is a peak torque increasing with the disc area and a critical speed that remains constant (Fig. 29).

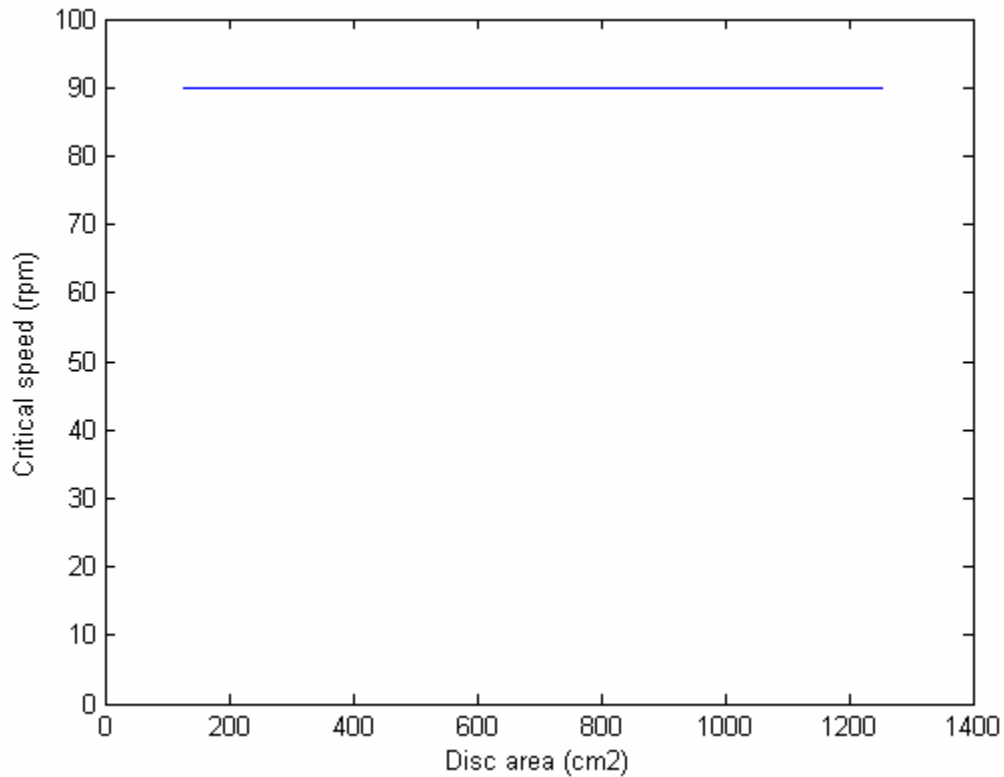


Fig. 29: Critical speed vs. disc area

3.3.3 – Impact of disc thickness

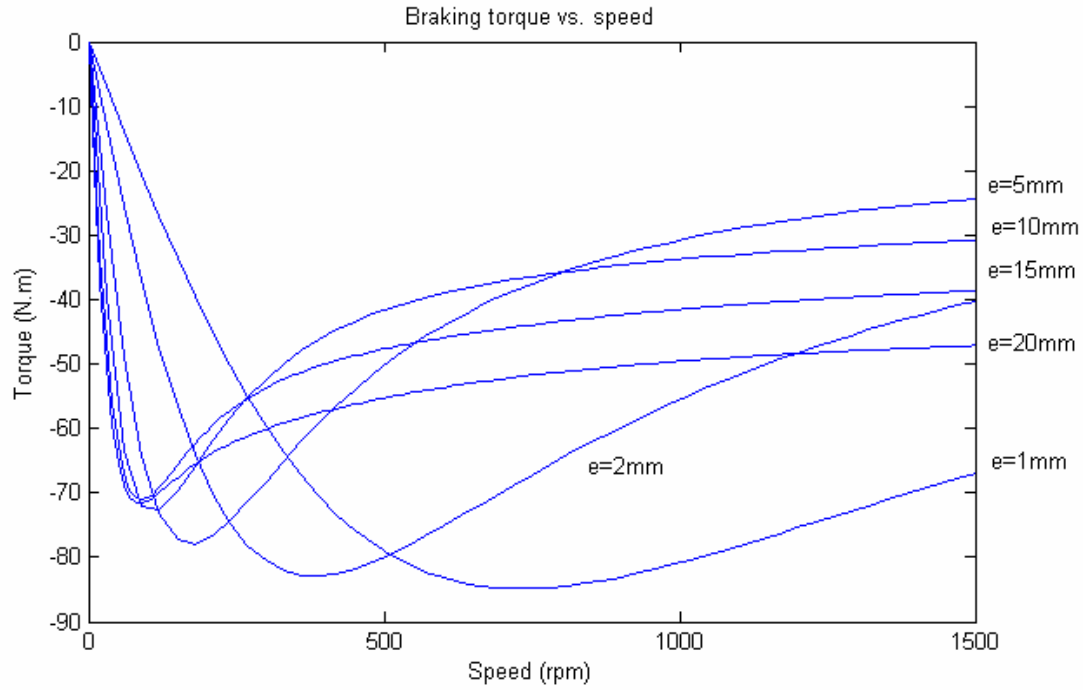


Fig. 30: Torque-speed curve dependency on disc thickness

The peak torque for a thin disc is slightly higher than for a thick disc (Fig. 31) because a thin disc constitutes a thinner current sheet that has a lesser weakening influence on the flux generated by the stator's magnets.

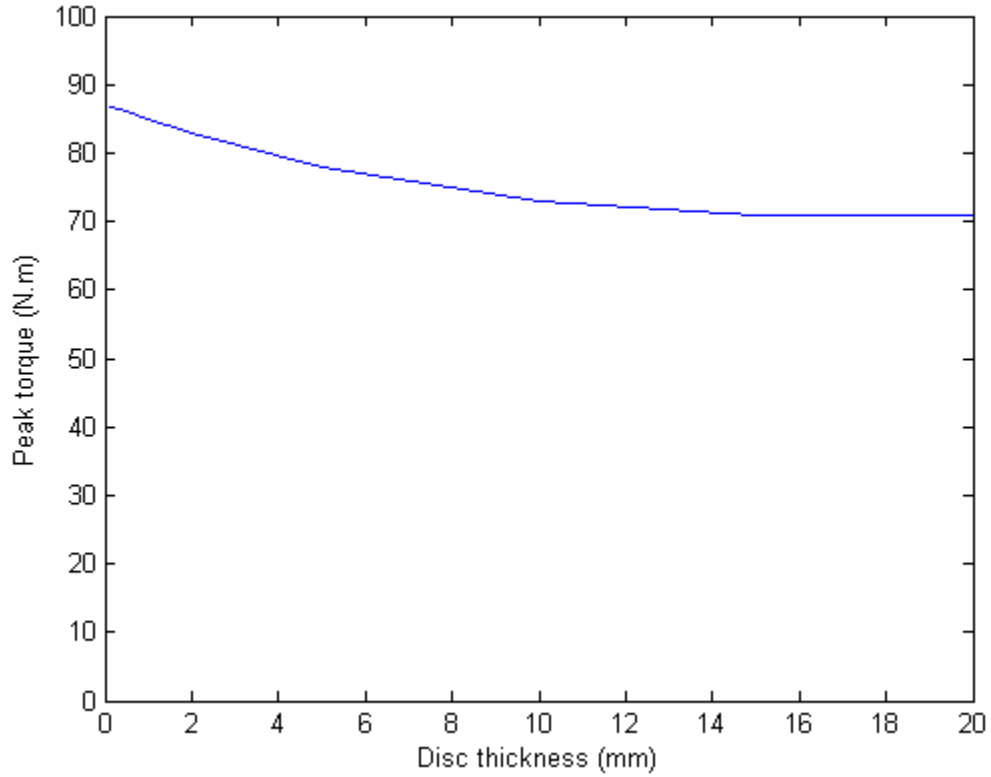


Fig. 31: Peak torque vs. disc thickness

The skin effect depends primarily on the electric and magnetic parameters of the disc. For a thick disc, the major part of the elemental force distribution is comprised in the disc and therefore integrated to determine the force (Fig. 23). Thin disc eddy-current brakes have a higher critical speed than thick disc brakes (Fig. 32). For a thin disc, only a small fraction of the distribution of variables is comprised and integrated (Fig. 33). Therefore, it will take a much higher speed to get a skin depth thin enough to affect the total braking force.

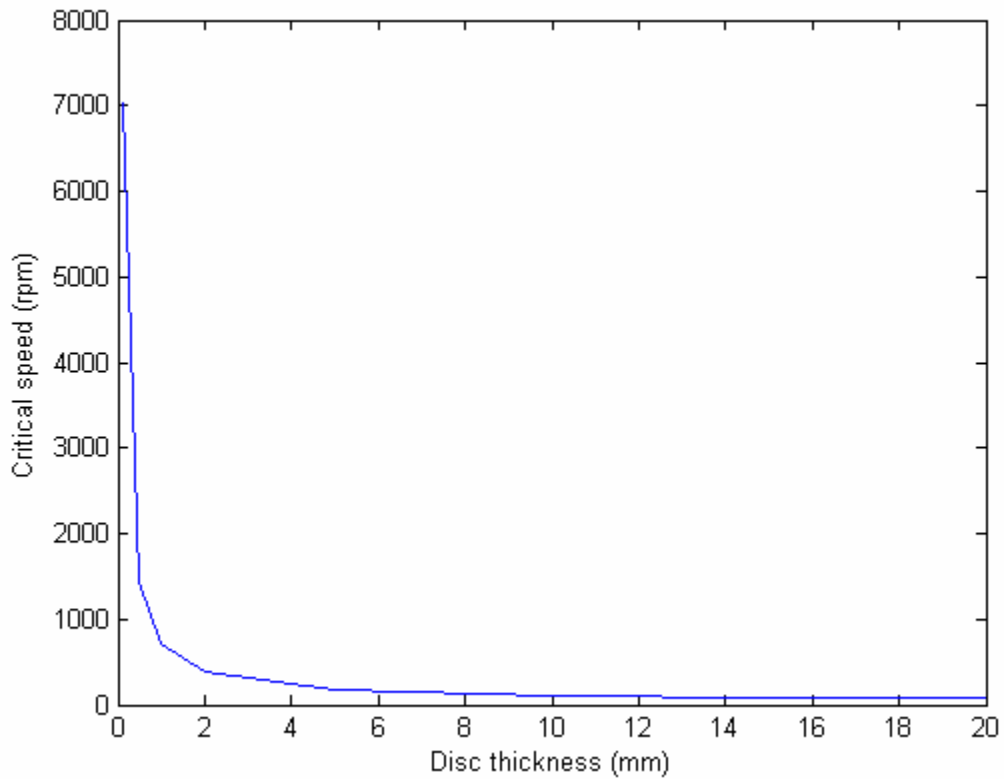


Fig. 32: Critical speed vs. disc thickness

Current density at critical speed is higher in thin discs because critical speed is higher than in thicker discs. However, this effect is minor compared to the variation of critical speed due to disc thickness.

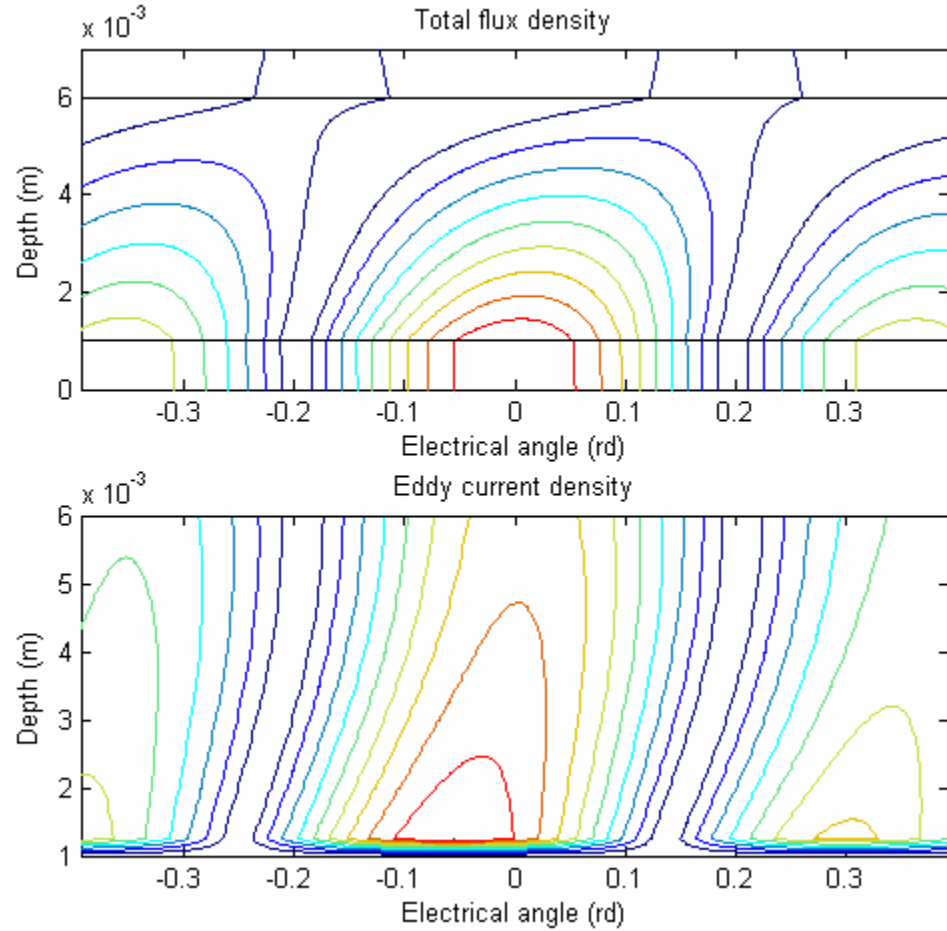


Fig. 33: Flux density and current density plots at 5x critical speed, $e=5\text{mm}$

3.3.4 – Impact of airgap width

The increasing airgap results obviously in a lower braking torque (Fig. 34). However, not all portions of the torque-speed characteristic are affected equally. The high-speed region is less affected than the peak torque. For a large airgap, the high-speed torque-

speed curve is flatter than for a small airgap because the eddy-currents are located farther from the magnets and thus have a lesser weakening influence on them.

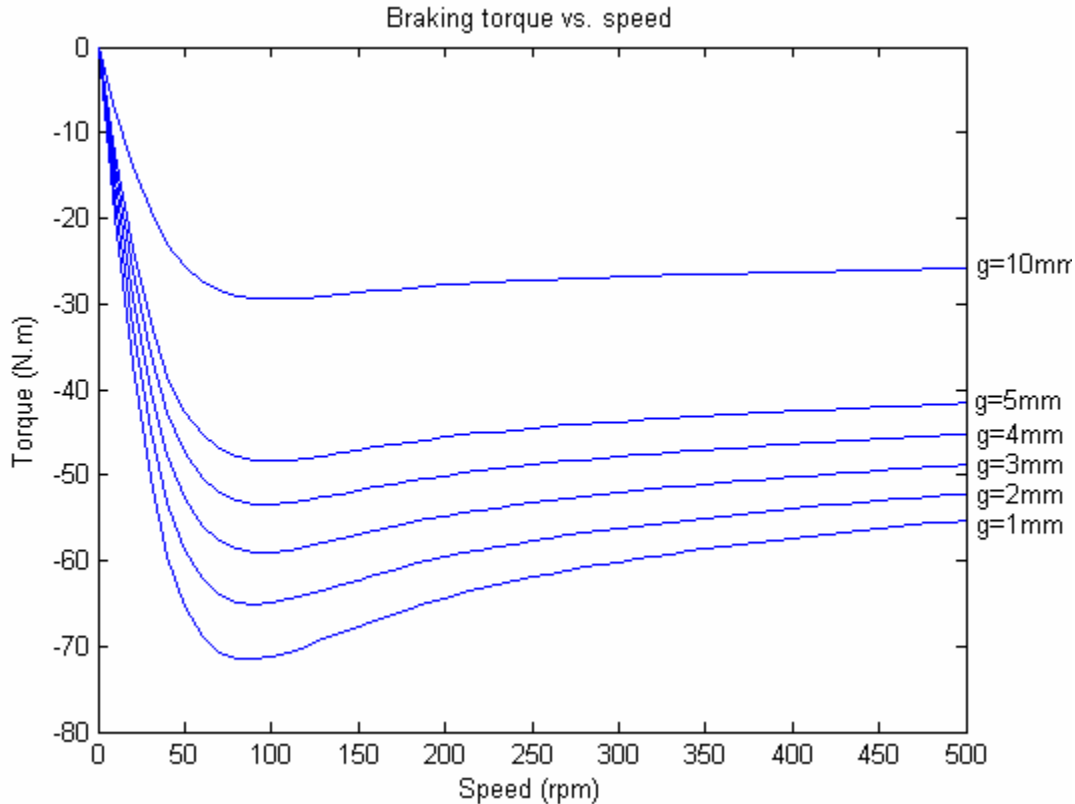


Fig. 34: Torque-speed curve vs. airgap width, $e=20\text{mm}$

It is worth noting that thin and thick discs are affected in similar proportions (Fig. 35). On the other hand, critical speed is affected in greater proportions for thick discs than for thin discs (Fig. 36). This is because a thin disc is a smaller current sheet and therefore has less influence on the magnet's flux. It takes a greater speed to induce larger currents in the disc that will weaken the magnet's flux enough to reach critical speed.

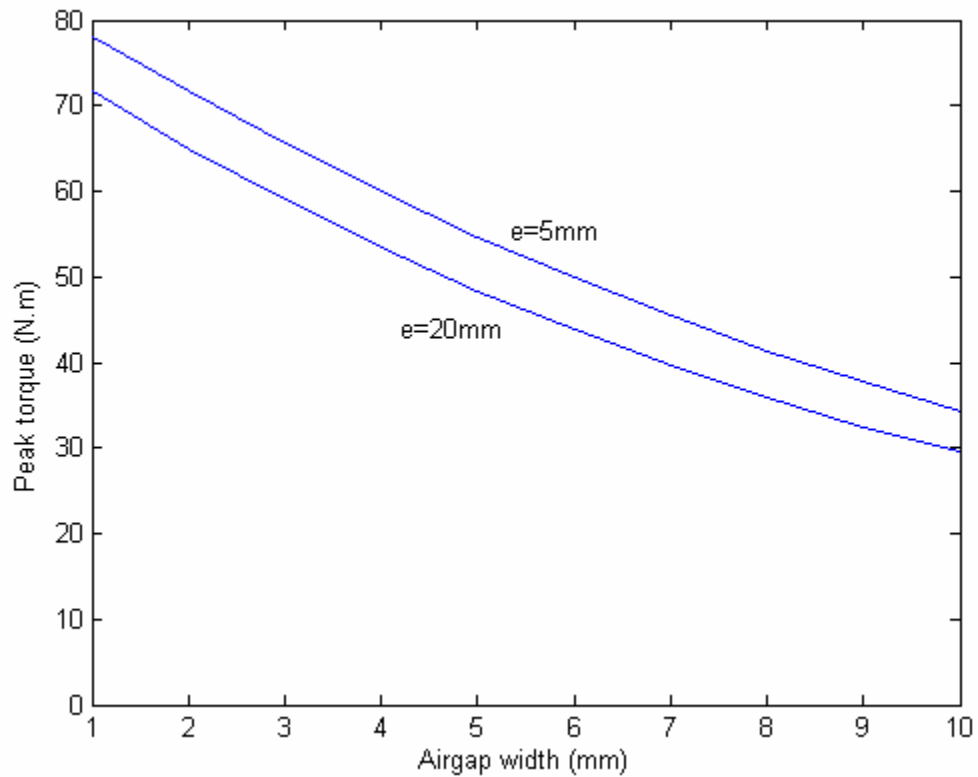


Fig. 35: Peak torque vs. airgap width

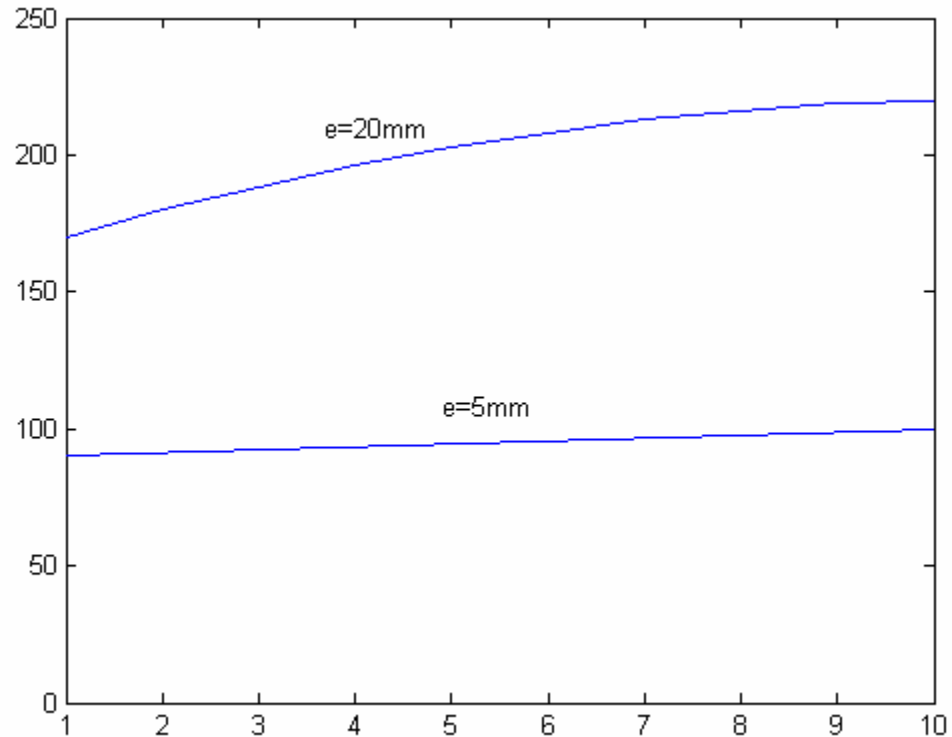


Fig. 36: Critical speed vs. airgap width

3.3.5 – Impact of stator pole width

Increasing the stator poles' angular width increases the poles' area but also affects the harmonic distribution of the stator flux by increasing the amplitude of the fundamental. The fundamental and all low frequency harmonics are less weakened than higher frequency harmonics at critical speed and beyond. Therefore, increasing the amplitude of lower frequency harmonics increases the peak torque in a complex function of the spectrum (Fig. 37).

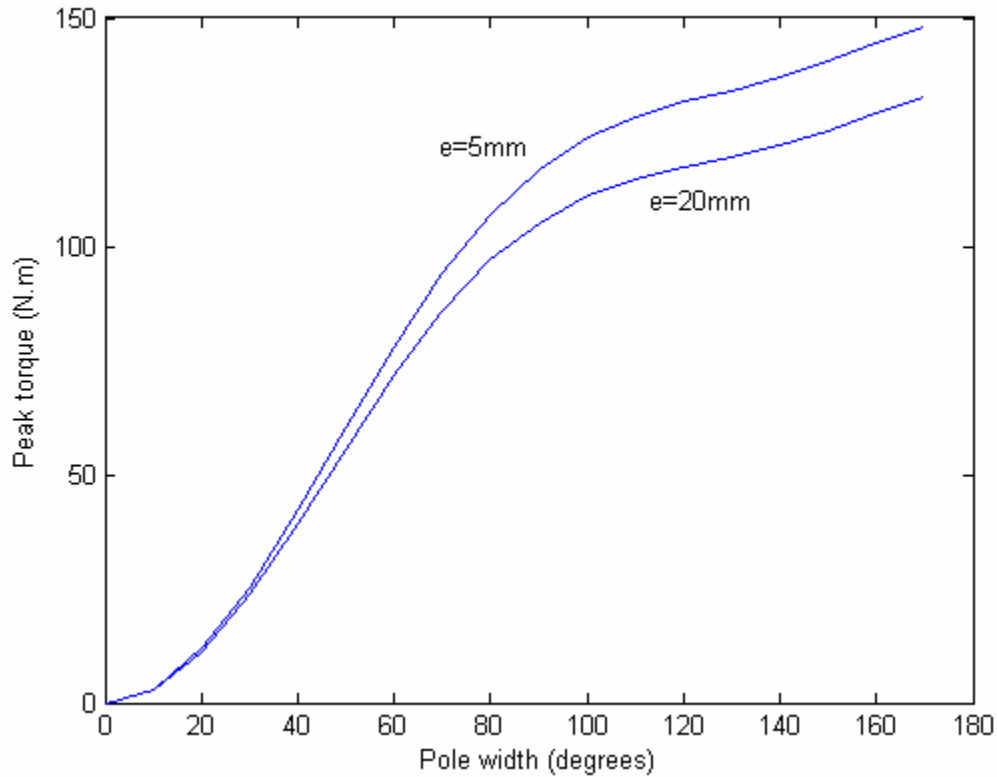


Fig. 37: Peak torque vs. pole width

The critical speed is also affected by the stator magnetization spectrum. It decreases with increasing pole angular width in a seemingly linear manner. However, the impact is lesser than on the peak torque. In thick discs, the critical speed decreases faster than for thin discs (Fig. 38). The torque in the high-speed region decreases much faster for large poles than for narrow poles.

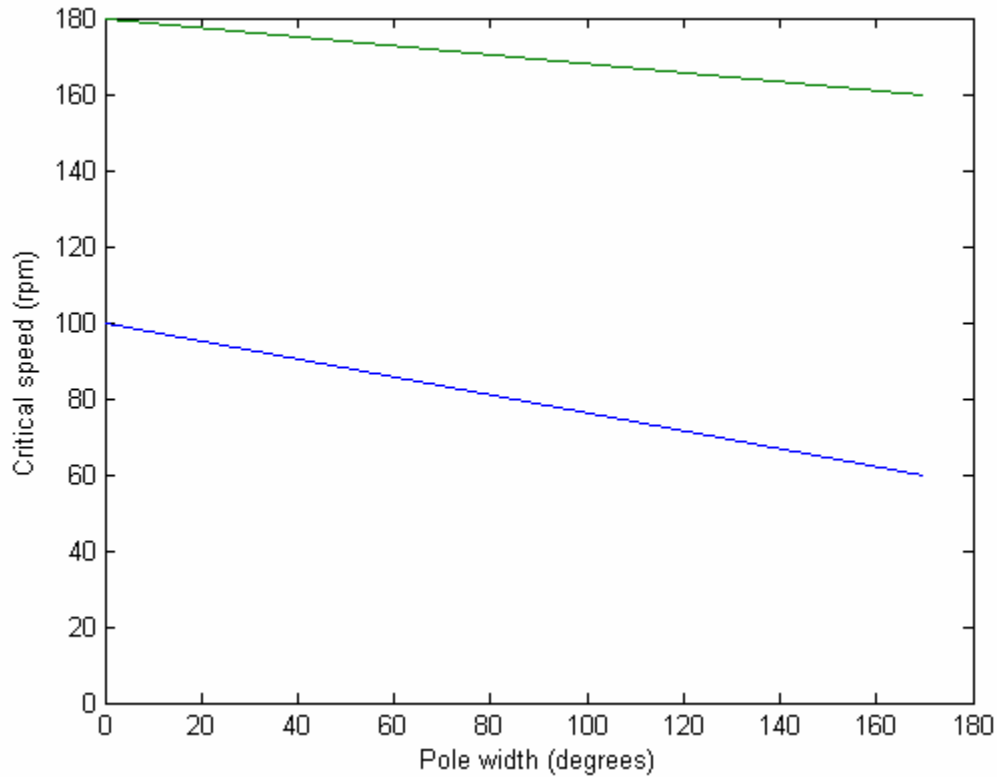


Fig. 38: Critical speed vs. pole width

3.3.6 – Impact of stator pole number

Intuitively, the number of stator poles dictates the ratio between mechanical speed and electrical speed (i.e. the frequency of the magnetic flux seen by the disc), while the peak torque should evolve inversely with the number of poles.

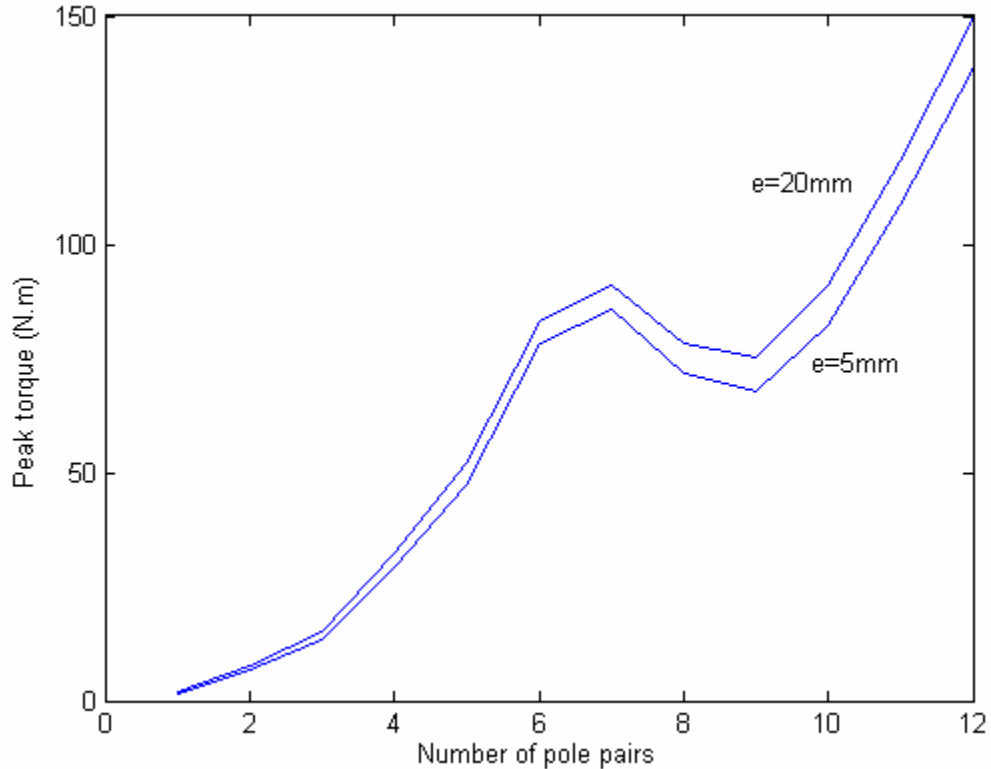


Fig. 39: Peak torque vs. number of pole pairs

Practically, the peak torque is greatly affected by the number of poles (Fig. 39), while the critical speed varies only slightly (Fig. 40). This is because the number of poles affects several other critical parameters:

- Pole width (in meters) to disc thickness ratio
- Pole width (in meters) to airgap width ratio
- Harmonic distribution of the stator magnetic flux

The peak torque is correspondingly affected, while the variation of the above parameters works to counter the increase in pole numbers and maintain the critical speed constant. It

should be noted however, that a very large number of poles results in a very low peak torque. Therefore, there is an optimum number of poles.

It is also interesting to note that a low number of poles yields a very weak torque despite the very large corresponding pole area. This is because eddy-currents are primarily generated underneath the leading and trailing edges of the magnets so that the increase in the pole area does not affect the torque significantly, while the reduction in the number of poles reduces the number of epicenters of eddy-current generation. Hence the drastic decrease in peak torque.

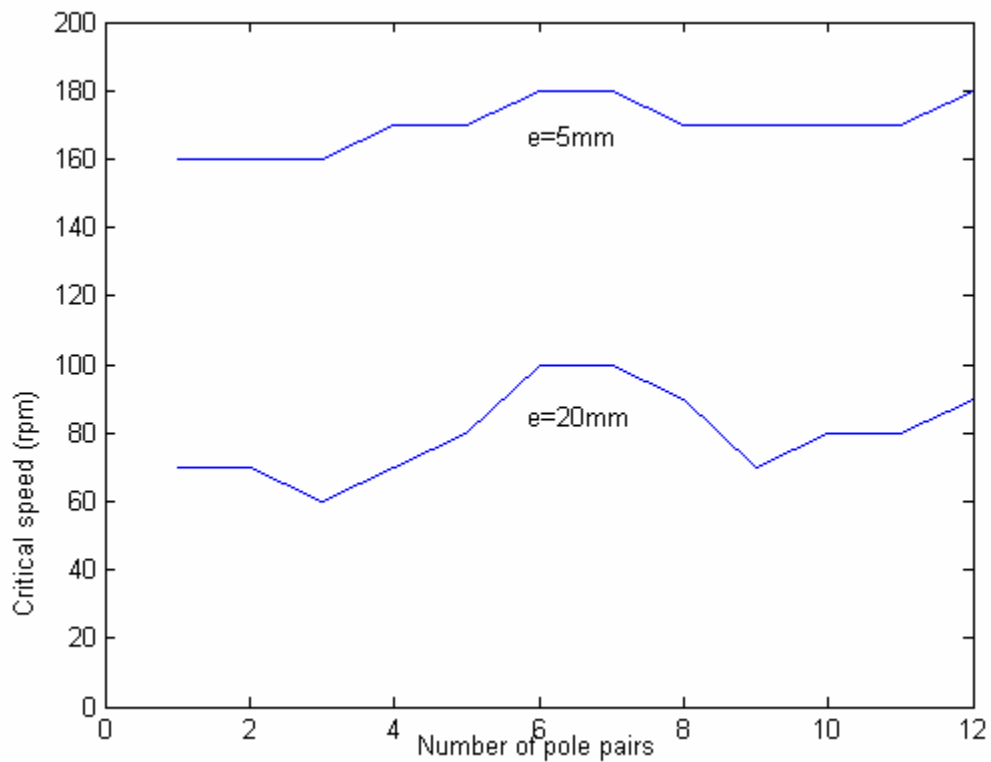


Fig. 40: Critical speed vs. number of pole pairs

3.3.7 – Impact of electrical conductivity

TABLE 4
Electrical conductivity of various metals at 20°C

MATERIAL	CONDUCTIVITY
Copper	$5.8 \times 10^7 \Omega^{-1}$
Aluminum	$3.7 \times 10^7 \Omega^{-1}$
Titanium	$0.25 \times 10^7 \Omega^{-1}$
Tungsten	$1.85 \times 10^7 \Omega^{-1}$
Zinc	$1.6 \times 10^7 \Omega^{-1}$
Iron	$1.0 \times 10^7 \Omega^{-1}$
Cobalt	$1.78 \times 10^7 \Omega^{-1}$
Nickel	$1.4 \times 10^7 \Omega^{-1}$

TABLE 4 provides an indication for the range within which the disc material's electrical conductivity is likely to evolve. The analogy between an induction motor and an eddy-current brake holds true. The material conductivity has no influence on the peak torque whatsoever (Fig. 41), but the critical speed is strictly an inverse function of the conductivity (Fig. 42). Conversely, the critical speed is a linear function of the disc material's electrical resistivity.

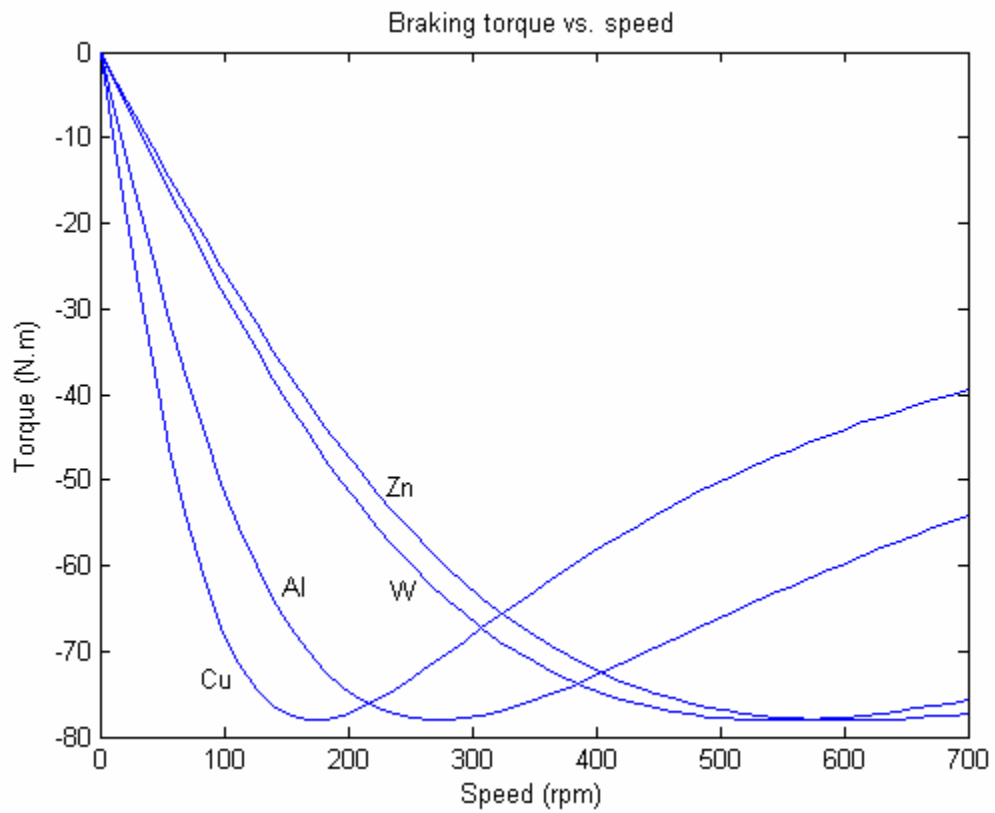


Fig. 41: Torque-speed curve for various materials

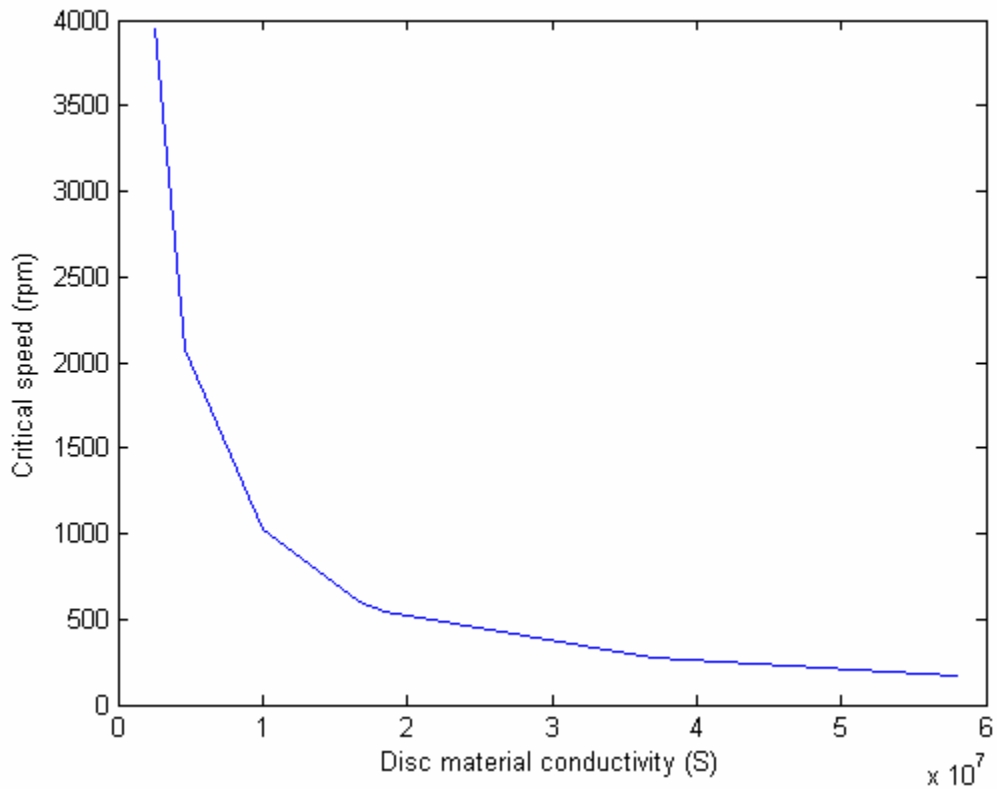


Fig. 42: Critical speed vs. disc material conductivity

3.3.8 – Impact of magnetic permeability

The influence of the disc material's relative magnetic permeability was investigated using values for characteristic soft magnetic materials (See TABLE 5).

TABLE 5
Relative magnetic permeability of various soft magnetic materials at 20°C

MATERIAL	MAXIMUM RELATIVE PERMEABILITY
Iron (Commercial, 99% pure)	6,000
Cobalt	250
Nickel	600
Silicon iron (4% Si)	7,000
Superalloy	1,000,000

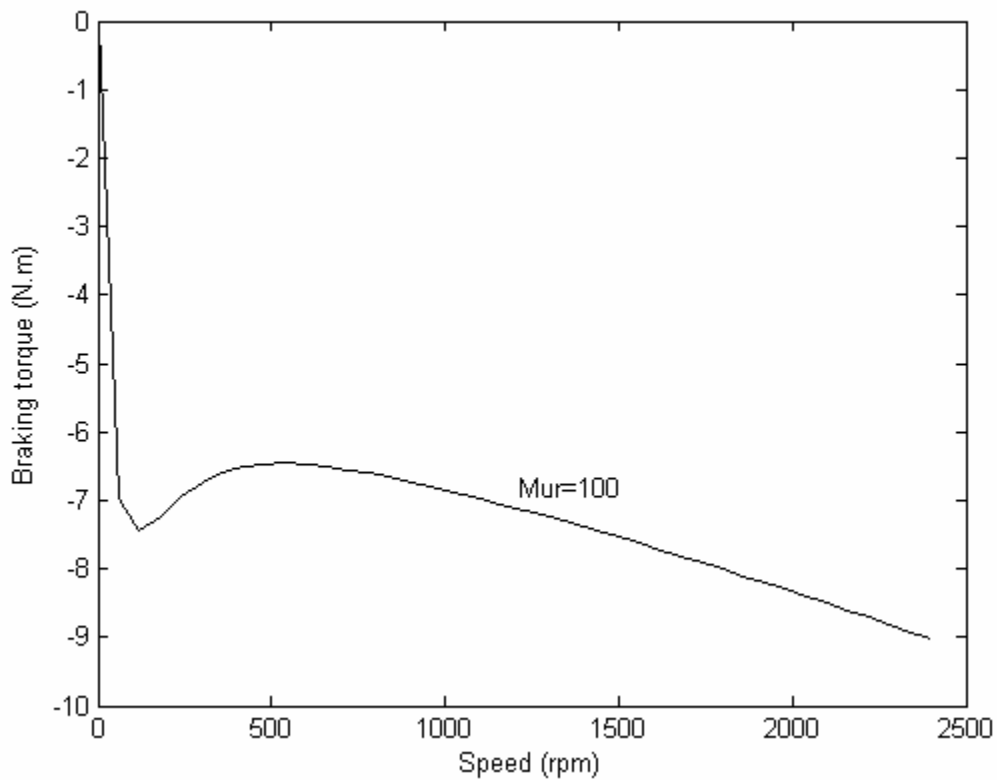


Fig. 43: Torque-speed curve for ferromagnetic material

It appears that the results diverge for relative magnetic permeabilities greater than 50. The reasons seems to be that there is no saturation to limit the evolution of flux density

within the disc so it rises unchecked. Fig. 43 illustrates this divergence for $\mu_r = 100$. It is thus impossible to conduct an investigation of the influence of relative permeability over a practical range of values.

3.3.9 – Impact of permanent magnet properties

TABLE 6
Saturation magnetization of various permanent magnet materials at 20°C

MATERIAL	$M_{sat}(\text{kA.m}^{-1})$
Ferrite	334
Alnico 9	875
SmCo_5	795
$\text{Nd}_2\text{Fe}_{14}\text{B}$	970

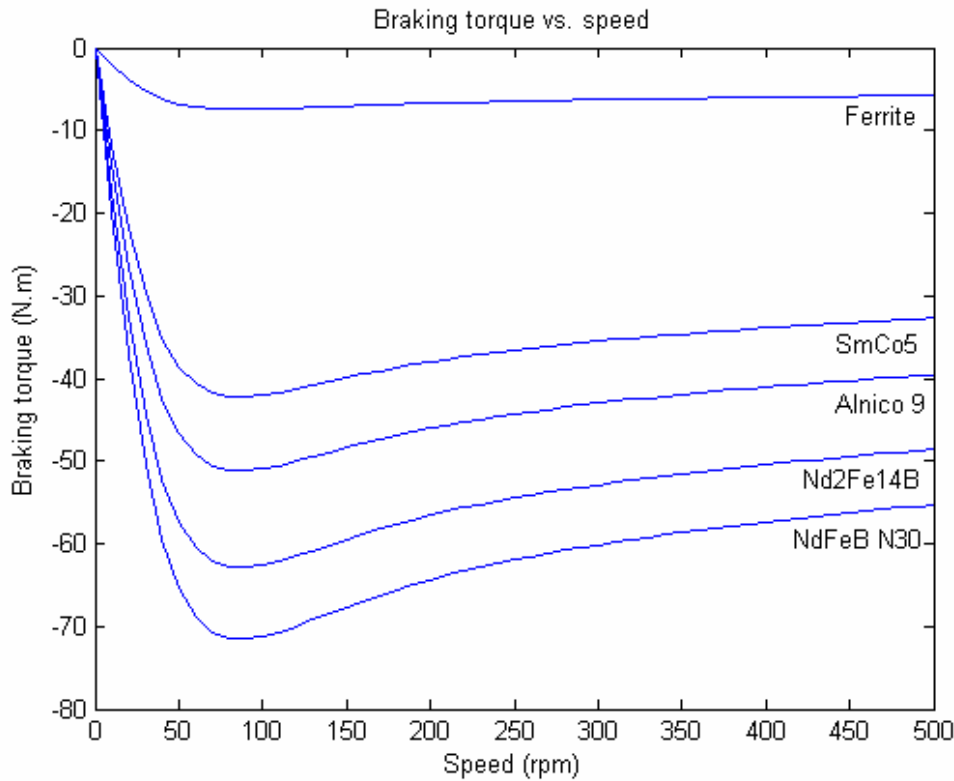


Fig. 44: Torque-speed curves for different permanent magnet materials

Simulations were run using typical hard magnetic materials magnetization values (TABLE 6). Because of the approximations of the analytical model, the height of the magnet has the same influence as its magnetization (Fig. 44). Indeed, these two parameters are combined into one, I_0 , which is the amplitude of the current sheet at the surface of the stator iron.

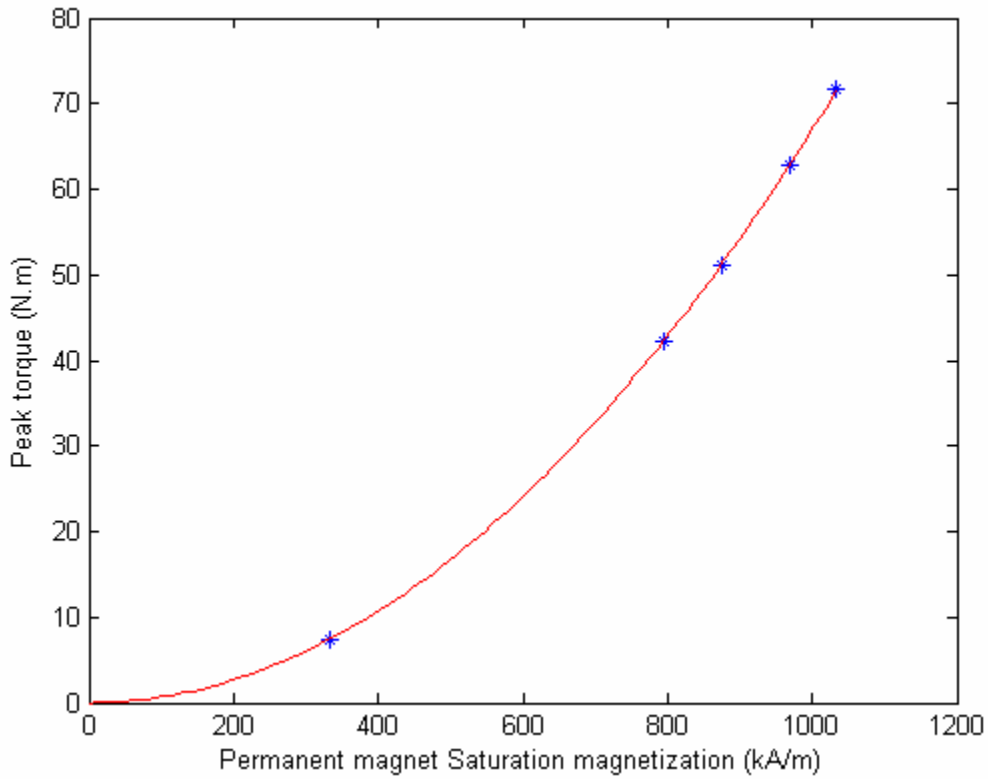


Fig. 45: Peak torque vs. magnet magnetization

The braking torque generated by the brake is proportional to the magnetization squared.

Fig. 45 demonstrates this proportionality for the peak torque. This is consistent with previously published findings, which indicate that the torque is proportional to the excitation flux density squared. The magnetization is proportional to the flux density generated by the permanent magnet at standstill. Note that the critical speed is unaffected by the permanent magnets' magnetization.

4 – Limitations of theoretical analysis

The analytical model has proven to be an insightful model that can provide a great wealth of results very rapidly. However, it has some serious limitations:

- Magnetic permeability and saturation: The results diverge when the relative permeability of the disc's material is increased beyond 50. This casts doubt on the results obtained with relative permeabilities greater than 1. The likely reason is that the analytical model does not take into account the saturation of the material thereby allowing the flux density to rise unchecked.
- Eddy-current return paths: Eddy-current paths are cited in the literature as having a non-negligible influence on the performance of eddy-current brakes. However, taking into account these return paths requires a three-dimensional model, which is much more complicated than the two-dimensional model presented in this chapter and would defeat the purpose of an analytical model.
- Influence of stator back-iron saliency: The analytical model assumes that the back-iron of the stator is flat and begins at the surface of the airgap. However, there is air between the poles and the magnets are located between the airgap and the surface of the back-iron. Furthermore, there is saturation in some locations of the back-iron. The actual magnetic flux will therefore follow patterns different from those exhibited in the analytical model. The reaction field generated by the eddy-currents will be affected. The analytical model provides no simple solution to deal with stator back-iron saliency.

- Influence of eventual rotor saliency: The analytical model must assume that the rotor has a uniform geometry. A non-uniform geometry could only be modeled with great complexity that defeats the purpose of an analytical model. Practical eddy-current brakes have fins on the back of the rotor to dissipate the heat generated by braking. These fins have a non-negligible influence on the braking torque.
- Demagnetization of permanent magnets: The analytical model assumes that the permanent magnets are linear in the operating quadrant (negative field and positive flux density), have a relative permeability close to vacuum, and that the magnetic field is too weak to demagnetize them. While this is mostly true for rare-earth permanent magnets, it is not for Alnico and ferrite magnets. While Alnico magnets typically have a higher magnetization than samarium-cobalt magnets, they also have a lower intrinsic coercive field. Therefore, they would be demagnetized much more easily and would provide much lower performance than samarium-cobalt magnets. A more accurate model for the permanent magnets is needed.
- Influence of temperature: The temperature of an eddy-current brake can rise as high as 800°C. The electrical and most importantly the magnetic properties of the rotor are greatly affected by temperature. It would be possible to take temperature in account if it was uniformly distributed over the rotor. However, it is not because forced air convection cools the back of the rotor while the airgap surface is the locus of heat generation. The non-uniform temperature distribution

is a difficult problem, seemingly impossible to treat with analytical methods and cited as very difficult to treat even with numerical methods.

In conclusion, while it has provided some deep insight into the physics of eddy-current braking and preliminary design data, the analytical model is limited in its scope by necessary simplifications. It is thus unable to explain all the phenomena occurring in actual brakes and unfit for design. From this point on, numerical methods are required for the analysis of eddy-current braking.

CHAPTER III

FINITE ELEMENT ANALYSIS OF EDDY-CURRENT BRAKING

1 – Fundamentals of finite element analysis

Finite element analysis is a numerical modeling technique that was developed to analyze engineering problems with complex geometries, complex excitation source characteristics, and non linear material properties. It operates by decomposing the structure to be analyzed into a large number of small elements over which the problem can be approximated and solved numerically. In practical applications, finite element analysis is either two-dimensional or three-dimensional.

The geometry of the problem is decomposed by meshing: a large number of points called nodes are created inside the volumes or surfaces. Each node is assigned a set of properties as a function of the material composing the object modeled. Boundary conditions are used to account for the air beyond the object modeled, and to reduce the size of the problem by taking into account its periodicities and symmetries. The physical equations are solved by minimizing the “potential function” at each node. The solution within each element is obtained by combination of the solutions of its nodes.

2 – Selection of finite-element analysis method

Applying finite element methods to the analysis of the eddy-current brake involves several choices:

- Choosing between two-dimensional and three-dimensional analysis
- Choosing between analysis methods
- Choosing boundary conditions, periodicities and symmetries
- Deciding on the level of approximation of the properties of the materials

In the past, most finite element analyses of eddy-current brakes published used two-dimensional analysis [32-37]. The use of only two dimensions yields a very limited number of nodes, which makes computations easy and fast. However, two-dimensional analysis does not account for three-dimensional effects directly and approximations must be made to account for these. The accuracy of the solution suffers greatly. Two-dimensional methods are typically better suited for the analysis of laminated geometries with well defined current paths, where end effects are either negligible or easily accounted for like electric motors or transformers. Three-dimensional methods on the other hand are better suited for geometries where end effects are non negligible and where current paths are ill-defined such as eddy-current brakes in particular and eddy-current problems in general [38-43]. However, three-dimensional analysis requires a powerful processor and a large memory and takes much longer than two-dimensional

analysis to reach a solution. This is the result of a much larger number of nodes to be solved for.

There are two methods suited for the analysis of eddy-current brakes: transport-term and transient methods [43]. The transport-term method is basically a magnetostatic method in which a velocity and conductivity dependent term has been added. It allows deriving torque-speed curves by solving the problem only once for each value of speed. It is as fast as a magnetostatic computation but it requires that the geometry be invariant along the direction of the motion for the part in motion. Consequently, it would be ideally suited for the analysis of eddy-current brakes featuring plain discs but it would not allow analyzing brakes with cooling fins, holes and notches [43]. Transient methods start with a disc at standstill, step-up the speed to the desired value and solve the problem for several time steps until a permanent regime has been reached. This allows studying the actual transients occurring in a brake and can be applied to geometries varying in the direction of motion. However, the computation of torque speed curves takes much longer than with transport term methods because of the necessity to compute for several time steps during the transients and because of the greater complexity of transient equations.

The analysis of the proposed eddy-current brake has been performed using a three-dimensional transient method, because of the necessity to investigate end effects and the necessity to take into account the cooling fins of the disc. The software used to

implement this analysis is Cedrat's FLUX 3D™ [44]. FLUX 3D provides several means to implement boundary conditions as well as periodicities and symmetries. The “infinite box” (Fig. 46) allows modeling the vanishing of electromagnetic fields in the air far beyond the geometry but with a limited number of elements.

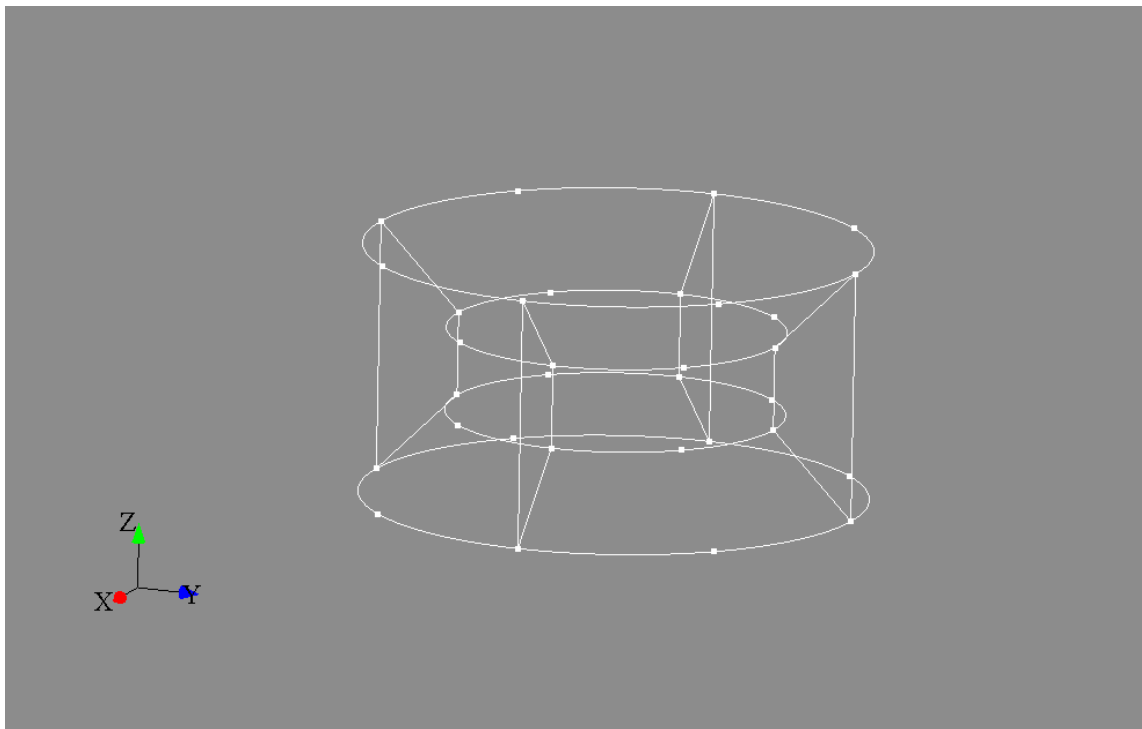


Fig. 46: FLUX 3D's infinite box

FLUX 3D allows modeling the geometry in one of three different systems of coordinates: Cartesian, cylindrical, or spherical. Obviously, the cylindrical system is best suited for the description of the eddy-current brake. Geometries including more than one pole can be reduced by defining a periodicity in FLUX 3D. The geometric periodicity is

necessarily coupled with an electromagnetic periodical condition, which can be either periodic or anti-periodic. With a periodic condition, the potentials on either side of the boundary are the same, while they are of opposite signs with an anti-periodic condition. The anti-periodic condition permits further reducing the size of the problem by describing only one pole instead of a pole pair. A brake with 2 pole pairs can thus be analyzed by describing only 1/4th of the geometry (Fig. 47).

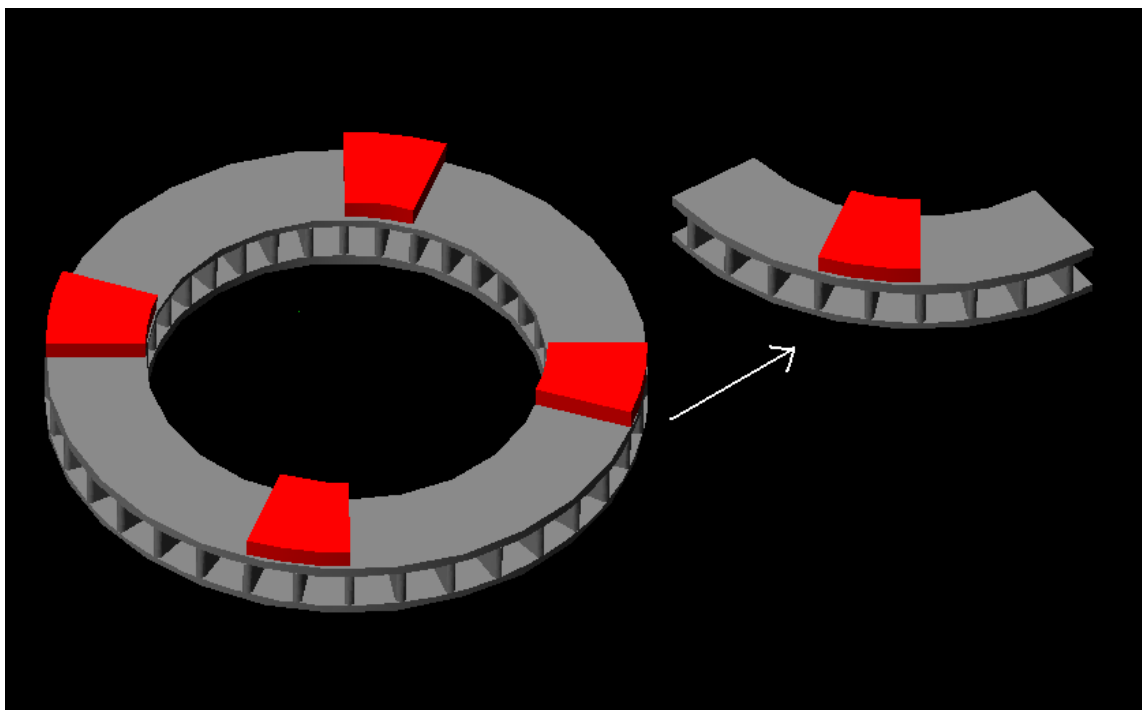


Fig. 47: Use of periodicities to reduce the size of a model

Symmetries can also be used to reduce the size of the problem. In FLUX 3D, symmetries are described with respect to a plane. The geometric symmetry is coupled with a boundary condition for electromagnetic fields. It is either a normal flux condition or a

tangential flux condition on the boundary. A normal flux condition corresponds to electromagnetic potentials with opposite signs across the boundary, while a tangential condition corresponds to potentials with the same sign (Fig. 48). The symmetries can be used to model only one half of a finned disc's thickness (Fig. 49).

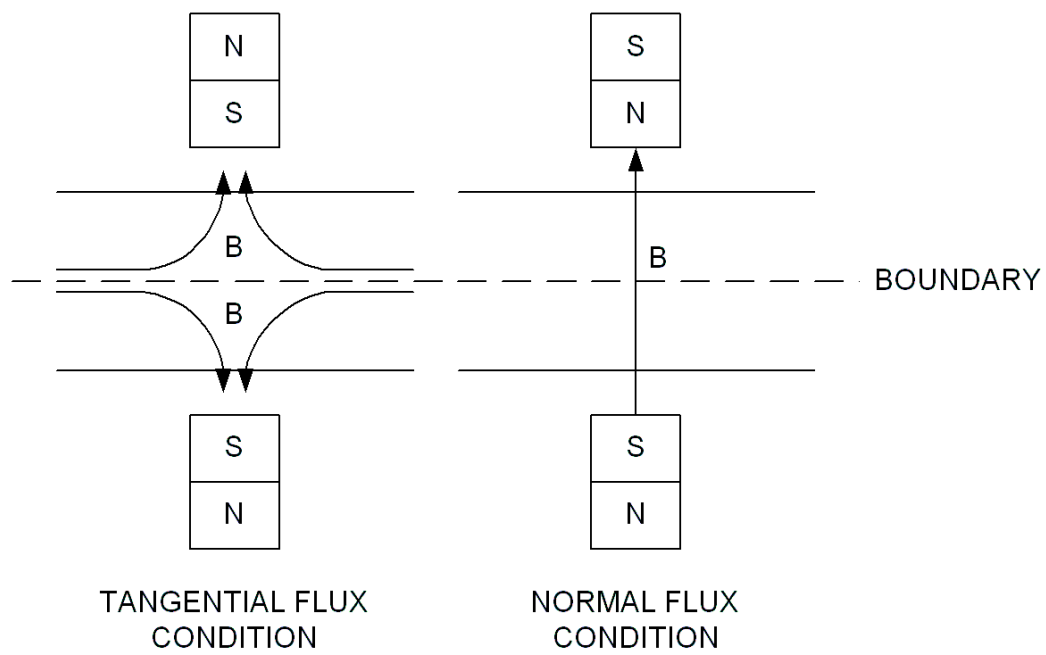


Fig. 48: Normal and tangential flux conditions

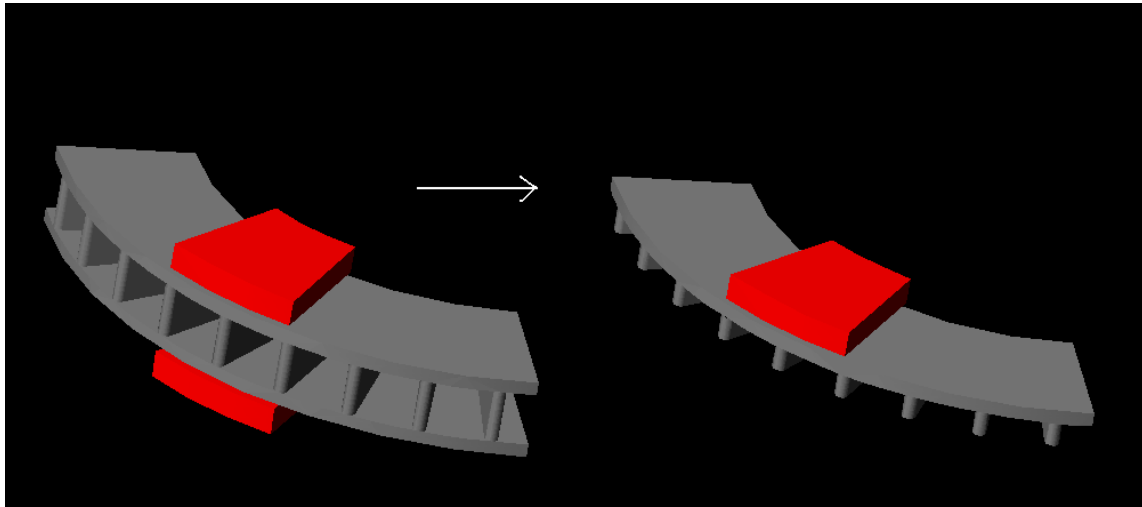


Fig. 49: Use of symmetries for the modeling of a finned disc

Finally, normal and tangential boundary conditions can be assigned to any surface in the geometry in order to account for non-meshed parts of the geometry. For instance, a normal flux condition can be used to model the stator back-iron made of infinitely permeable material because of the conservation of the magnetic field across an interface (Fig. 50).

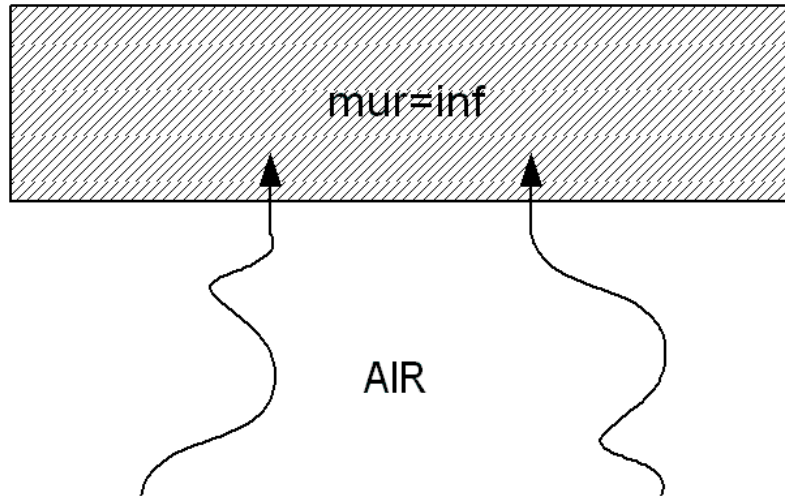


Fig. 50: Use of normal flux condition

The magnetic and electrical properties of the material can both be defined as linear or not, and isotropic or anisotropic. FLUX 3D does not allow defining a temperature dependence of the properties for transport-term or transient methods. Consequently, the electrical conductivity of the material is simply defined as isotropic and constant. The description of the magnetic properties however, is more delicate. The motivation for using finite element methods is the necessity to model the impact of ferromagnetic properties on the brake's performance. Therefore, the magnetic properties of the material must be defined as non linear. Furthermore, ferromagnetic materials used in eddy-current brakes are usually isotropic as a result from being shaped by casting rather rolling. FLUX 3D provides two models for the BH curve of isotropic ferromagnetic materials (Fig. 51).

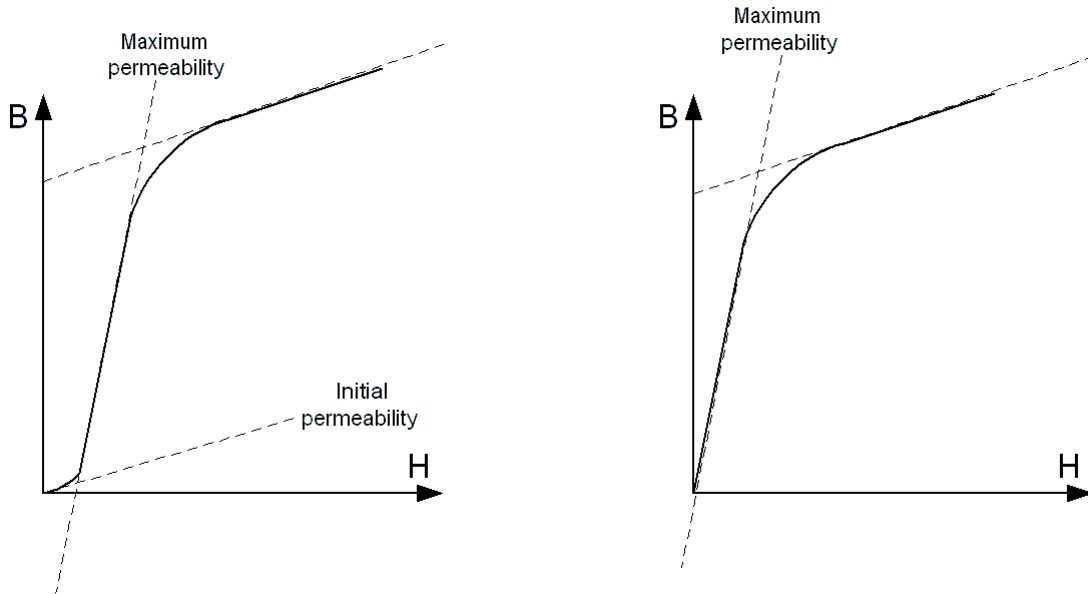


Fig. 51: Two different BH curve models for ferromagnetic materials

The first model is primarily intended for applications where the field strength varies greatly with operating conditions and where low-field behavior needs to be investigated. Such is not the case with eddy-current brakes, for which performance (i.e. torque) is overwhelmingly defined by high-field behavior throughout the entire torque-speed curve. Therefore, the second model is best suited for the analysis of eddy-current brakes. It also has the advantage of being simpler and therefore more easily computed. The second model requires only defining the magnetization at saturation (J_s , in Tesla), the maximum relative permeability, μ_r and the knee coefficient, a . The BH curve is defined by the following equations [44]:

$$B(H) = \mu_0 H + J_s \frac{H_a + 1 - \sqrt{(H_a + 1)^2 - 4H_a(1-a)}}{2 \cdot (1-a)} \quad (126)$$

$$H_a = \mu_0 H \frac{\mu_r - 1}{J_s} \quad (127)$$

Permanent magnets are modeled in the operating quadrant ($H < 0, B > 0$) with a two-parameter Cartesian linear model including residual flux density (B_r) and relative permeability (μ_{rm}), to be described for each of the three axes. This model is ideally suited for rare-earth permanent magnets, less so for Alnico or ferrite magnets and does not take into account demagnetization in high field situations.

3 – Comparison of analytical and finite-element results

The example computed analytically in chapter 2 (see TABLE 3), has been computed with FLUX 3D. Fig. 47 shows the geometry reduced by making use of periodicities. A normal flux condition on the surface above the magnet models the infinitely permeable stator back-iron, while the “infinite box” models air beyond the brake. The disc material is copper for this simulation. Fig. 52 shows the geometry meshed prior to solving.

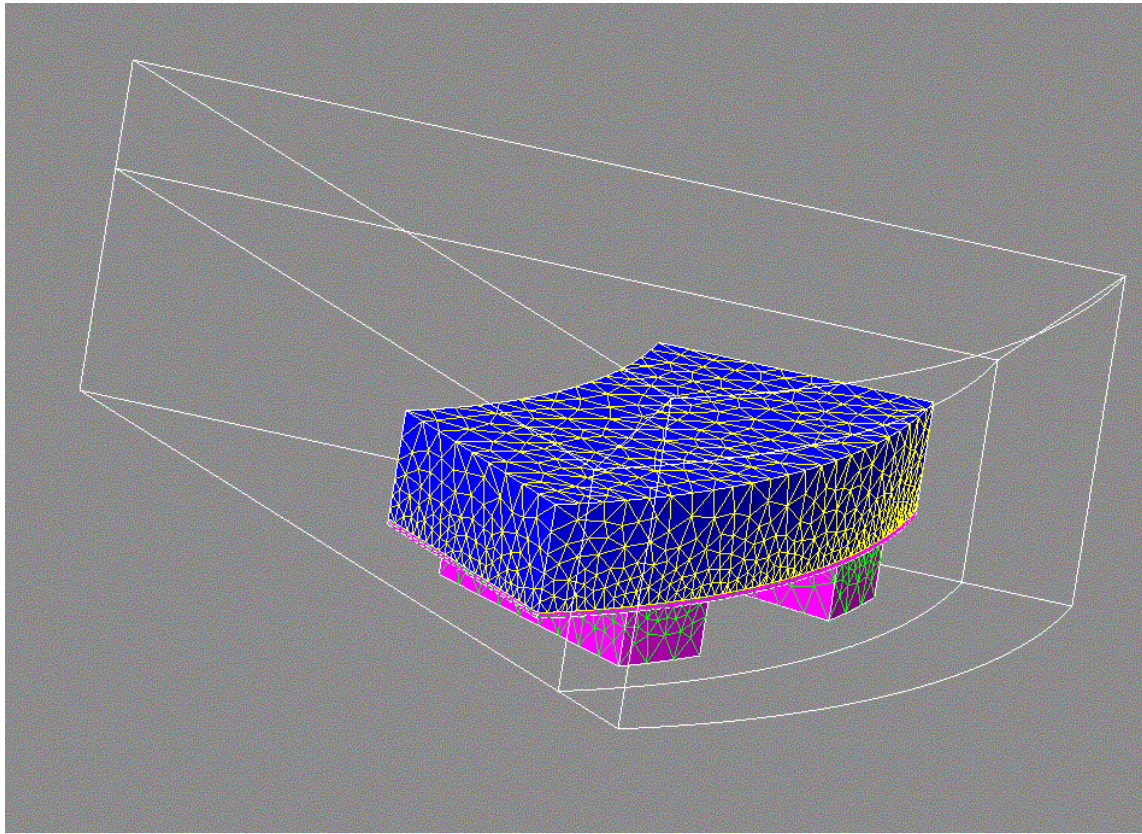


Fig. 52: Meshed geometry

FLUX 3D requires that the relative permeability of the materials on either side of the sliding surface separating two kinematic ensembles in motion must be the same. Therefore, the airgap is modeled using two equally-sized boxes containing air, with one belonging to the kinematic ensemble of the stator and the other belonging to the kinematic ensemble of the rotor. The best results are obtained with a mesh that is constant in the direction of motion, which is achieved by using a mesh extruded from the outer surface of the geometry.

The speed is stepped in increments of 250 degrees per second (approximately 41.7rpm), every 30 milliseconds. The time step for the transient analysis is 3 milliseconds, which allows nodes on either side of the sliding surface to be matched at every time step. This yields the best results, devoid of any “numerical” perturbation. Fig. 53 shows the results of the transient analysis of the brake.

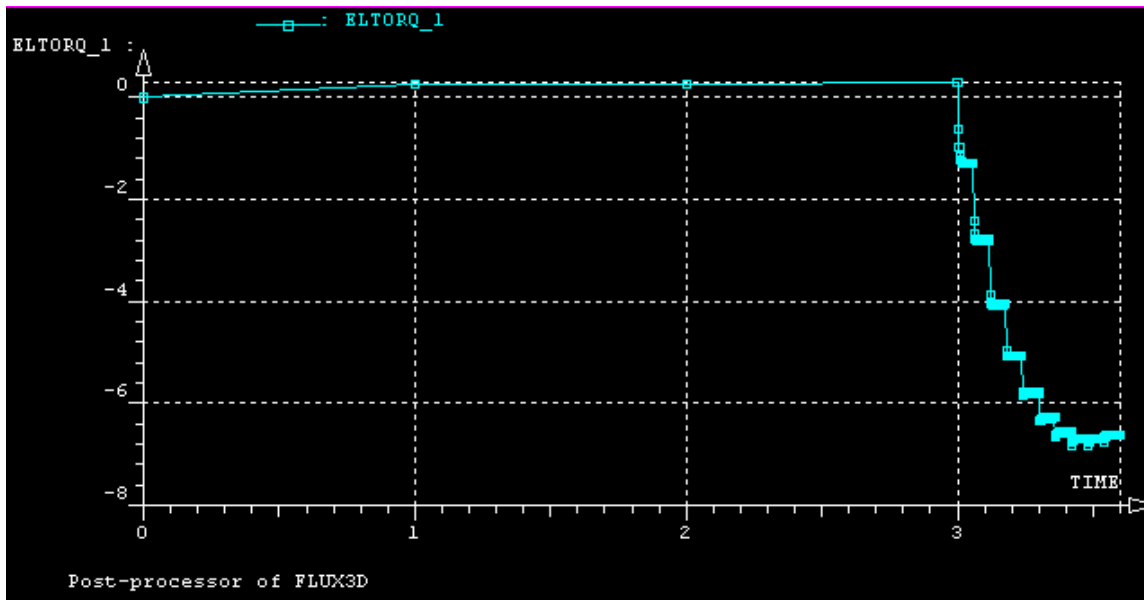


Fig. 53: Transient analysis results

Fig. 54 shows the steady state results of the three-dimensional finite element analysis compared to the analytical results for the same brake.

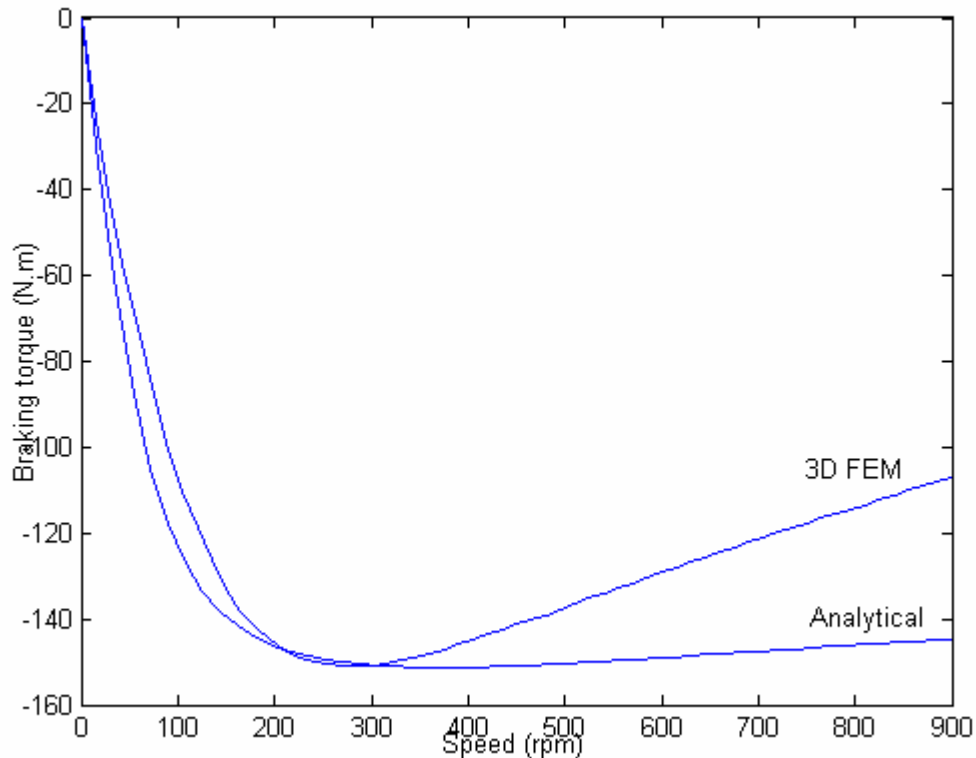


Fig. 54: Compared results of 3D finite element and analytical models

The salient feature of Fig. 54 is the accuracy of the peak torque calculated by analytical means. However, the critical speed is a gross mismatch with the critical speed computed by finite element analysis. This points that the most significant shortcoming of the analytical model is the modeling of eddy-current current paths. These paths influence the apparent electrical resistance of the disc, which influences the critical speed but not the value of the peak torque, much like an induction motor.

The inability of the analytical model to take into account the eddy-current paths is even more prominent at high speed, when skin effect limits the currents to a thin skin underneath the poles and when the returns paths become comparatively more important. As a result, the actual torque computed by the finite element method is actually much lower than the torque computed analytically. Fig. 55 shows the current density on the surface of the disc at critical speed.

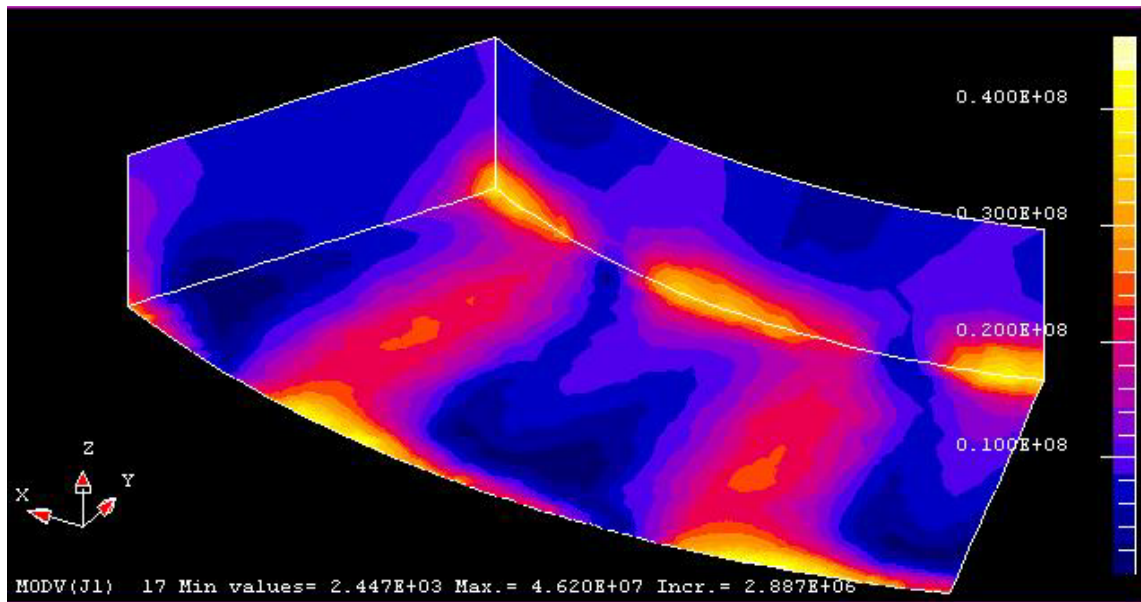


Fig. 55: Surface current density at critical speed

Both figures clearly shows the returns paths for the currents to be very significant, more so as speed increases beyond critical. These results justify the recourse to finite element analysis beyond a preliminary analytical investigation. The impact analysis of design parameters performed analytically in chapter 2 needs to be reevaluated numerically.

4 – Analysis of the impact of design parameters on performance

In order to limit the computation time by keeping the number of elements low, the disc thickness has been reduced to 5mm. The resistivity of the material has been increased to $6 \times 10^{-8} \Omega.m^{-1}$ in order to yield results in a limited number of time steps. The material is either nonmagnetic ($\mu_r=1$) or ferromagnetic ($\mu_r=250$, $J_s=1.8T$). All other parameters are kept to the values given in TABLE 3 unless otherwise required by the analysis.

4.1 – Similarities with theoretical analysis

Numerical analysis reveals the same trends as the analytical model for the following design parameters:

- Mean disc radius for non-magnetic and ferromagnetic discs
- Airgap width for non-magnetic discs
- Stator pole width for non-magnetic and ferromagnetic discs
- Stator pole number for non-magnetic and ferromagnetic discs

These parameters do not influence significantly the currents paths or the distribution of the flux density. Therefore, their impact on the performance of the brake follows trends outlined by the analytical model although the finite element analysis takes into account the return paths of the currents and magnetic saturation.

4.2 – Impact of disc area

Increasing the disc area by increasing the difference between inner and outer radii impacts the performance of the brake differently whether the disc is made of nonmagnetic or ferromagnetic materials. In nonmagnetic materials, the increase of the disc area diminishes the relative importance of the return current paths on the side. IN ferromagnetic materials, the material is more saturated at the outer edge of the disc than at the inner edge. The cross section of the disc is constant in the angular direction, while the pole widens at the outer edge. Therefore more flux is pushed through a constant cross section, which pushes the material further into saturation. The trend is exactly opposite at the inner edge, where the material moves further away from saturation.

The trend depends on the flux density through the pole, and the saturation magnetization of the disc material. If the disc is very saturated initially, then increasing the disc area will increase the peak torque more slowly then in a nonmagnetic disc. If the disc is not saturated initially, then increasing the disc area will first increase the peak torque faster than in a nonmagnetic disc, then slower as the disc material becomes more saturated. Fig. 56 and Fig. 57 show the trend for peak torque and critical speed in a material initially below from saturation.

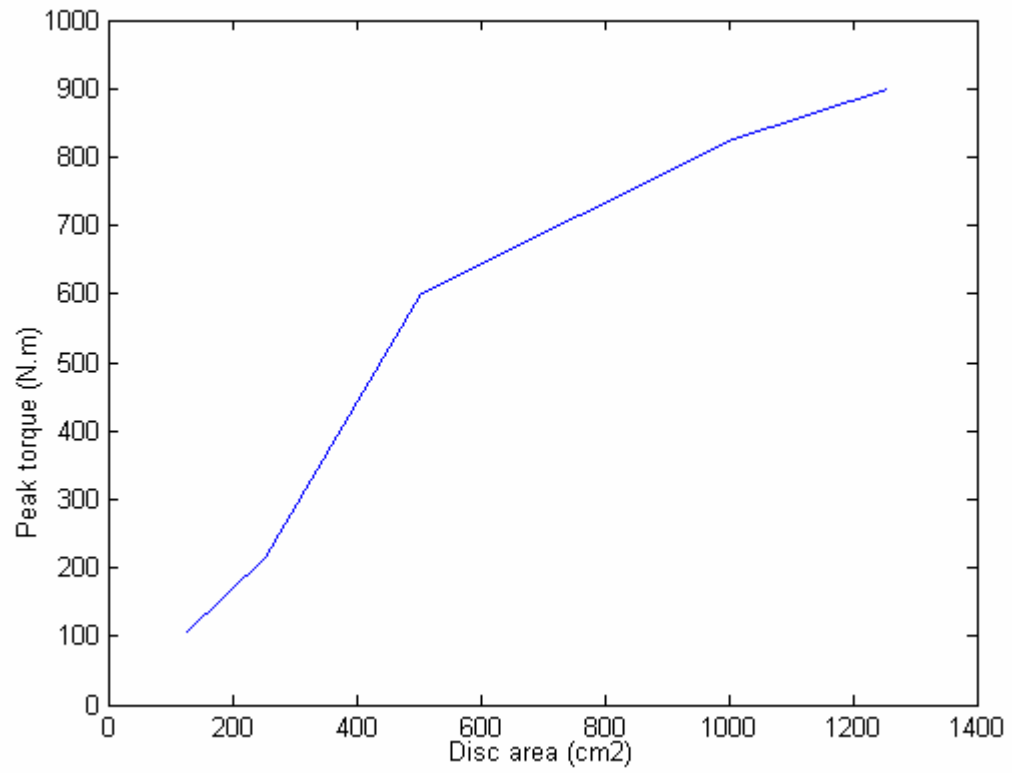


Fig. 56: Peak torque vs. disc area

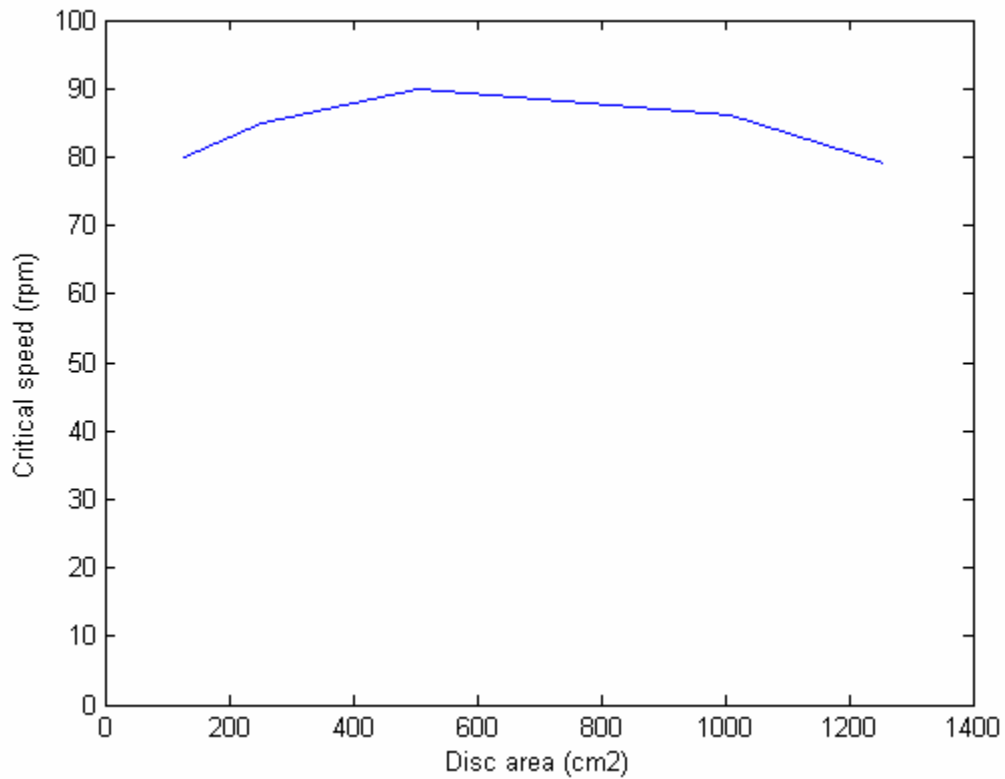


Fig. 57: Critical speed vs. disc area

4.3 – Impact of disc thickness

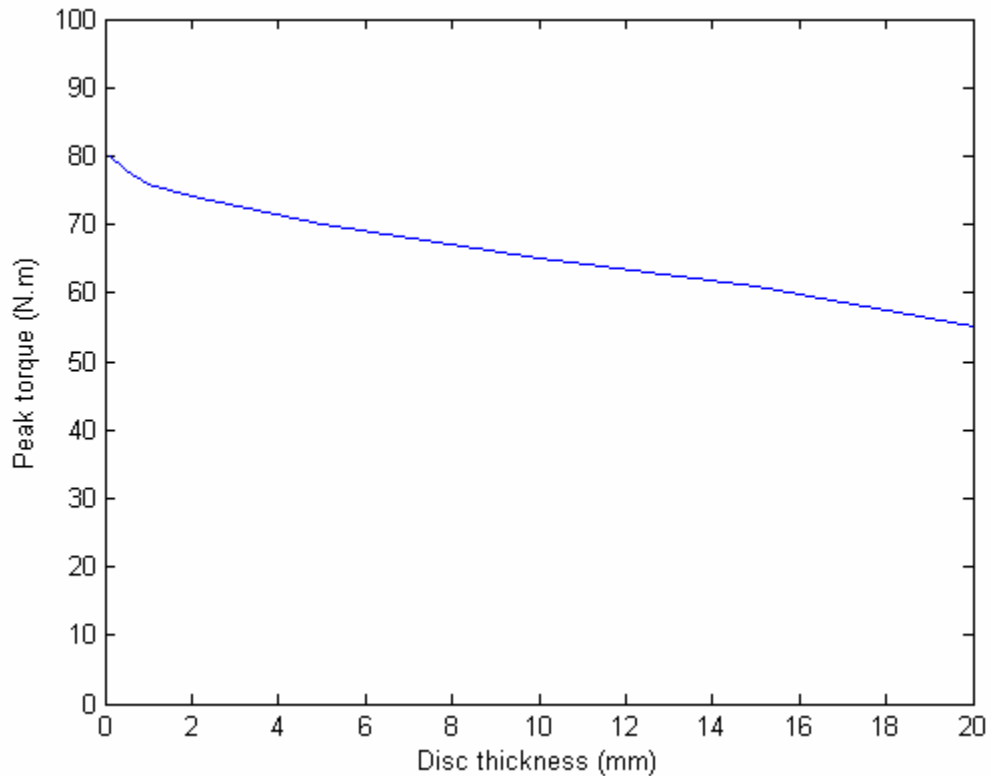


Fig. 58: Peak torque vs. disc thickness, nonmagnetic material

Increasing the thickness of the disc increases the length of the sides, where the current return paths develop. The electrical resistance of the disc thus increases, which shifts the critical speed to higher speeds and reduces the peak torque. Fig. 58 and Fig. 59 show the impact of disc thickness on peak torque and critical speed respectively for a nonmagnetic disc.

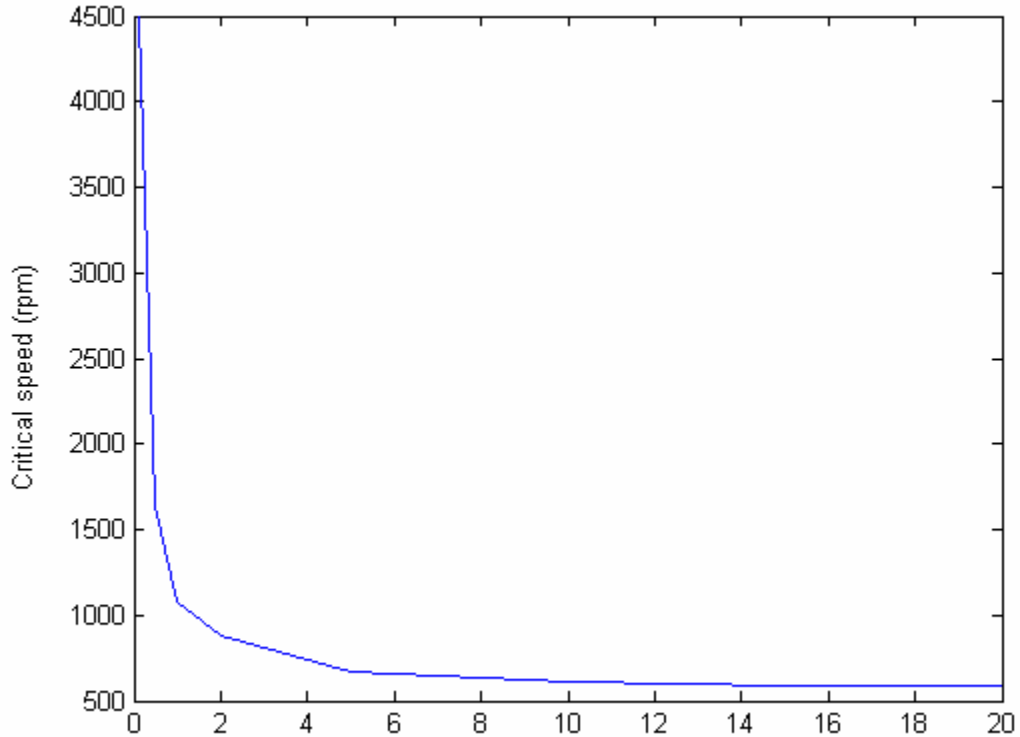


Fig. 59: Critical speed vs. disc thickness, nonmagnetic material

Fig. 60 shows the impact of the disc thickness on the peak torque of a brake with a ferromagnetic disc. The peak torque is limited for thin discs because the cross section of the disc decreases, which limits significantly the flux density. The peak torque for a ferromagnetic disc increases more slowly than for a nonmagnetic disc with the same thickness decrease. The peak torque decreases with increasing thickness like it does in nonmagnetic materials. However, it decreases faster for thicker discs. Indeed, as the disc gets thicker, the cross section diminishes and the material is no longer saturated. The

incremental relative permeability of the disc is thus high, which means eddy-currents result in a large reaction flux density that weaken the magnets' flux more easily.

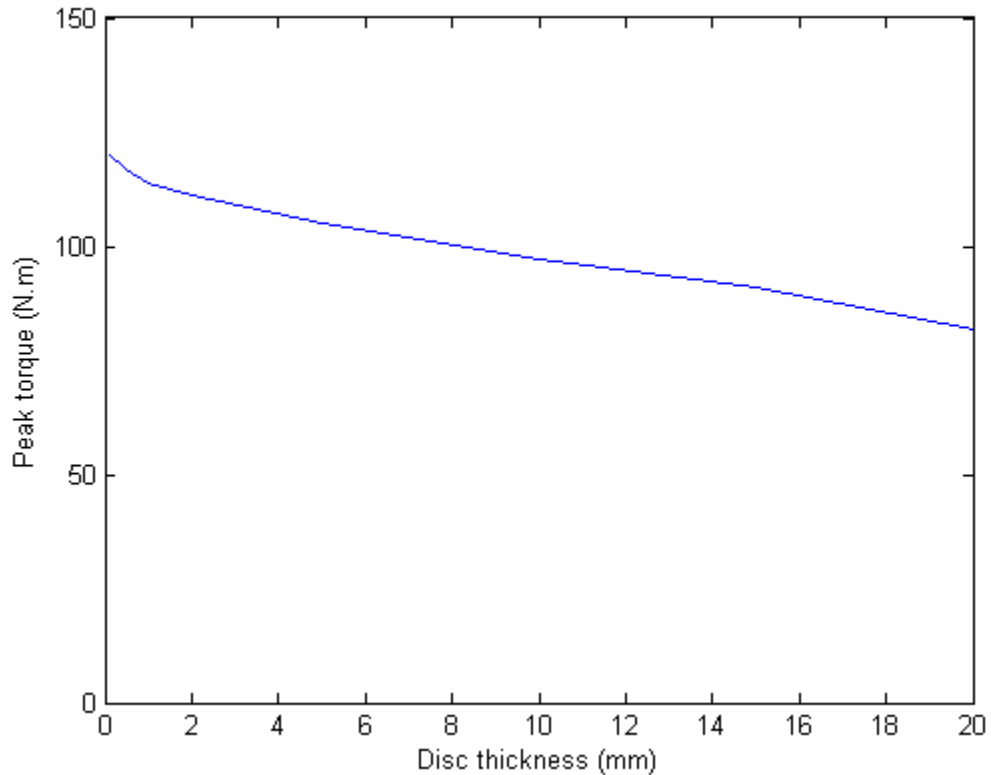


Fig. 60: Peak torque vs. disc thickness, ferromagnetic material

The trend for critical speed (Fig. 60 and Fig. 61) is similar to the trend followed for nonmagnetic materials, although the curve is shifted to lower speeds. Indeed, the increased permeability of the magnetic materials allows the eddy-currents to generate a reaction flux density at lower speeds than in nonmagnetic materials.

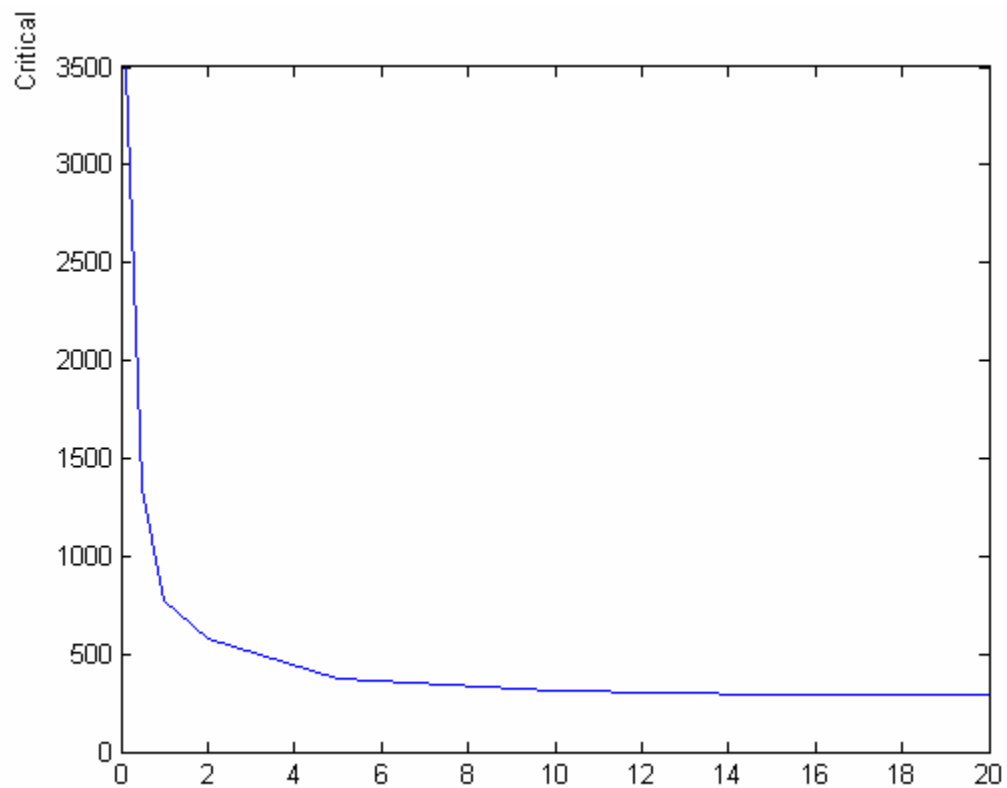


Fig. 61: Critical speed vs. disc thickness, ferromagnetic material

4.4 – Impact of airgap width

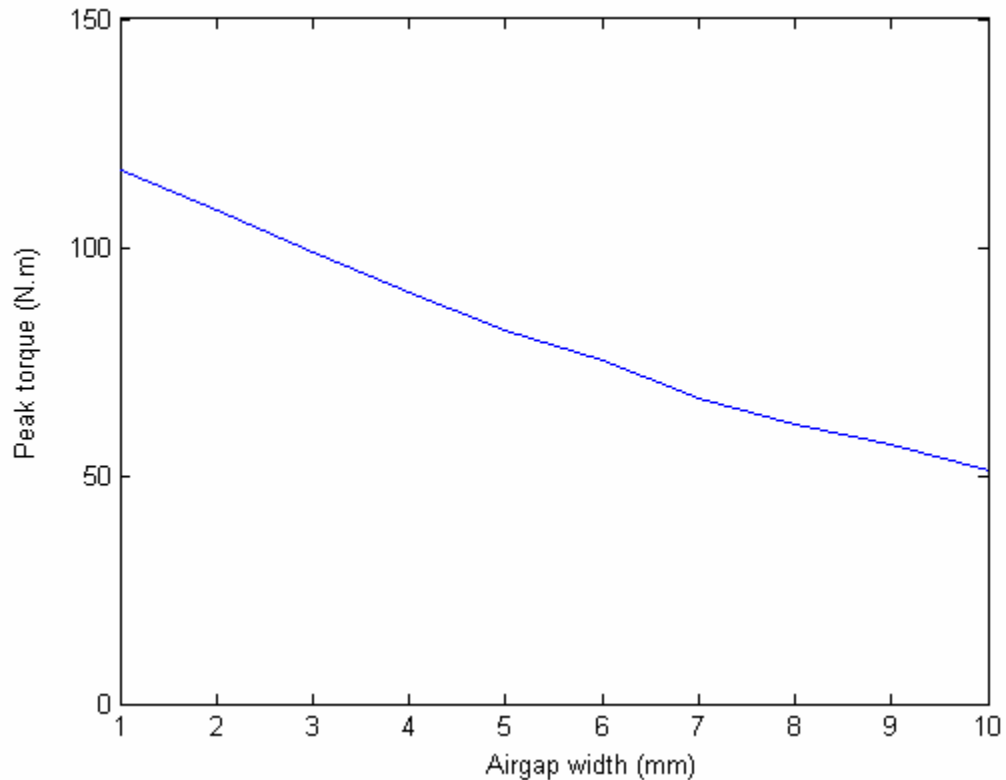


Fig. 62: Peak torque vs. airgap width, non-saturated ferromagnetic disc

The airgap width affects the reluctance of the magnetic circuit that the magnets excite.

The impact of the airgap is greater with ferromagnetic materials because of their higher magnetic permeability. The airgap thus dominates the reluctance of the magnetic circuit.

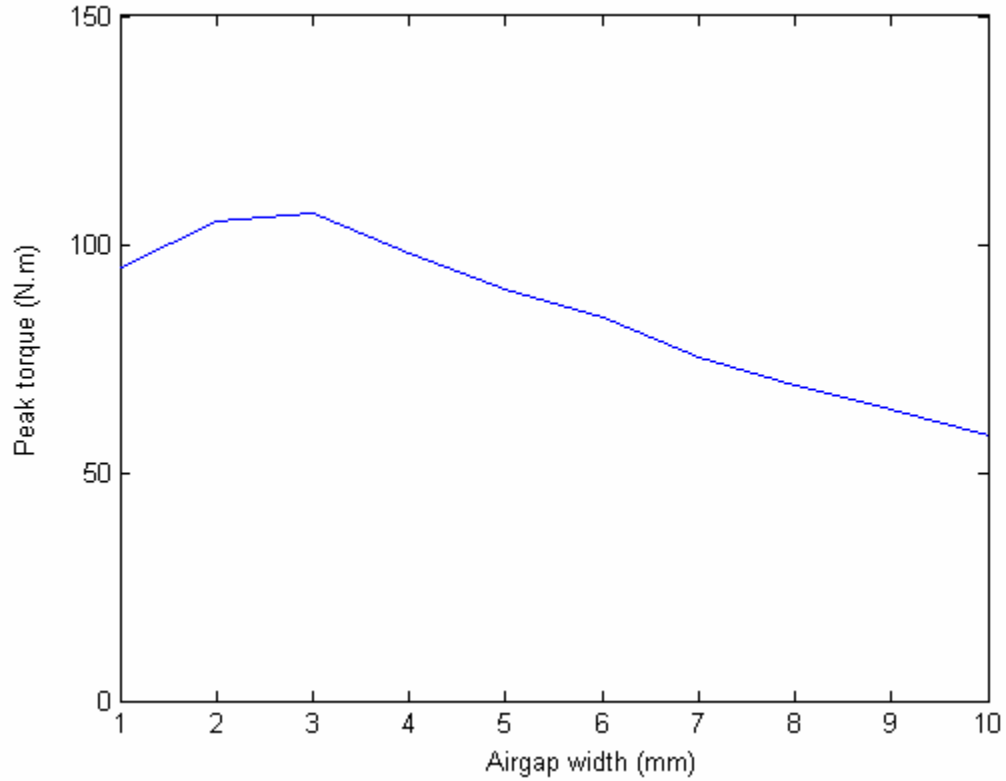


Fig. 63: Peak torque vs. airgap width, saturated ferromagnetic disc

The peak torque follows two trends depending on the level of saturation of the material. If the material is well below saturation, the trend is close to linear and the peak torque decreases faster with increasing airgap width in a ferromagnetic material than in a nonmagnetic material (see Fig. 62). If the material is very saturated, the peak torque initially increases then drops and follows the trend shown on Fig. 62 when the material is well below saturation. Fig. 63 shows the trend for a saturated material. Fig. 64 shows the impact of airgap width on the critical speed. The impact of saturation and other magnetic parameters is analyzed in greater details in a following subsection.

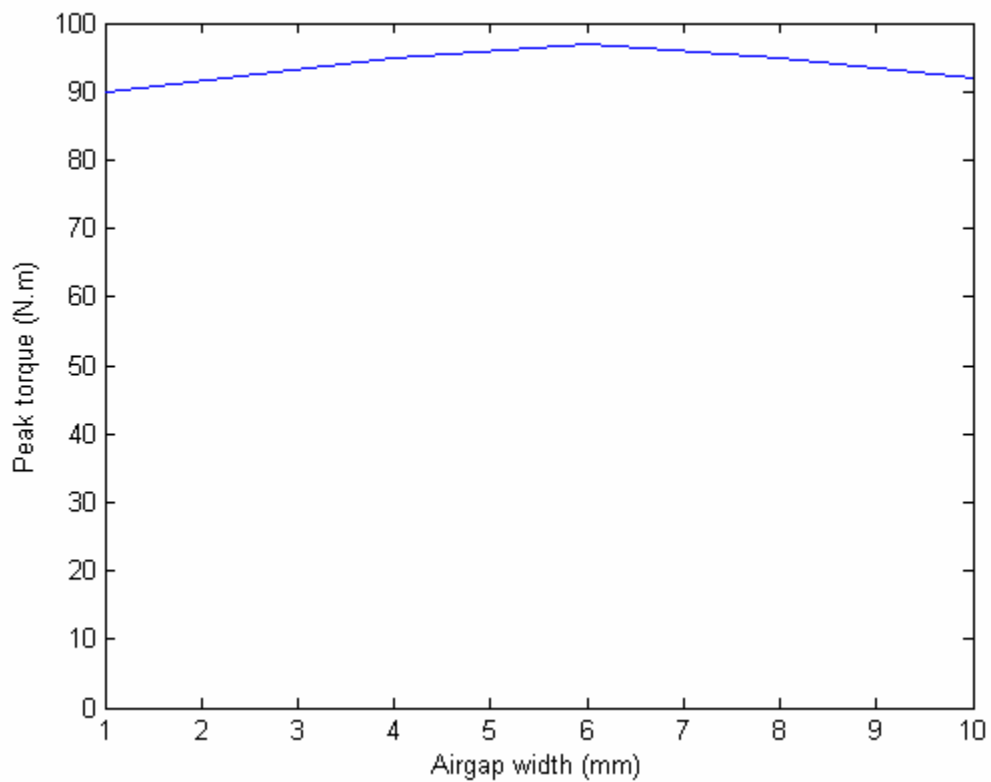


Fig. 64: Critical speed vs. airgap width, ferromagnetic disc

4.5 – Impact of electrical conductivity

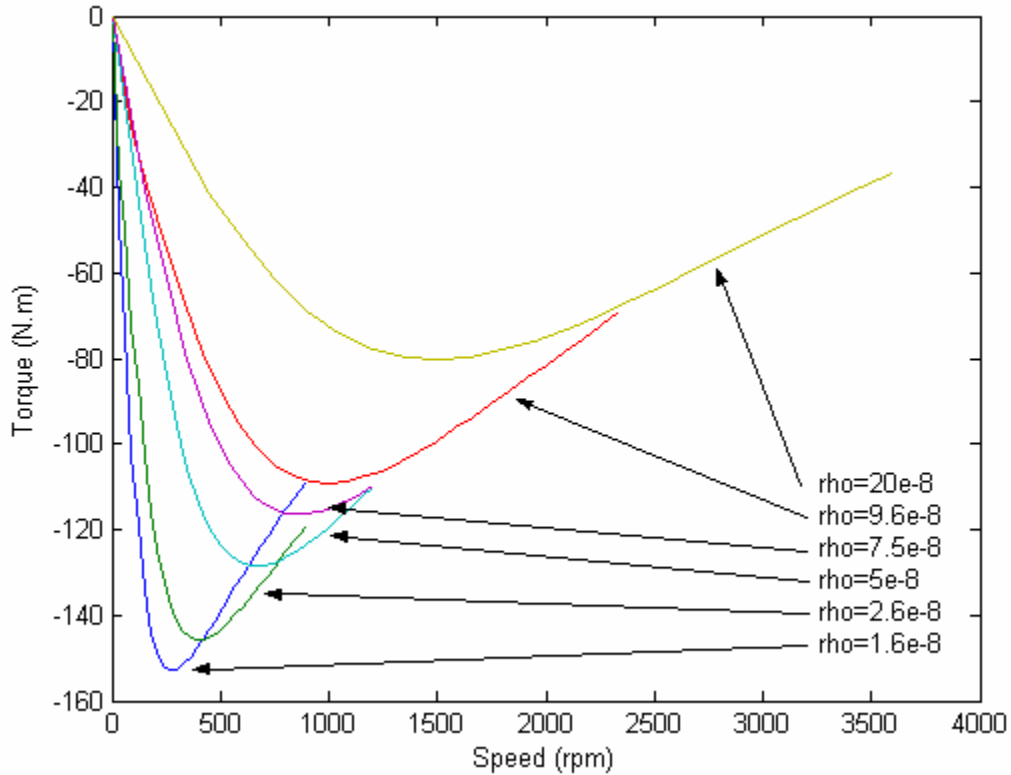


Fig. 65: Torque-speed curves for nonmagnetic materials of various resistivities

In staunch contrast with analytical results and previously published results [43], numerical analysis reveals that the peak torque does vary with the conductivity of the material (Fig. 65 and Fig. 66).

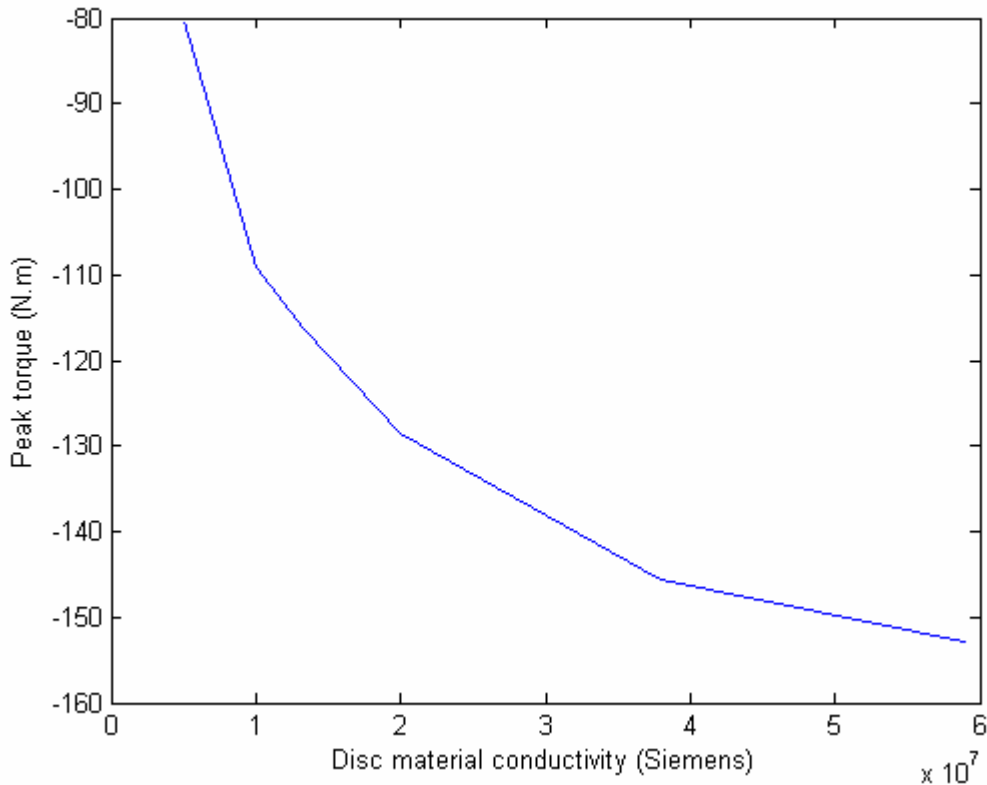


Fig. 66: Peak torque vs. disc material conductivity

The main difference between the analytical and finite element analyses is presence of the current return paths in the finite element model. Because of the return path, the braking force is no longer the sole function of the axial flux density and radial current density as was assumed in the analytical model, but is also a function of the radial flux density and axial flux density on the inner and outer sides of the disc:

$$\Delta F_\theta = J_z \cdot B_r - J_r \cdot B_z \quad (128)$$

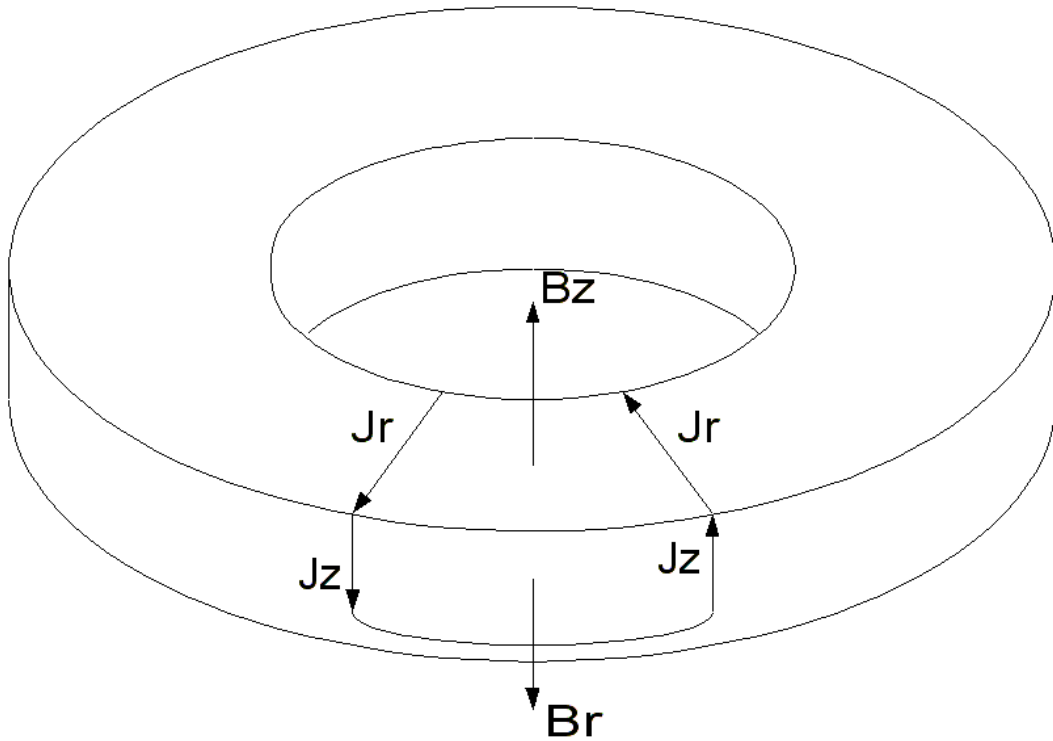


Fig. 67: Presence of radial flux density due to return current path

The radial component of the flux density is not induced by the magnets but by the eddy-currents flowing on the sides of the disc (Fig. 67). The elemental force generated by the interaction of the radial flux density and axial current density actually adds to the total force generated by the axial flux density and radial current density (Fig. 67). In an eddy-current brake, the braking force would be null if the eddy-current lines were not shifted in space with respect to the magnetic poles (Fig. 68).

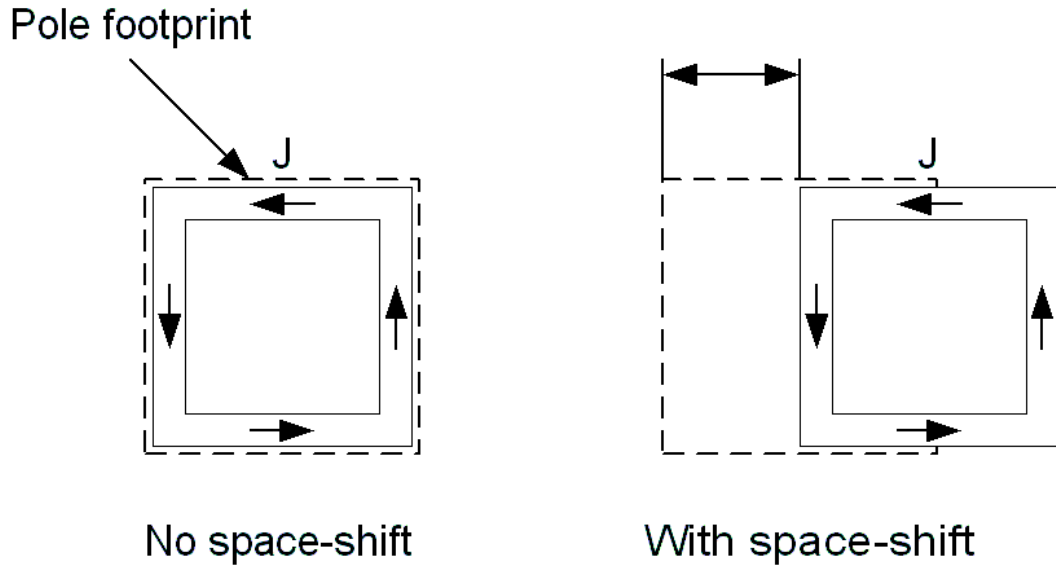


Fig. 68: Generation of eddy-current braking force by space-shift of eddy-currents

The space-shift is in fact a time shift combined with velocity. The disc acts as an RL circuit because the current (density) lags the voltage (flux density). It therefore has a time constant, which can be written in terms of the materials' properties:

$$\tau = \frac{L}{R} \propto \frac{\mu_0 \mu_r}{\rho} \quad (129)$$

If the resistivity of the material increases, the time shift diminishes. Therefore, the total braking force due to the return loop is decreasing because some of the eddy-current lines in the opposite direction are interacting with the radial flux density. Therefore, the peak braking force decreases with increasing resistivity. Fig. 69 and Fig. 70 show the difference in the shape of current return paths between high and low conductivity materials respectively.

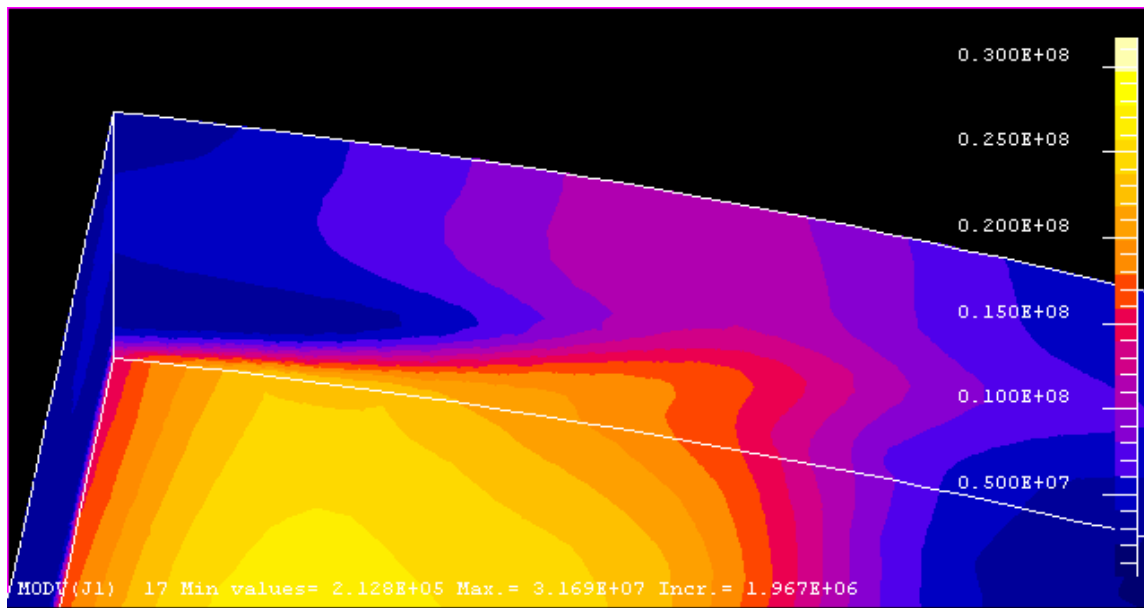


Fig. 69: Current return path in a high conductivity material

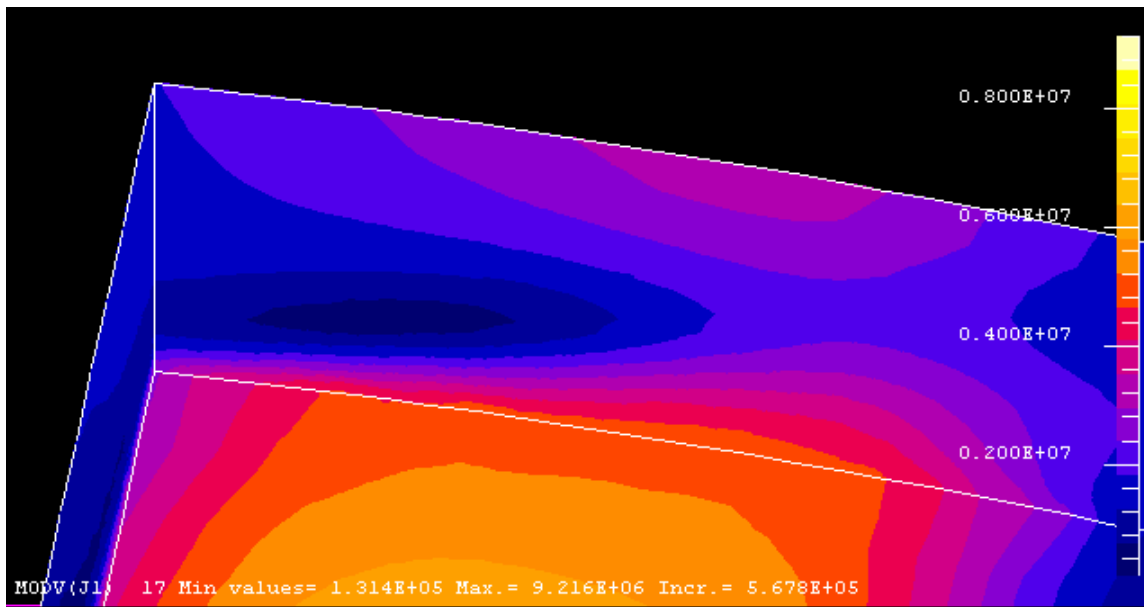


Fig. 70: Current return path in a low conductivity material

This constitutes the main difference between an eddy-current brake and a DC-fed wound-field induction motor which rotor is connected to a rheostat. The current return paths impact the total torque on the eddy-current brake, while they don't on the induction motor because the return path (i.e. the rheostat) is not mechanically connected to the rotor. If the impact of the return paths was to be diminished, the rotor would have to be built by stacking of laminations, which would constrain the currents in the angular – radial plane.

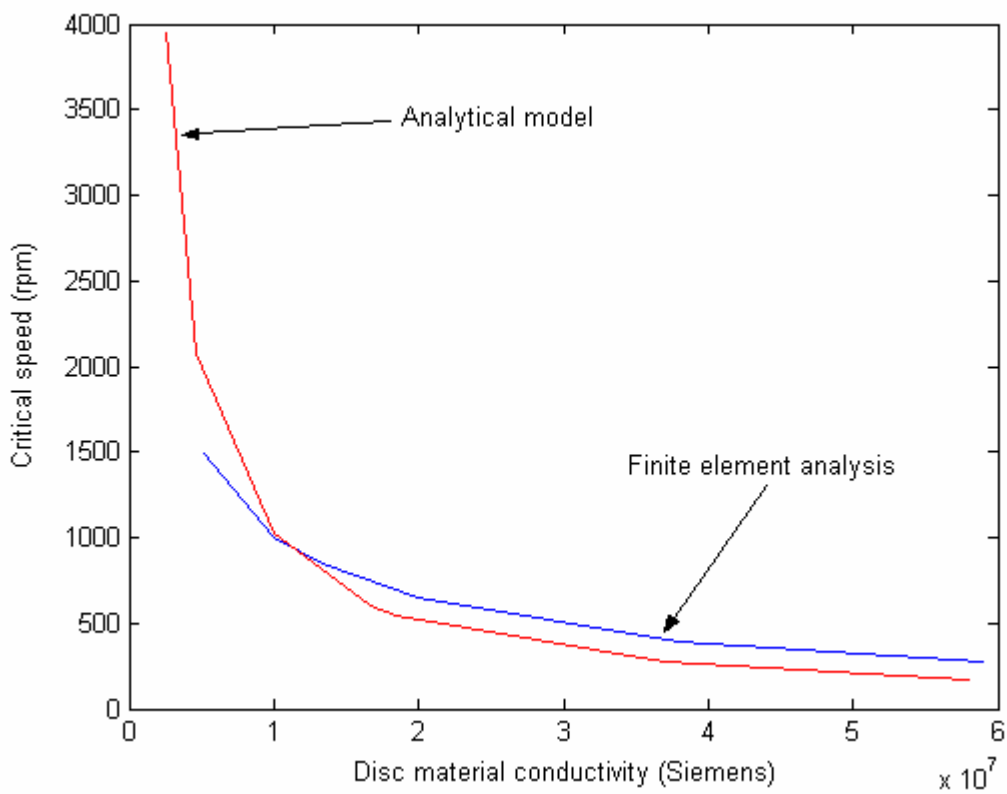


Fig. 71: Critical speed vs. disc material conductivity, nonmagnetic material

Fig. 71 shows the evolution of critical speed with the disc's conductivity for a nonmagnetic material. As a result of the finite element analysis taking into account eddy-current paths, the critical speed computed is significantly different (+59%) but parallels the analytical results for high conductivities. For low conductivities, the skin effect is weaker so the error due to eddy-current paths is less important. The two curves actually cross and the error is reversed. Note that the analysis was not pushed to very low conductivities as it was in the analytical study, because of the peak torque decreasing rapidly, which renders low conductivities useless for practical applications.

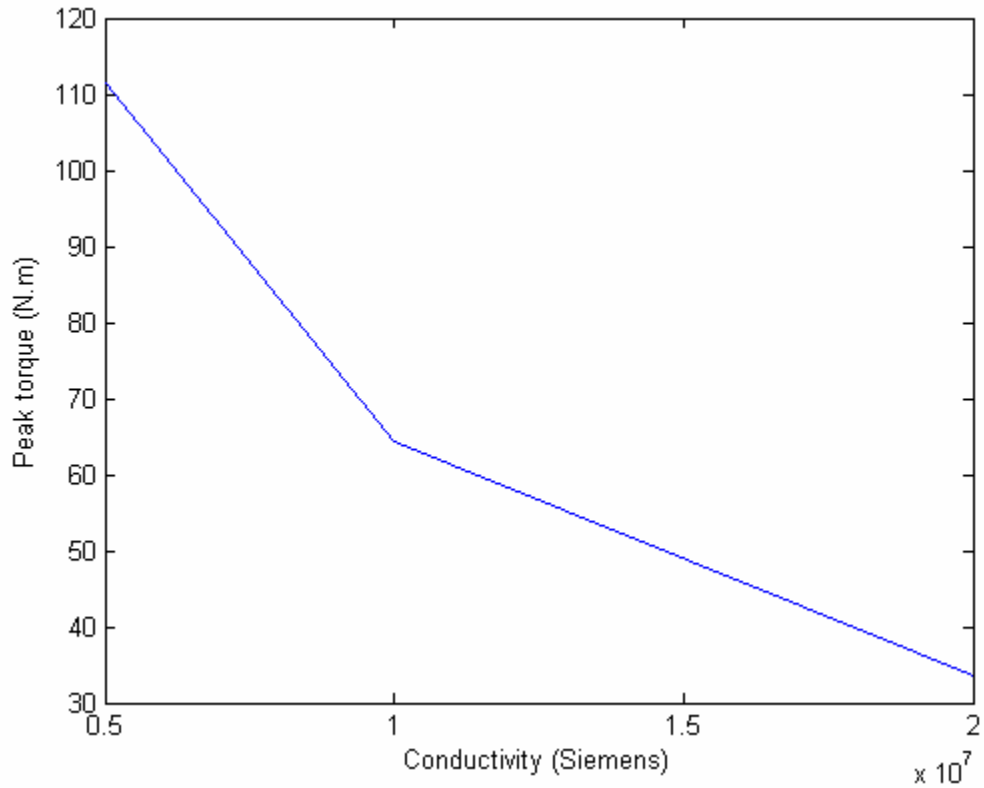


Fig. 72: Peak torque vs. disc material conductivity, ferromagnetic

The results of varying the electrical conductivity of the disc's material is similar in ferromagnetic material, although the trend does not parallel the trend followed by nonmagnetic materials because of the relative permeability and saturation. Fig. 72 shows the impact of electrical conductivity on the peak torque and Fig. 73 shows the impact on the critical speed.

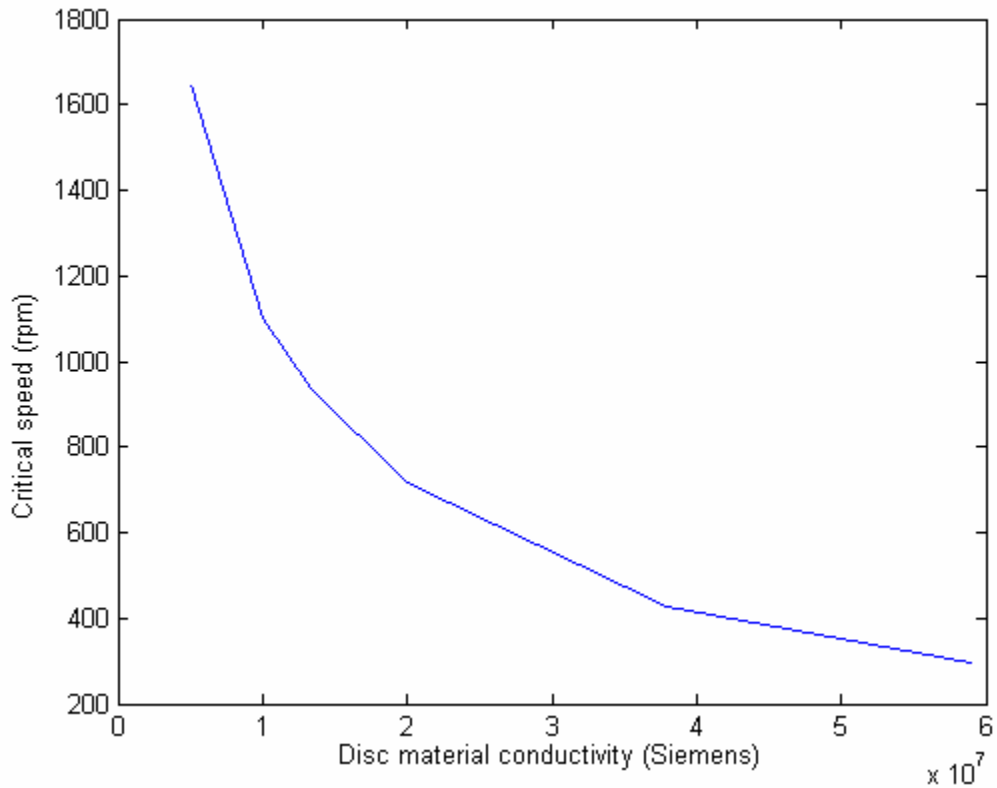


Fig. 73: Critical speed vs. disc material conductivity, ferromagnetic

4.6 – Impact of ferromagnetic properties

The disc ferromagnetic parameters are the relative permeability and the saturation magnetization. In an eddy-current brake, the relative permeability determines how much flux density results from a given current density, while the saturation magnetization determines the flux density below which a material is magnetic, and beyond which it behaves like air. Fig. 74 shows the impact of relative permeability on the peak torque.

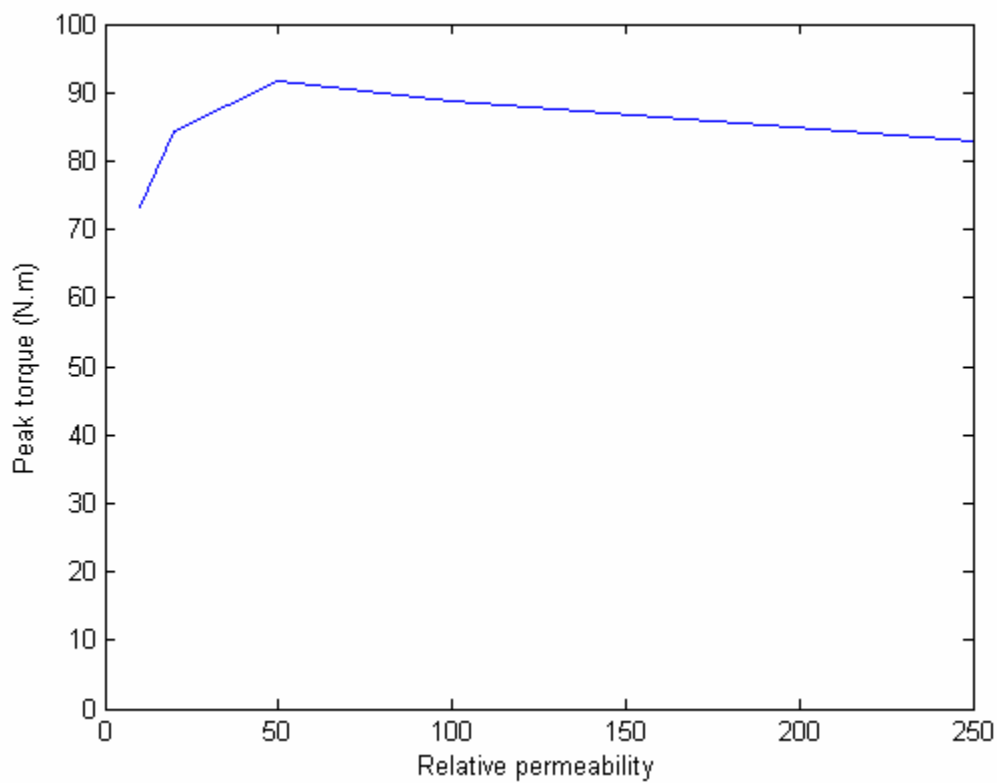


Fig. 74: Peak torque vs. relative permeability, $J_s=1.8T$

The peak torque is maximized for a relatively low value of the relative permeability. The response to the excitation field of the permanent magnets is increasing with the relative permeability, so the flux density tends to increase, which increases the peak torque. However, the reaction field resulting from the eddy-currents also increases with the relative permeability. The value of the permeability at which the peak torque is maximized depends on the saturation magnetization because this later determines how much flux density the material can be induced with.

The peak torque is maximized at lower relative permeabilities for high saturation magnetization and at higher relative permeabilities for low saturation magnetization. In materials with low saturation magnetization, a high relative permeability tends to restrict the flux density within a thin skin, while saturation tends to spread it. Saturation is the dominant effect for low saturation magnetization values. Therefore, it takes a very high relative permeability for eddy-currents to result in a reaction flux density high enough to make the torque-speed curve peak. However in high saturation magnetization materials, saturation is very limited. Therefore, skin effect is the dominant effect and decreases the peak torque very rapidly with increasing relative permeability.

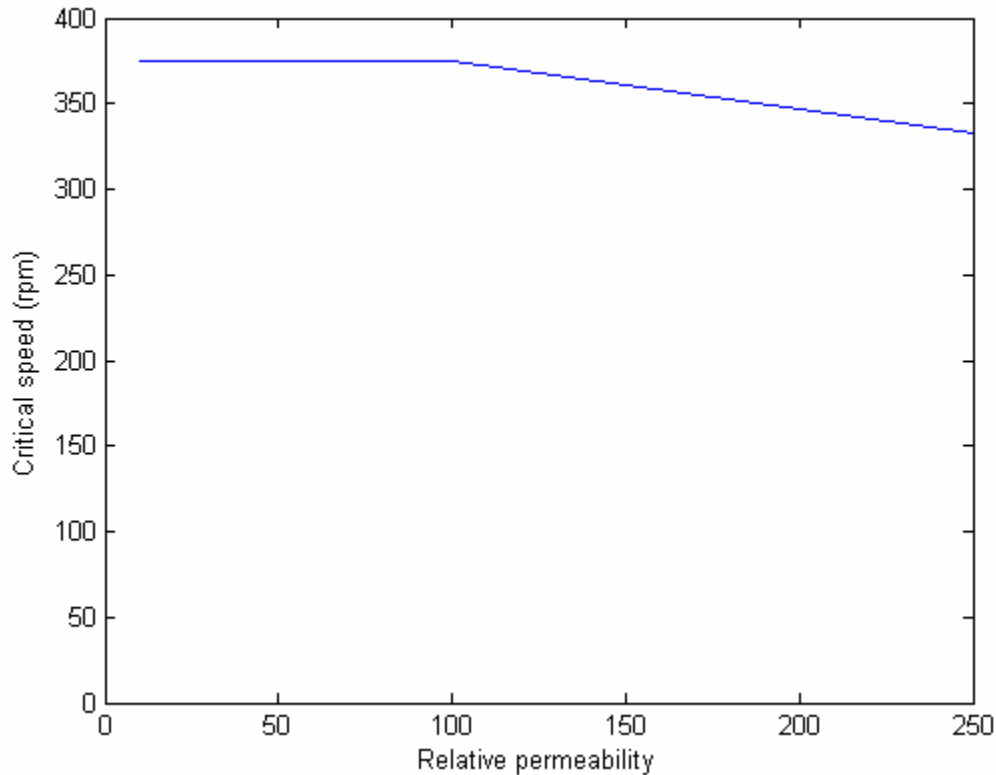


Fig. 75: Critical speed vs. relative permeability, $J_s=1.8T$

Because of the competing effects of skin effect and saturation, the critical speed is initially only lightly impacted by the relative permeability (Fig. 75). Saturation magnetization has a profound impact on the peak torque because it determines how much flux density can be induced in the material (see Fig. 76). The impact is amplified by the fact that the peak torque is proportional to the square of the flux density.

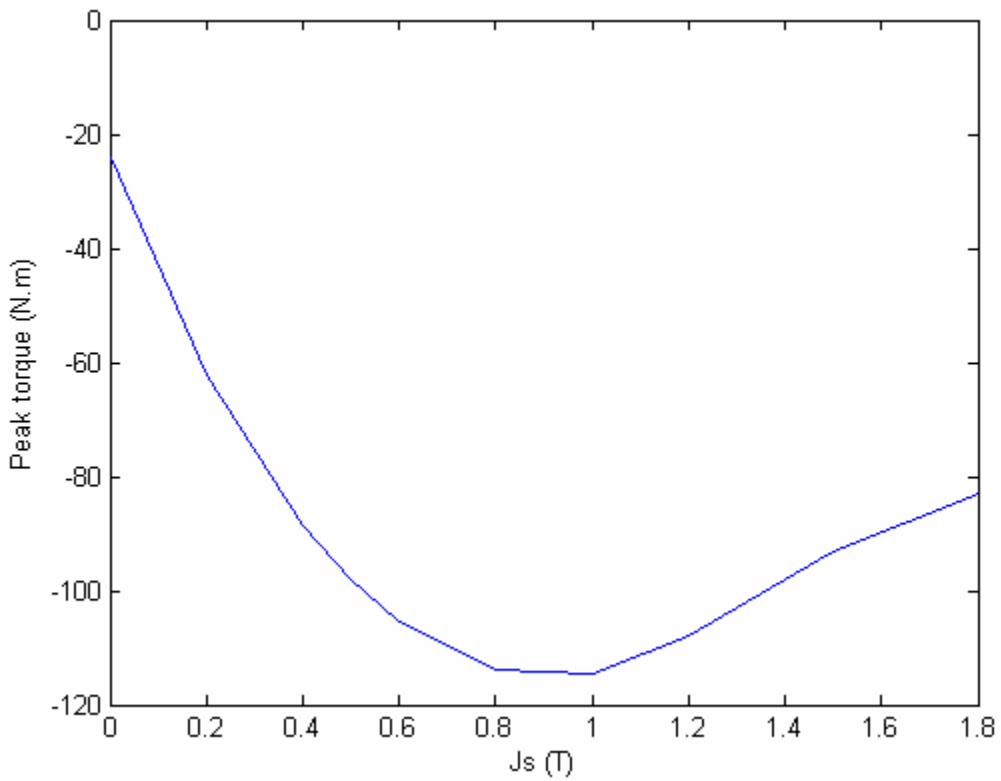


Fig. 76: Peak torque vs. saturation magnetization

For an equal cross-section, if the saturation magnetization of the disc's material is slightly lower than the permanent magnet's residual flux density, the peak torque is maximized. The disc is heavily and uniformly saturated (Fig. 77).

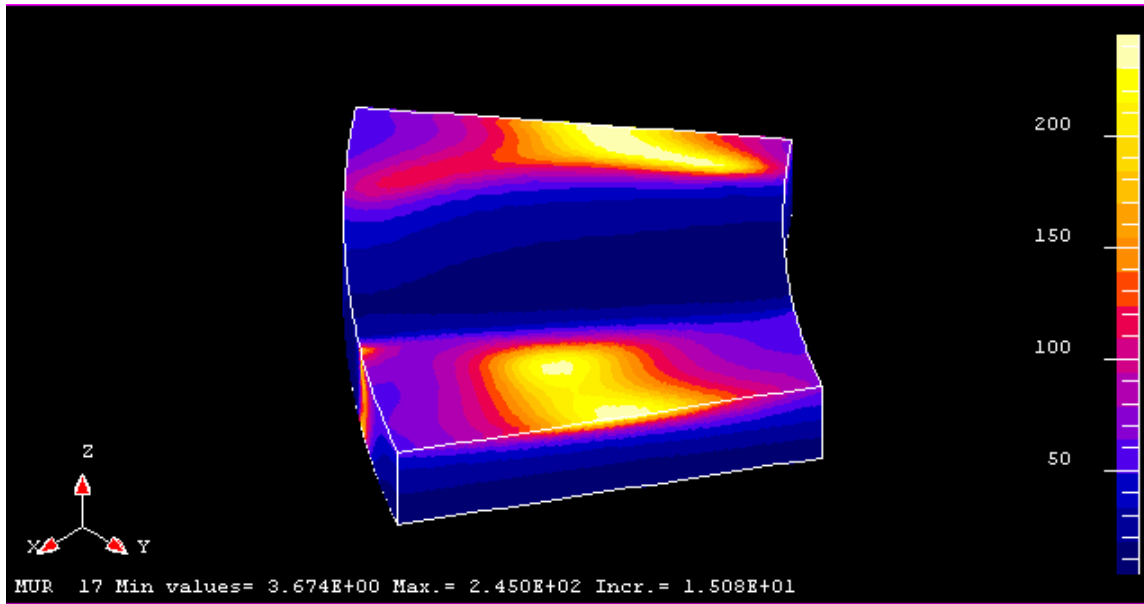


Fig. 77: Relative permeability in saturated disc, $J_s=0.8\text{T}$, $B_r=1.4\text{T}$

The uniformity of the flux density distribution is due to the high reluctance of saturated spots, which pushes the magnetic field to less saturated spots. The magnetic field “prefers” to magnetize lower reluctance spots. Therefore the average flux density is high (Fig. 78), and so is the torque.

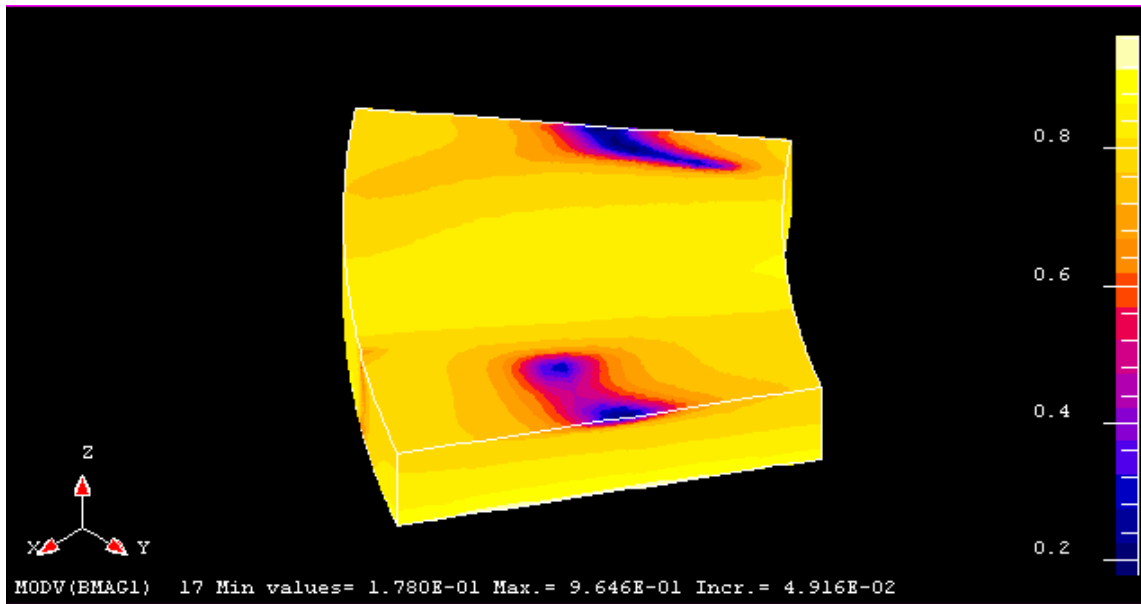


Fig. 78: Flux density in disc, $J_s=0.8\text{T}$, $Br=1.4\text{T}$

Furthermore, when the material is heavily saturated, the incremental permeability is low. This means that a given current density will result in a smaller reaction flux density (Fig. 79). Therefore, the current density can increase higher than it would in a non-saturated material.

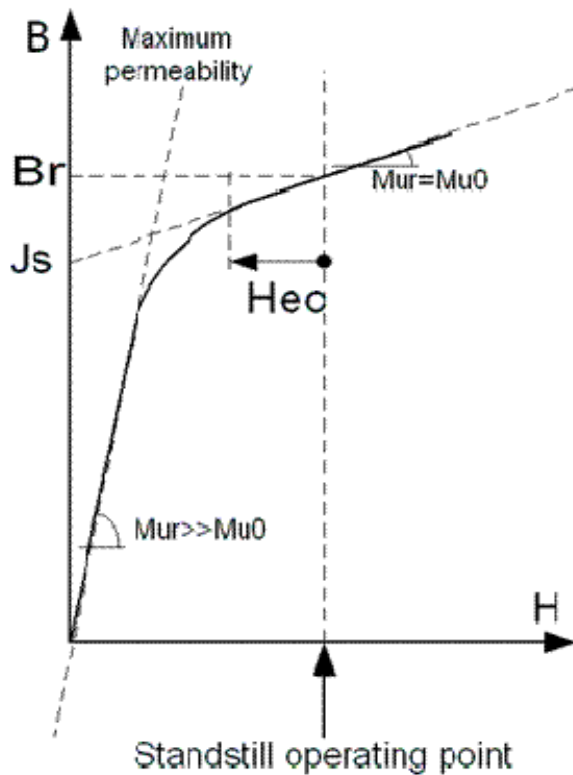


Fig. 79: Reaction of saturated material to eddy-currents

When the saturation magnetization of the disc's material is greater than the permanent magnet's residual flux density, the peak torque is lower. This is due to the fact that the material is operated well below saturation. The average flux density throughout the disc is low (Fig. 80) and therefore so is the torque.

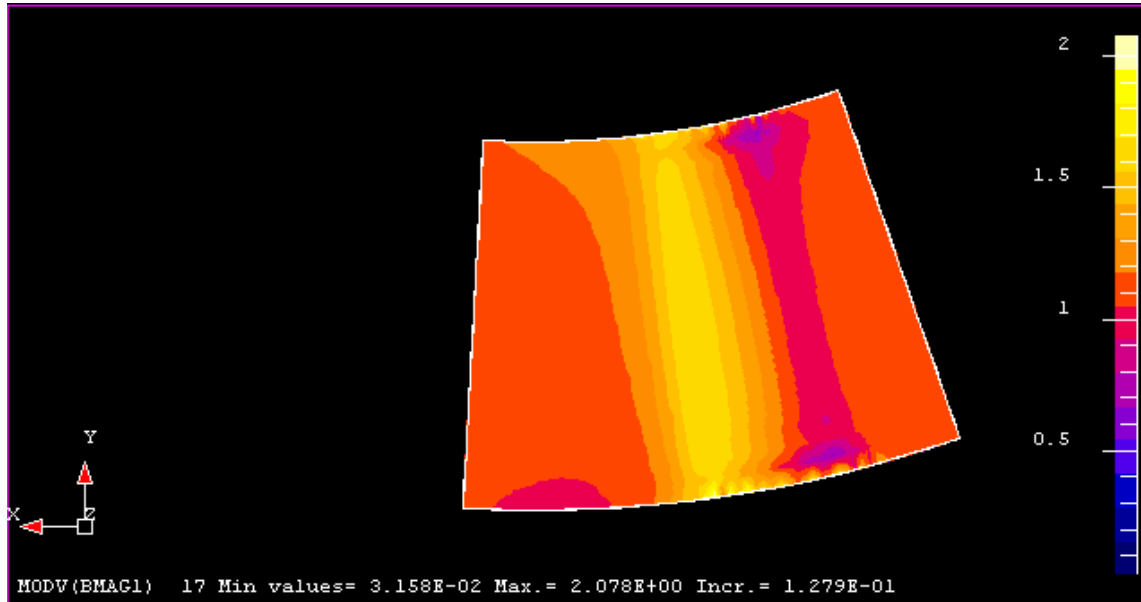


Fig. 80: Flux density in non-saturated disc, Js=2.2T, Br=1.4T

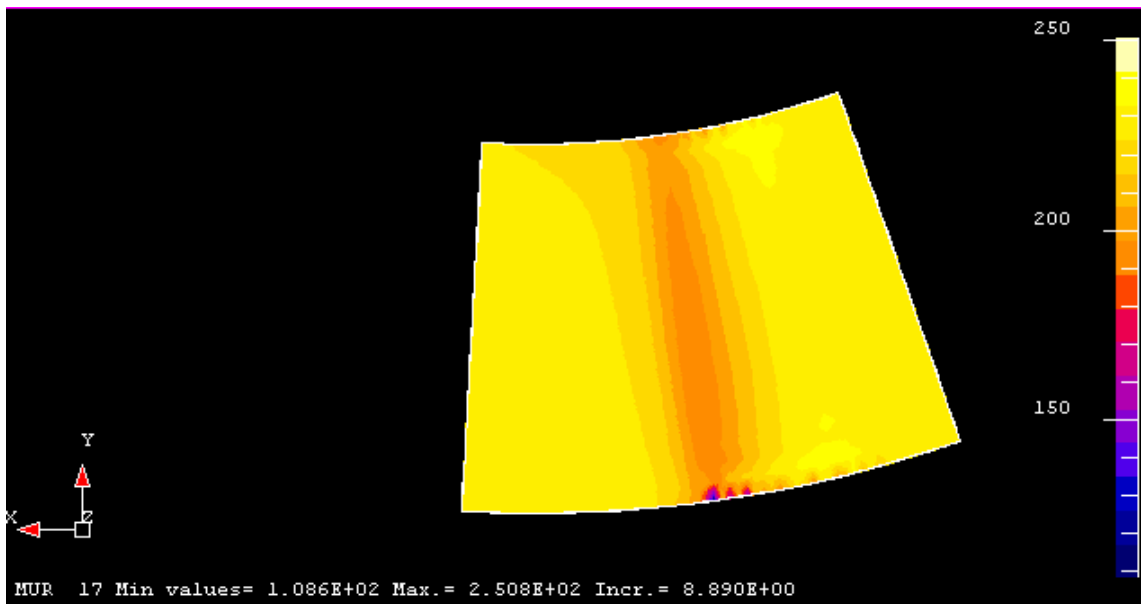


Fig. 81: Relative permeability in non-saturated disc, Js=2.2T, Br=1.4T

Furthermore, the incremental relative permeability is high (Fig. 81) so the eddy-current's magnetic field quickly opposes the excitation field and the skin effect reduces the effective portion of the material in which the braking torque is generated. Below the point of maximum torque, the peak torque decreases rapidly with the saturation magnetization of the disc's material. Once the material is fully saturated, saturation decreases the flux density uniformly throughout the material, which lowers the performance consequently.

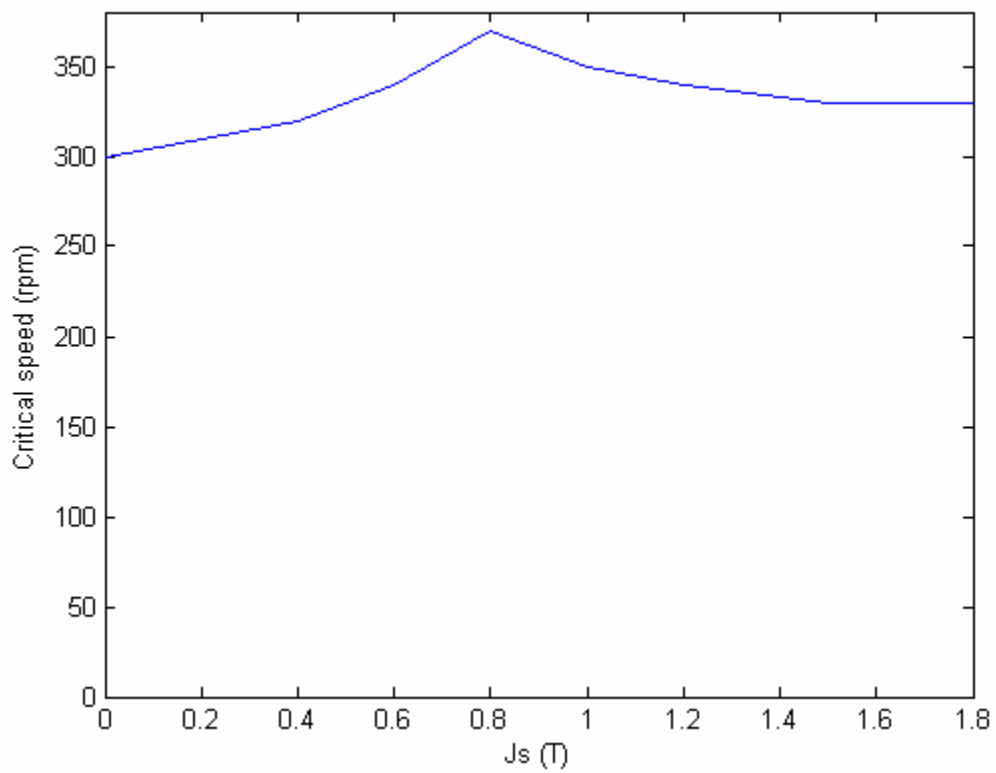


Fig. 82: Critical speed vs. saturation magnetization

Saturation magnetization has a secondary influence on the critical speed because this later is primarily determined by the incremental relative permeability (Fig. 82). If the disc is very saturated, then the disc behaves like air. Critical speed increases slowly because of the de-saturation of the material and reaches a maximum when the saturation magnetization is slightly below the magnet's residual flux density. Beyond that point, the material has an increasingly magnetic behavior and the critical speed diminishes. Indeed, the incremental relative permeability makes it easier for the eddy-current to generate a reaction flux density to oppose the excitation field.

4.7 – Impact of permanent magnet properties

As shown in the previous subsection, the influence of the residual flux density of the permanent magnet is linked to the magnetic parameters of the disc's material. If the permanent magnet's residual flux remains well below saturation, the peak torque and critical speed follow closely the trends outlined by analytical analysis: the peak torque is a function of the residual flux density squared, while the critical speed remains constant. However, as the value of the residual flux density of the magnet approaches the value of the saturation magnetization of the disc's material, the peak torque increases faster than the residual flux density squared. It peaks for B_r slightly greater than J_s , then slowly decreases with increasing B_r . The critical speed begins to slowly decrease as B_r approaches J_s . Then it decreases more rapidly beyond that value. The trend is exactly the opposite of that observed for decreasing J_s in the previous subsection.

5 – Conclusions on numerical analysis

Numerical analysis has confirmed the trends computed by the analytical model that depend on geometric parameters. It has however, infirmed the trends that depend on the electrical conductivity of the disc. This result confirms the need to use numerical analysis to compensate for the limitations of analytical models.

Finite element analysis provides an applicable insight of the impact of ferromagnetic properties. Despite limitations, it indicates that the optimum design is located within the computable range of ferromagnetic properties. The limitations are due to the current state of the art in finite element analysis. These limitations primarily arise from non-linearities of the materials. Computations are typically difficult in heavily saturated materials because the software's solver has to go through many Newton-Raphson iterations to accurately take into account the saturation. For low values of the disc material's saturation magnetization, the computations proceed normally up to a certain speed where the results diverge and the computation stops.

Attempts to simulate discs with a relative permeability beyond a few hundreds (approximately 400) have been unsuccessful. The computation time increased exponentially and the results oscillated and finally diverged.

CHAPTER IV

EXPERIMENTAL VALIDATION

1 – Objective and experimental procedure

The objective of the experiment is to establish the ability of the finite element analysis software to model the performance and behavior of eddy-current brakes excited by rare-earth permanent magnets and using a disc made of ferromagnetic material. Therefore, the numerically modeled brake and the experimentally tested brake must be as similar as possible. Because of some constraints imposed by the software, the test bed had to be adapted to the numerical model instead of the opposite.

Most soft magnetic materials applications require a combination of a high relative permeability with an electrical conductivity as low as possible. Such is the case for transformers, inductor cores, and electric motors. Therefore, magnetic properties are listed only for useful materials, which have a high relative permeability. However, finite element analysis indicates that eddy-current brakes require low permeability soft magnetic materials with a high electrical conductivity. There are indications that cast iron and some steels do possess these properties but because they are almost never used in electromagnetic applications, their properties are not available. The only ferromagnetic material with a relative permeability low enough to be modeled by FLUX 3D is cobalt. 99.9% pure cobalt has at most a maximum relative permeability of 250 and

a magnetization at saturation of 1.8 Tesla. Consequently, cobalt is chosen as the material for the test bed's disc.

Furthermore, the geometry modeled by finite elements has been kept as simple as possible in order to keep the computation times reasonable. Only the functional part of the disc has been modeled, as a ring. Therefore, the experiment must preserve the ring and use a nonmagnetic and non-conducting material for the hub. The stator has been modeled as a smooth surface delimiting an infinitely permeable region beyond the stator. This must be preserved by using a thick ring of ferromagnetic material with a high relative permeability and a saturation magnetization much higher than the magnets' remnant flux. The material chosen is a mild steel (1018, 0.18% C), which has a maximum relative permeability up to 1100 and a saturation magnetization up to 1.8 Tesla [5].

Finally, the performance can only be simulated for a constant temperature. The easiest way to ensure a constant and uniform temperature in the experiment is to use water to cool the disc.

2 – Test bed design

The test bed general architecture is shown on Fig. 83. It includes a motor drive, a torquemeter, the eddy-current brake, a handheld ampmeter and a handheld infrared thermometer.

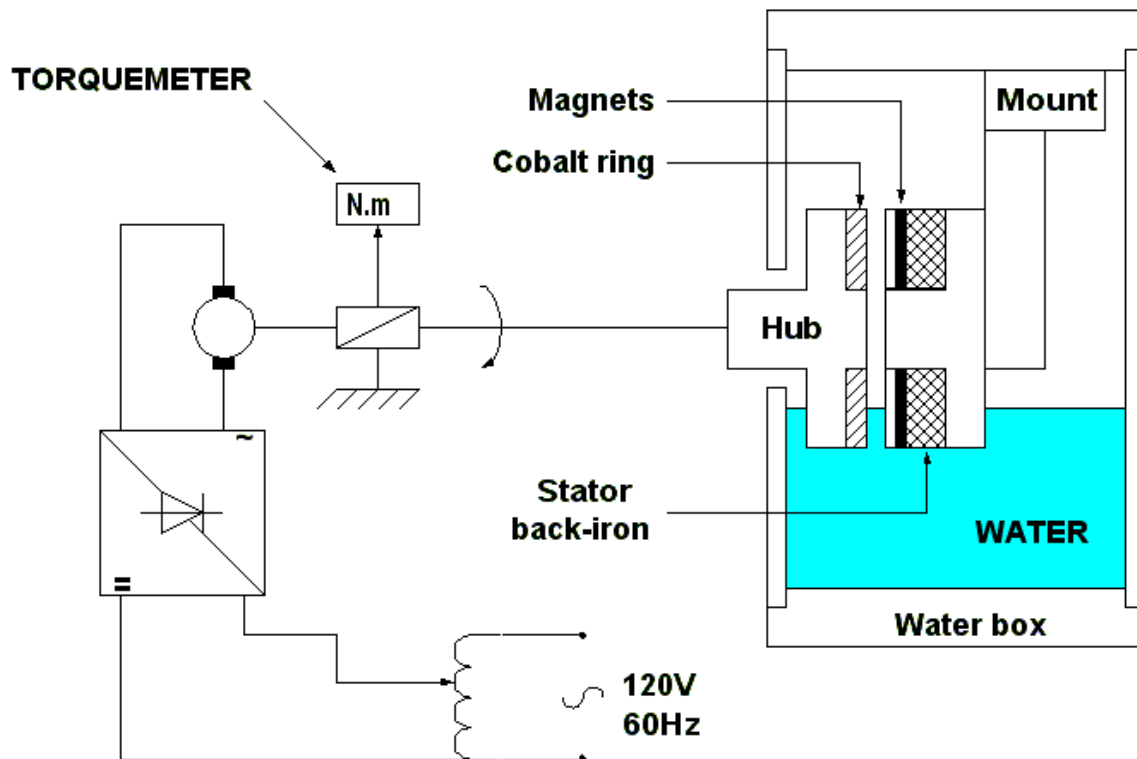


Fig. 83: Test bed architecture

The operation of the eddy-current brake will only be investigated at steady state. Therefore, a DC motor is sufficient to provide torque to the test bed. The DC motor is driven by a diode rectifier fed by an autotransformer adjustable up to 130V from a 120V

wall outlet. The maximum DC voltage supplied to the motor thus matches the 180V on the nameplate. The characteristics of the DC motor are summarized in TABLE 7 below:

TABLE 7
DC motor characteristics

PARAMETER	VALUE
Nominal armature voltage	180 V
Nominal armature current	14 A
Armature resistance	1.43 Ω
Maximum speed	1750 rpm
Nominal shaft power	3 hp
Maximum torque	12.2 N.m
Torque constant	0.872 N.m/A

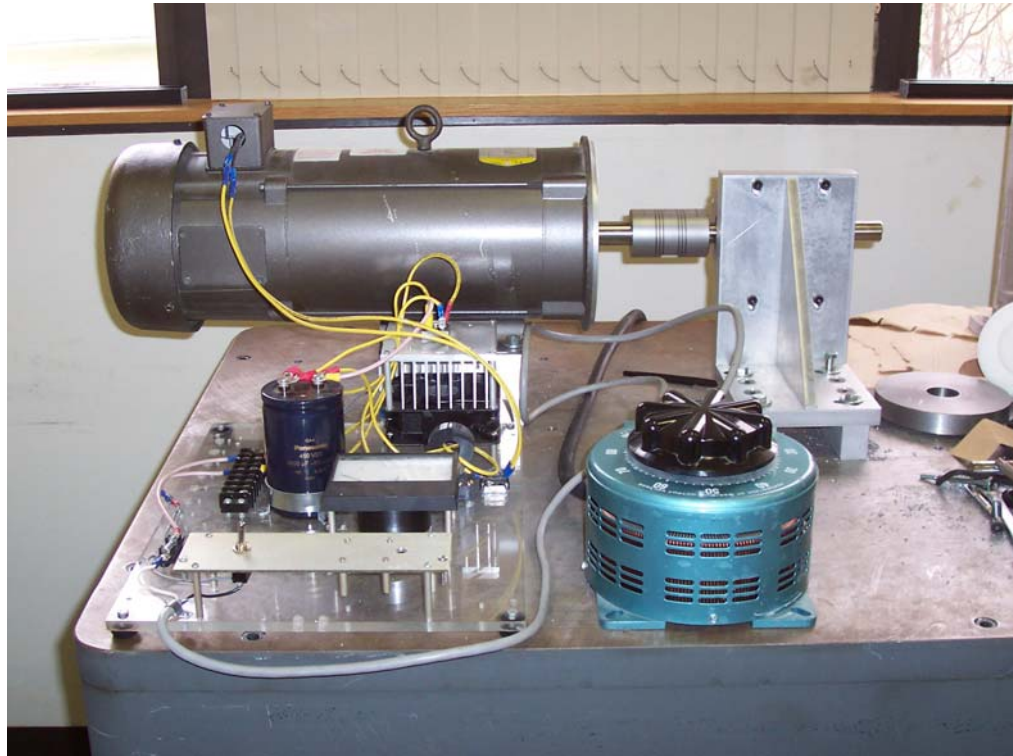


Fig. 84: DC motor and drive

The DC motor and its drive are pictured on Fig. 84.

The DC motor is controlled through its armature voltage by the drive. Fig. 85 shows the torque-speed curves for different armature voltages superposed over a typical eddy-current brake torque-speed curve. It demonstrates that the ensemble dc motor and eddy-current brake is stable at any given speed.

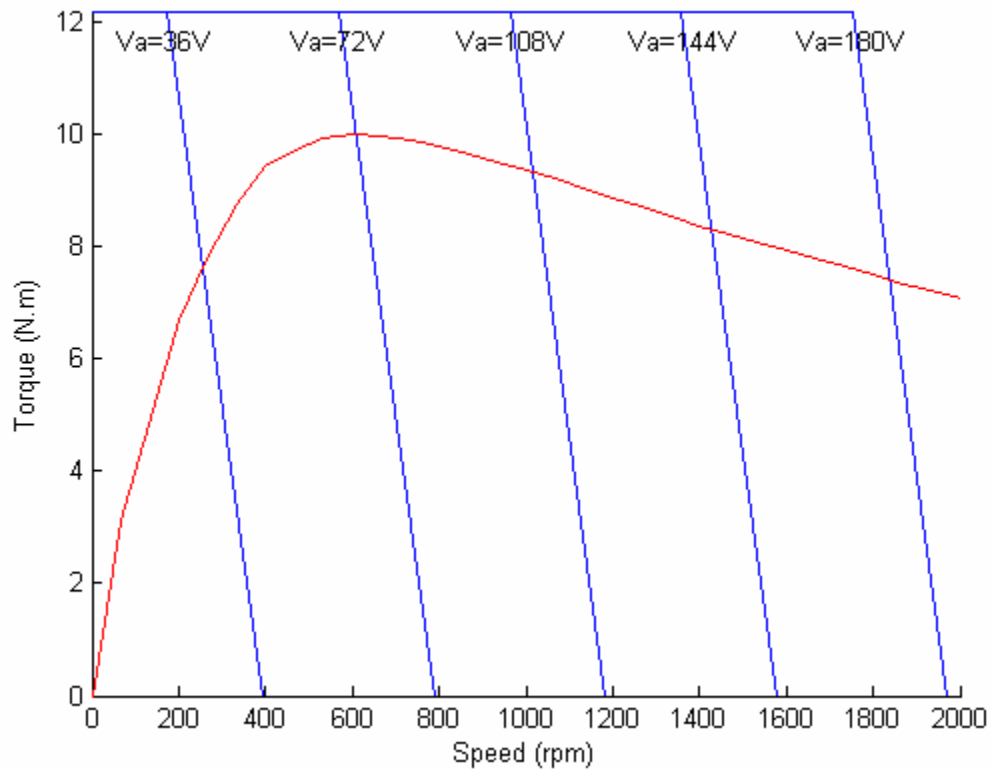


Fig. 85: DC motor and eddy-current brake torque-speed curves

The eddy-current brake is designed to fit the characteristics (maximum torque and speed) of the dc motor drive. TABLE 8 gives the geometric characteristics of the test eddy-current brake. The geometry is the same as that shown on Fig. 10.

TABLE 8
Test eddy-current brake characteristics

PARAMETER	SYMBOL	VALUE
Permanent magnet residual flux density	B_r	1.4T
Height of permanent magnet	h_{magnet}	0.125in
Resistivity of disc material	ρ	$6 \times 10^{-8} \Omega.m$
Number of pole pairs	p	8
Pole width	τ_p	60°
Arc between north and south pole	τ	120°
Airgap width	g	1mm
Disc thickness	e	0.125in
Disc inner radius	R_{inner}	1.5in
Disc outer radius	R_{outer}	2.5in

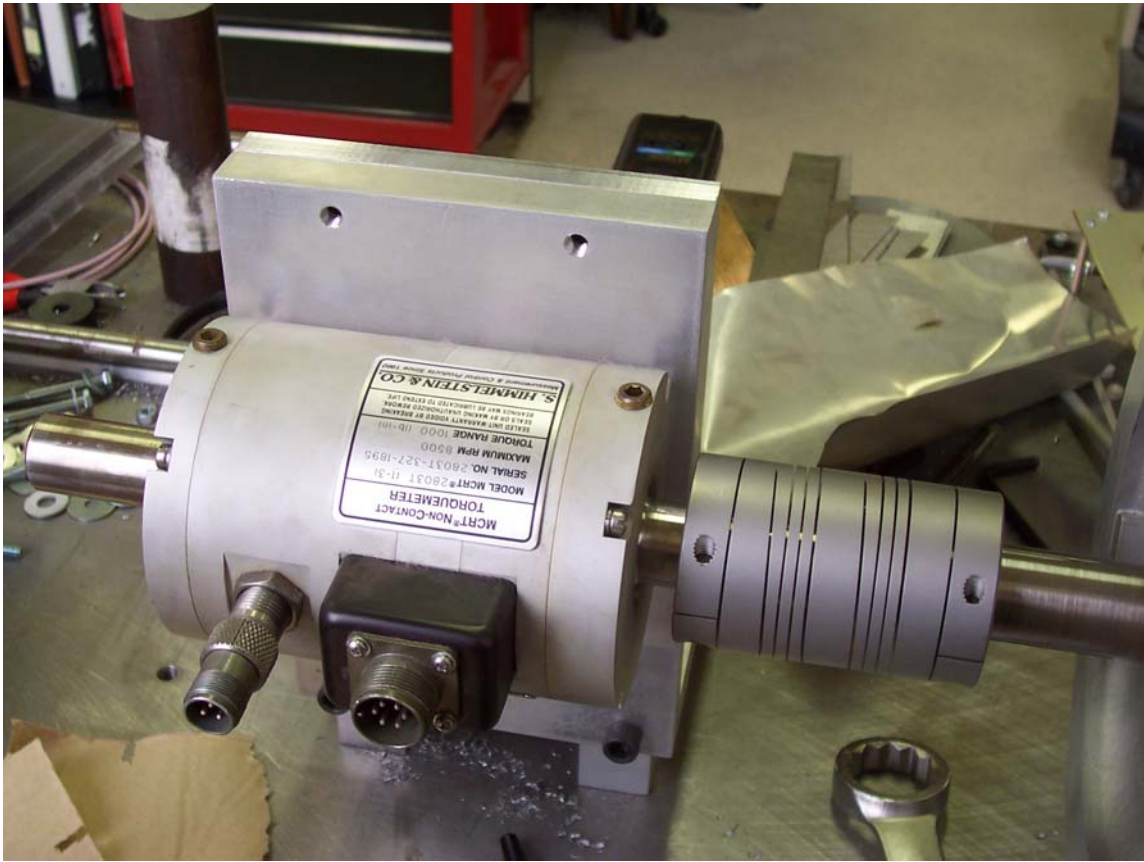


Fig. 86: Torquemeter

The torquemeter (Fig. 86) is rated for a maximum torque of 1000 lb.in or 113 N.m. It can operate at a maximum speed of 8000 rpm.



Fig. 87: Plastic hub

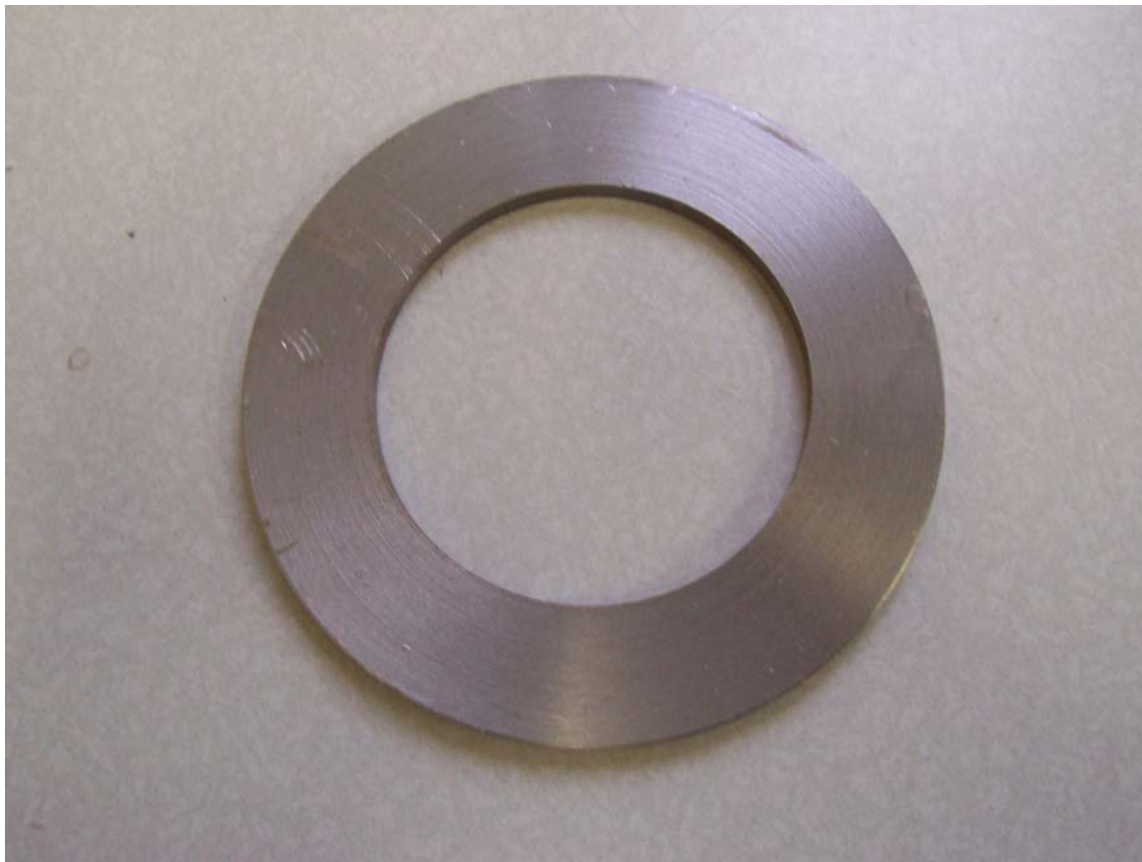


Fig. 88: Cobalt ring

The eddy-current brake is composed of a plastic (acetate) hub (Fig. 87) holding the ring of cobalt (Fig. 88) which constitutes the armature of the brake. The disc is bathed in water, which keeps the armature at a constant and approximately uniform temperature. The water is held in a transparent water box (Fig. 89).

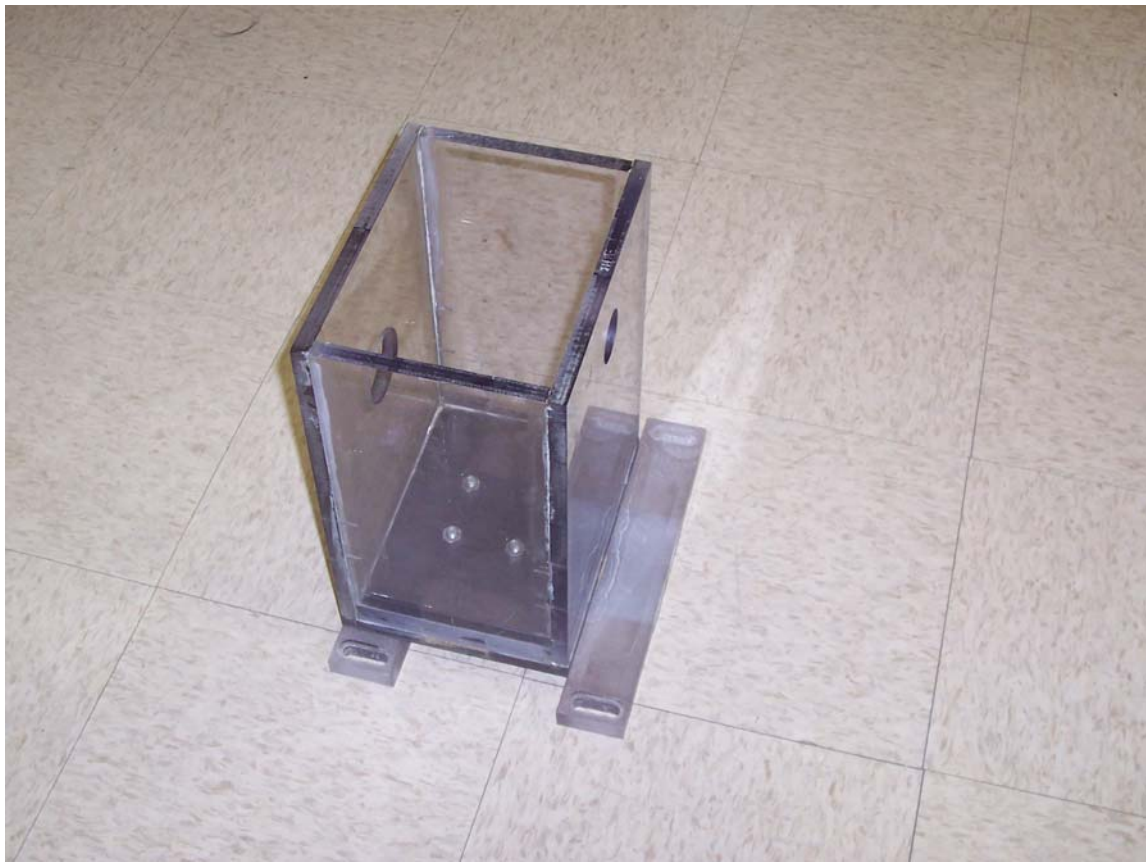


Fig. 89: Water box

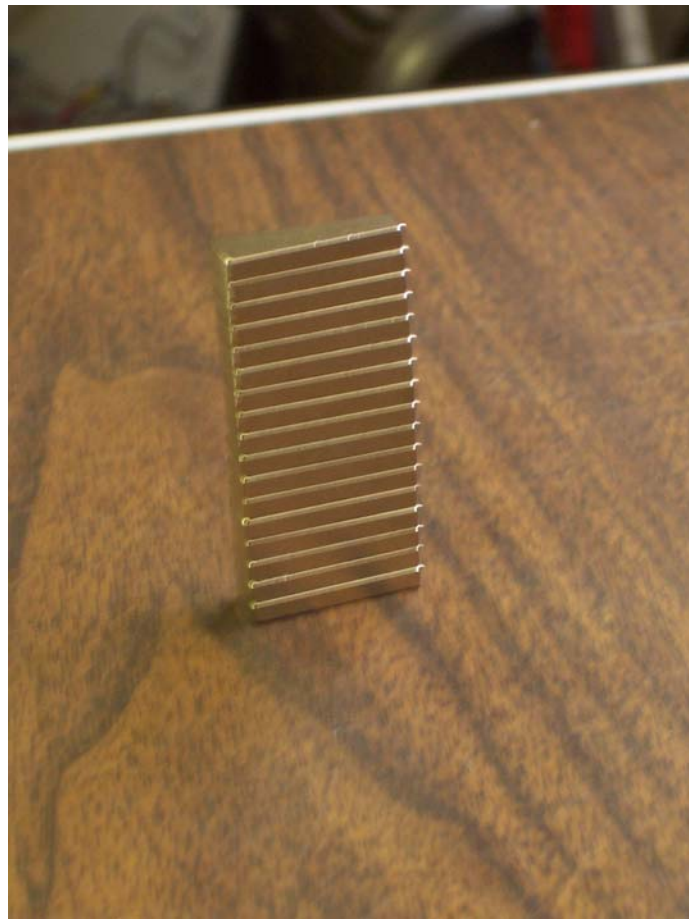


Fig. 90: NdFeB permanent magnets

The 16 arc-shaped NdFeB permanent magnets (Fig. 90) are attached to the back-iron, a ring of highly permeable AISI 1018 steel (Fig. 91). Once attached, the magnets are locked laterally by using a mask (Fig. 92).



Fig. 91: Stator back-iron



Fig. 92: Stator assembly

The magnets are also locked axially by a round aluminum plate and radially by a plastic ring. A sheet of Teflon is glued to the top of the stator assembly, and coated with a water-resistant grease. This will allow maintaining a constant airgap despite the magnets exerting a strong attraction force on the cobalt disc. The Teflon and the grease significantly lower the friction, which can be simply subtracted from the measured torque-speed curve. The friction torque can be determined by measuring the zero-speed torque on the test-bed. The friction is uniform regardless of the speed because the

friction is mostly Coulombic. The stator and its mount are bolted to the top of the water box (Fig. 93).



Fig. 93: Complete stator assembly and mount

Fig. 94 shows the eddy-current brake completely assembled.

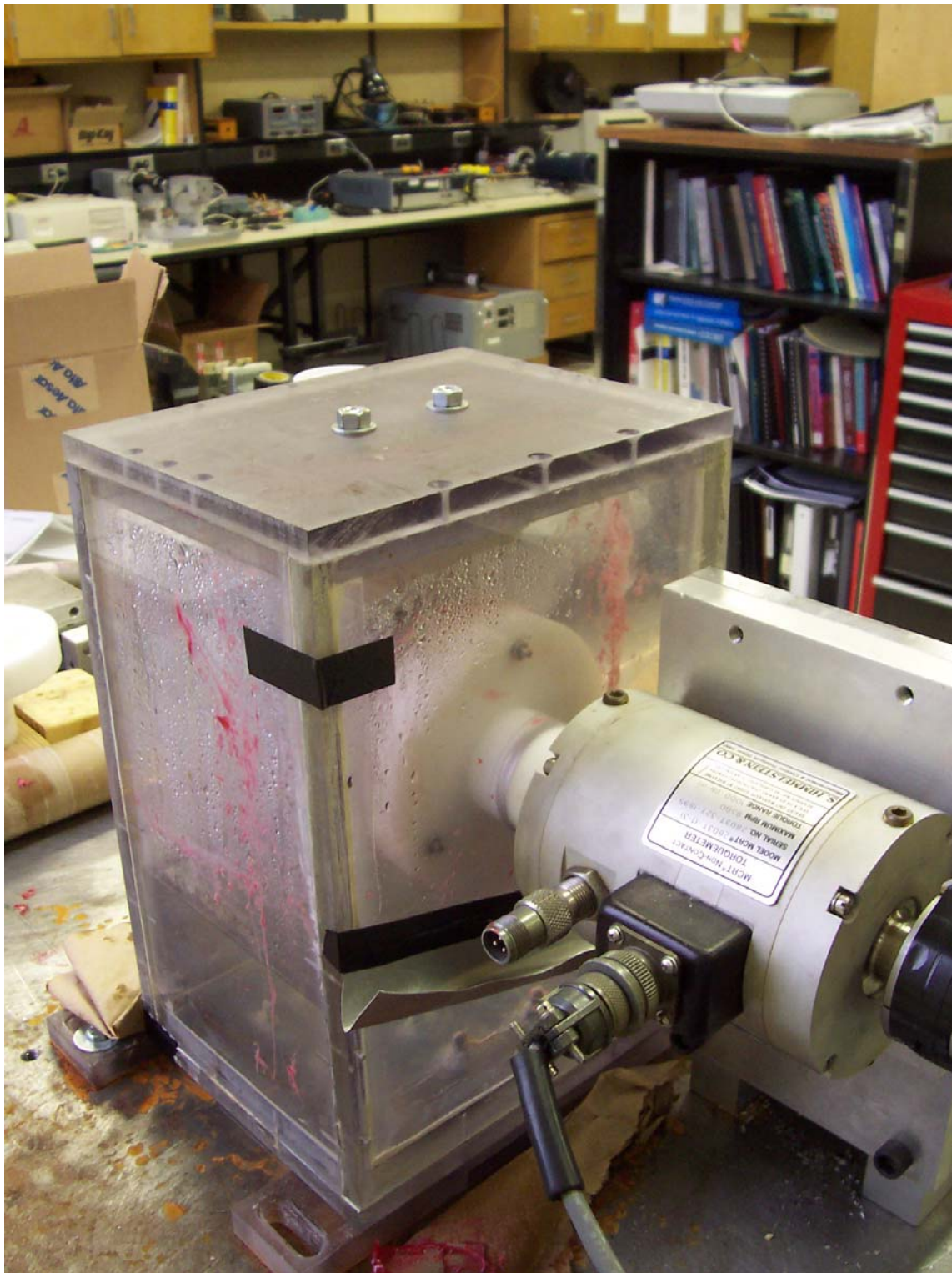


Fig. 94: Assembled eddy-current brake



Fig. 95: Complete test bed

Fig. 95 shows the complete test bed.

3 – Measurement of the disc's properties

The electrical resistivity of the disc is easy to obtain because of the purity of the cobalt employed (99.9%). The data for pure cobalt may thus be used ($\rho_{Co} = 6 \times 10^{-8} \Omega.m$)

The magnetic properties of the disc material are heavily dependent on the metallurgical fabrication process. In [45], the properties of cobalt are given for an annealed sample. Annealing is a thermal treatment process by which the sample is heated above the Curie temperature and cooled down at a rate of approximately 20°C per hour. This process relieves all mechanical stress in the material and provides a uniform and isotropic distribution of the magnetic domains in ferromagnetic materials.

However, the cobalt supplied has been rapidly cooled from a melt to room temperature, then cold-rolled and machined with no particular care before delivery. Therefore, the magnetic properties of the material must be measured prior to testing the eddy-current brake. A small sample (a few milligrams) was obtained from the disc and tested with the help of Texas A&M's Chemistry department SQUID magnetometer (see Fig. 96 and Fig. 97). SQUID stands for Superconductive Quantum Interference Device. The SQUID magnetometer measures the flux density in a sample by measuring the phase imbalances that it induces in two symmetrical Josephson junctions in which circulates the current that induces the sample.



Fig. 96: SQUID magnetometer, instrument



Fig. 97: SQUID magnetometer, processing electronics

Fig. 98 and TABLE 9 show the data obtained from the SQUID magnetometer for the cobalt sample at 293K. Due to the rapid and uncontrolled cooling and several machining steps in between, the ring exhibits a maximum relative permeability well below the theoretical value for an annealed sample.

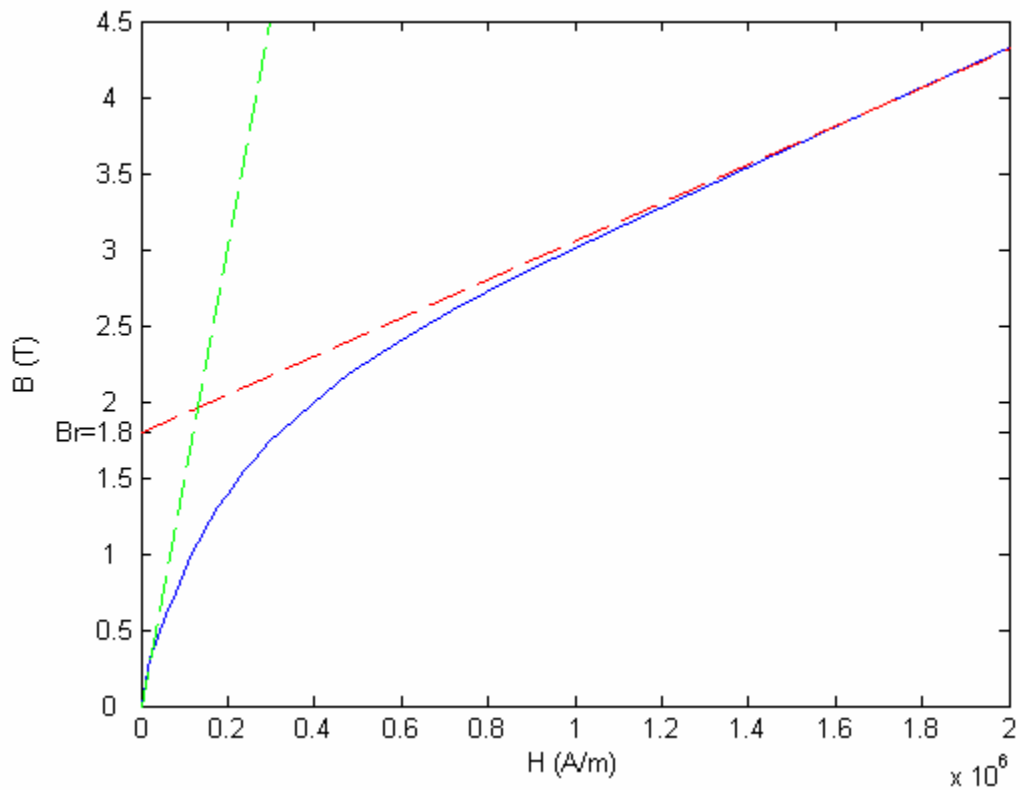


Fig. 98: Initial magnetization BH curve for cobalt sample

TABLE 9
Magnetic data for the cobalt ring

PARAMETER	VALUE
Maximum relative permeability	12
Magnetization at saturation	(1.801 T)

4 – Comparison of experimental and finite-element data

The measured torque-speed curve is shown on Fig. 99 with the curve from finite element analysis. TABLE 10 summarizes the characteristic parameters of the two curves.

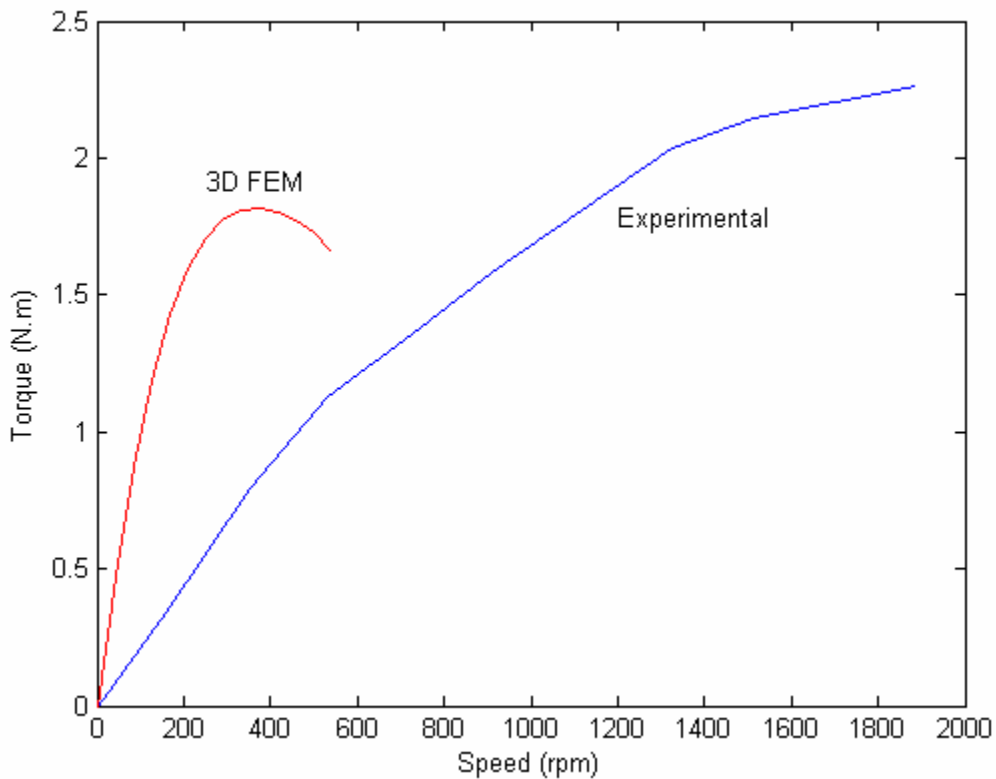


Fig. 99: Finite element and experimental torque-speed curves

TABLE 10
Curve parameters

PARAMETER	3D FEM	EXPERIMENTAL	DISCREPANCY
PEAK TORQUE	1.82N.m	>2.26N.m	>+24%
CRITICAL SPEE	375rpm	>1800rpm	>480%

There is obviously a large difference between the finite element and the experimental data, although the data is within the same order of magnitude. The discrepancy is far greater for critical speed than for the peak torque. Several reasons may explain the wide discrepancies:

- Finite element model for eddy-currents in saturated ferromagnetic materials: the finite element simulation of eddy-currents in ferromagnetic materials is notoriously difficult, especially by transient models [43]. Part of the problem is due to the large variations of relative permeability throughout the disc, which forces the solver to perform many iterations to approach the solution. The relative motion of the disc and magnets adds to the difficulty, by increasing making the problem time and position dependent. Finally, it is the fundamental fact that eddy-currents are intimately coupled to the flux density distribution that renders the problem difficult to solve [18]. Publications confronting finite element data with experimental data for ferromagnetic rotors are rare and succinct which suggests that the problem has not been solved in the past, either totally or completely.
- Impact of temperature on electrical and magnetic properties of cobalt and magnets: after a few minutes of operation (less than 5), the temperature of the water had risen from 15°C to approximately 33°C. Ice was added to the water, but it melted away. The discrepancy was reduced, but remained significant nonetheless. The Teflon coating seems to insulate the cobalt disc and reduce the dissipation of heat into the water, therefore allowing the cobalt's temperature to

rise significantly more than that of the water, thereby altering the results. The neodymium magnets are very sensitive to temperature changes because of their low Curie temperature (300°C, [5]).

- Magnets: The magnets were not tested due to lack of adequate equipment. The SQUID magnetometer cannot test a whole magnet, and cannot provide three-dimensional magnetization information. It is therefore possible that the magnets are not all magnetized exactly in the axial direction, which would significantly impact the torque. The magnitude of the magnetization is also in question, as an x percent discrepancy in magnetization translates into an x squared percent error in terms of torque. Furthermore, the variation of magnetization across the set of magnets would affect the harmonic distribution of the flux along the angular direction of the stator [47]. This would have an effect similar to varying the number of poles, and their width, both of which have been shown in previous chapters to affect the peak torque and critical speed significantly.
- Anisotropy of cobalt: The rapid cooling of the cobalt used for the disc and subsequent cold rolling has impacted the metallurgical state of the material [46]. The absence of annealing makes it impossible to guarantee that the material is uniformly isotropic. Therefore, local and global anisotropies are possible. Fig. 100 shows the microscopic BH curve depending on the orientation of the crystals of cobalt. The impact on the macroscopic properties is non negligible in the absence of annealing.

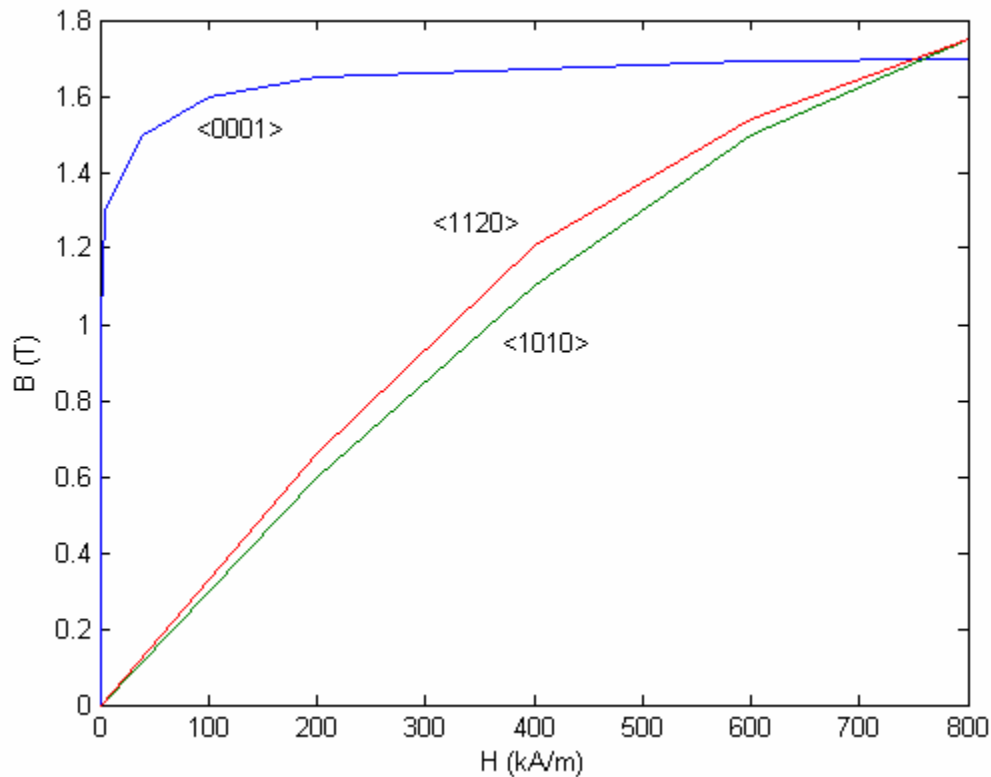


Fig. 100: Microscopic BH curves for cobalt

- Parasitic friction: The friction between the Teflon and the disc is Coulombic, but the presence of grease introduces viscous and fluid components to the friction torque. These components are not constant with speed: viscous friction evolves linearly with speed, while fluid friction evolves with the square value of speed. The water in which the test bed bathes also adds to the fluid friction acting on the disc. Viscous and fluid friction can be shown to account for some of the torque discrepancy. Fig. 101 shows a series of curves (in red) calculated from finite element data (in black) by addition of a viscous and a fluid friction torque, with a

viscous friction coefficient ranging from 0 to $20 \cdot 10^{-6}$ N.m.rpm $^{-1}$ and a fluid friction coefficient ranging from 0 to $5 \cdot 10^{-6}$ N.m.rpm $^{-1}$. The total torque is computed according to:

$$T_{RED} = T_{FEM} + k_v \cdot speed + k_f \cdot speed^2 \quad (130)$$

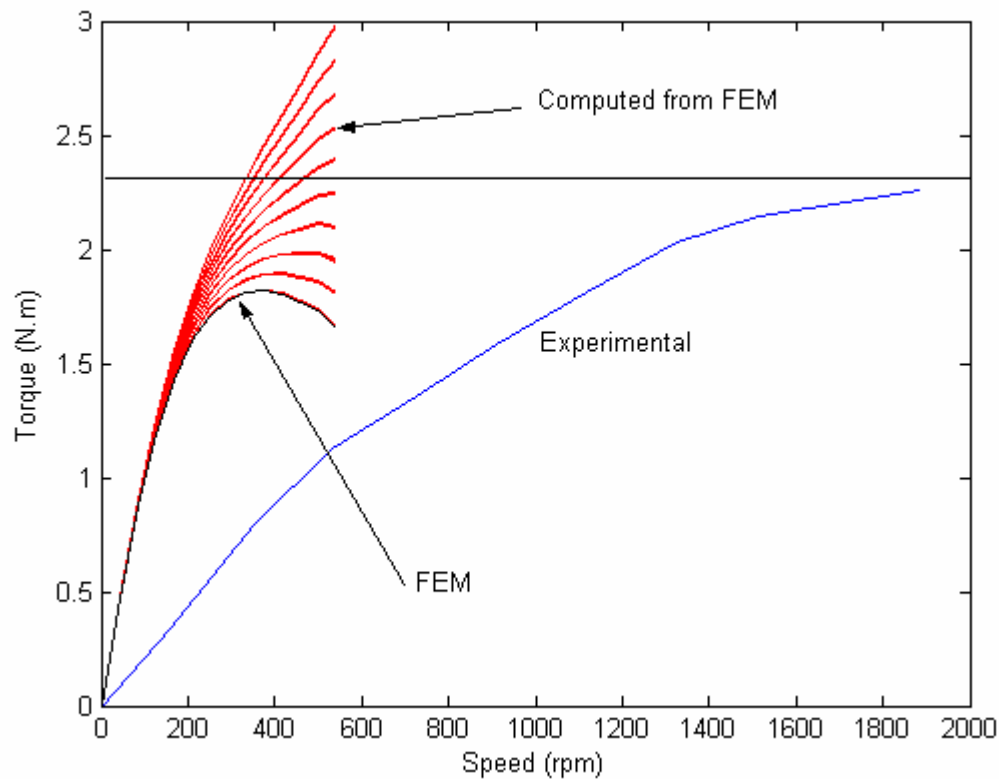


Fig. 101: Impact of viscous and fluid friction on torque

- The cobalt disc was initially glued to the plastic hub. However, the pull force from the magnets proved too great and the disc has been bolted to the hub. The 3 holes drilled in the cobalt, as well as the 3 stainless steel bolts used may account

for some minor discrepancy. It should be noted that the formulations used by Flux 3D do not allow taking into account holes in “massive conductors” such as the disc.

5 – Conclusions on experimental validation

Experiments with a ferromagnetic rotor have shown a significantly different result compared to finite element analysis. While the peak torque was within the correct order of magnitude, the critical speed was far greater than expected. The experiment seems to indicate that finite element models can predict the main indicator of performance, i.e. the torque, albeit with a wide error margin. The prediction of critical speed is far more inaccurate. Past literature and the finite element analysis suggests that the error could be due to the return current paths, which have been shown to impact the apparent resistance of the rotor and shift the critical speed to much higher values.

Due to lack of proper equipment and expertise in finite element modeling, the experimental results are inconclusive. However, it is possible to pursue the investigation of eddy-current braking for vehicular applications because the main indicator of braking performance (peak torque) was predicted accurately enough to prove the concept viable. The impact of critical speed could be determined experimentally by testing a broad range of rotors and magnets, varying the design parameters each time.

The next chapter will consist of an analysis of the integration of eddy-current braking in vehicular applications. Two different cases will be considered:

- Constrained critical speed: the exact impact of the design parameters on the critical speed has not been determined and the brake has to be designed by scaling up of the experimental brake. The critical speed is thus not freely chosen, and only the peak torque can be adjusted by design.
- Designed critical speed: the impact of design parameters on critical speed can be determined accurately, either through finite element or experimental analysis. Critical speed can thus be adjusted by design to fit the application.

CHAPTER V

INTEGRATION OF THE BRAKE IN VEHICLE SYSTEMS

The advantages of the integrated brake concept as opposed to conventional friction brakes are:

- Reduced wear of friction pads
- Reduced sensitivity to fading
- Reduced sensitivity to wheel lock
- Faster control dynamics
- Easier integration with vehicle electronic driving aids
- Reduced fuel consumption of power assistance

In this chapter, the objective is to investigate the respective requirements for the friction and eddy-current brakes that yield the above advantages while providing at least the same performance as conventional friction brakes. Then these requirements are used to conceptually design a practical integrated brake for conventional and hybrid vehicle use as well as its control strategy. The operational gains permitted by the use of the integrated brake are determined over standard drive cycles.

1 – Braking with eddy-current brakes

This section investigates the dynamics of a mass in linear or rotational motion as it is braked by an eddy-current brake. Two cases are considered that represent actual

situations. The first case is that of a mass braked solely by eddy-current braking, where the braking force acting on the mass is not limited by an adhesive contact. A practical example would be found in an electric motor with an eddy-current brake on its shaft. The second case is that of a vehicle braked by a combination of eddy-current and friction braking, where the braking force decelerating the vehicle is limited by the adhesive contact between the tires and the ground. This second case is representative of nearly all wheeled vehicles.

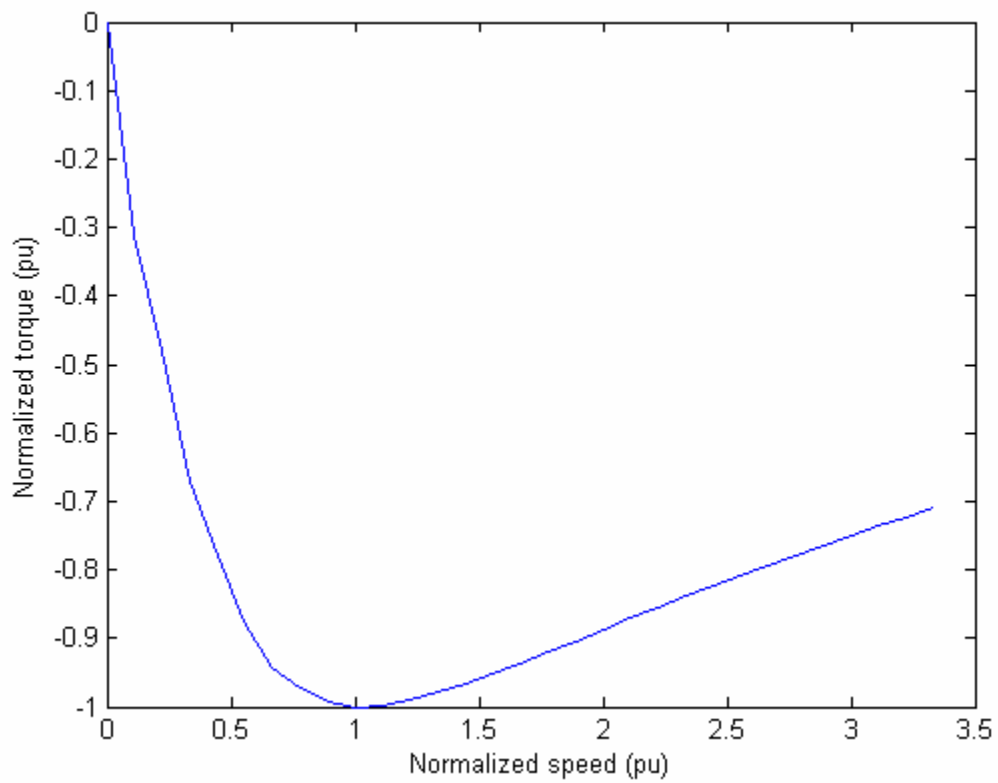


Fig. 102: Normalized torque-speed curve

This investigation of eddy-current braking dynamics uses a normalized torque-speed curve (Fig. 102). The normalized torque speed curve is specific to the disc material, airgap width and magnet residual magnetization. Other parameters do influence the shape of the curve, but much less significantly.

1.1 – Pure eddy-current braking with unlimited force

The dynamics of a braked mass are fully described by the Newton equation if the braking force is not limited by an adhesive contact. For a rotating mass, the equation is as follows:

$$J \frac{d\omega}{dt} = T_{braking} - T_{friction} \quad (131)$$

1.1.1 – Brake with constrained critical speed

It is necessary to consider the case where the critical speed of the brake is not freely chosen by the designer because of the difficulty in predicting the performance of an eddy-current brake especially if the rotor is made of a ferromagnetic material. In that case, the brake would be designed by sizing up (or down) a brake evaluated experimentally. The peak braking torque will be the primary design target and design parameters will be adjusted by trial and error to achieve the desired value. Theory and finite element simulations indicate that the critical speed will also vary as a function of design parameters. However, experiments have shown wide discrepancies with finite

element and analytical models predictions regarding critical speed. It is thus likely that the critical speed will not be chosen freely by the designer.

The present case study analyzes the dynamics of a rotating mass decelerated by an eddy-current brake with a critical speed equal to that determined experimentally in chapter 3 ($N_c \approx 2000\text{rpm}$) and a peak torque adjusted by design. A rotating mass with a moment of inertia of $J = 1\text{kg.m}^2$ and a peak eddy-current braking torque of $T_p = 200\text{N.m}$ are chosen.

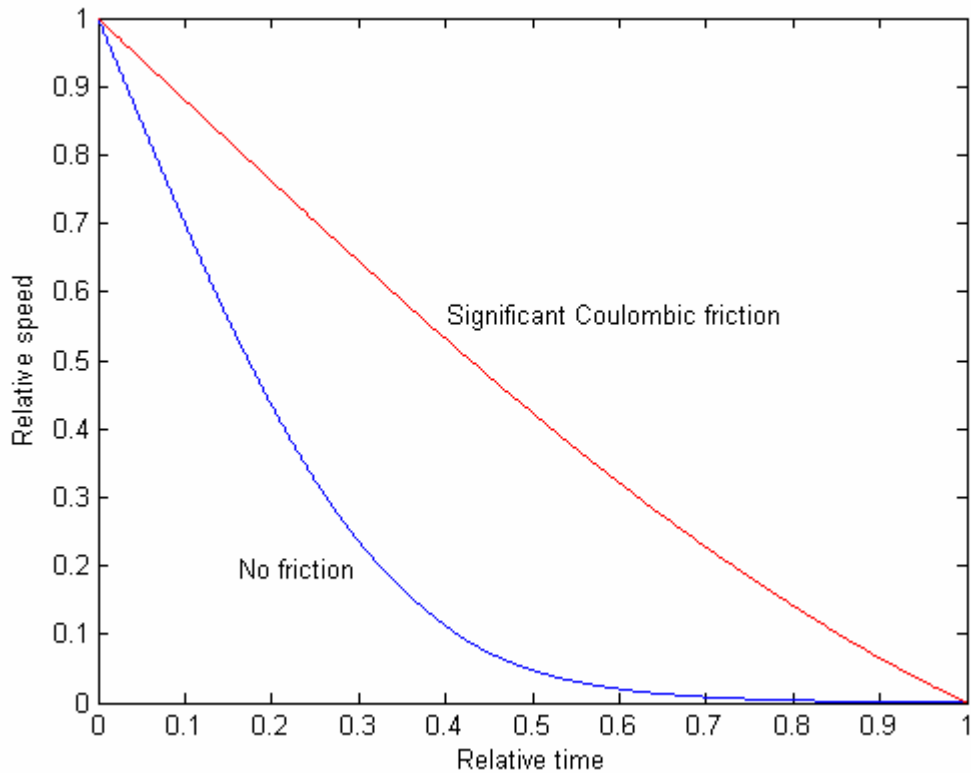


Fig. 103: Relative speed vs. relative time, low initial speed

Fig. 103 shows two cases of a rotating mass decelerating from an initial speed equal to critical speed. The time and speed are normalized to stopping time and initial speed respectively. If the rotating mass is decelerated exclusively by eddy-current braking, the speed decreases sharply at first. As the eddy-current braking torque decreases, the deceleration diminishes and the mass keeps rotating slowly for a long time. Decreasing from 10% of the initial speed to a complete stop requires about 60% of the stopping time. On the other hand, if the mass is affected with a significant Coulombic friction torque, the deceleration is more uniform and tends to be dominated by the Coulombic friction torque. In the case study, the Coulombic friction torque had the same value as the eddy-current peak torque. 46.3% of the kinetic energy of the rotating mass was dissipated by eddy-current braking.

Fig. 104 shows deceleration curves for the same rotating mass with an initial speed of five times the critical speed of the eddy-current brake. Speed and time are normalized to initial speed and stopping time respectively. The difference between a friction-free rotating mass and one affected by Coulombic friction is much less significant than for a deceleration starting at critical speed. This demonstrates an eddy-current brake with a constrained critical speed is more adapted to brake a high-speed machinery than low-speed machinery. Low-speed braking requires the help of friction braking if the deceleration is to be effective and rapid.

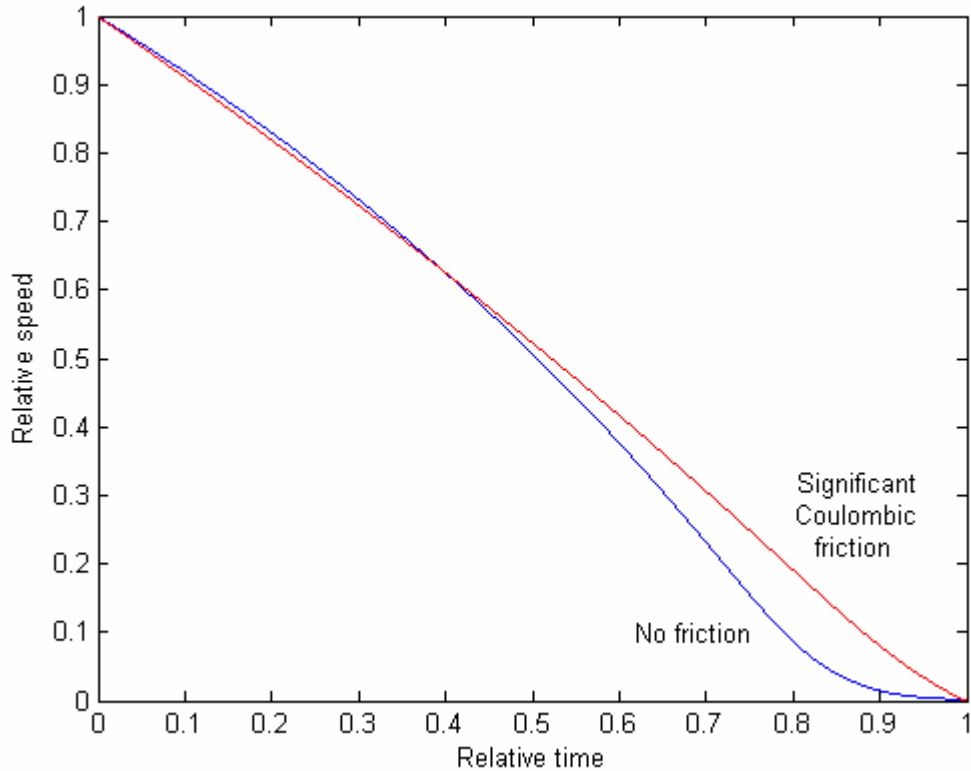


Fig. 104: Relative speed vs. relative time, high initial speed

The impact of initial speed and eddy-current braking peak torque on the stopping time is plot on Fig. 105. The analysis was performed for a brake with a critical speed of 2000rpm. The plot shows that a rapid decrease in stopping time is achieved in the low torque region at both low and high speed. For a given peak torque, the stopping time increases rapidly at low speed and evolves seemingly linearly with speed past a certain point. The slope of the linear portion decreases steadily as the peak torque increases. The linear portion becomes almost flat in the high torque region indicating a significantly reduced impact of the low-speed portion of the torque-speed curve of the eddy-current

brake. The plot also demonstrates that there is a diminishing return to increasing the peak torque beyond a certain point. This consideration is of prime importance in the design of a brake for a practical application.

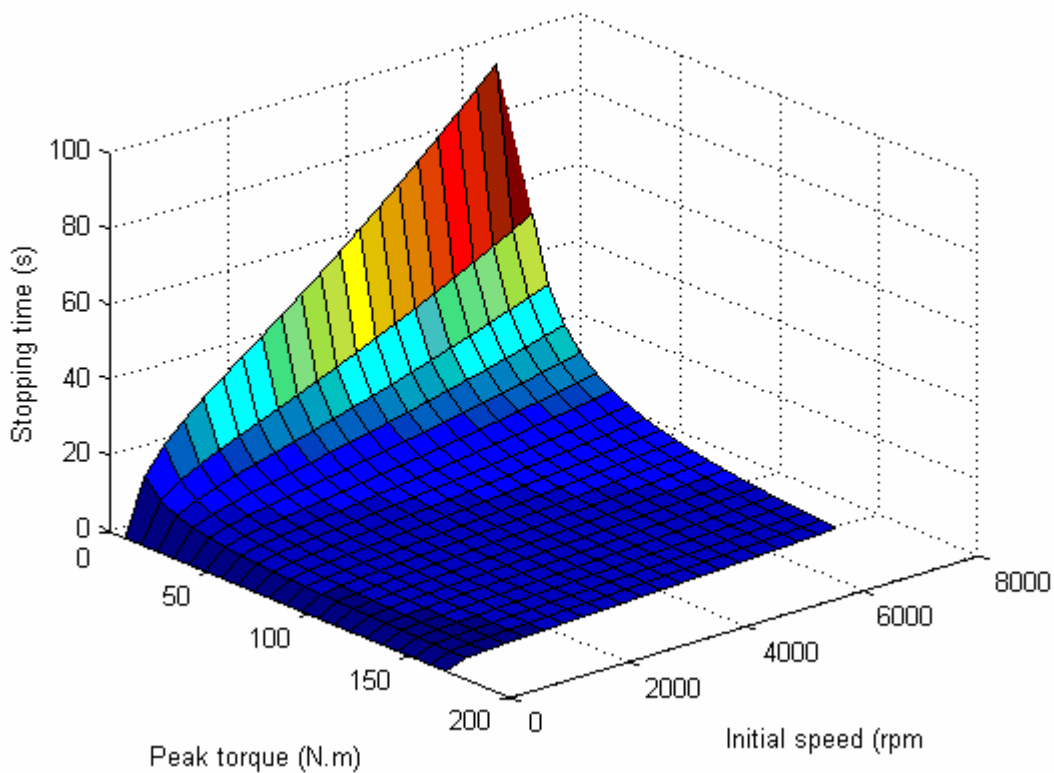


Fig. 105: Stopping time vs. initial speed, no significant friction

Fig. 106 shows the sensitivity analysis plot for the same rotating mass but affected with a Coulombic friction torque of the order of the eddy-current brake's peak torque. As expected, the surface plot is much flatter showing a seemingly linear dependency of the stopping time on the initial speed and a nearly linear dependency on the peak torque.

This plot indicates that an eddy-current brake is adapted for either low-speed or high-speed braking. Although there is a diminishing return to increasing the peak torque, it is not significant until the peak torque is much larger than the Coulombic friction torque. If the mass to be decelerated is naturally affected by Coulombic or viscous friction, then there is a definite advantage to increasing the peak torque of the eddy-current brake.

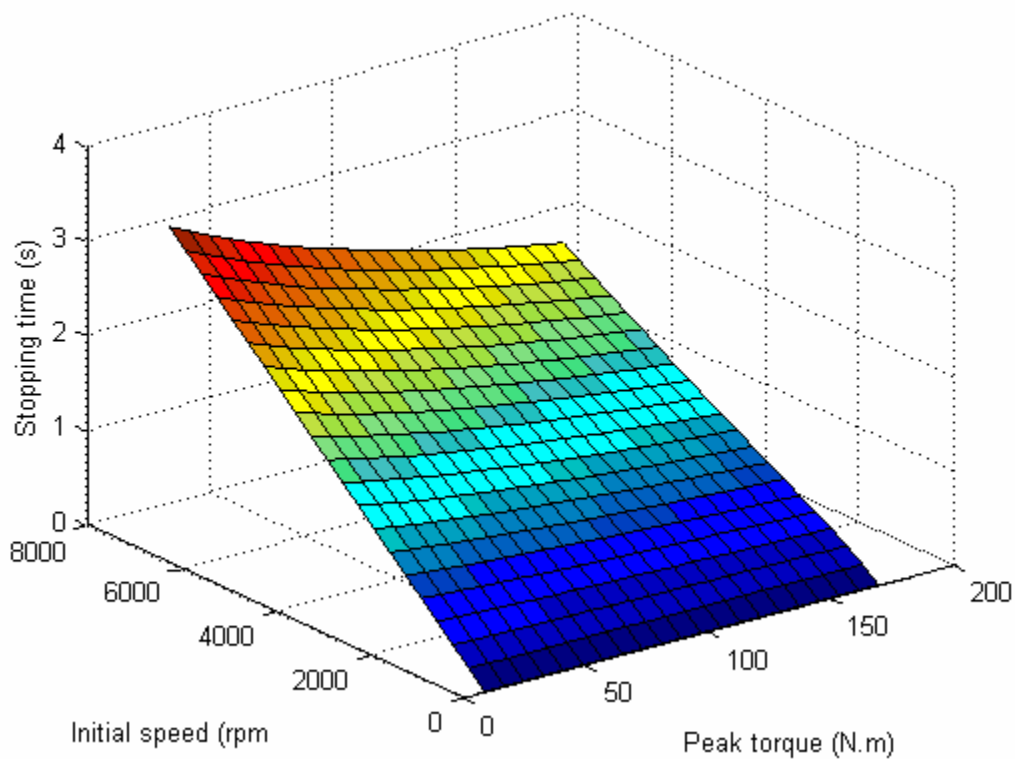


Fig. 106: Stopping time vs. initial speed, significant friction

1.1.2 – Brake with optimized critical speed

In this subsection, the sensitivity of braking performance to critical speed is analyzed. This analysis assumes that the impact of the design parameters on the critical speed is known. The simulation uses the same rotating mass that was used for the constrained critical speed case. Fig. 107 shows the stopping time for the rotating mass affected by a Coulombic friction torque with the same magnitude as the peak torque. The stopping time evolves seemingly linearly with initial speed and critical speed. There is only a slight non linearity for very low initial speeds. Each sheet on the plot corresponds to a value of the peak torque (80, 160, and 240N.m). The plot shows that performance is not significantly influenced by critical speed.

Fig. 108 shows the results of the same analysis for a rotating mass with no friction at all. Each sheet on the plot corresponds to a value of the peak torque (80, 160, and 240N.m). The curves show a significant downward concavity if the initial speed is below a certain fraction of the critical speed and a slight upward concavity above that same speed. The concavity is primarily along the initial speed axis.

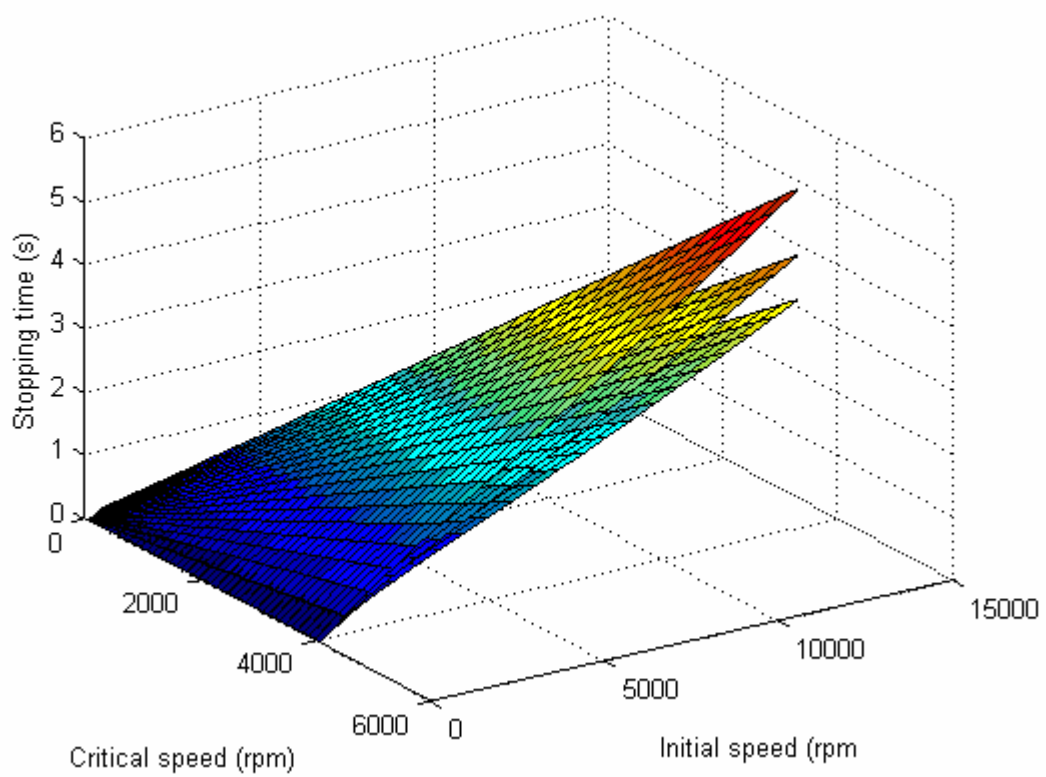


Fig. 107: Stopping time vs. critical speed and initial speed, significant friction

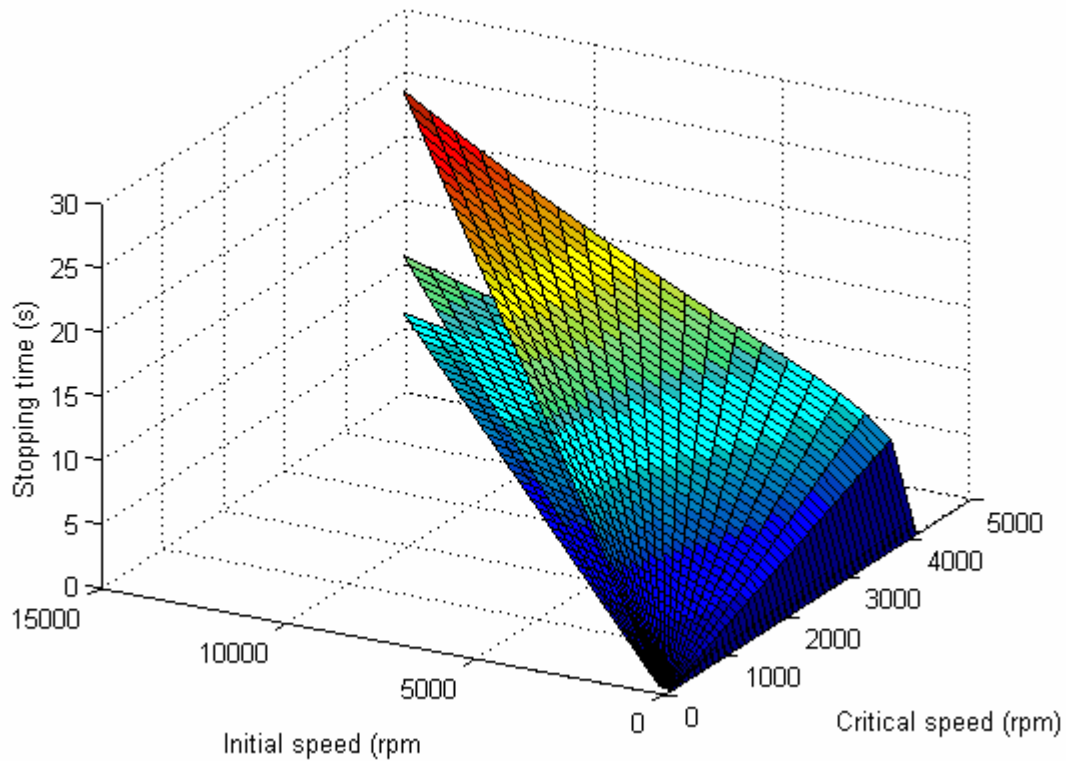


Fig. 108: Stopping time vs. critical speed and initial speed, no friction

Fig. 109 shows a contour plot of the sheet corresponding to a peak torque of 240N.m. A short stopping time is illustrated by a dark blue color and a long stopping time is illustrated by a dark red color. This plot shows that for a given initial speed, the best braking performance is achieved for a critical speed several times lower (about 5.7 times).

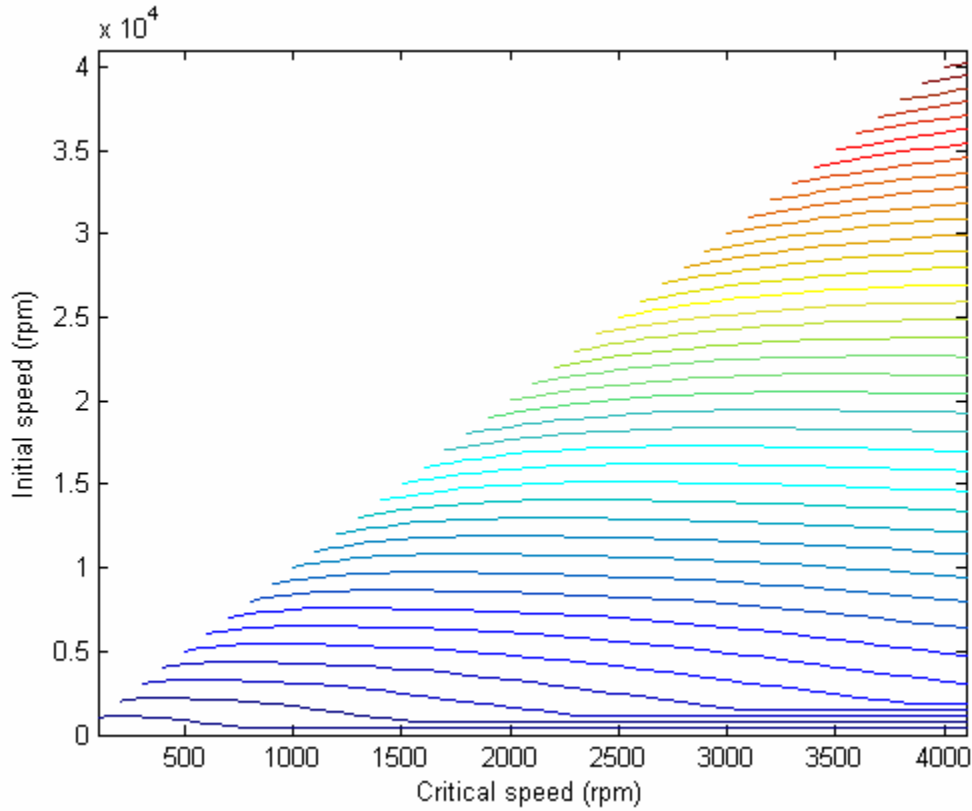


Fig. 109: Stopping time vs. critical and initial speed, no friction, $T_p=240\text{N.m}$

1.2 – Integrated braking with limited force

Mixed braking involves a combination of friction and eddy-current braking. Mixed braking provides shorter stopping times because the friction component supplements eddy-current braking at very high speed and low speed. In vehicles, the braking force is transmitted to the ground through the adhesive contact of the tires. This latter limits the braking force and consequently limits the performance of the brake [48]. Through proper modulation of eddy-current and friction braking, it is possible to ride that limit at any

instant during the braking phase and thus achieve an ideal deceleration. The case study is performed for a vehicle having the characteristics listed in TABLE 11 below.

TABLE 11
Test vehicle parameters

PARAMETER	VALUE
Vehicle mass	1500 kg
Rolling resistance coefficient	0.015
Aerodynamic drag coefficient	0.35
Air density	1.25 kg.m ⁻³
Vehicle body frontal area	2 m ²
Wheel radius	0.3 m
Center of gravity height	0.5 m
Center of gravity position from front wheel	1.5 m
Tire adhesion coefficient	0.8

1.2.1 – Brake with constrained critical speed

The simulation was run for a broad range of eddy-current brake peak forces and vehicle initial speeds. The braking performance is evaluated by the stopping time.

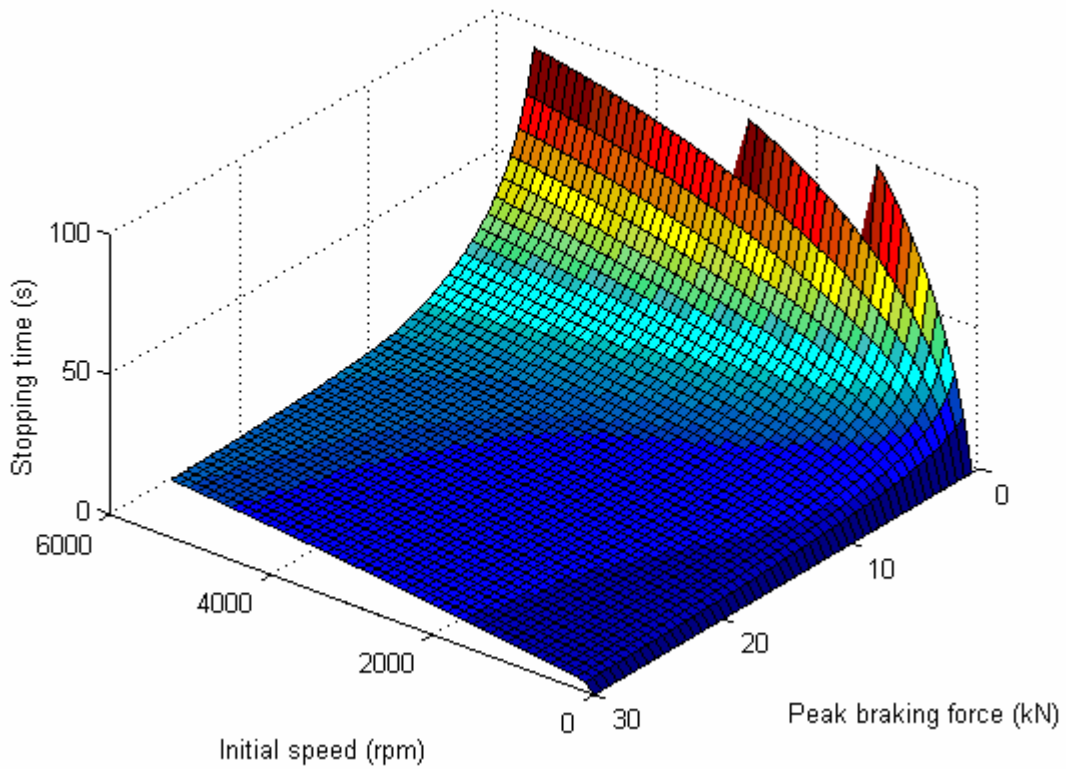


Fig. 110: Stopping time vs. initial speed and peak braking force, tire limited

Fig. 110 shows the stopping time versus the initial speed of the vehicle in rpm and the peak total braking force of the brake system. The plot shows a diminishing return in increasing the peak torque. This is due to the limitation of the braking torque resulting from the adhesive contact between the tire and the pavement. Increasing the peak force significantly improves performance until the peak force reaches the limit set by the tires. Then the performance improves more slowly than the peak force. When the high speed region is also truncated by the adhesive limit, the performance improves only

marginally. Fig. 111 illustrates the process as the peak force is increased beyond the adhesive limit (in red on the figure).

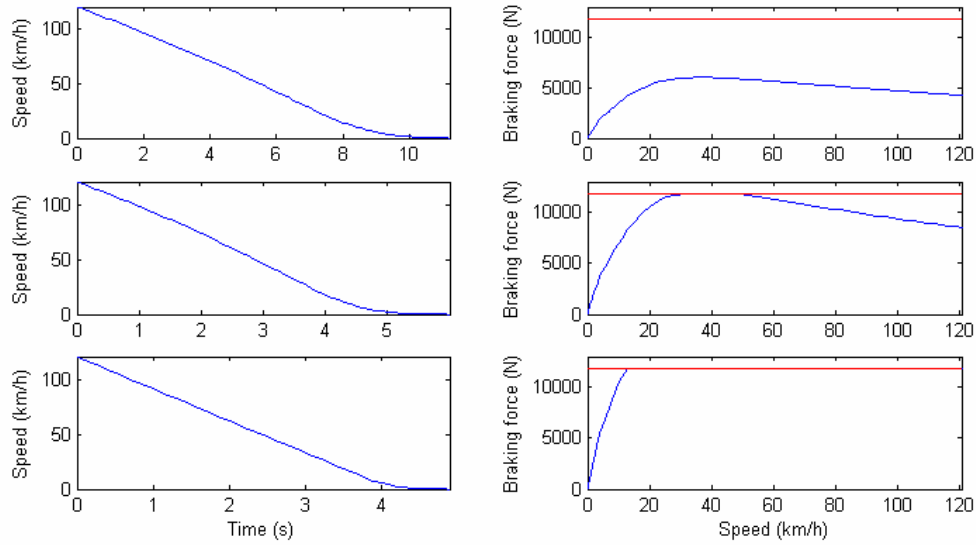


Fig. 111: Diminishing return in increasing peak force

The peak force of the eddy-current brake only needs to be marginally greater than the adhesive limit of the tire. In mixed braking, the peak force should thus be equal to the tire adhesive limit on dry pavement. The friction braking force should also be equal to the tire adhesive limit, so that the combination of the two brakes can provide a braking force exactly equal to the tire's limit at all speed. This maximizes braking performance.

1.2.2 – Brake with optimized critical speed

Fig. 112 shows the results of a simulation run for a vehicle starting at the maximum legal speed in the United States (75mph) for a broad range of eddy-current brake critical speeds and peak braking forces. The braking performance is evaluated by the stopping time. Because, it is desirable to use the eddy-current brake as much as possible, its design should be optimized without interference from the friction component. The eddy-current brake will thus be designed to handle most of the braking energy. The impact of the friction component will then be investigated in a second time.

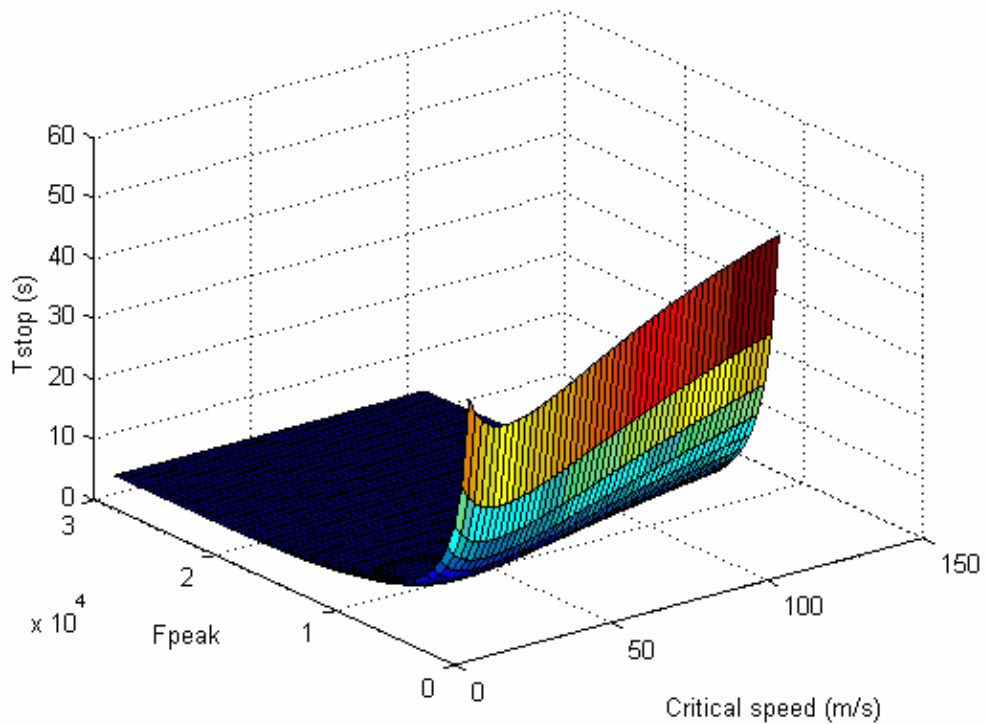


Fig. 112: Deceleration time vs. maximum peak torque and critical speed

Fig. 113 shows that there is an optimum critical speed that minimizes the stopping time. It also shows that there is a diminishing return to increasing the peak force of the eddy-current brake.

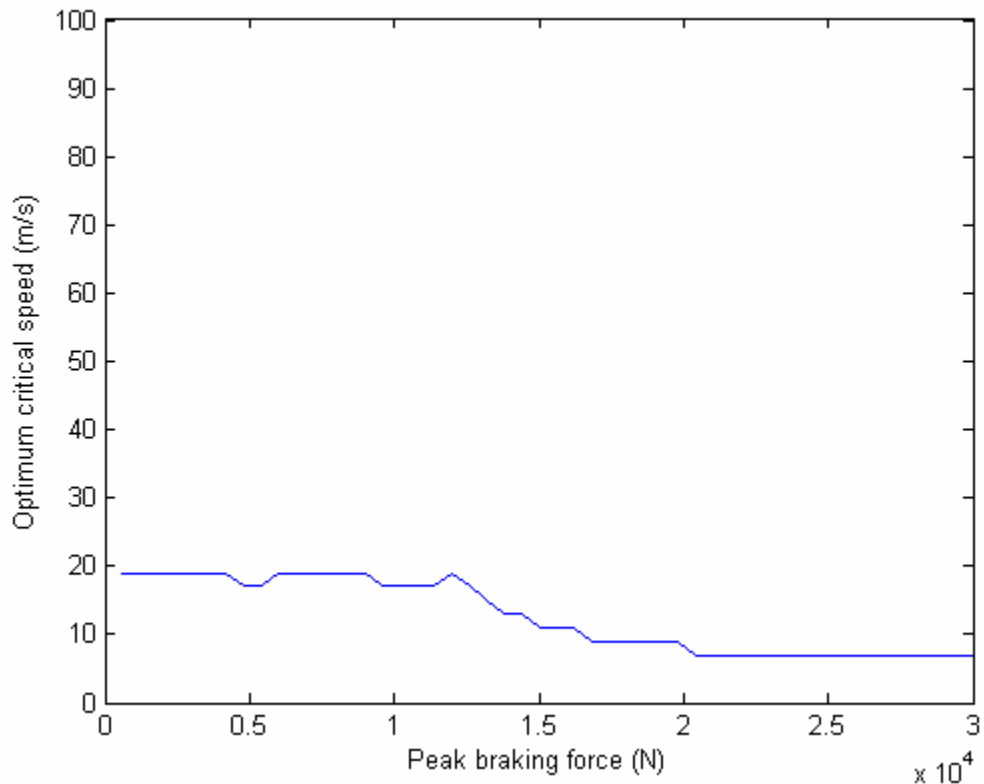


Fig. 113: Optimum critical speed vs. peak braking force

The stopping time is minimized for a peak braking force equal to 12,600 Newton and more (Fig. 114). The corresponding critical speed (Fig. 113) is 17 m/s and the vehicle comes to a complete stop in 7 seconds. The long stopping time is due to the low braking force generated by the eddy-current brake at low speed. Low-speed braking should be

handled by the integrated friction brake, which is capable of producing a maximum braking force independent of speed. The friction brake should be designed to provide as much braking force as the tire adhesive contact with the pavement can handle and used to complement the eddy-current brake to achieve the desired braking force.

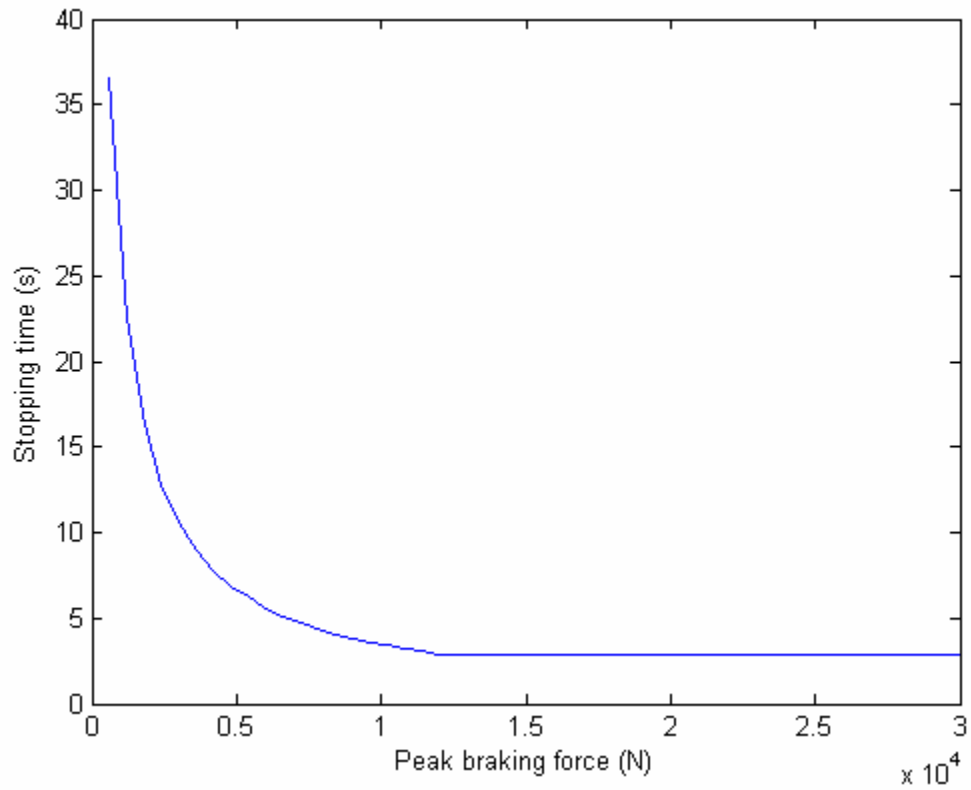


Fig. 114: Stopping time vs. peak braking force

The impact of the friction component has been investigated for a broad range of critical and initial speeds and two values of the peak braking force (8,000N and 40,000N). One value has been chosen well below the maximum force allowed by the tire adhesive

contact with the pavement and the other one was selected well above. Friction braking was used to complement the eddy-current brake so that the combined braking force was always equal to the limit. Fig. 115 shows the complementarity of the eddy-current and friction braking for an eddy-current brake with an optimum peak force of 12,600N and an optimum critical speed of 17m/s.

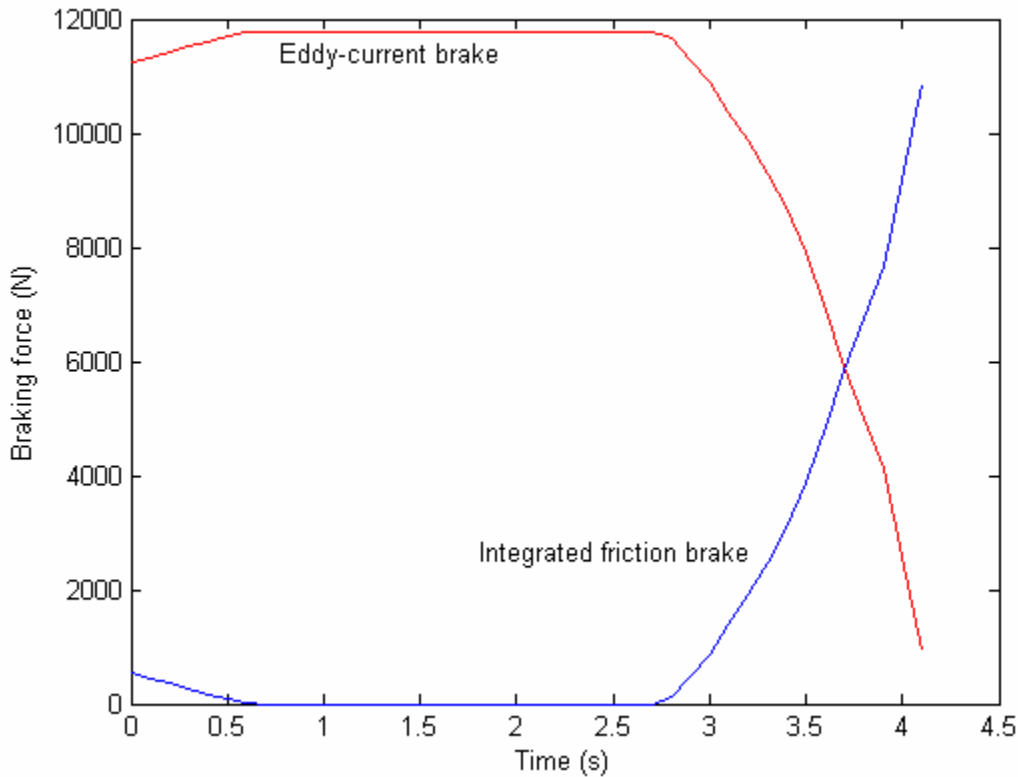


Fig. 115: Eddy-current and friction force, emergency braking

It is important to note that the amount of kinetic energy dissipated by the integrated friction brake is minimal (25kJ) compared to the amount of energy dissipated by the

integrated eddy-current brake, equal to 811kJ (Fig. 116). This is a 97% reduction compared to a vehicle using only friction brakes. This significant reduction is the result of the near-ideal complementarity between eddy-current and friction brakes. Indeed, friction brakes are only needed when the speed and kinetic energy are low so that the eddy-current component supports most of the duty.

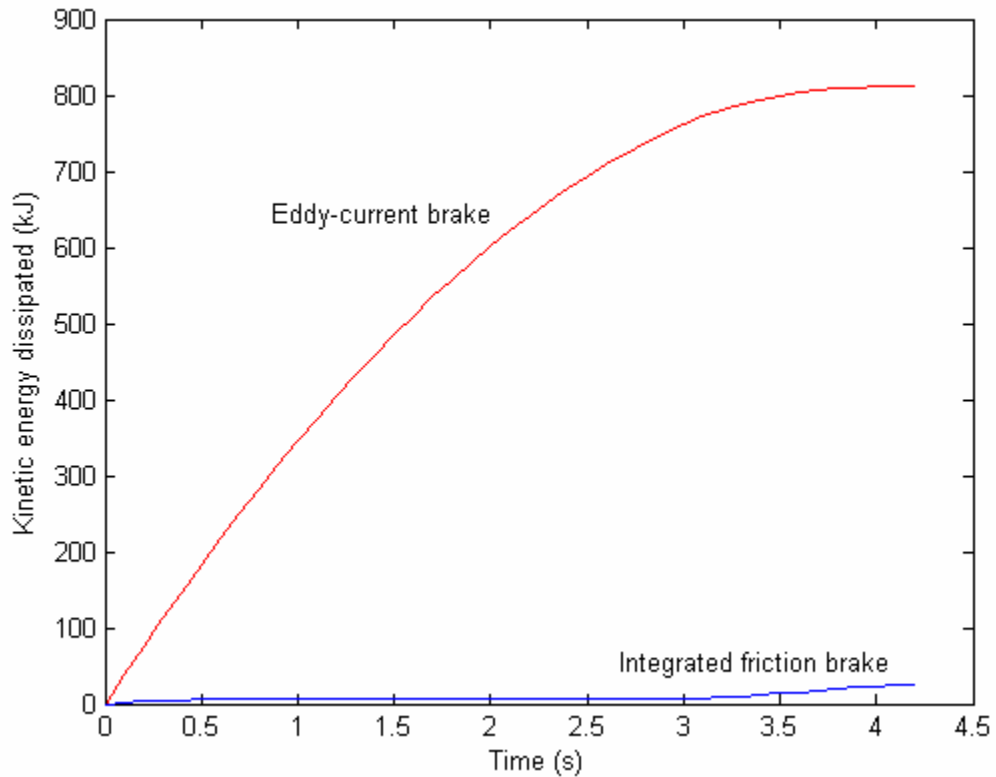


Fig. 116: Eddy-current and friction brake dissipated energy, emergency braking

Fig. 117 shows the fraction of the vehicle's kinetic energy dissipated by eddy-current braking for a vehicle with tires having an adhesive coefficient of 0.8. The resulting limit for the tire-pavement adhesive contact is 11,772N.

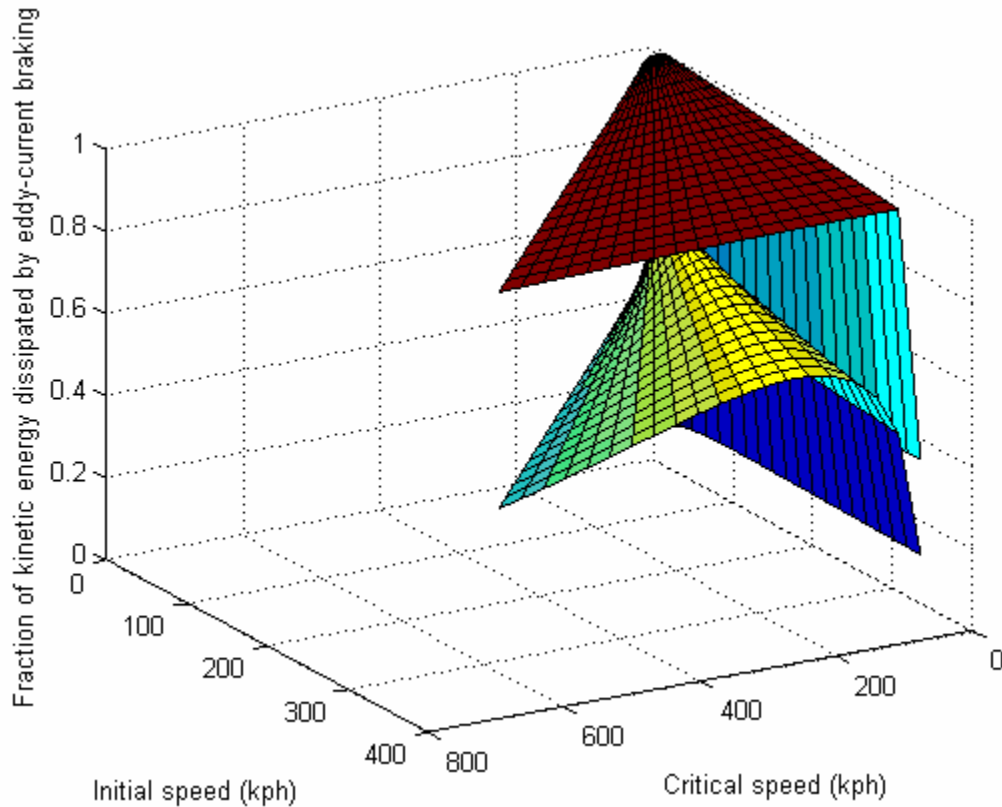


Fig. 117: Fraction of kinetic energy dissipated by eddy-current braking, $\mu=0.8$

The upper surface represents the fraction of kinetic energy dissipated by eddy-current braking with a peak braking force of 40,000N, while the lower surface represents the same fraction for a peak force of 8,000N. The most salient feature of the plots is the dependency of the fraction on the ratio of critical speed to initial speed. There is a sharp

rise of the fraction from zero critical speed to a critical to initial speed ratio of about 0.6, followed by a more moderate decline for higher ratios. The rise is much steeper if the peak braking force exceeds the tire-pavement adhesive contact limit. However, the decline for higher ratios is much less pronounced than for a lower peak braking force. This is due to the high-speed region of the torque-speed characteristic that remains truncated in the high peak force case, while it is not in the low peak force case. Fig. 118 and Fig. 119 show the same data as the lower and upper surfaces in contour plots, which clearly demonstrate the dependency of the fraction on the critical to initial speed ratio.

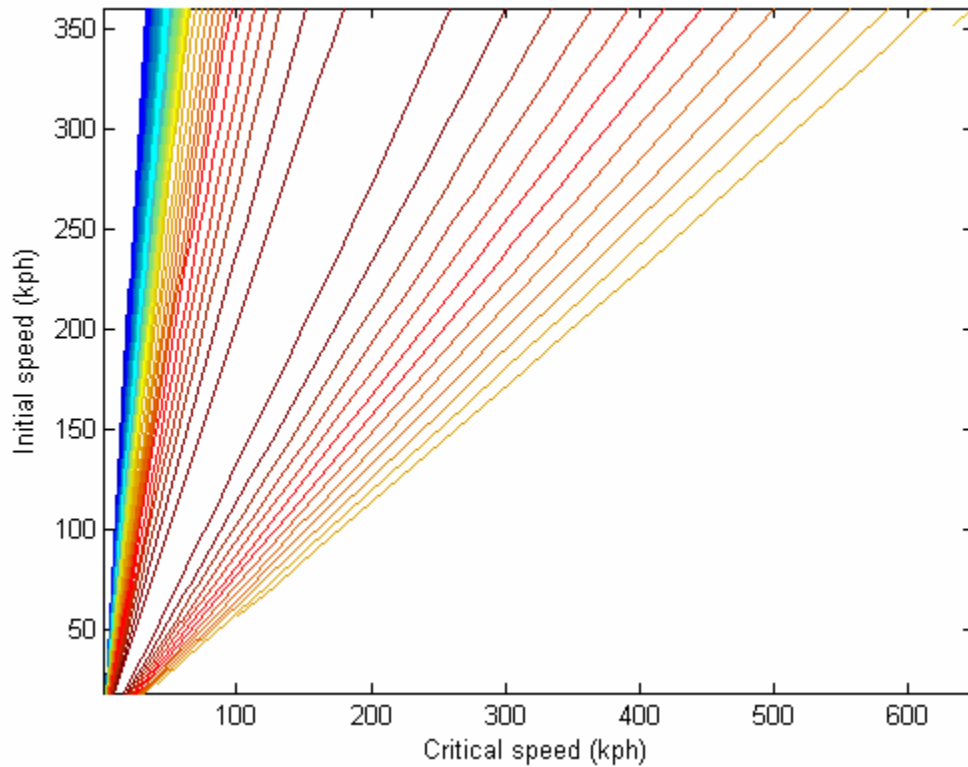


Fig. 118: Fraction of kinetic energy dissipated by eddy-current braking, $F_p=8\text{kN}$

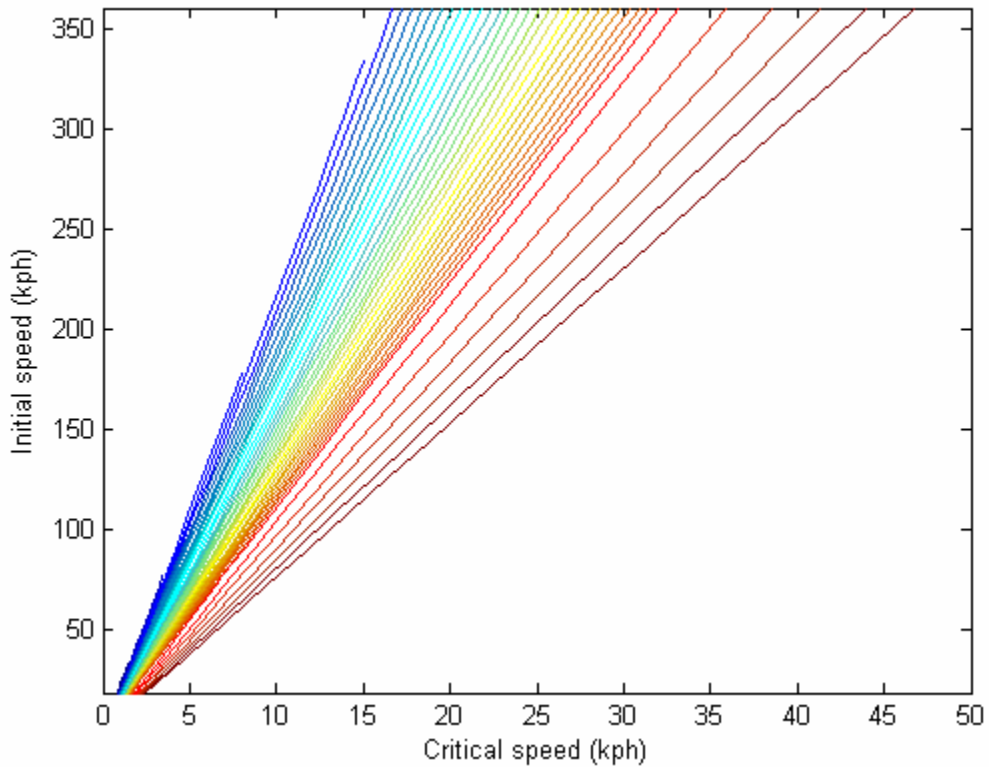


Fig. 119: Fraction of kinetic energy dissipated by eddy-current braking, $F_p=40\text{kN}$

Important design guidelines can be inferred from these plots. Predictability is desirable when designing such a safety critical system as the braking system. Therefore, the marginal sensitivity of the fraction in the high peak force case is an asset. If the critical speed and peak torque can be varied independently and at will by design, then an optimum design would have a high peak force and a high critical speed. The high peak force will result in a maximized and constant fraction of kinetic energy dissipated by eddy-current braking, while the high critical speed will provide a broad range of maximized fraction.

It should be noted that the sharp decrease of the fraction is not problematic because it occurs at very low speed, where the absolute kinetic energy dissipation is minimal. Finally, the increase in peak force beyond the tire-pavement only needs to be moderate as is demonstrated by Fig. 120, which shows a variation of the fraction under 14% across the entire range of critical and initial speeds for a peak force of 16,000N.

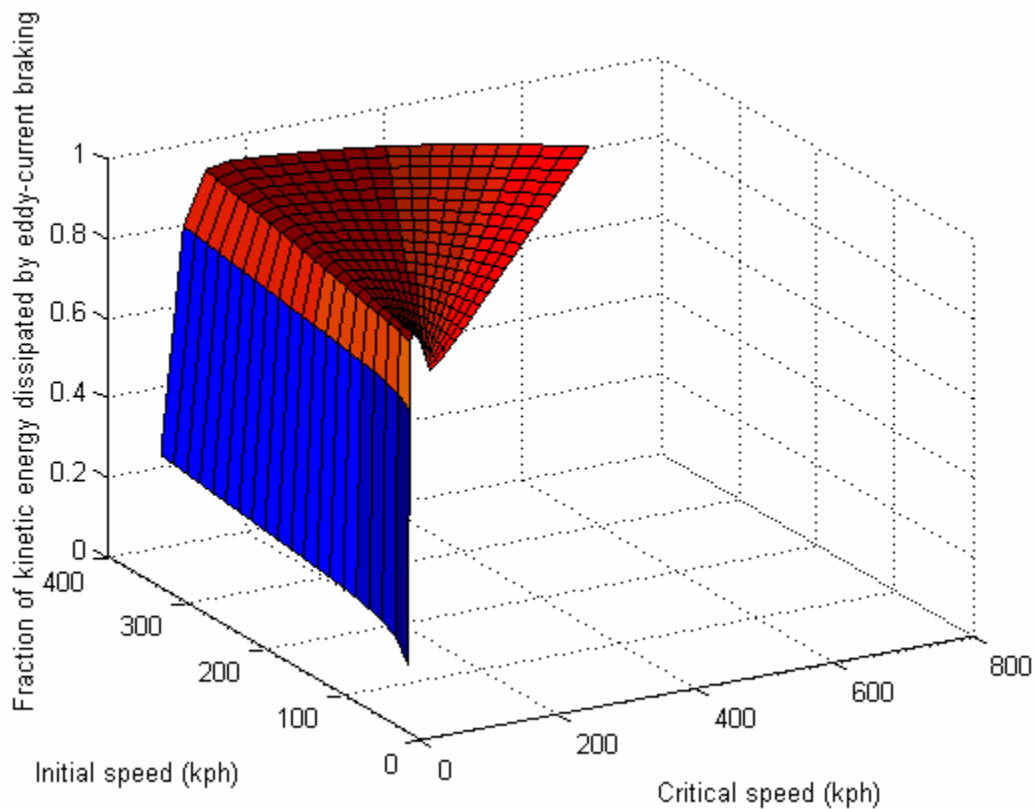


Fig. 120: Fraction of kinetic energy dissipated by eddy-current braking, $F_p=16\text{kN}$

The choice between a brake with a peak force only slightly greater than the tire-pavement adhesive contact limit and a brake with a much greater force depends on the application. In low-duty, initial cost-sensitive applications such as personal automobiles, the most logical choice would be a brake with a moderate peak force, designed for optimal performance in a deceleration from the maximum operating speed (see Fig. 113). The optimal design will result in a minimized cost of the brake. However, in heavy-duty, operational cost-sensitive applications such as commercial vehicles an eddy-current brake with a peak braking force significantly exceeding the limit of the tire-pavement adhesive contact would be a more logical choice since it will reduce the wear of the friction brake. The relation between kinetic energy dissipation and friction brake wear is discussed in the subsection about automobiles.

2 – Integrated braking of automobiles

2.1 – Braking performance requirements

In conventional vehicles, the integrated brake completely replaces the conventional friction brake system. The performance requirements are evaluated for a test vehicle having the parameters listed in TABLE 12.

TABLE 12
Vehicle parameters

PARAMETER	VALUE
Vehicle mass	1500 kg
Rolling resistance coefficient	0.015
Aerodynamic drag coefficient	0.35
Air density	1.25 kg.m ⁻³
Vehicle body frontal area	2 m ²
Wheel radius	0.3 m
Center of gravity height	0.5 m
Center of gravity position from front wheel	1.5 m
Tire adhesion coefficient	0.8

The best braking performance is achieved with the brakes operating exactly at the adhesive limit of the tires. The forces against the motion are thus the braking force, the aerodynamic drag and the rolling resistance. Fig. 121 shows the braking force, deceleration rate and speed profiles for the test vehicle during a maximum (emergency) deceleration from the maximum legal speed in the United States (75mph).

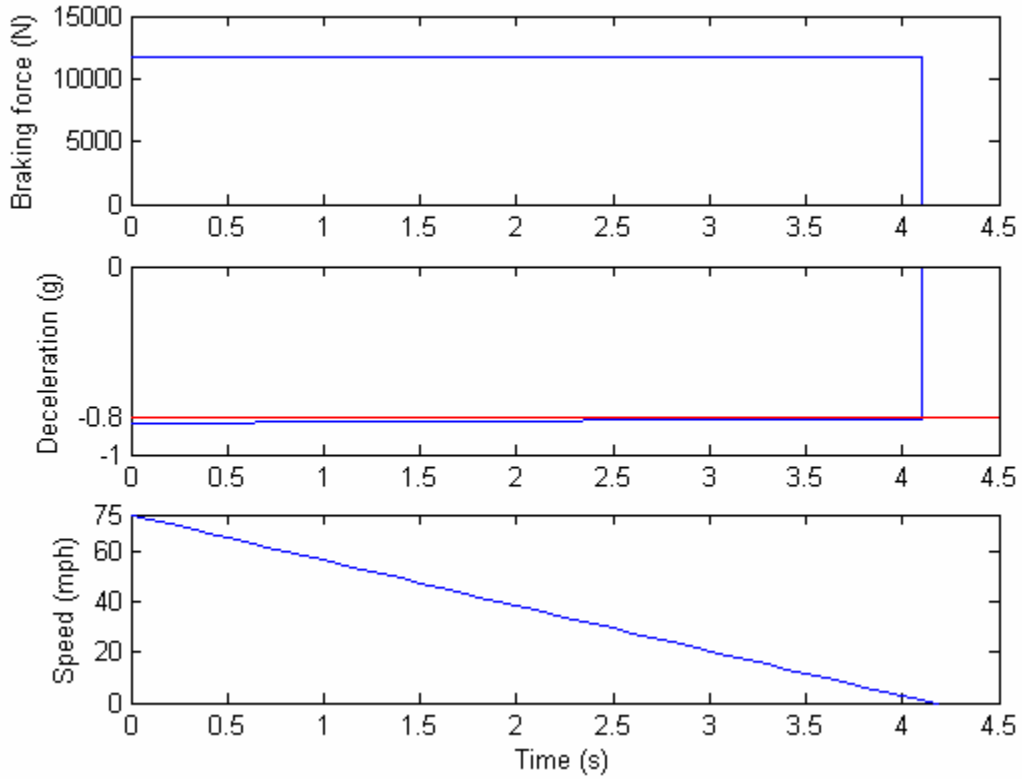


Fig. 121: Test vehicle maximum braking curves

The maximum total braking force that a conventional friction braking system must provide is determined by:

$$Fb_{\max} = \mu_{tire} \cdot M_{vehicle} \cdot g \quad (132)$$

In the case of the test vehicle, this force is equal to 11,772 Newtons. The braking system stops the car in 4.2 seconds and reduces its kinetic energy to 10% of its initial value in 2.9 seconds. The maximum braking force is required from the integrated friction brake when the eddy-current brake force is zero, i.e. when speed is zero. The integrated friction brake must then produce the total vehicle braking force and is therefore sized

accordingly (See TABLE 13). The eddy-current brake parameters are the optimal parameters for the case study as determined from Fig. 113, Fig. 114 and Fig. 115 in the previous subsection.

TABLE 13
Target integrated brake parameters

Parameter	Value
ECB peak torque	883 N.m
ECB critical speed	541 Rpm
Friction brake maximum torque	883 N.m

2.2 – Conceptual design of an automobile integrated brake

Fig. 122 shows a three-dimensional CAD picture of functional parts of the integrated brake concept. The friction brake caliper and pads are colored in yellow and brown respectively. The stator of the eddy-current brake is colored in blue, while the permanent magnets are red. The disc is gray and the actuation mechanism is green. Note that a rotated magnet architecture has been chosen against a shunted magnet architecture because this latter results in a bulkier brake.

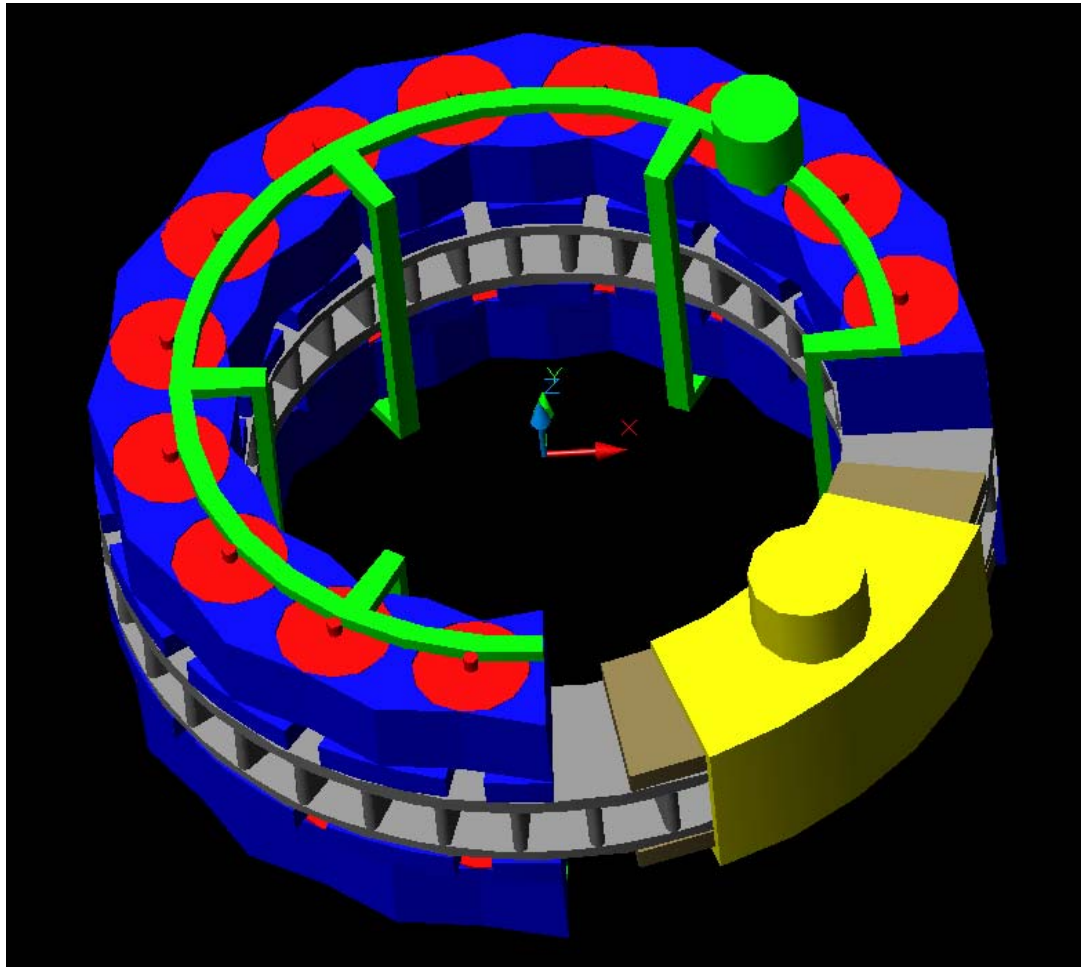


Fig. 122: Integrated brake conceptual design

The actuation mechanism is composed of an electric motor and of a circular rack that engages with pinions on top of the magnet. Therefore, when the electric motor turns, the motion is transmitted equally to all the magnets. Fig. 123 shows one pole in detail. The stator may cover the whole lateral surface of the magnet but numerical analysis has revealed that this increases significantly the flux leakage around the magnet in aligned position as well as the effort required to actuate the magnet. An acceptable compromise

has been found with an angle of 20 degrees between the two contact points of the stator on the lateral surface of the magnet.

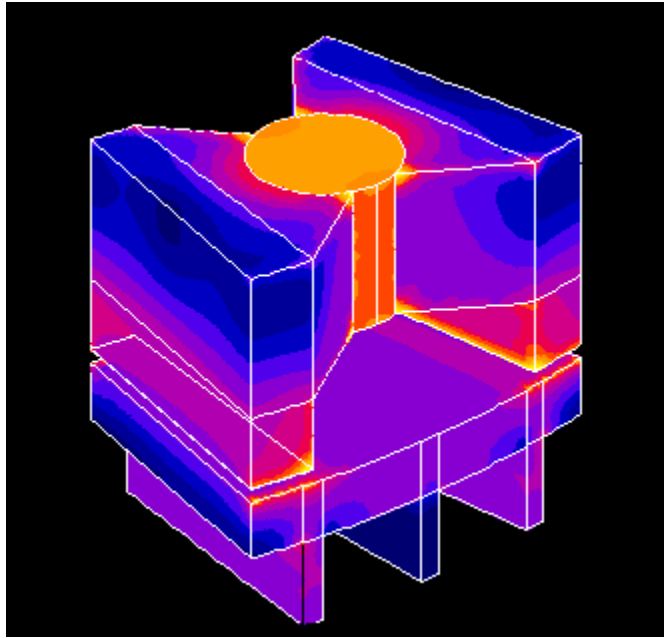


Fig. 123: View of individual pole configuration

TABLE 14 shows the parameters of an integrated brake designed for the target parameters listed in TABLE 13. The designed brake has a peak torque of 974N.m at room temperature at a critical speed of 515rpm. The design is thus 10.3% above requirements for peak torque and 5% off for critical speed. This is the result of the number of poles being discrete and greatly affecting the performance. The actual values of the brake will be altered slightly as the design was performed for a brake having poles distributed uniformly around the disc. The conceptual design has poles that cover only a fraction of the disc (135deg), which means that there is no periodicity below 360deg

strictly speaking. The slight difference comes from breaking the periodicity. Fig. 124 shows the torque speed curve of the designed brake as computed by FLUX 3D[®].

TABLE 14
Conceptual design geometric and material parameters

PARAMETER	VALUE
Outer radius	195mm
Inner radius	145mm
Disc thickness	5mm
Airgap width	1mm
Number of poles	20
Pole arc	22.5deg
Pole shoe arc	20deg
Magnet diameter	40mm
Magnet height	18.5mm
Residual magnetization	1.3T
Saturation magnetization	0.7T
Relative permeability	350

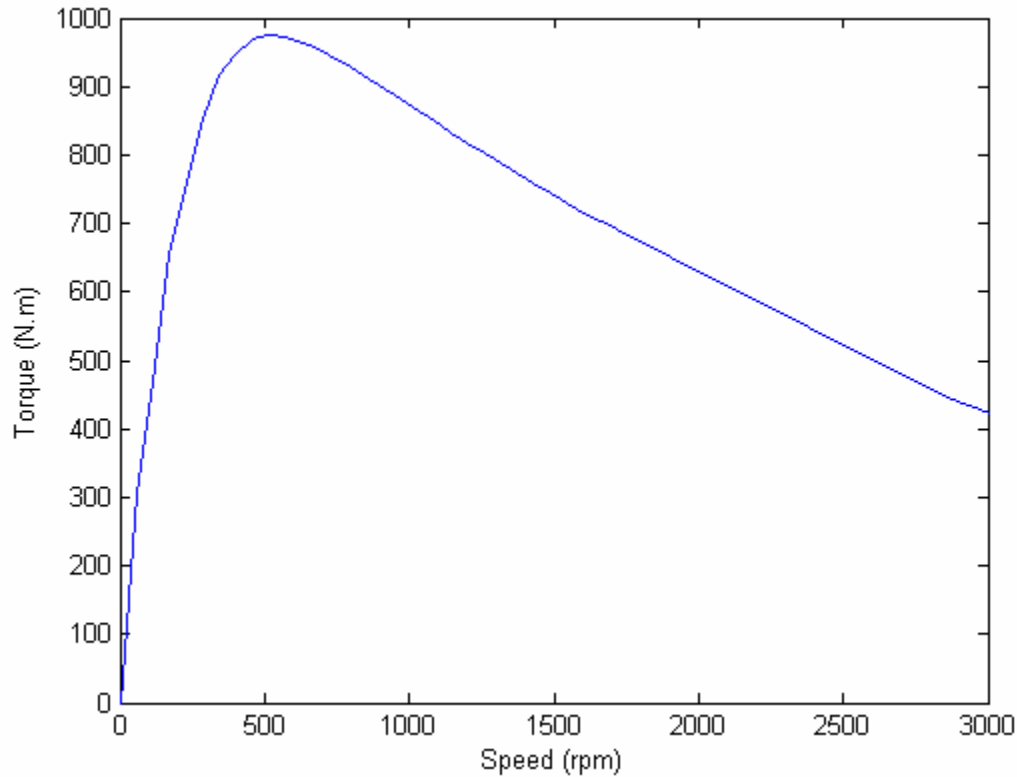


Fig. 124: Conceptual design eddy-current brake torque-speed curve

The torque on the magnets versus their angular position was computed by finite element analysis. A magnetostatic analysis was performed, which is equivalent to neglecting the eddy-currents arising in the stator as a result of the variable flux density induced by the rotation of the magnet. This assumption is reasonable given that the stator material would be a low-conductivity silicon iron and that the rotation of the magnet is slow compared to the frequencies at which these materials are normally operated (50-60Hz). It is also assumed that the disc is at standstill, where it is not saturated and therefore, where the force on the actuator is the greatest.

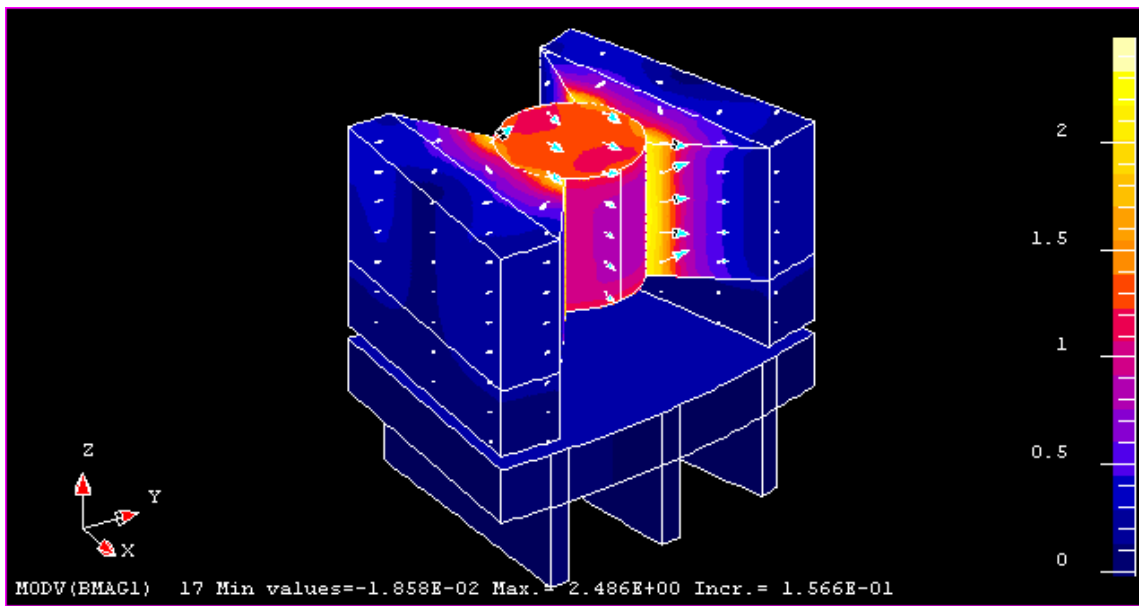


Fig.125: Pole flux pattern in quadrature position

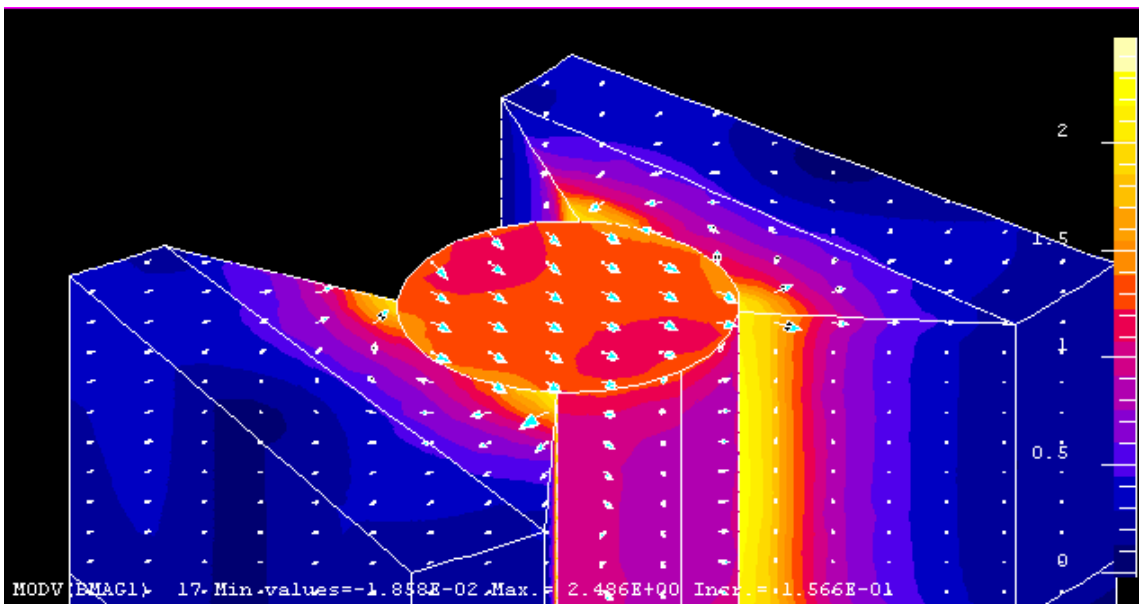


Fig. 126: Pole flux pattern in quadrature position, zoom

Fig. 125 and Fig. 126 show the flux patterns when the magnet is its quadrature position, and Fig. 127 shows the flux patterns when the magnet is in its aligned position.

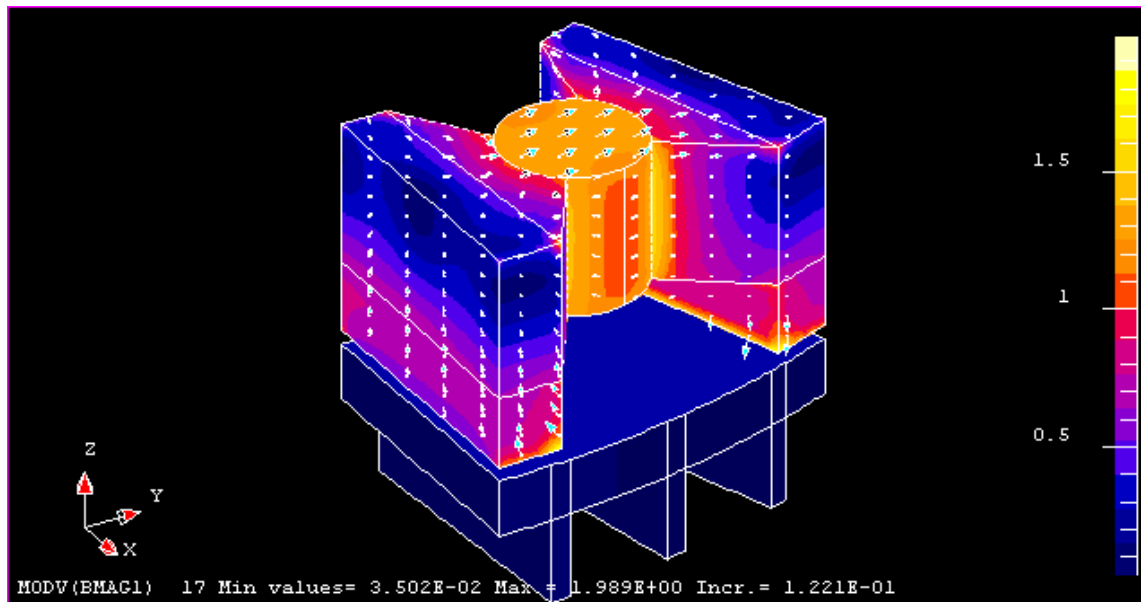


Fig. 127: Pole flux pattern in aligned position

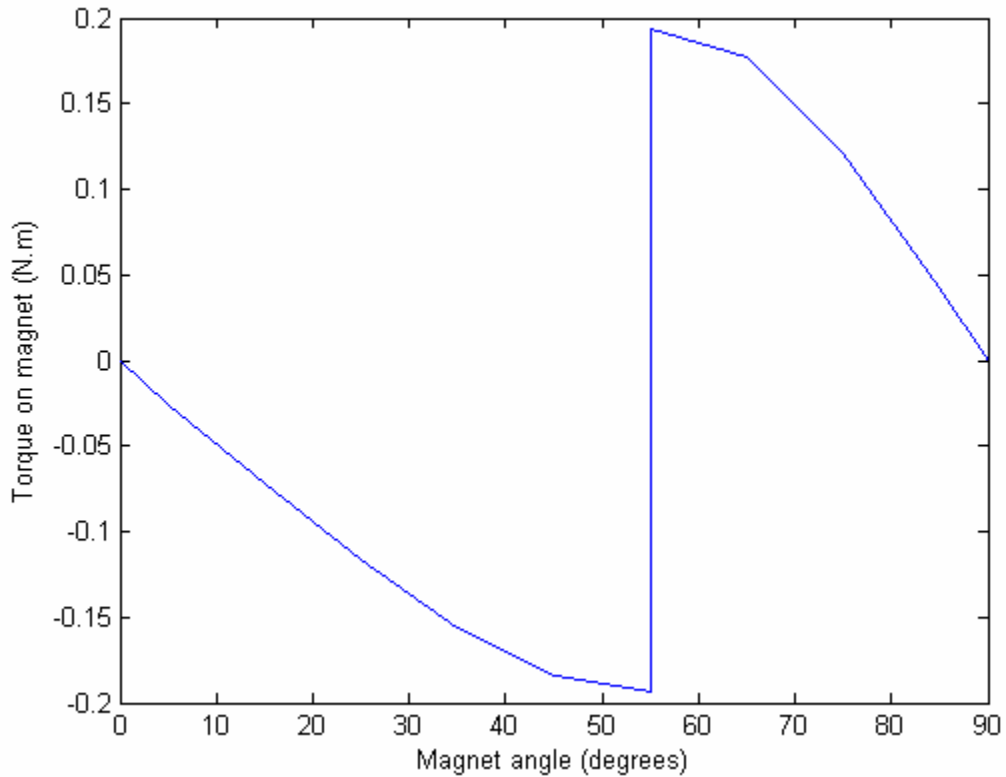


Fig. 128: Torque on one magnet vs. magnet angle

Fig. 128 shows a plot of the torque on the magnet versus its angle from the quadrature position. The torque on the magnet reverses its polarity around 55 degrees. From 0 to 55 degrees, the magnet is attracted back towards the quadrature position. Then, from 55 degrees to 90 degrees, it is attracted to the aligned position. It is a bi-stable system. This curve was used in the simulation of the actuation dynamics of the eddy-current component. During this simulation, it was assumed that the actuator would be operated at constant torque as opposed to constant power. Although constant power is the best

mode to accelerate a mass, the actuator must also be operated in static mode and therefore be capable to provide a torque that always counters that of the magnets.

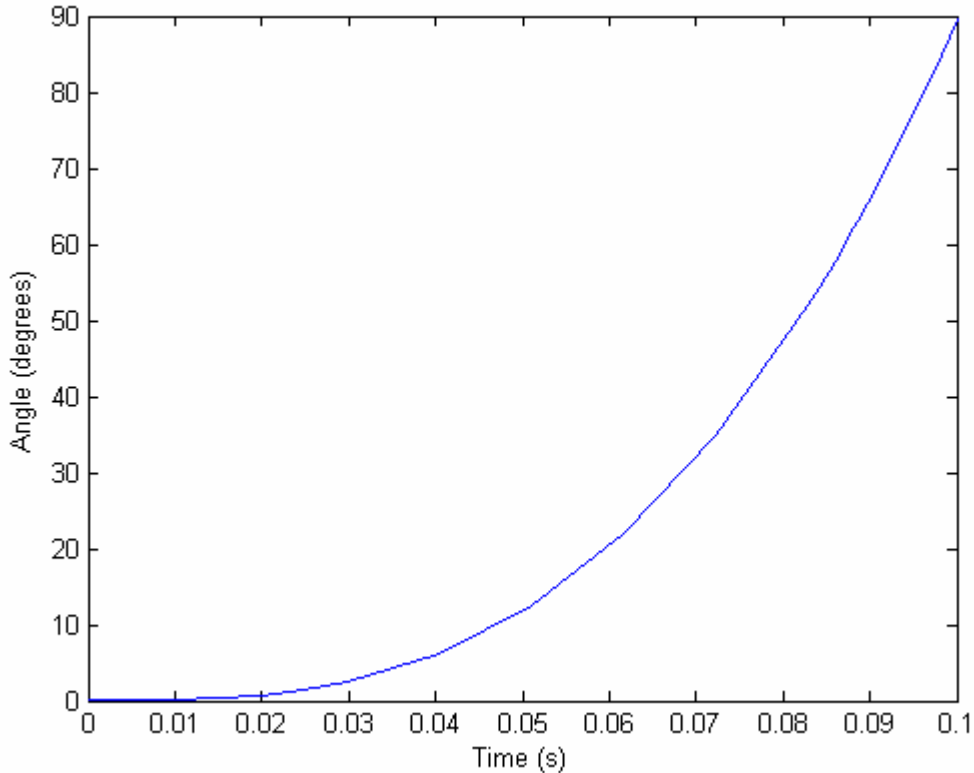


Fig. 129: Magnet angular position vs. time

Fig. 129 shows the position of one magnet versus time. The actuator is rated to bring all the magnets from 0 to 90 degrees in 100ms. The actuator must be designed to bring the magnets from a quadrature to an aligned position at least as fast as the best power assisted conventional friction brakes (100ms). TABLE 15 shows the actuator torque and

power requirements if the magnets are rotated in 100ms by a constant torque actuator.

The values indicated take into account the inertia of the magnets.

TABLE 15
Actuator torque and power requirements

PARAMETER	VALUE
Maximum actuator speed	434 rpm
Maximum actuator torque	3.6 N.m
Maximum actuator power	163.6 W

It is important to note the low power and the low effort required to actuate the eddy-current brake as opposed to the large effort required to apply friction pads and to the large power required to provide power assistance in a conventional friction brake system. The next section provides more details on this subject. The energy consumed by the actuator during this motion, neglecting its efficiency is 0.565 Joules. TABLE 16 shows the characteristics of a possible electric motor for the actuation of the eddy-current brake.

TABLE 16
Possible actuator [49]

Parameter	Value
Maximum torque	0.0411N.m
Maximum speed	73,464rpm
Maximum power	316W
Rated armature voltage	50V
Peak current	6.59A
Efficiency at maximum power	96%
Diameter	12.7mm
Length	60mm
Reduction gear ratio	1/170

The actuator has been designed to respond from zero to maximum braking torque in 100 milliseconds. The proposed motor is actually more powerful and can rotate the magnet from quadrature to aligned position in 67 milliseconds. However, the reaction time is much lower if the magnet only needs to be rotated partially. For angle variations below 3 degrees, a reaction time of 20 milliseconds can be achieved, which corresponds to the maximum time constant of the eddy-current response to a change in excitation flux.

A reaction time of 67 milliseconds is sufficient for a human operator, especially given the large time constant of a vehicle, which is of the order of a few seconds. However, this may be too slow for electronic driving aids, which rely on fast actuation to achieve great performance. Although fast actuation can be achieved, it is restricted to very small angular variations, which may not be suitable for anti-lock, traction or dynamic stability

control. The issue of interfacing with electronic driving aids will be investigated in later subsections.

A reaction time of 20 milliseconds from quadrature to aligned position may be achieved but at the expense of a prohibitively powerful actuator. The power required is in excess of a few kilowatts. Even with a high-speed actuator, it is impractical to achieve such response time from quadrature to aligned position.

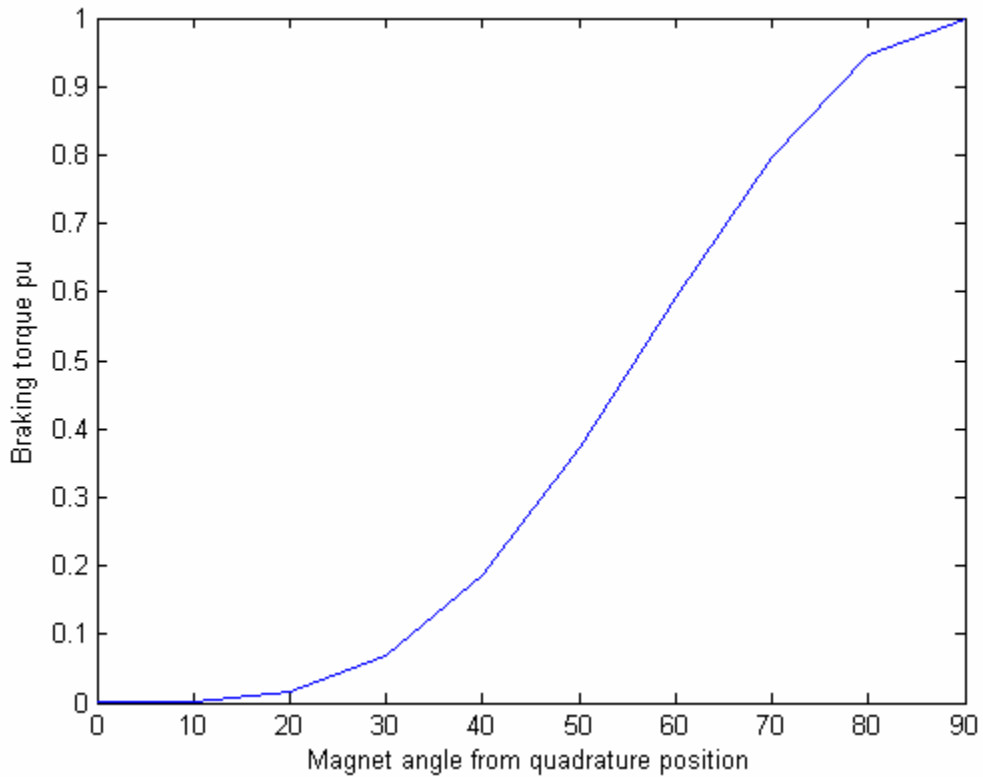


Fig. 130: Conceptual design peak torque vs. magnet angle

Fig. 130 shows the peak braking torque per unit versus the angle of the magnet. The peak braking torque is referenced to the peak braking torque obtained for a fully aligned magnet. There is a seemingly linear range between 40 degrees and 75 degrees but significant nonlinearities otherwise. The control loop of the actuator will therefore need to include linearization steps in order to guarantee the performance of the control system (Fig. 131). When the magnet is in quadrature position, the residual peak braking torque is at $1.9 \times 10^{-5} pu$, which corresponds to a negligible residual braking force of 0.24 Newton.

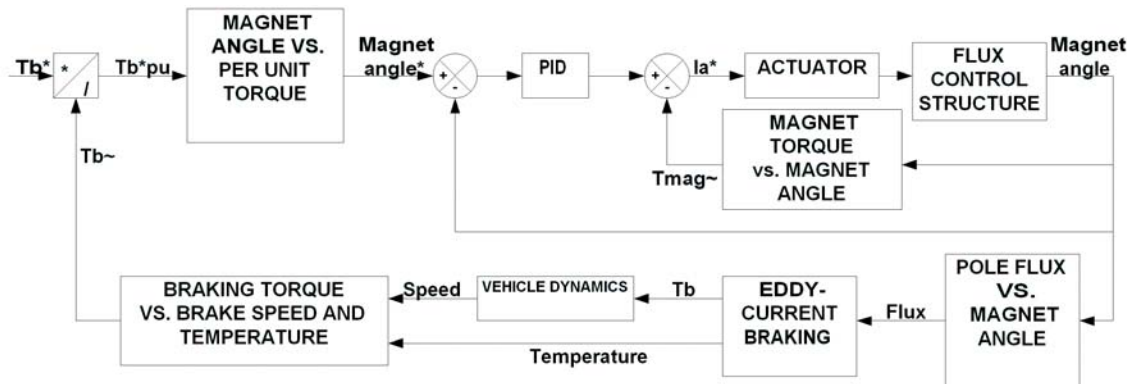


Fig. 131: Individual eddy-current brake control and actuation system

It is important to note that an accurate open-loop control of the braking torque requires an adjustment of the linearization steps with temperature. Because it is difficult to predict the impact of temperature by finite element simulations, and because the temperature of a brake is not uniform, the adjustment is extremely difficult to predict by design. The two linearization steps could be designed by neural networks, and trained on

a test-bed while being fed information from a torquemeter. The learning could continue during the commercial operation of the brake if a torque measurement or an accurate estimation is available. Such a solution would have the advantage of compensating for a drift in the brake's characteristics as it ages.

Another viable alternative is the closed-loop control of the brake, where the inaccurate knowledge of the impact of temperature can be compensated for by a feedback from accelerometers and an estimator block. This solution however requires a fairly accurate estimation of the braking torque by the estimator.

It is worth noting that the dynamic response of the eddy-current brake to the driver's command should not suffer greatly due to inaccuracies in the linearization steps because the reaction time of the driver is much greater than that of the control system. However, electronic driving aids depend critically on the fast reaction of the brakes to perform effectively their function of preserving the integrity and safety of the vehicle and its occupants. The importance of a fast reaction time will be stressed in following subsections on driving aids.

2.3 – Integrated braking in conventional drive trains

A conventional drive train is composed of an engine, a transmission and mechanical brakes. This is the type of drive train found in nearly all automobiles today. The vehicle in this subsection uses the brake designed in section 2.2 above.

2.3.1 – Braking system control strategy

The control of the integrated brake follows the following philosophy: the eddy-current component is the primary component and is used to provide as much of the braking as its torque-speed characteristic allows. The friction component is used as a secondary component to supplement the eddy-current component. Fig. 132 shows the block diagram of the integrated brake controller.

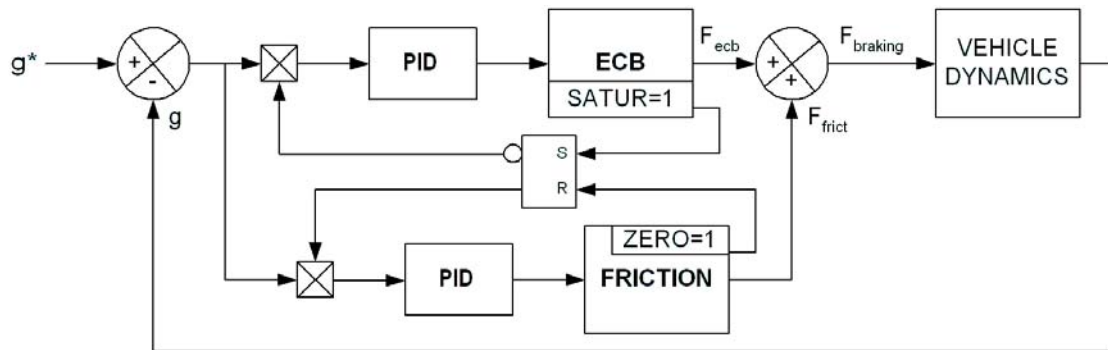


Fig. 132: Conventional vehicle integrated brake controller

2.3.2 – Performance in the FTP 75 Urban drive cycle

Fig. 133 shows the distribution of the braking forces between the eddy-current and friction components of the integrated brake over the FTP 75 Urban drive cycle. It appears that the eddy-current brake handles all the braking for this drive cycle. Fig. 134 actually demonstrates that this is true. This is possible despite the eddy-current braking force going to zero at zero speed because of the rolling resistance of the tires. The integrated brake allows not using the friction component at all during urban drive cycles, thereby saving them from wear.

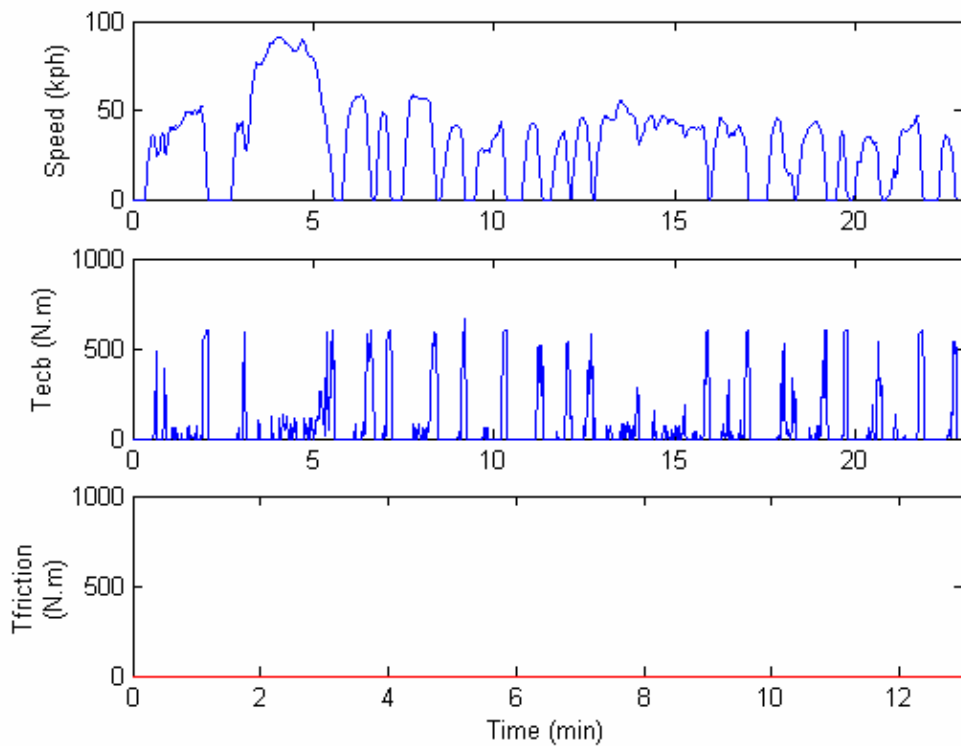


Fig. 133: Braking torque distribution, FTP75 Urban drive cycle

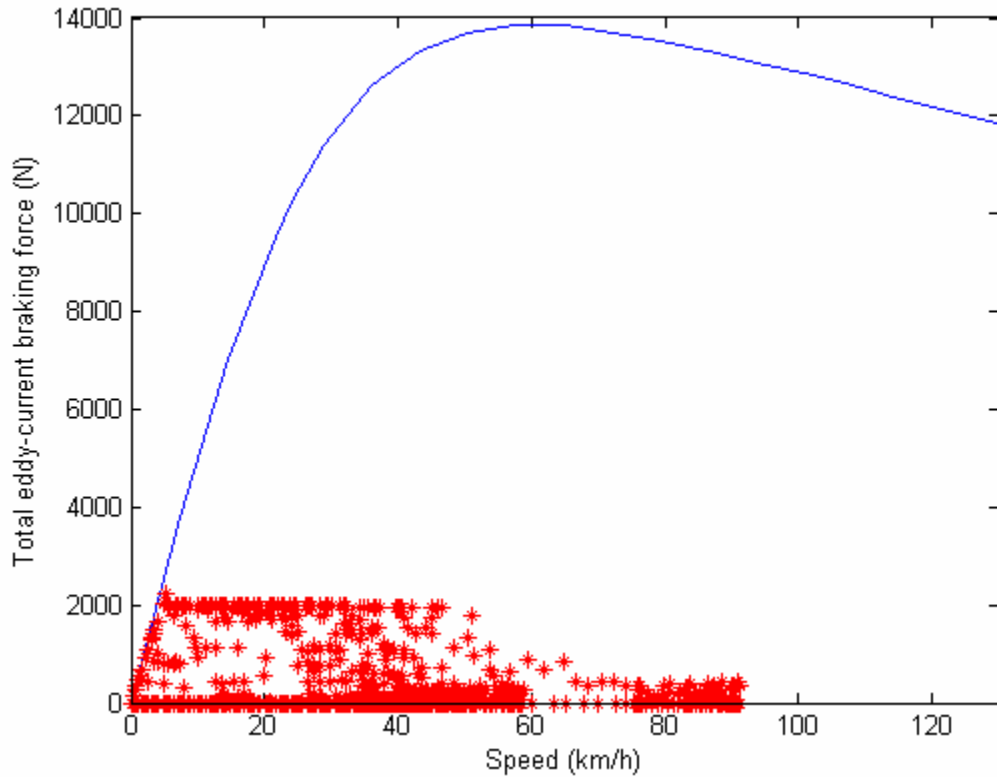


Fig. 134: Eddy-current braking force locus against rated braking force curve

On Fig. 135 the temperature of the brake rotor is plot versus time and against the speed profile. The temperature of the brake reaches a maximum of 162°C. The temperature elevation alters the electrical conductivity and magnetic properties of the rotor, which results in a decrease of the critical speed and peak torque of the eddy-current component. However, this shift is without consequence on the ability of the brake to provide the necessary braking force at all times. Fig. 134 shows that even if the critical speed decreases significantly, the operating points are still within the range of braking forces achievable with the eddy-current component.

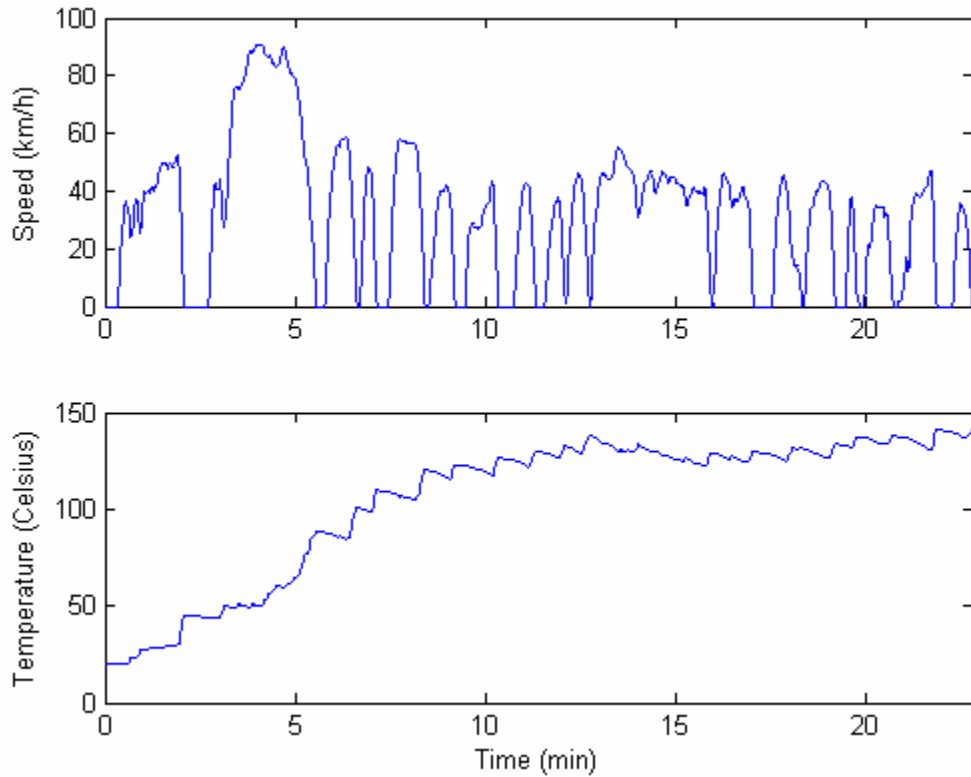


Fig. 135: Integrated brake speed and temperature profile, FTP75 Urban cycle

Fig. 136 shows that the critical speed varies widely over the drive cycle, while the peak torque varies very little. The widely varying critical speed is not detrimental to the urban drive cycle operation because of the low force and speed requirements of this cycle. Fig. 137 demonstrates this graphically with a plot of the brake operating points against the torque speed curve of a warm brake, with a critical speed of 80rpm and a peak torque of 900N.m.

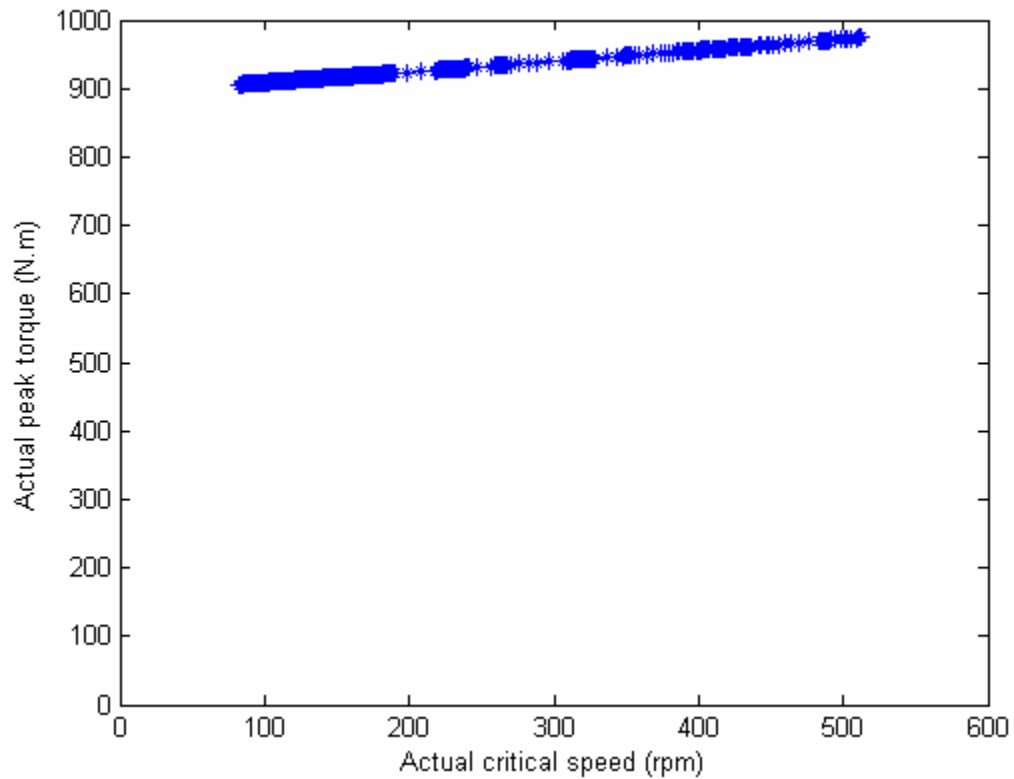


Fig. 136: Critical speed and peak torque locus, FTP75 Urban drive cycle

Note that a warm brake has a steeper torque-speed characteristic below critical speed, which improves its ability to stop the vehicle without the help of friction brakes.

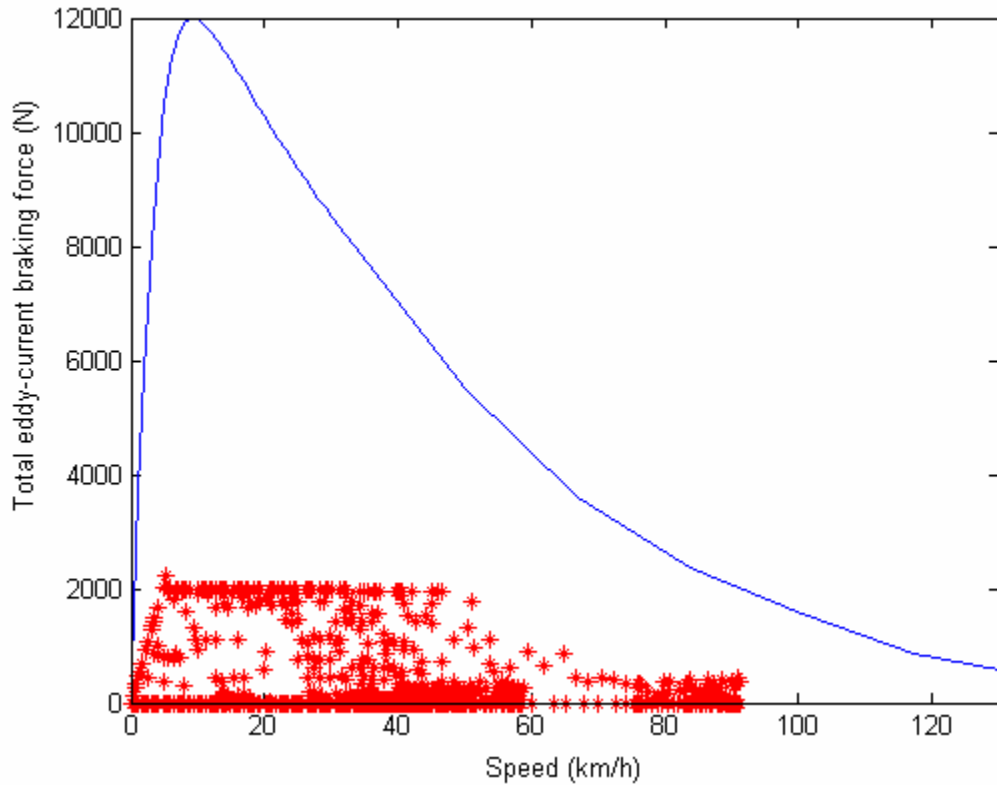


Fig. 137: Eddy-current braking force locus against warm brake force-speed curve

2.3.3 – Performance in the FTP 75 Highway drive cycle

Fig. 138 shows the distribution of braking forces between the eddy-current and friction components of the integrated brake over the FTP 75 Highway drive cycle. As was the case for the FTP 75 Urban drive cycle, the eddy-current brake component is sufficient to handle all the braking required by the Highway drive cycle, including the steep braking at the end. Throughout most of the cycle, very small braking forces are required and are

required at high speed, which is an ideal fit for the eddy-current braking component's torque-speed characteristic.

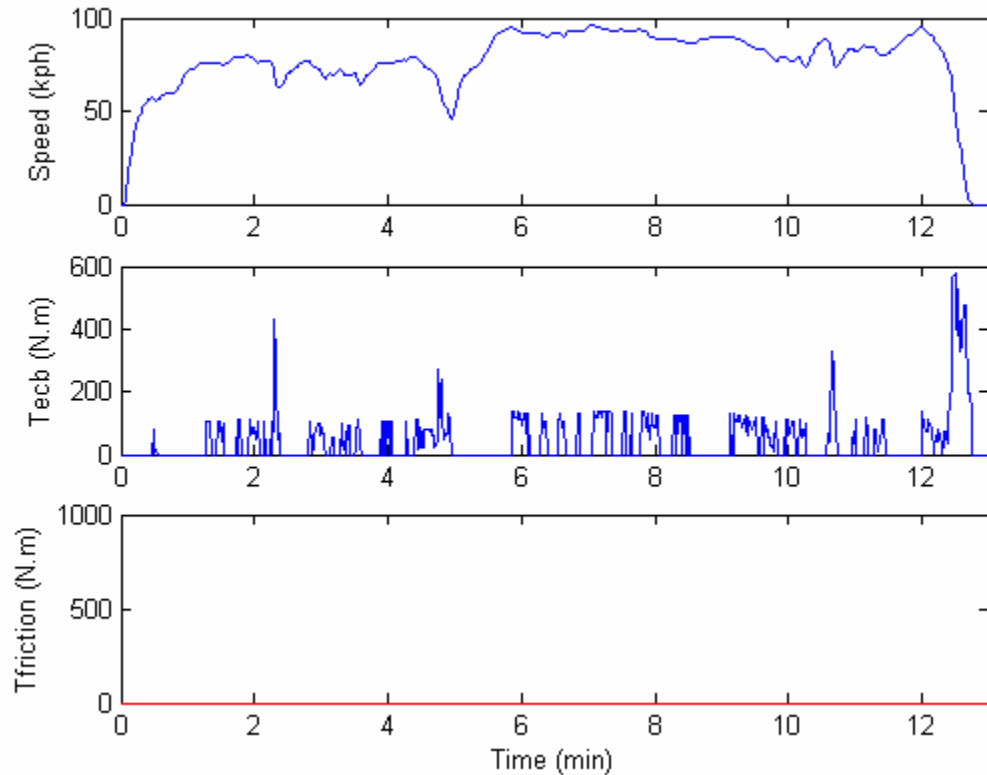


Fig. 138: Braking torque distribution, FTP75 Highway drive cycle

Fig. 139 demonstrates that the operating points are well within the range of braking forces that the eddy-current component can provide. It also demonstrates that braking on the highway is even less sensitive to critical speed and peak torque variation than urban braking. The friction component of the integrated brake is not required at all over the highway drive cycle and is therefore totally preserved from wear.

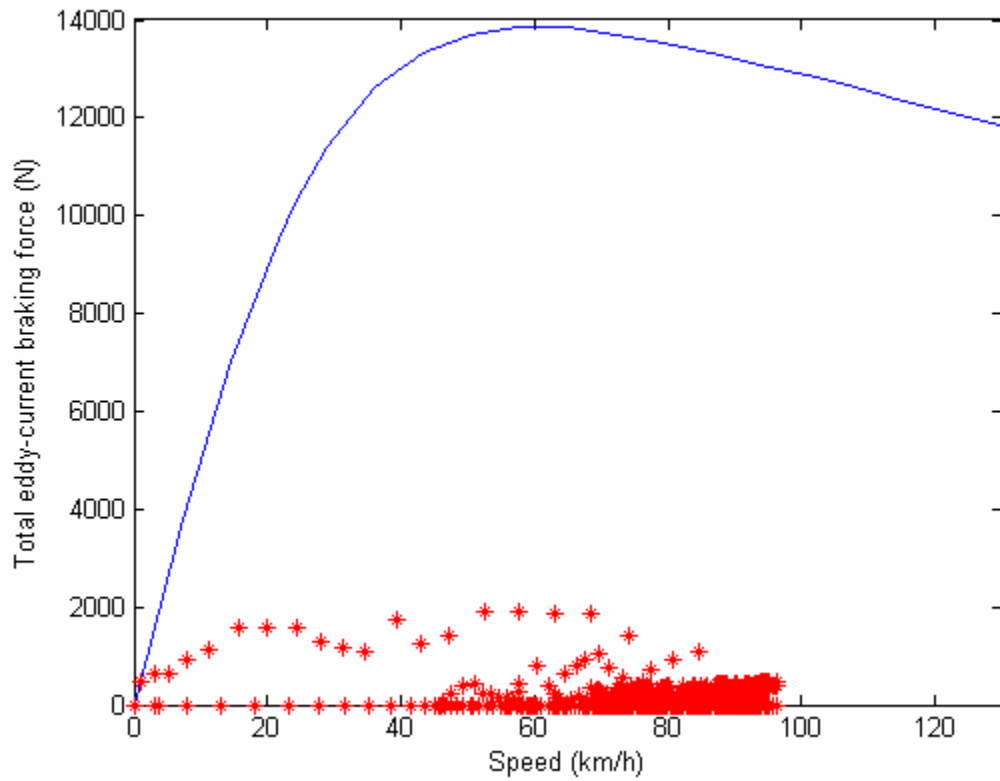


Fig. 139: Eddy-current braking force locus against maximum braking force curve

Fig. 140 shows that the brake reaches a maximum temperature of 142°C, which is less than during the urban drive cycle. The drift of critical speed and peak torque is therefore smaller than for the urban drive cycle.

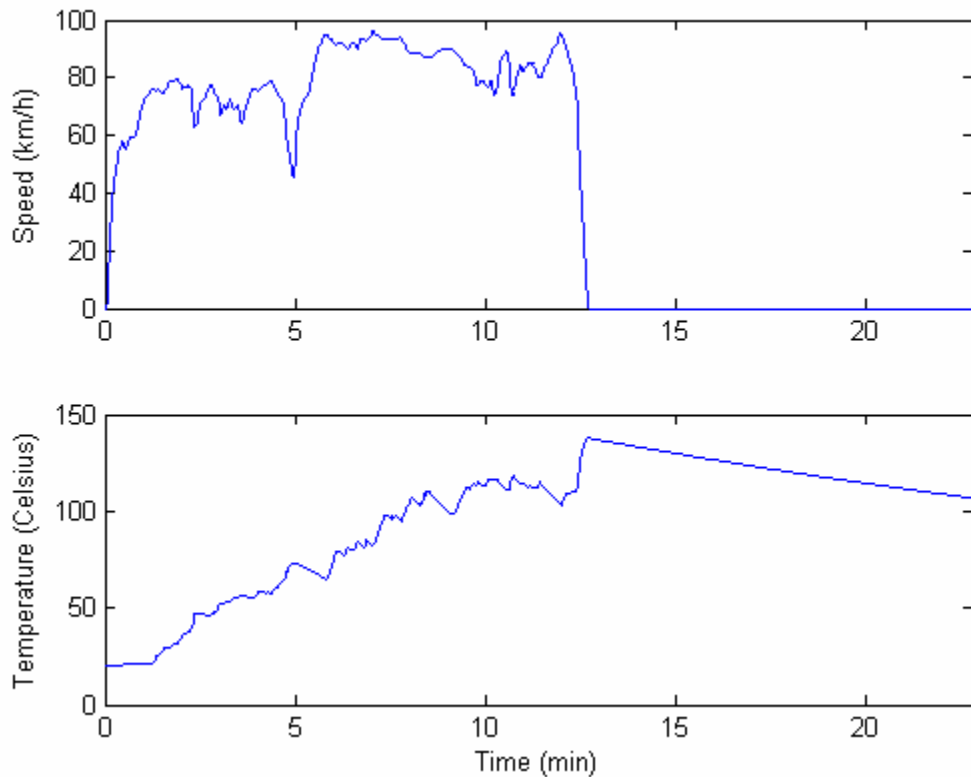


Fig. 140: Integrated brake speed and temperature, FTP 75 Highway drive cycle

Fig. 141 shows the locus of critical speed and peak torque over the FTP 75 Highway drive cycle. It appears clearly that the drift of critical speed is less significant than over the urban drive cycle. Fig. 142 demonstrates that the drift of critical speed is not detrimental to the ability of the conceptual brake to perform along the highway drive cycle.

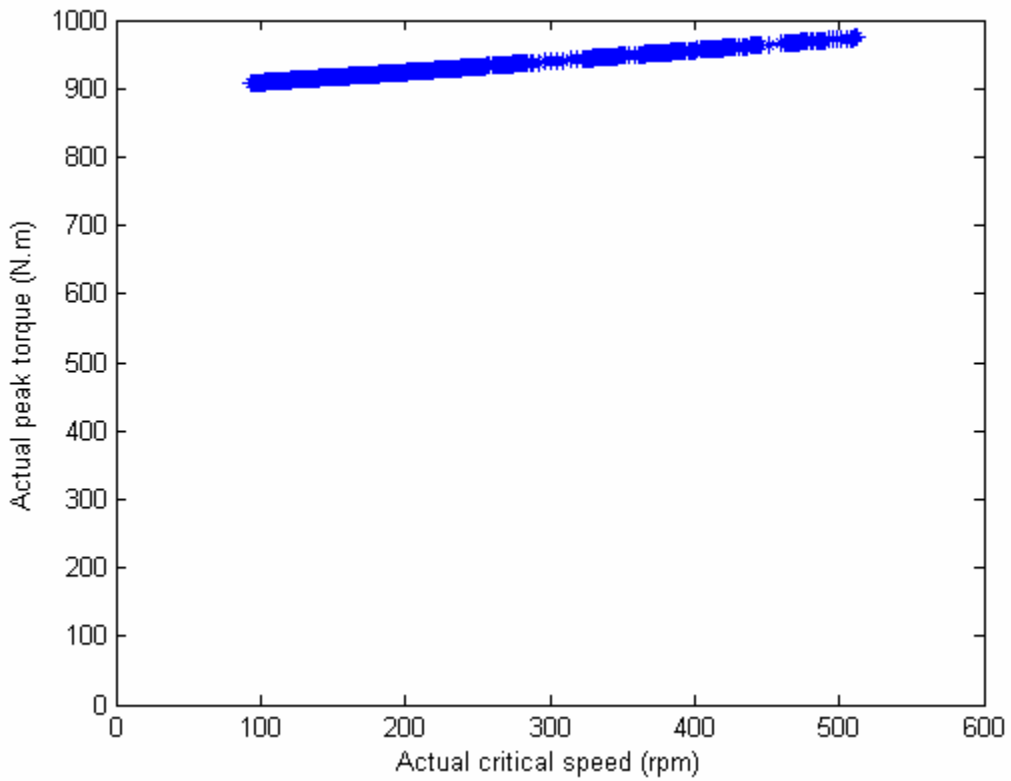


Fig. 141: Critical speed and peak torque locus, FTP 75 Highway drive cycle

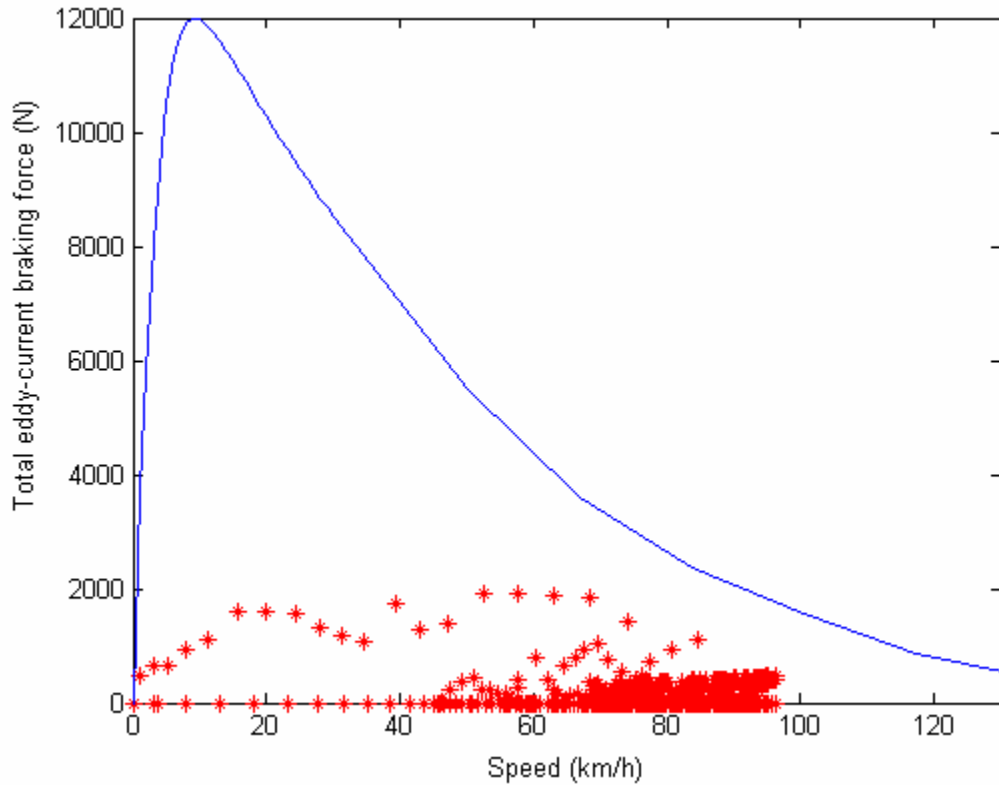


Fig. 142: Eddy-current braking force locus against hot brake force-speed curve

2.4 – Integrated braking of series hybrid drive trains

The example of a series hybrid vehicle controlled by a hysteresis strategy is chosen for simplicity. Series hybrids are also equivalent to electric and fuel cell vehicles as far as the distribution of braking forces is concerned. For braking performance, parallel hybrids fall in between series hybrids and conventional vehicles. Therefore, the results of the analysis of series hybrid vehicles will apply to electric vehicles and will define the range of possible results for parallel hybrid vehicles.

The vehicle parameters are those of the conventional vehicle studied in the previous subsection. The hybrid drive train parameters are listed in TABLE 17 below. The design calls for a maximum acceleration from 0 to 75mph in 15 seconds. Series hybrid drive train design rules are given in [50].

TABLE 17
Hybrid drive train parameters

PARAMETER	VALUE
Engine power rating	60kW
Traction motor power rating	70kW
Traction motor max. to base speed ratio	5
Minimum battery state of charge	0.4
Maximum battery state of charge	0.6
Battery energy capacity	2MJ

The braking performance requirements for a hybrid vehicle are the same as for a conventional vehicle.

2.4.1 – Braking system control strategy

In hybrid vehicles, the integrated brake replaces conventional friction brakes and is used only to supplement regenerative braking when this latter is not available or able to provide the commanded deceleration. Fig. 143 shows the block diagram of a controller for the braking system of a hybrid vehicle equipped with an integrated brake.

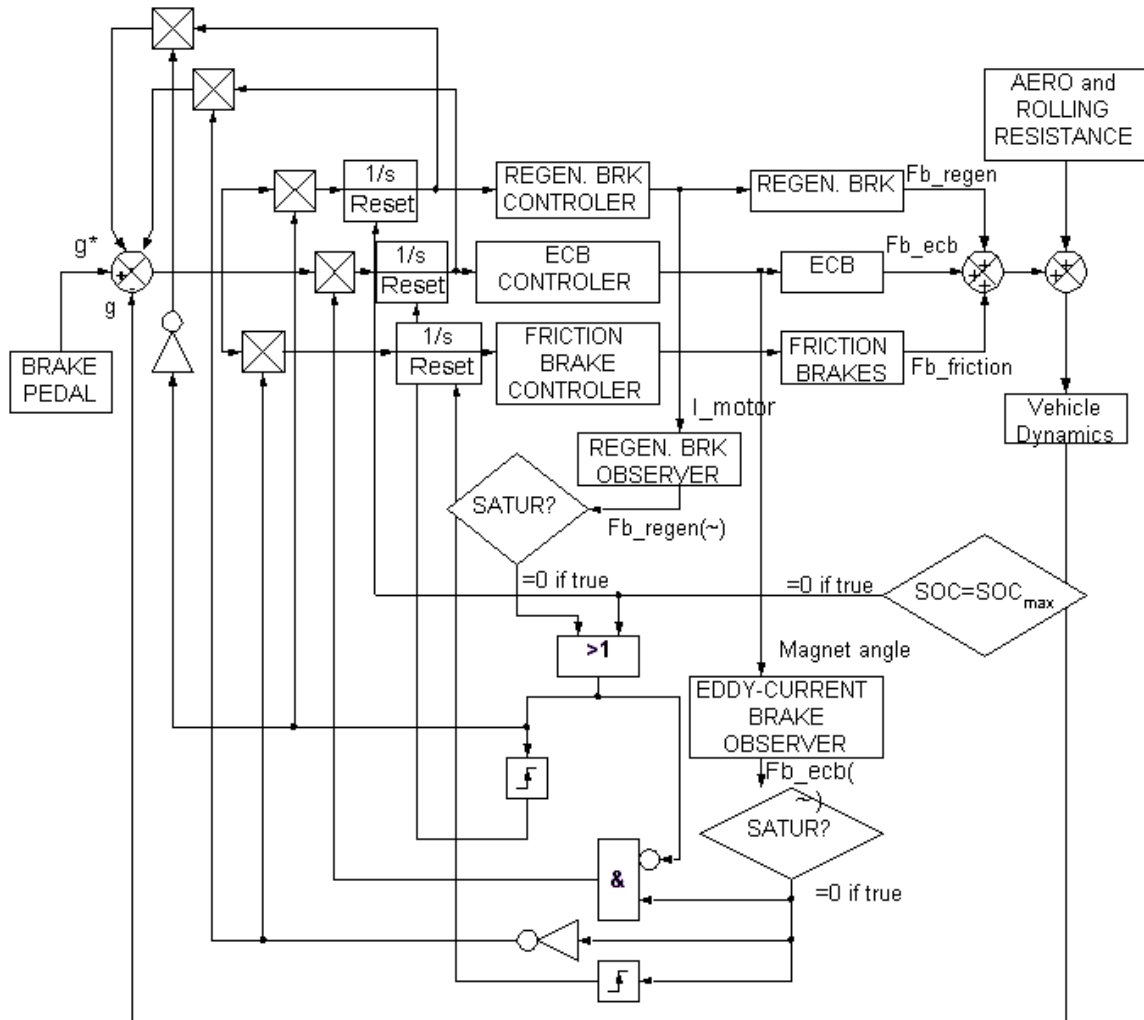


Fig. 143: Braking system control block diagram

The driver's command to brake is converted from a pressure on the brake pedal into a deceleration rate command. This deceleration rate command is fed to a comparator and compared to the actual deceleration of the vehicle, measured by an accelerometer.

The regenerative brake is the primary brake, the eddy-current brake is the secondary brake and the friction brake is the tertiary brake. This arrangement follows the following logic: it is preferable to regenerate kinetic energy than to dissipate it, and it is preferable to dissipate the kinetic energy without wear.

There are two cases for which the deceleration cannot be achieved by the regenerative brake alone: either the energy storage is full or the braking torque required is greater than the torque the regenerative brake can provide at the current speed. In the first case, a battery state of charge observer is required. The second case is detected by monitoring the traction motor's armature current through an observer that compensates for the dynamics of the current-to-torque conversion. If maximum current is reached, then maximum torque is reached for regenerative braking.

If the regenerative brake is not powerful enough or if the energy storage is full, then the error must no longer be fed to its PI controller. The deceleration provided by the regenerative brake (i.e. the output of the regenerative brake's PI controller) must be subtracted to the deceleration error fed to the other brake's controllers. The same is true if the eddy-current brake is not sufficient. If the regenerative brake is unavailable because the energy storage is full, then the integrator of its controller must be reset so that nothing is subtracted from the deceleration error which is then fully applied to the other brakes.

If the regenerative brake is sufficient to brake the vehicle then the deceleration error is fed solely to the regenerative brake's PI controller. If the regenerative brake is not sufficient or not available, there are two cases. Either the eddy-current brake can supply the remaining braking torque or it cannot. If it can, then its PI controller is fed the deceleration error. Whether it can or cannot is determined by the position of the magnet through an observer that compensates for the transfer function between magnet position and eddy-current braking torque.

In case the eddy-current brake is not sufficient, the deceleration error is no longer fed to its PI controller and is fully applied to the friction brake's PI controller. The integrators in the PI controllers for the eddy-current and friction brakes must be reset if the regenerative brake or eddy-current brakes become available or sufficient again, respectively. This is detected by a rising edge of the saturation signals.

The PI controllers do not need to be adjusted in order to take into account the aerodynamic friction, rolling resistance, and grade resistance. Aerodynamic friction and rolling resistance have time constants counted in several hundreds of milliseconds or seconds, while the regenerative brake and eddy-current brakes have reaction times in the order of a few milliseconds. Friction brakes react more slowly so its PI controller would have to be adjusted. However, friction brakes are not linearly controlled due to their mode of actuation so this issue would need a deeper investigation. Grade resistance is

either constant or varying with time constants of the order of several seconds. Therefore, it does not interfere with the dynamics of the braking system.

There are two options to optimize the eddy-current brake in a hybrid vehicle: assuming that regenerative braking is always available or assuming that it may regularly be unavailable. Except for failures, regenerative braking may be regularly unavailable when the battery has reached its maximum state of charge. This would occur primarily in downhill driving or if braking is required immediately after the engine has just finished replenishing the battery. It is thus more realistic to assume that regenerative braking is regularly unavailable and that the dissipative brakes must handle the emergency braking alone. Assuming otherwise would result in significantly reduced braking performance if regenerative braking became unavailable. The validity of this assumption will be proven in the subsection “Performance gains” below. The optimization of the eddy-current brake thus yields the same results as for a conventional vehicle.

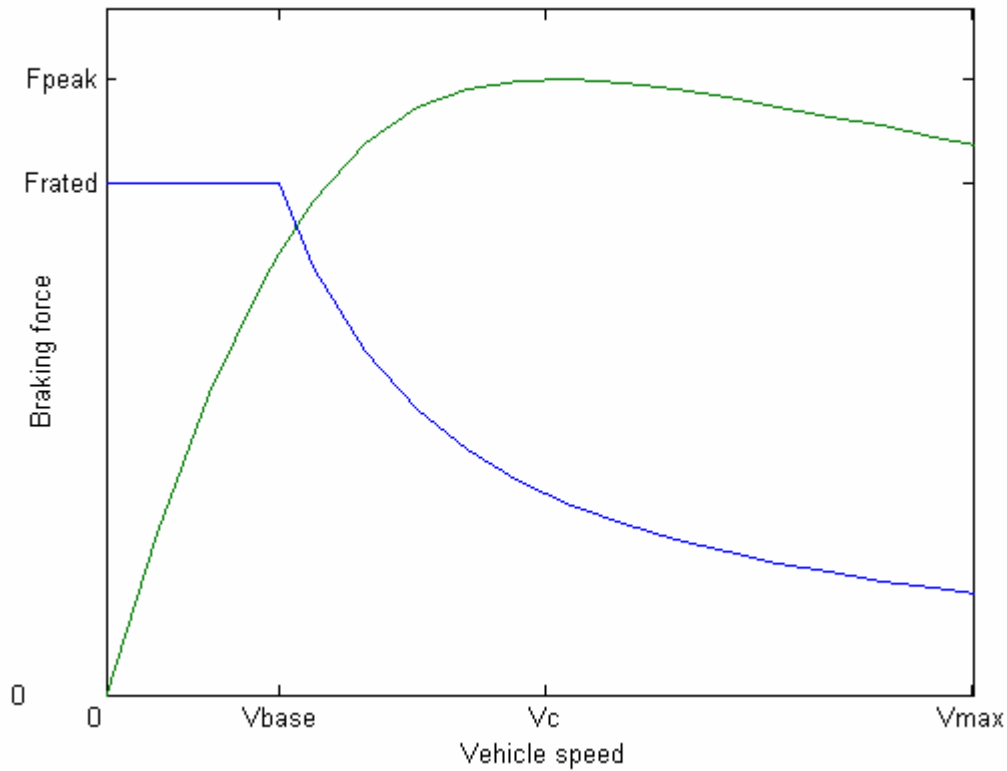


Fig. 144: Complementarity of regenerative and eddy-current braking

Fig. 144 shows the complementarity of regenerative braking and eddy-current braking when the former is available. Regenerative braking provides most of the braking torque at low speed, where the eddy-current brake is inherently limited. On the other hand, the eddy-current brake peaks well into the constant power region of the regenerative brake.

2.4.2 – Performance in the FTP 75 Urban drive cycle

Since a hybrid drive train is designed to maximize the fuel economy of the vehicle it powers, regenerative braking should be designed to handle most of the braking for standard urban and highway drive cycles. Eddy-current and friction brakes are used only during emergency braking, downhill driving and occasionally when braking is required just after the battery has been replenished by the engine. In emergency braking, more braking force is required than the regenerative braking can handle because it is designed to handle decelerations at most as high as its accelerations. In downhill driving, the regenerative braking quickly replenishes the battery by recuperating the potential energy of the vehicle. Once the battery is full, all potential and kinetic energy must be dissipated. It should be noted that a battery large enough to recuperate the potential energy would be unrealistically large for an automobile.

The control strategy influences heavily the occurrence of braking while the battery is already fully charged. An optimum control strategy would minimize or eliminate such occurrences. The hysteresis control strategy is suboptimal and consequently forces the drive train to use dissipative braking on urban and highway drive cycles.

Fig. 145 shows that regenerative braking is mostly used in the FTP 75 Urban drive cycle, while the eddy-current brake is used only sporadically when the battery is fully charged.

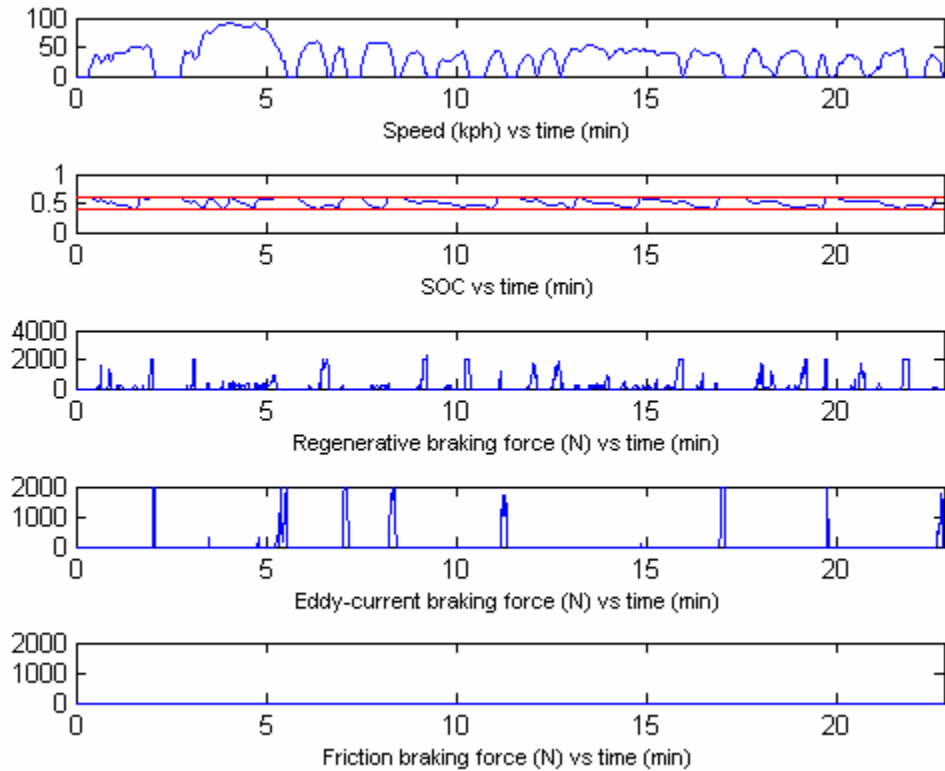


Fig. 145: FTP75 Urban drive cycle braking curves

Since regenerative braking is the primary brake, the integrated brake's temperature remains well below the levels encountered in a conventional vehicle (Fig. 146). Regenerative braking explains why the elevation of temperature is not necessarily coupled to all the deceleration events.

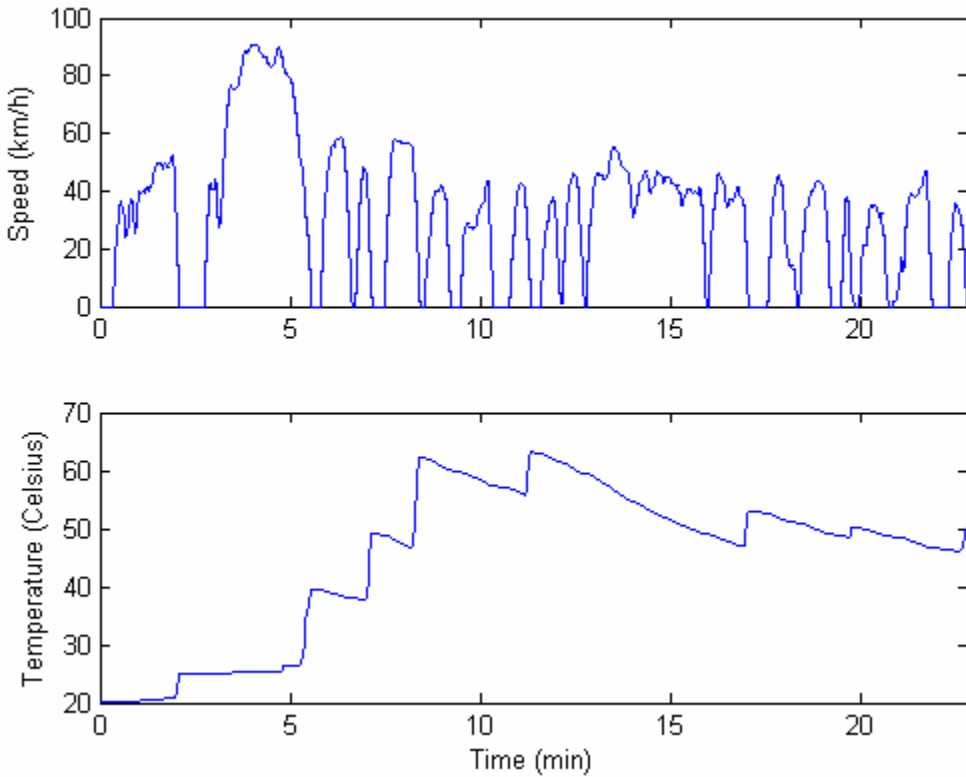


Fig. 146: FTP75 Urban drive cycle, brake temperature profile

The use of eddy-current brakes reduces the wear of the brake pads by 100% in the FTP 75 Urban drive cycle (TABLE 18).

TABLE 18
Balance of dissipated energy, FTP 75 Urban drive cycle

	Series hybrid w/o ECB	Series hybrid w/ ECB
Energy regenerated	1.7MJ	1.7 MJ
Energy dissipated, eddy-current brake	0	0.577 MJ
Energy dissipated, friction brake	0.577 MJ	0

2.4.3 – Performance in the FTP 75 Highway drive cycle

Fig. 147 shows the distribution of braking forces over the FTP 75 Highway drive cycle. As was the case for the conventional vehicle, the friction brakes do not need to be used. The braking forces are primarily provided by the regenerative brake. In all of the drive cycle, the eddy-current brake is used only when the battery reaches its maximum state of charge and cannot accept more regenerated energy. Because braking forces are so small over standard drive cycles, there are no instances of the eddy-current brake supplementing the regenerative brake because this latter cannot provide enough force.

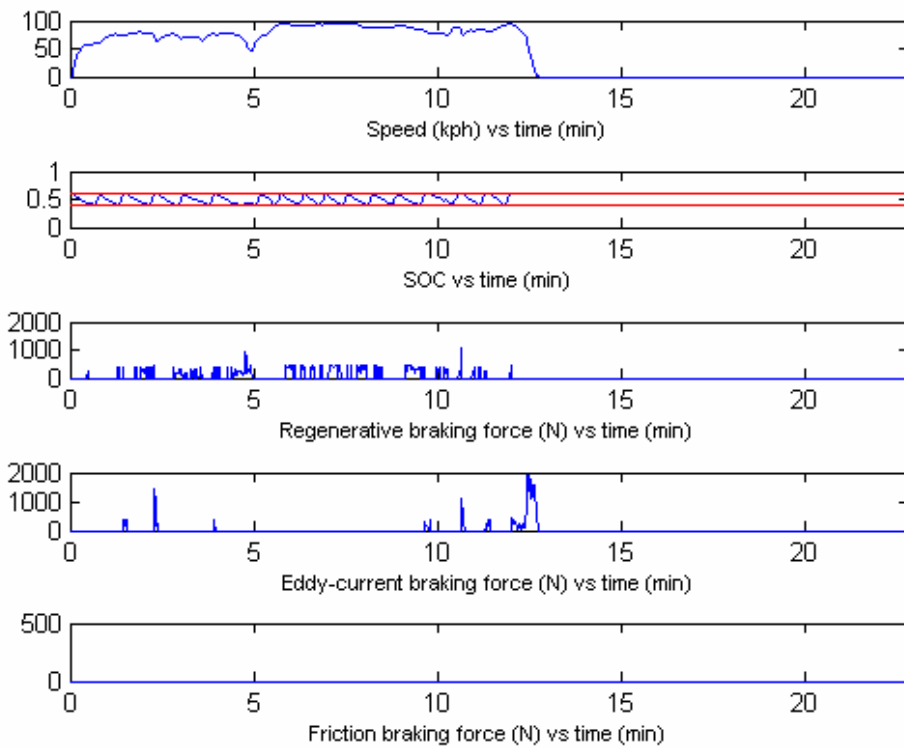


Fig. 147: FTP75 Highway drive cycle braking curves

The temperature profile of the integrated brake rotor is plot on Fig. 148. The temperature is very close to room temperature throughout all of the cycle, and rises significantly only at the very end during the last deceleration. The brake otherwise remain very cold, as a consequence of most of the braking energy being handled by the regenerative brake.

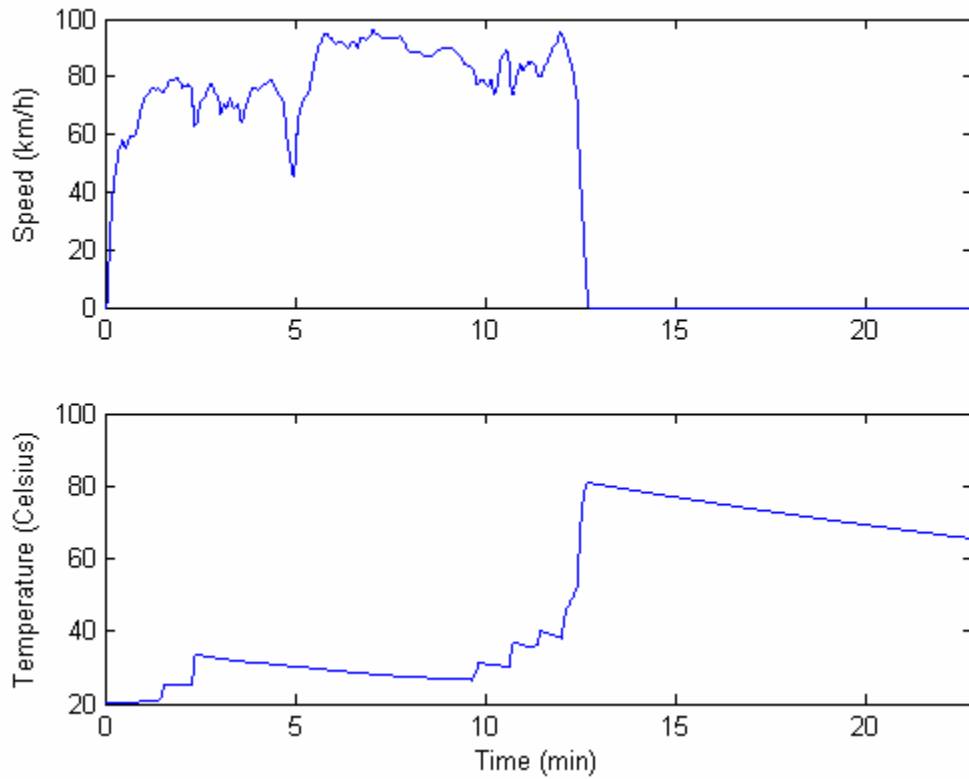


Fig. 148: FTP75 Highway drive cycle, brake temperature

The use of eddy-current brakes reduces the wear of the brake pads by 100% in the FTP 75 Highway drive cycle (TABLE 19).

TABLE 19
Balance of dissipated energy, FTP 75 Highway drive cycle

	Series hybrid w/o ECB	Series hybrid w/ ECB
Energy regenerated	1.6MJ	1.6 MJ
Energy dissipated, eddy-current brake	0	0.625 MJ
Energy dissipated, friction brake	0.625 MJ	0

2.4.4 – Performance in the NREL drive cycle

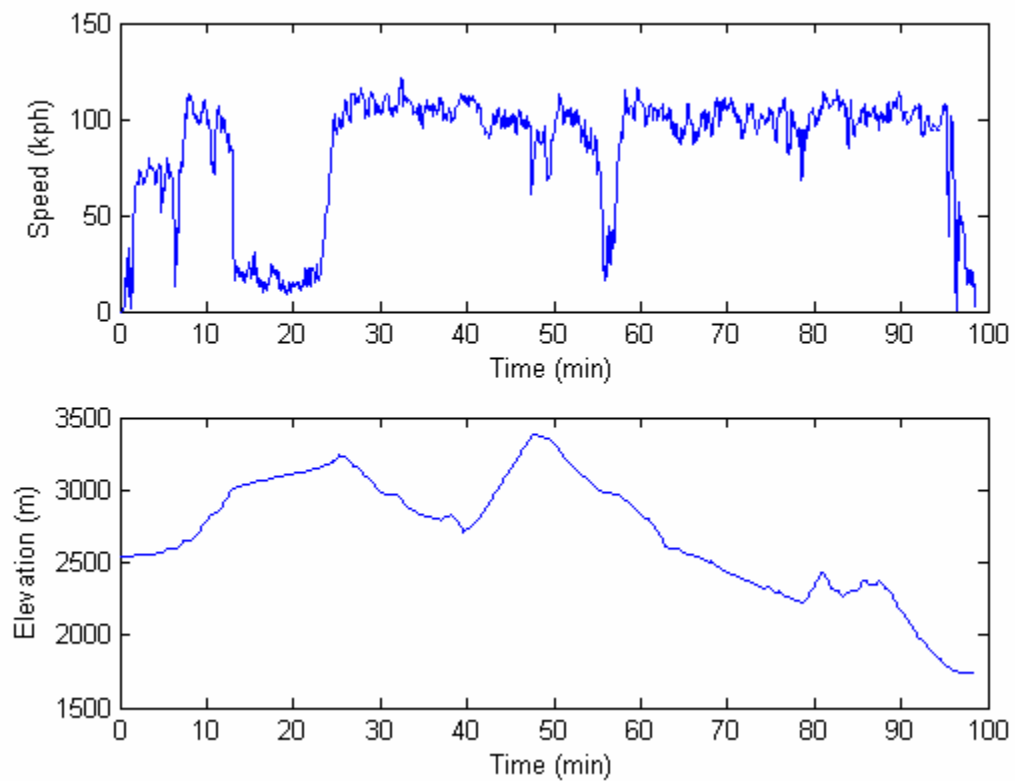


Fig. 149: Speed and elevation profiles, NREL drive cycle

Standard FTP drive cycles do not allow demonstrating the performance gains conferred by the integrated brake in situations where regenerative braking is unavailable. Furthermore, they do not allow demonstrating the ability of the integrated brake to handle braking in downhill driving situation. A drive cycle including steep downhill portions is required. Advisor ® includes a drive cycle called “NREL” recorded between Vail, Colorado and the National Renewable Energy Laboratory in Golden, Colorado. It includes very wide variations of elevation. The speed and elevation profiles are shown on Fig. 149. This drive cycle is a good candidate for testing the eddy-current brake in downhill driving situations.

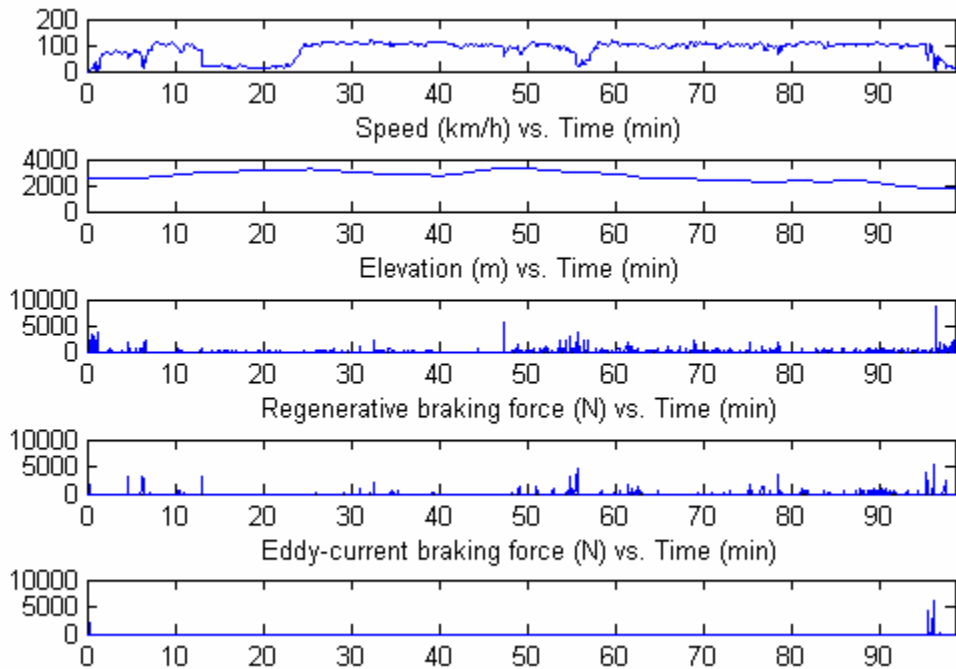


Fig. 150: Braking force distribution, NREL drive cycle

The braking force distribution is plot on Fig. 150. Despite high decelerations and steep downhill grades, the NREL drive cycle only rarely requires the use of friction brakes. This simulation therefore demonstrates the superiority of integrated brakes over friction brakes. They reduce the wear of the pads to a marginal value.

Fig. 151 shows that eddy-current brakes are applied more often during downhill driving. This is because a lot of energy is recovered by regenerative braking during downhill driving. Consequently, the battery is recharged very quickly and regenerative braking is no longer available. Therefore, eddy-current braking has to take the relay.

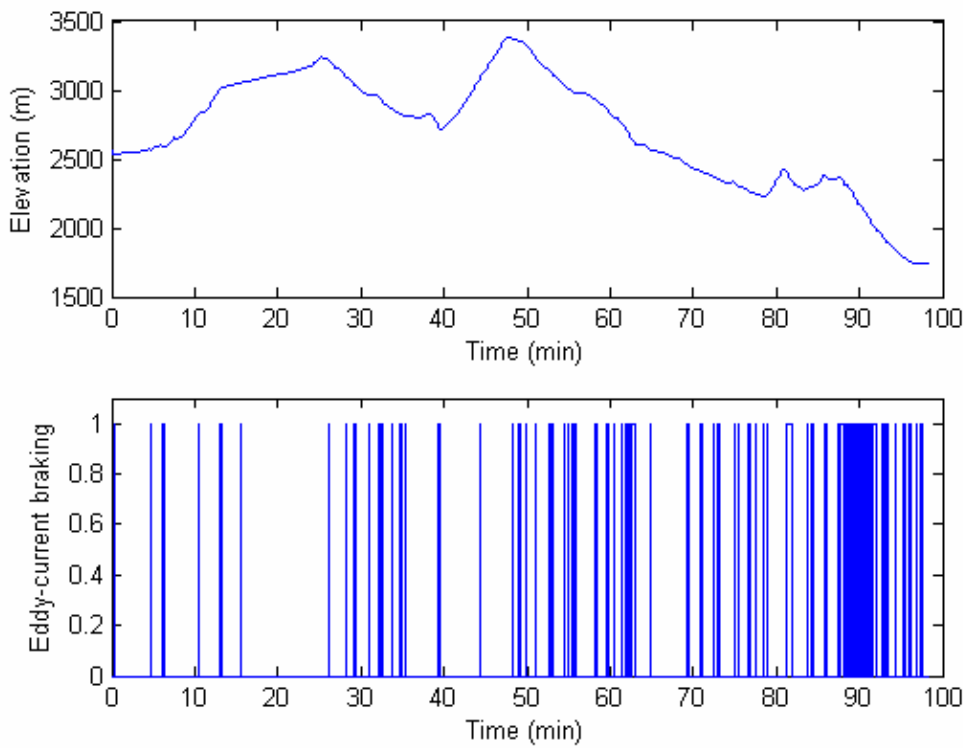


Fig. 151: Occurrence of eddy-current braking

Fig. 152 shows the cumulative energy dissipated by the eddy-current brake over the NREL drive cycle. It appears clearly that not only are eddy-current brakes applied more often during downhill driving, but they also generate greater braking forces and dissipate much more kinetic energy.

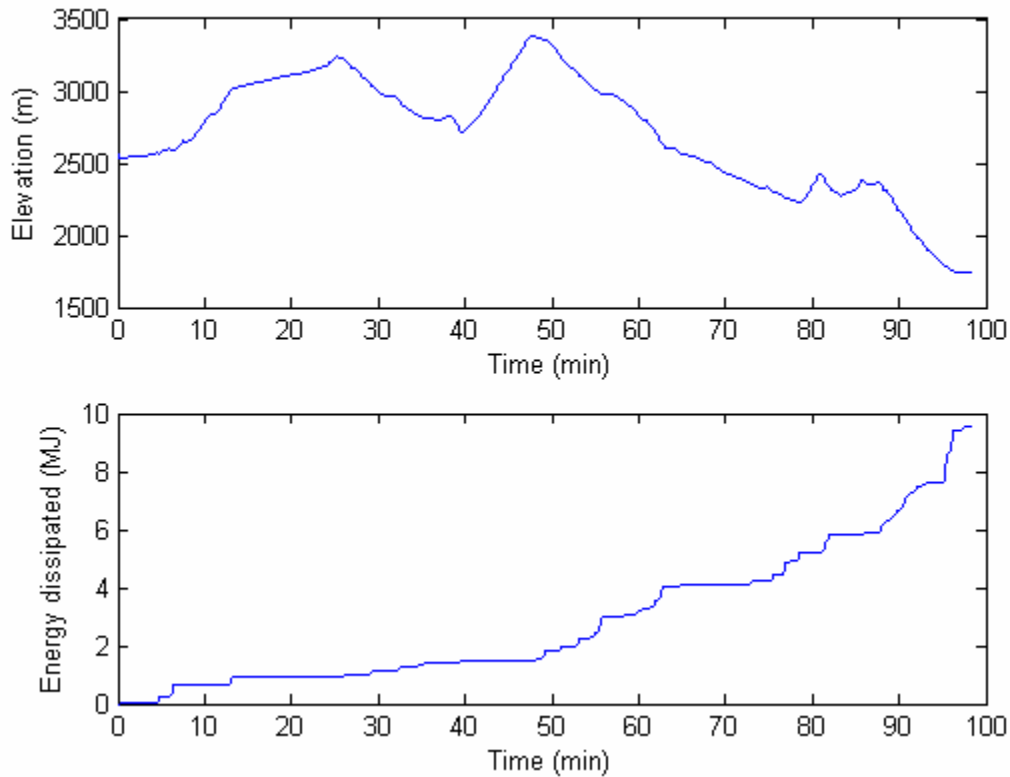


Fig. 152: Cumulative energy dissipated by eddy-current braking

The temperature profile of the integrated brake rotor is shown on Fig. 153. Obviously, the temperature rises more sharply during downhill driving than otherwise. It is

interesting to note that the maximum temperature reached by the rotor is 163°C. This is very close to the temperature reached by the same rotor over the FTP 75 Urban drive cycle in a conventional vehicle. The conclusion is that the combination of regenerative and integrated brakes renders fast, downhill braking no more challenging than urban driving. Although more energy is dissipated than in urban driving, the higher average speed results in better cooling of the brakes.

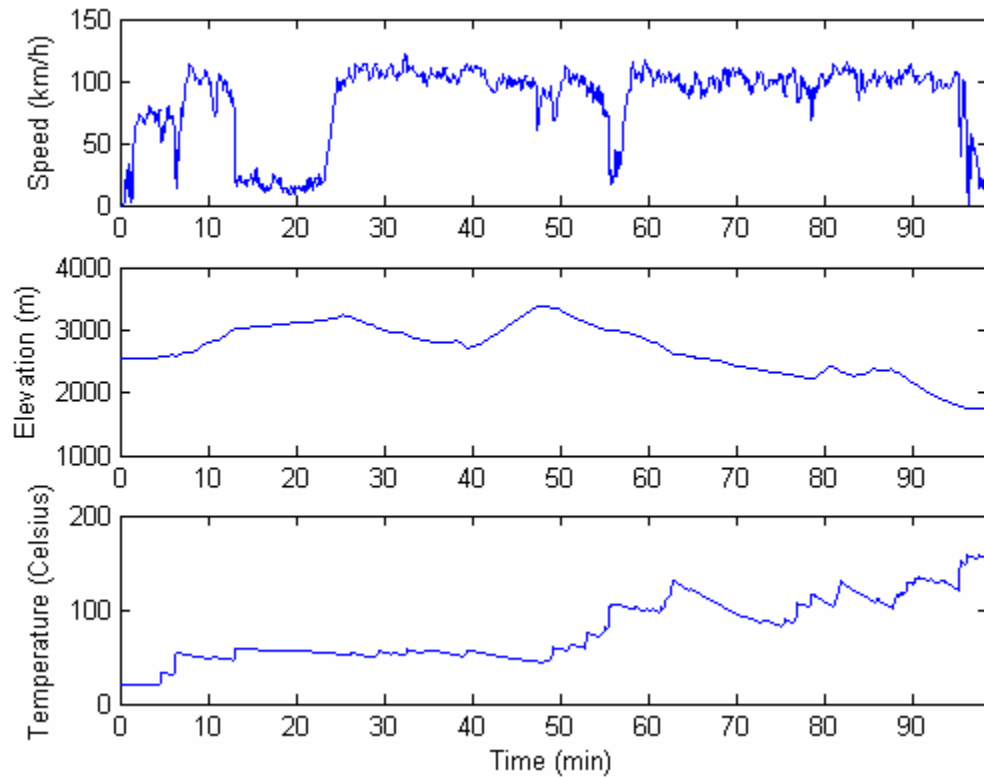


Fig. 153: Speed, elevation and brake temperature profile

Fig. 154 shows the detail of a situation where the battery is fully charged and braking is required. Regenerative braking provides all of the braking force until the state of charge reaches its maximum allowable value (0.6). Then the braking controller switches all of the braking force from the regenerative brake to the eddy-current brake. The braking controller must be carefully designed to take into account the dynamics of the system as a whole. The event that triggers the switch is the battery state of charge reaching its maximum value. If the value is below 1.0, then a slight overshoot may be tolerated. But if it is 1.0, then an overcharge may be destructive to the battery or ultracapacitor. Therefore, the regenerative brake must be turned off very quickly upon the state of charge reaching its maximum allowable value. However, the total braking force must not be allowed to drop significantly at any moment below the value commanded by the driver. It is thus important to compensate for the reaction time of the eddy-current brake when designing the brake controller.

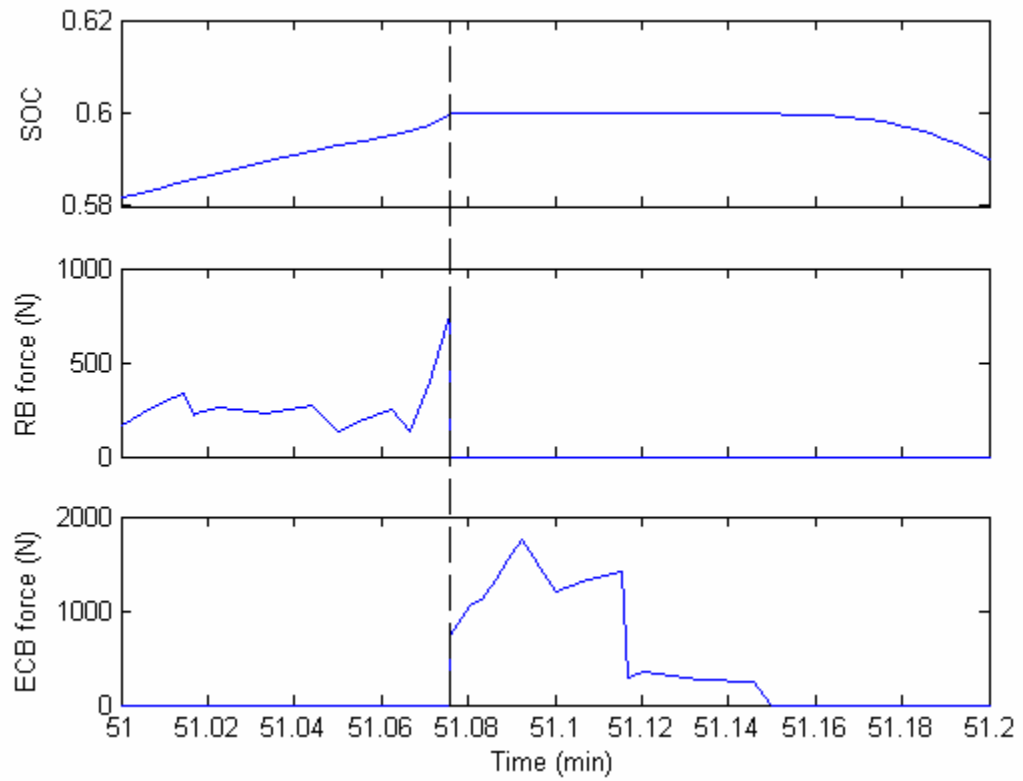


Fig. 154: Switching between regenerative and eddy-current braking

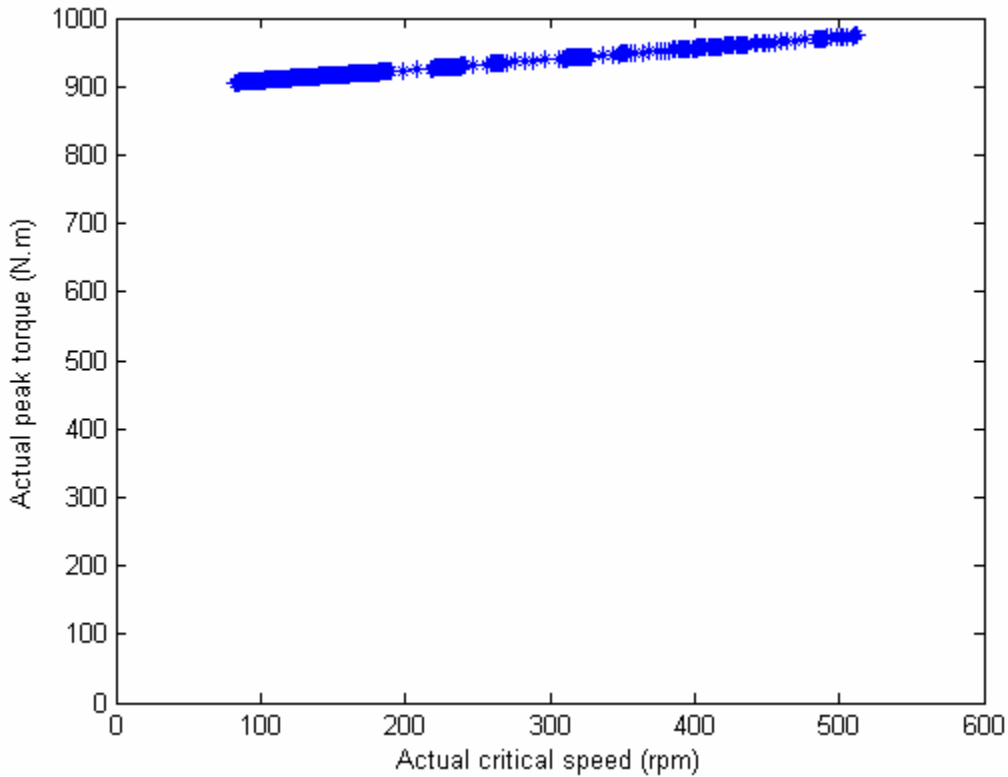


Fig. 155: Drift of critical speed and peak torque, NREL drive cycle

Fig. 155 shows the locus of critical speed and peak torque over the NREL drive cycle. The peak torque shifts more than it does over the standard FTP drive cycles but the variation is still small. The critical speed varies widely but this does not degrade the performance because the brake is designed to provide much greater braking forces than are required by the NREL drive cycle. Fig. 155 demonstrates the large difference between the brake design and the actual operating points.

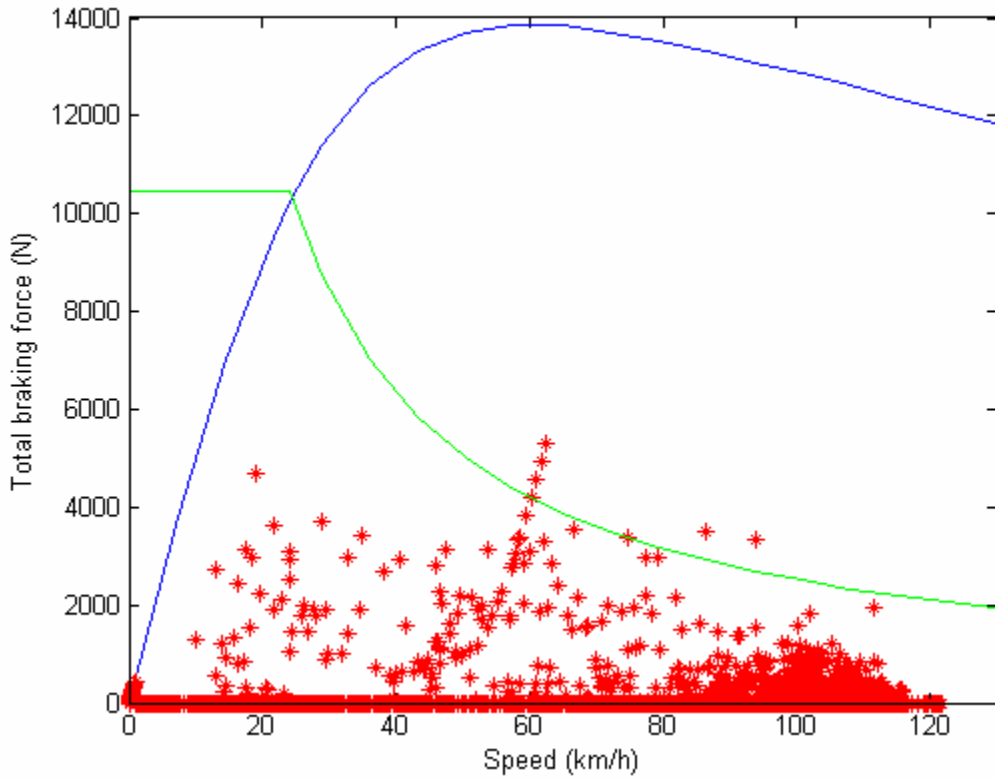


Fig. 156: Eddy-current braking force points against maximum braking force curve

Fig. 156 shows the operating points of the braking system against the force-speed curves of the regenerative and eddy-current brakes. Although some points are outside of the force-speed curve, this does not necessarily mean that the eddy-current brake cannot actually operate at these values.

Fig. 157 shows the eddy-current brake operating points against the torque-speed curve of a warm brake. The curve corresponds to the hottest brake, while the outside points may have been required when the brake was colder and therefore capable of a higher braking

torque at that speed. This is what the plot of braking force distribution on Fig. 150 demonstrates. The friction brake is needed only sparingly to compensate for the inability of the eddy-current brake to provide the necessary braking force.

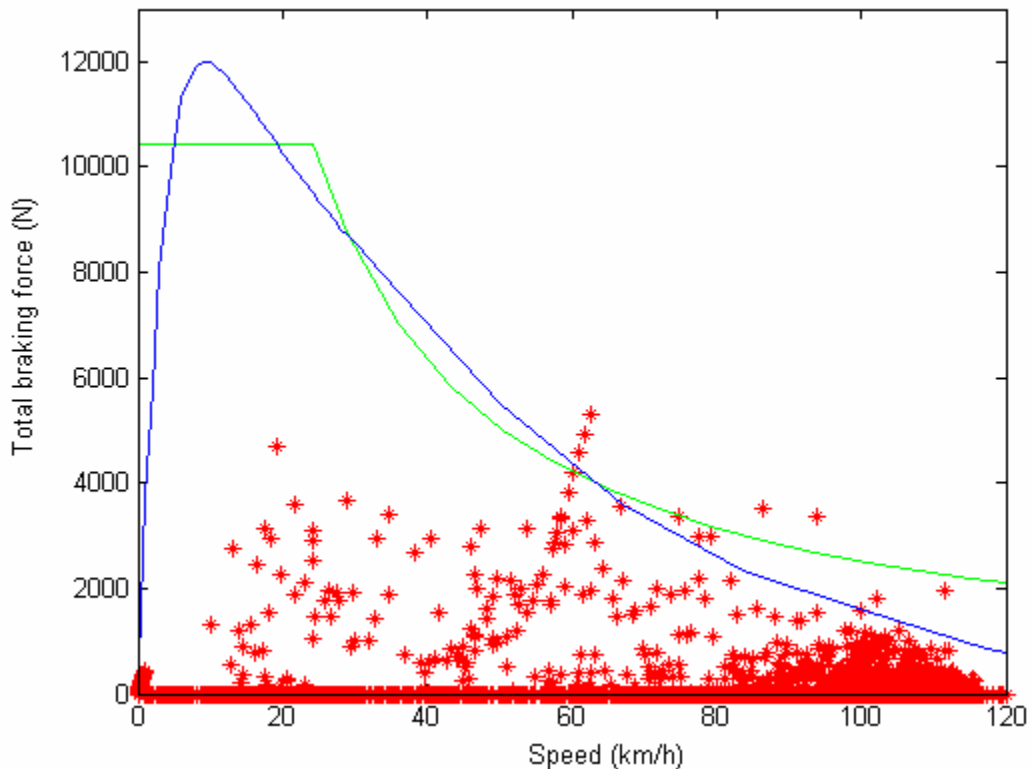


Fig. 157: Eddy-current braking force points against warm brake force-speed curve

TABLE 20 shows the braking energies handled by different braking systems for conventional, series hybrid vehicle without eddy-current brakes and series hybrid vehicles with eddy-current brakes. Compared to a conventional vehicle, the use of eddy-current brakes on a series hybrid vehicle reduces the wear by 95.5%. Compared to a

series hybrid vehicle, the wear is reduced by 91.7%. Indeed, wear is proportional to the energy dissipated by friction.

TABLE 20
Kinetic energy balance, NREL drive cycle

	Conventional w/o ECB	Series hybrid w/o ECB	Series hybrid w/ ECB
Energy regenerated	0	7.76 MJ	7.76 MJ
Energy dissipated, eddy-current brake	0	0	8.29 MJ
Energy dissipated, friction brake	16.8 MJ	9.04 MJ	0.75 MJ

2.5 – Impact of temperature on braking performance

There is a significant drift of the critical speed due to temperature. The average critical speed is 388rpm, compared to the design critical speed of 515rpm. However, this drift does not affect performance significantly because the eddy-current brake is used at a fraction of its rated performance. There is only one occurrence of a low critical speed limiting the performance during a heavy downhill braking at the end of the NREL drive cycle. Increasing the design critical speed above 515rpm to adjust the average critical speed around 515rpm will not reduce noticeably the wear of friction brakes because braking performance is very insensitive to critical speed.

It is important to note that the calculations in this chapter were performed with a very simple thermal model for the eddy-current brake. Obviously, a more realistic model is

required to accurately model the performance of the integrated brake. However, taking into account thermal effects in eddy-current brakes is extremely complicated [43]. Heat generation occurs primarily in the immediate proximity of the surface of the rotor, but other significant heat generation spots exist elsewhere in the rotor. Heat dissipation occurs everywhere with different mechanisms: conduction with the hub, convection everywhere but primarily on the inner surface and the fins of the rotor, and radiation everywhere but primarily within the airgap and the outer edge of the rotor. Temperature impacts the conductivity of the disc, the relative permeability and the saturation magnetization, which in turn have a significant impact on performance. The difficulty comes from the cross coupling between the thermal and electromagnetic phenomena. Furthermore, at high temperature the deformation of the disc under the normal force induced by eddy-currents becomes significant and alters the effective width of the airgap. Analyzing the eddy-current brake is thus a tri-disciplinary problem. Such an analysis is beyond the scope of the present research.

2.6 – Impact of eddy-current braking on friction brake wear

The eddy-current component of the integrated brake reduces very significantly the use of friction brakes in all driving situations, for both conventional and hybrid vehicles. TABLE 21 summarizes the reduction in friction brake kinetic energy dissipation achieved through the use of eddy-current braking compared to vehicles not using eddy-current braking at all.

TABLE 21
Reduction of friction brake kinetic energy dissipation

Drivetrain	Drive cycle	Reduction
Conventional	FTP 75 Urban	100%
Conventional	FTP 75 Highway	100%
Series HEV	FTP 75 Urban	100%
Series HEV	FTP 75 Urban	100%
Series HEV	NREL	91.7%

Friction between two materials pressed together occurs because of three phenomena [51]:

- Elastic hysteresis: The two surfaces pressed in contact are not perfectly smooth and present bumps and asperities. The bumps in one material force the other material to deform under the pressure. As the bumps travel during motion, the other material returns to its initial position with a delay. This delay results in a hysteretic loss of energy at the microscopic level and to a friction force at the macroscopic level.
- Plastic deformation: The pressure exerted on the two materials is not constant over the contact surface because of the unevenness of the materials. There is a local concentration of constraints around the bumps. The local constraint may exceed the limit of elastic deformation and thus induce permanent deformation of the material. This plastic deformation results in a loss of energy, which is akin to a friction force at the macroscopic level.
- Fracture and creation of new surfaces: This is the phenomenon responsible for wear. This particular form of wear is referred to as abrasive wear. It occurs

because of the bumps and ridges in one material scrape material from the other surface as they move under pressure.

Only a fraction of the friction force actually results in wear of the rubbing materials. Several models exist for abrasive wear. A simple model considers a cone on one material removing material from the material it is rubbed against. The volume of material removed is written as:

$$dV = a \cdot h \cdot dL \quad (133)$$

dL is the length traversed by the cone, a is the radius of the base surface of the cone and h is the height of the cone. The assumption is that the whole height of the cone is indenting the other material. θ is the semi-apex angle of the cone:

$$dV = \frac{a^2 \cdot dL}{\tan(\theta)} \quad (134)$$

The reaction from the material being ploughed through applies only to half the base area of the cone. If dN is the normal load on the cone and H is the hardness of the material being abraded, then:

$$\frac{1}{2} \pi \cdot a^2 = \frac{dN}{H} \quad (135)$$

$$a^2 = \frac{2 \cdot dN}{\pi \cdot H} \quad (136)$$

By substituting () in ():

$$dV = \frac{2 \cdot dN \cdot dL}{\pi \cdot H \cdot \tan(\theta)} \quad (137)$$

The rate of abrasion of the material is thus:

$$\frac{dV}{dL} = \frac{2 \cdot dN}{\pi \cdot H \cdot \tan(\theta)} \quad (138)$$

The rate of wear of the materials is thus proportional to the normal load pressing them together. But the length indented is proportional to speed and time. Therefore, the time rate of wear is proportional to the normal load and speed integrated over time:

$$V \propto \int \frac{2 \cdot dN \cdot (\omega \cdot r)}{\pi \cdot H \cdot \tan(\theta)} \cdot dt \quad (139)$$

Wear is thus proportional to the kinetic energy dissipated. Wear is nonexistent for both urban and highway drive cycles regardless of the drivetrain. In the NREL drive cycle, the reduction is very significant, of the order of 12 to 1. This is despite the fact that a mountain drive cycle is naturally very demanding for the braking system.

2.7 – Power assistance energy consumption of integrated brake

The reduction in power assistance consumption is difficult to estimate. While the normal effort on the pads can be estimated fairly easily, the consumption of the actuator itself depends heavily on its technology. It is worthwhile noting that a vacuum assistance mechanism cannot be used for the integrated brake because it does not lend itself very well to electronic control. A hydraulic pump could be used but would still result in a waste of energy when the friction brakes are not required. It is easy to see on the braking effort plots that friction brakes are not used very often. The waste would thus be

consequent. It would be more beneficial to use electric actuators that are energized only when friction brakes are required. The saving would be much more significant.

2.8 – Anti-lock control of the integrated brake

Intuition dictates that eddy-current brakes are inherently immune from wheel-lock because they produce no braking torque at zero-speed. The idea is that if the eddy-current braking torque exceeds the tire's adhesive limit, then the wheel will slow down, consequently decreasing the braking torque until it no longer exceeds the tire's adhesive limit. However, physics dictate otherwise. The Newton equation for the wheel explains why:

$$J_{\text{wheel}} \frac{d\omega}{dt} = F_{\text{ground}} \cdot r_{\text{wheel}} - T_{\text{braking}} \quad (140)$$

If the braking force is below the tire's adhesive limit, then the braking force is fully transmitted to the ground and there is no acceleration of the wheel with respect to the ground speed (i.e. vehicle speed). If the braking force exceeds the tire's adhesive limit, there will be a negative force difference, which will decelerate the wheel with respect to the ground speed. This is when the tire starts slipping. At this point there are two cases to consider:

- The initial speed is below the eddy-current brake's critical speed: As the wheel decelerates, the braking force decreases until it matches the tire adhesive limit. Then it stops decelerating but maintains its speed differential with the ground. The

tire is still slipping and the driver has no longitudinal or directional control over the vehicle.

- The initial speed is above the eddy-current brake's critical speed: As the wheel decelerates, the braking force increases thereby increasing the deceleration rate of the wheel. When the speed finally goes below critical the process is the same as for the first case.

As long as the tire is slipping the force transmitted to the ground is strictly limited to the tire's adhesive limit. Fig. 158 shows the wheel and ground speeds (normalized to linear speeds) for a vehicle braked by an eddy-current brake with a braking force superior to its tire's adhesive limit. The initial speed is below the critical speed. Note that when the ground speed finally matches the wheel speed, this latter catches and the slippage phase ends. This happens when the ground speed results in a braking torque that no longer exceeds the tire's adhesive limit.

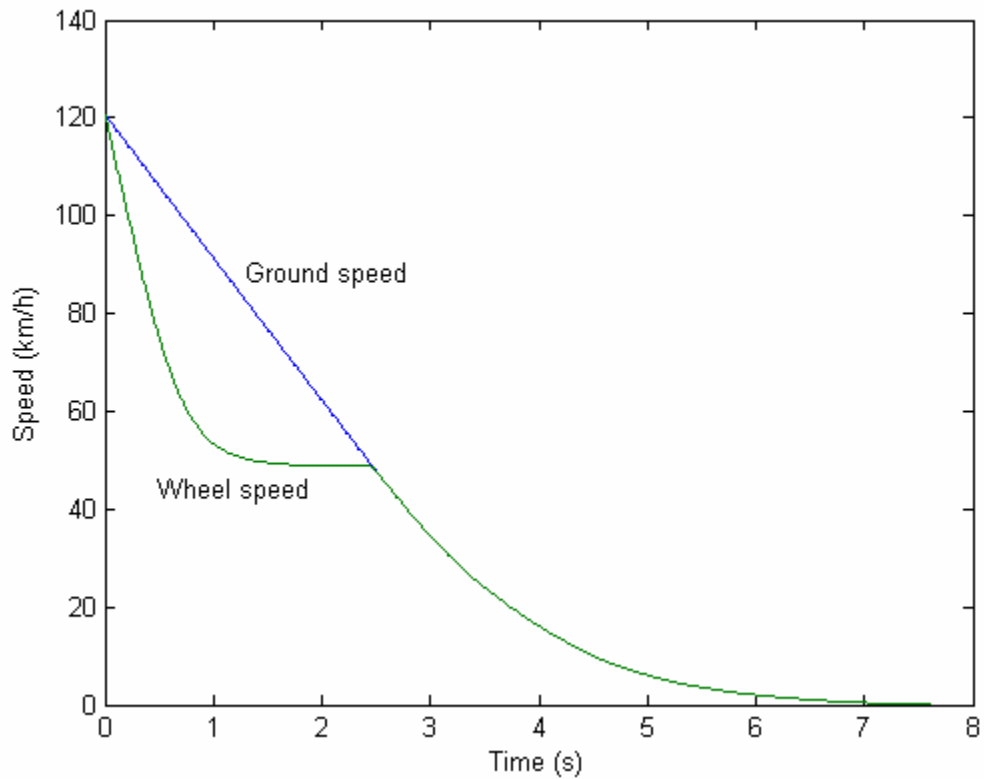


Fig. 158: Wheel and ground speeds, initial speed below critical speed

Fig. 159 shows the forces acting on the wheel throughout the deceleration.

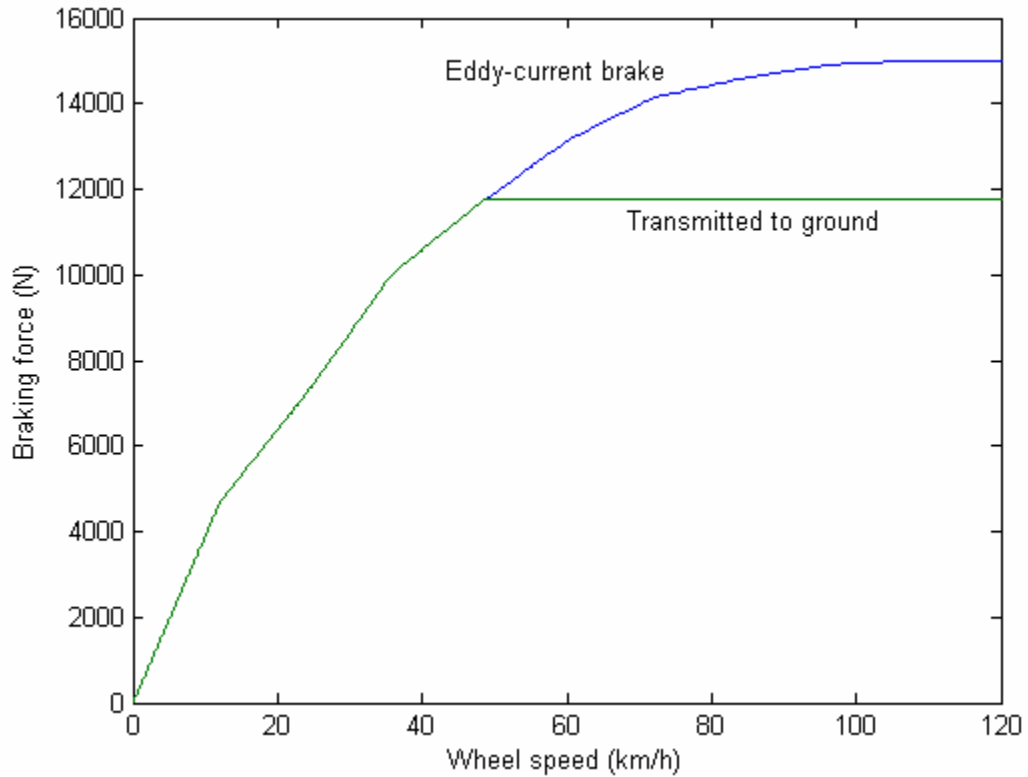


Fig. 159: Forces on a slipping wheel

Fig. 160 shows the wheel and ground speeds when the initial speed is above the critical speed. Note that the deceleration of the wheel is much more sudden than when the initial speed was below the critical speed.

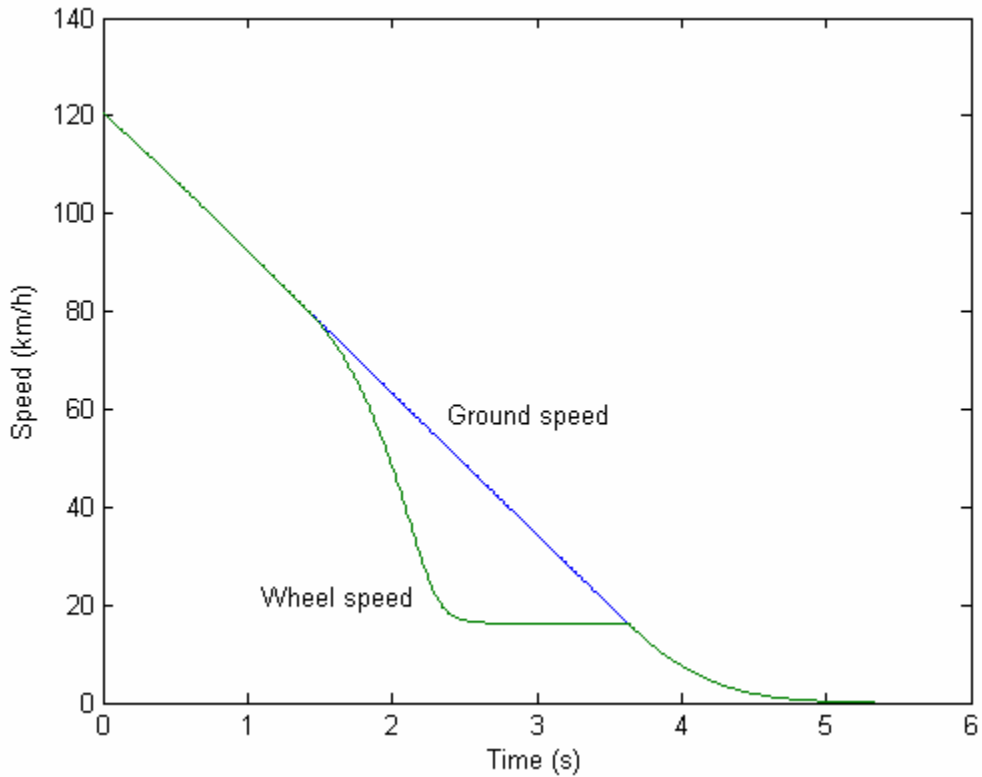


Fig. 160: Ground and wheel speeds, initial speed above critical speed

Because it is not inherently immune to wheel-lock, the eddy-current brake must be controlled to implement the anti-wheel lock function. The implementation is straightforward because of the electrical actuation of the eddy-current brake. Fig. 161 shows how minimal the difference in speed between the wheel and the road is 67 milliseconds after slipping has begun. This demonstrates that a reaction time of 67 milliseconds for the brake is not detrimental to anti-lock control performance because the inertia of the wheel prevents a large speed difference to build up. In the particular

case study shown, at the vehicle's maximum legal speed (75mph) and after 67 milliseconds the wheel speed only decreased to 98.9% of the road speed.

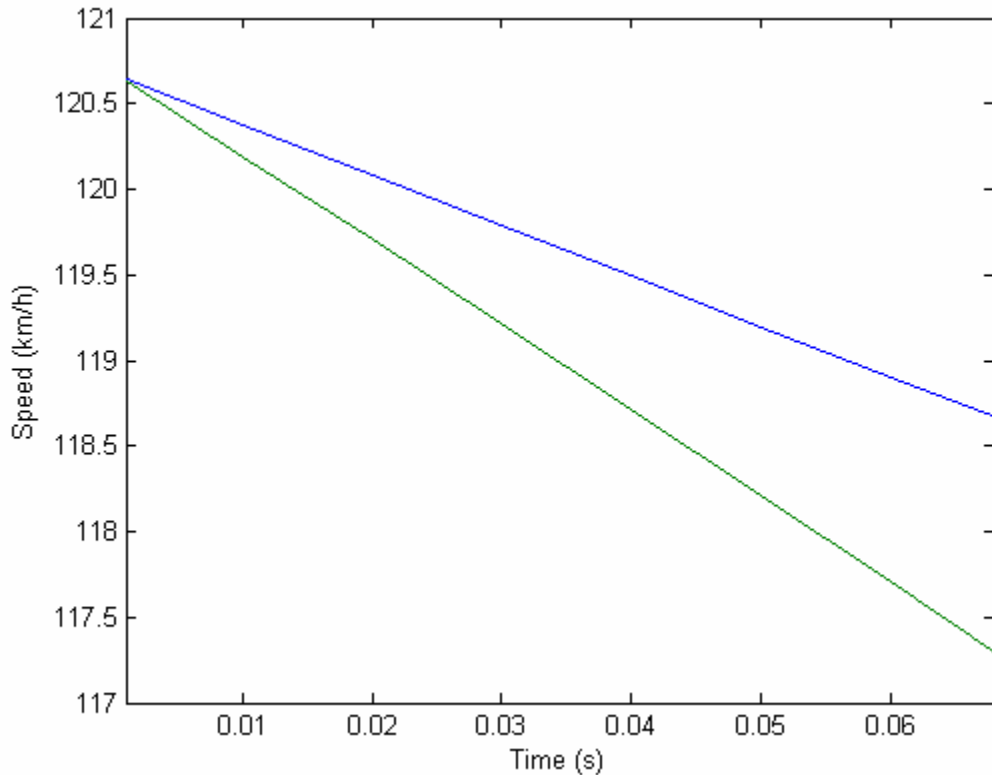


Fig. 161: Ground and wheel speeds after 67ms, initial speed below critical speed

2.9 – Traction control with the integrated brake

Traction control is a driving-aid function that limits the torque transmitted to the road in order to prevent wheel-slipage during acceleration. The control system traditionally acts on two engine variables: ignition timing and fuel flow rate. If the spark ignites the

fuel in the cylinder before this later reaches the optimal point, the flame front will hit the piston as it is still ascending in the cylinder, thus opposing its motion and reducing the engine torque. However, this mode of operation is destructive for the engine. Consequently, the preferred mode of operation for traction control is ignition timing retardation. The fuel-air mixture is ignited after the piston has reached the optimum point. The flame front hits the piston as it has already begun traveling down the cylinder. This reduces the mean effective pressure on the piston and therefore the engine torque. Ignition timing can reduce the engine torque from maximum to zero in as little as one revolution of the crankshaft but it can severely reduce the fuel economy of the vehicle. Fuel flow rate control preserves the fuel economy of the vehicle but it is slower than ignition retardation. The reaction time of ignition retardation is a function of the speed of the crankshaft and ranges from 10ms (6000rpm) to 100ms (600rpm).

Applying the brakes can be an effective way of controlling the amount of engine torque applied through the tire-ground contact. Its major advantage is that it allows controlling the torque applied on each wheel independently, while ignition retardation and fuel flow rate control act on all driven wheels at the same time. It should be noted that eddy-current braking in traction control applications will however deteriorate the fuel economy of the vehicle. If the vehicle only occasionally slips during acceleration, then the penalty is tolerable. If the vehicle is driven on an extremely slippery surface such as snow or ice, where slipping is easily achieved, then the traction control should also rely

on fuel flow rate control because the overall traction force may exceed the maximum allowed by the adhesive contact.

If all driven wheels are slipping then energy is being wasted and fuel flow rate reduction is an effective way of limiting the waste and eliminating the slippage. However, one of the driven wheels is not slipping then reducing the fuel flow rate would decrease performance. It is thus more effective for the traction controller to actuate the brakes on the slipping wheels and to let the non slipping wheel(s) receive engine torque normally.

This mode of operation performs a function similar to a limited-slip differential. A differential gear is used to let the two wheels of an axle turn at different speeds in corners. The drawback is that it will allow one wheel to slip while the other receives no torque at all if one wheel is over a slippery surface. Various mechanisms (friction discs, Torsen differential) have been invented throughout the years to reduce or eliminate that problem but usually incur an increase in cost. The brakes are already present in a vehicle so their use for traction control incurs only additional software costs, which are much lower than hardware costs.

With friction brakes, reaction time and lack of proportionality of the response make it difficult to use brakes for traction control purposes. However, eddy-current brakes are easily controlled by electrical signals, have a broad dynamic range, a short reaction time,

and a proportional response to control inputs. They are thus ideally suited for application to traction control.

A traction control system using eddy-current braking would act based on the following control strategy: the control system monitors the speed of each driven wheel through individual speed sensors and the speed of the vehicle by the means of an accelerometer. Additional information such as yaw rate and steering angle are required to compute the actual ground speed for each wheel. When the wheel speed exceeds the ground speed, the traction control intervenes by actuating the eddy-current brake on the slipping wheel. The braking torque counters the excess of torque and slows the wheel down until it matches the ground speed. When the wheel and ground speeds match again, the traction controller maintains enough eddy-current braking torque until the driver lifts off the throttle or until the ground traction condition improve or until it has reduced the fuel flow rate.

2.10 – Dynamic stability control with the integrated brake

Dynamic stability control systems control the yaw rate (rotation around the vertical axis) of a vehicle to and keep the vehicle on trajectory intended by the driver in case of changing adherence conditions and driver mistakes. The system is obviously limited by the laws of physics and will not compensate for a gross overestimation of adherence.

Fig. 162 shows how a dynamic stability control system compensates for yaw when the two front wheels hit a slipper surface.

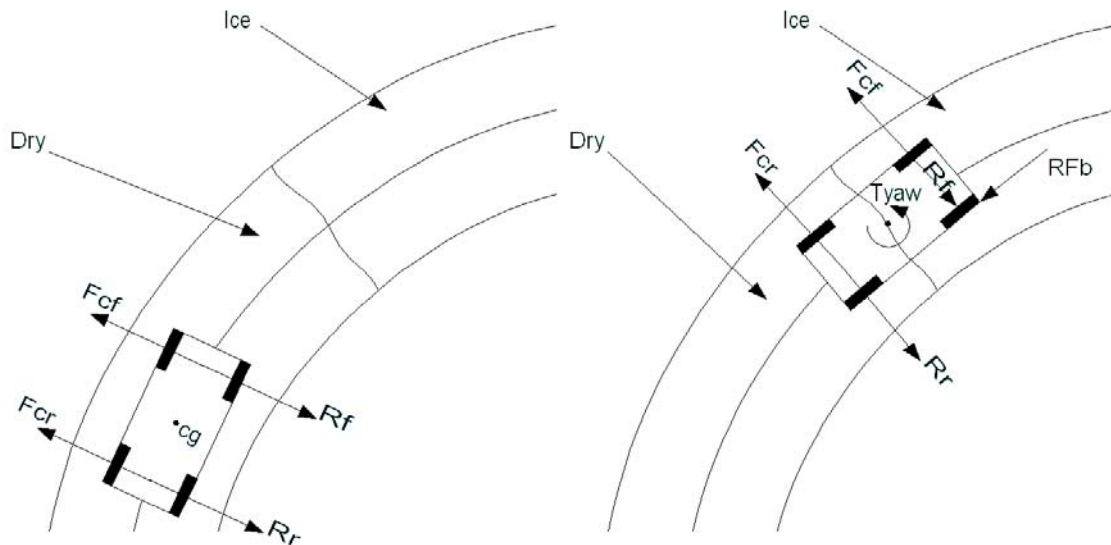


Fig. 162: Dynamic stability control principle

When all four wheels are on dry pavement, the reaction of the ground (R_r and R_f) compensates for the centrifugal forces on each axle (F_{cr} and F_{cf}). No yaw torque is induced. When the front axle hits snow, the ground reaction on the front tires suddenly diminishes, while the centrifugal force does not change. A net force results that tends to pull the front axle towards the exterior of the corner. The same force results in a yaw torque that tends to rotate the car around the vertical axis. The dynamic stability control system actuates the front right brake (RF_b), which creates a yaw torque that opposes the

torque generated by the force imbalance. Fig. 163 shows a more detailed diagram of the forces acting on the vehicle when the front axle meets a zero-adherence surface.

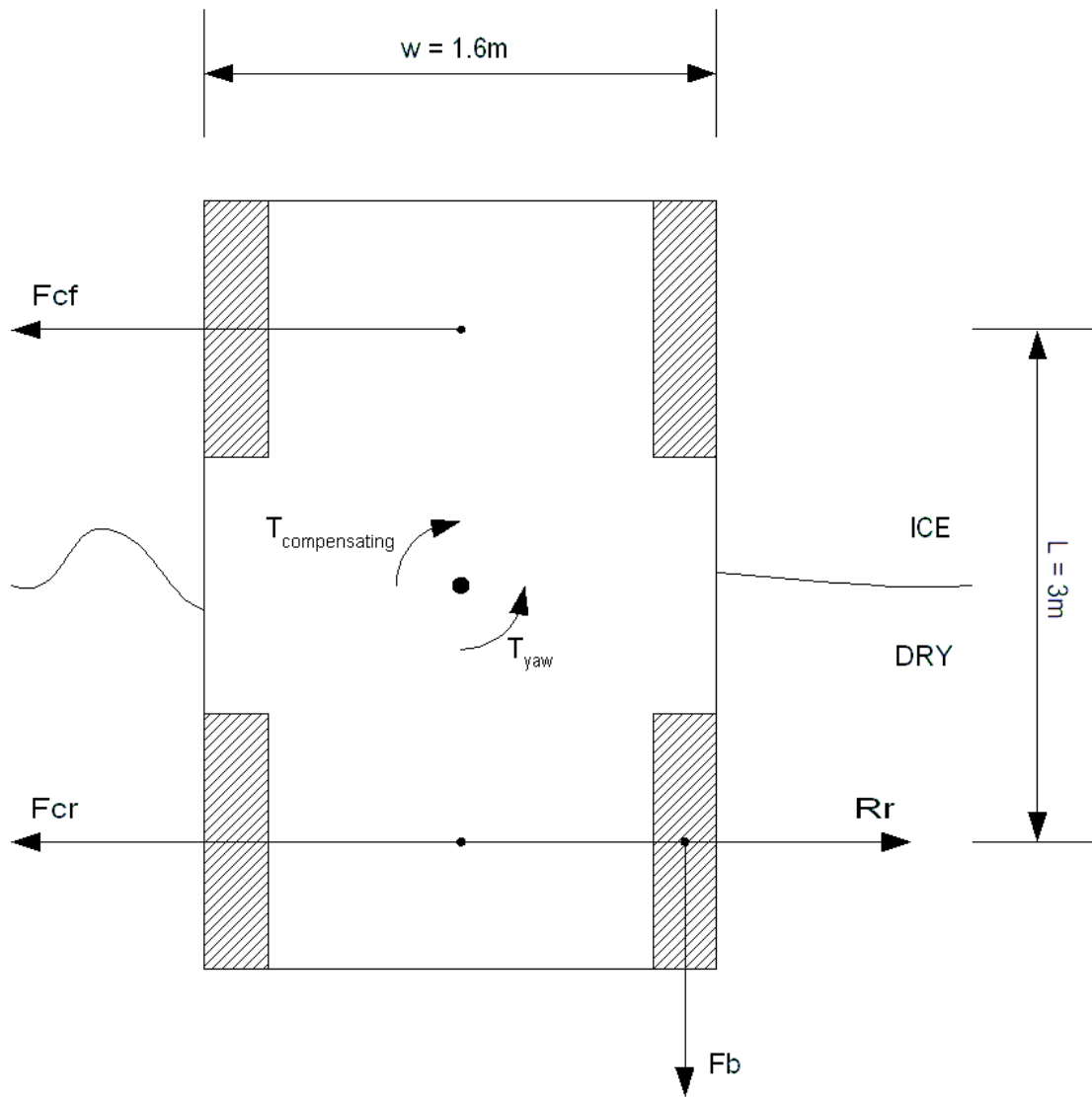


Fig. 163: Forces on a vehicle with the front axle on zero-adherence surface

Fig. 164 shows the yaw torque acting on a vehicle if one of the axles is on a zero-adherence surface and the other axle is on dry pavement. The yaw torque is plot versus the vehicle speed and the cornering radius. The lateral acceleration is limited by the adherence of the tires on dry pavement. This limit impacts the yaw torque and is reflected on the plot.

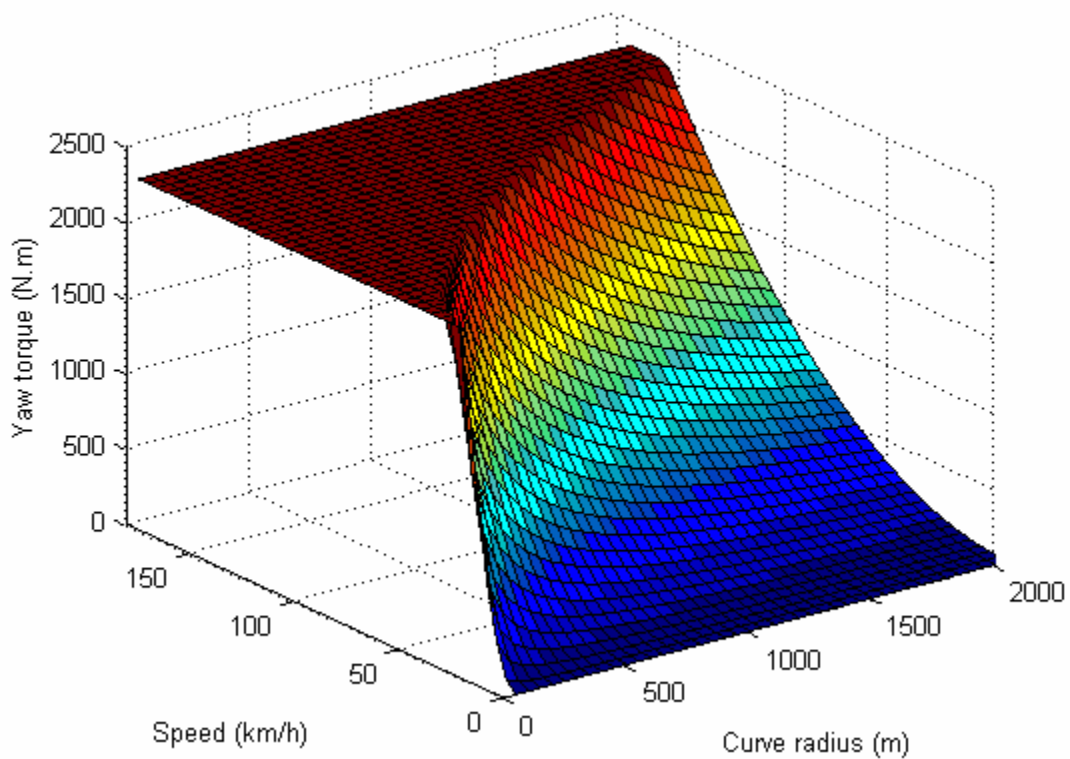


Fig. 164: Yaw torque on a vehicle with one axle on a zero-adherence surface

The dynamic stability control system compensates for the yaw torque by actuating the brake of the wheel on dry pavement on either side of the vehicle depending on the direction of the torque. The torques balance as follows:

$$F_{cf} \cdot \frac{L}{2} = F_b \cdot \frac{w}{2} \quad (141)$$

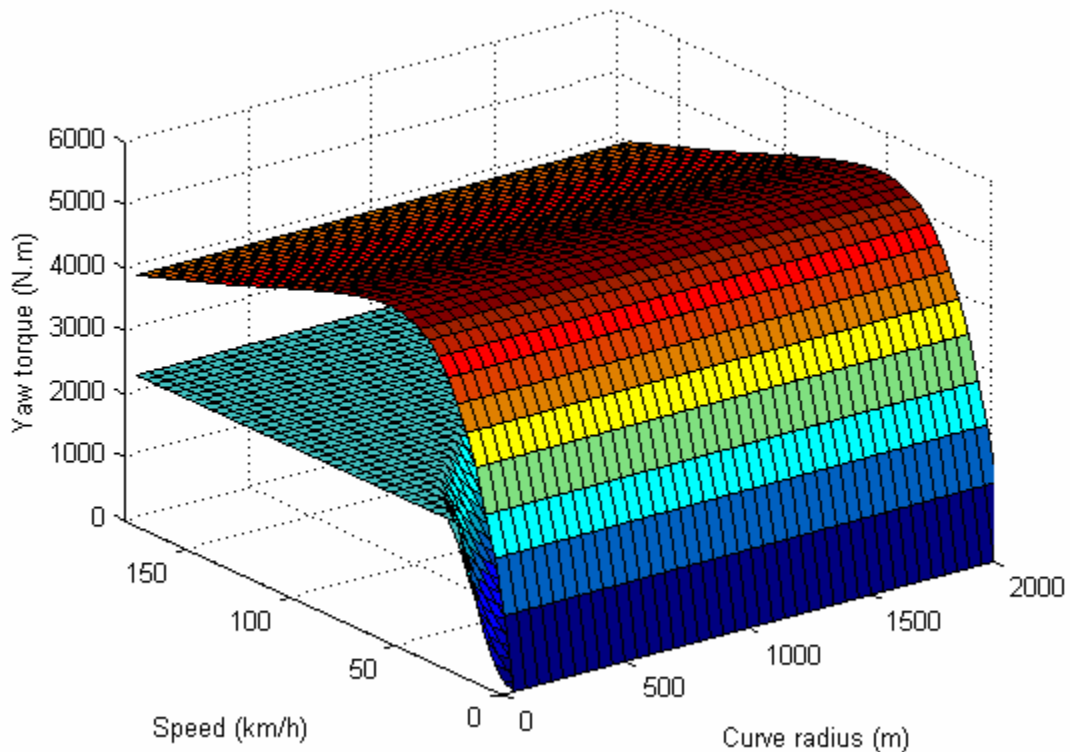


Fig. 165: Yaw torque and compensating torque, conceptual design

Fig. 165 shows the compensating torque generated by the conceptual brake plot versus the yaw torque. It shows that the conceptual brake is capable of compensating for the yaw torque induced by the axle on the snow at any speed and cornering radius, provided

that the lateral force is below the adhesive limit of the tires of the axle on dry pavement. Since the compensating torque exceeds greatly the yaw torque, the dynamic stability control system has enough dynamic range to steer the vehicle back onto the trajectory intended by the driver.

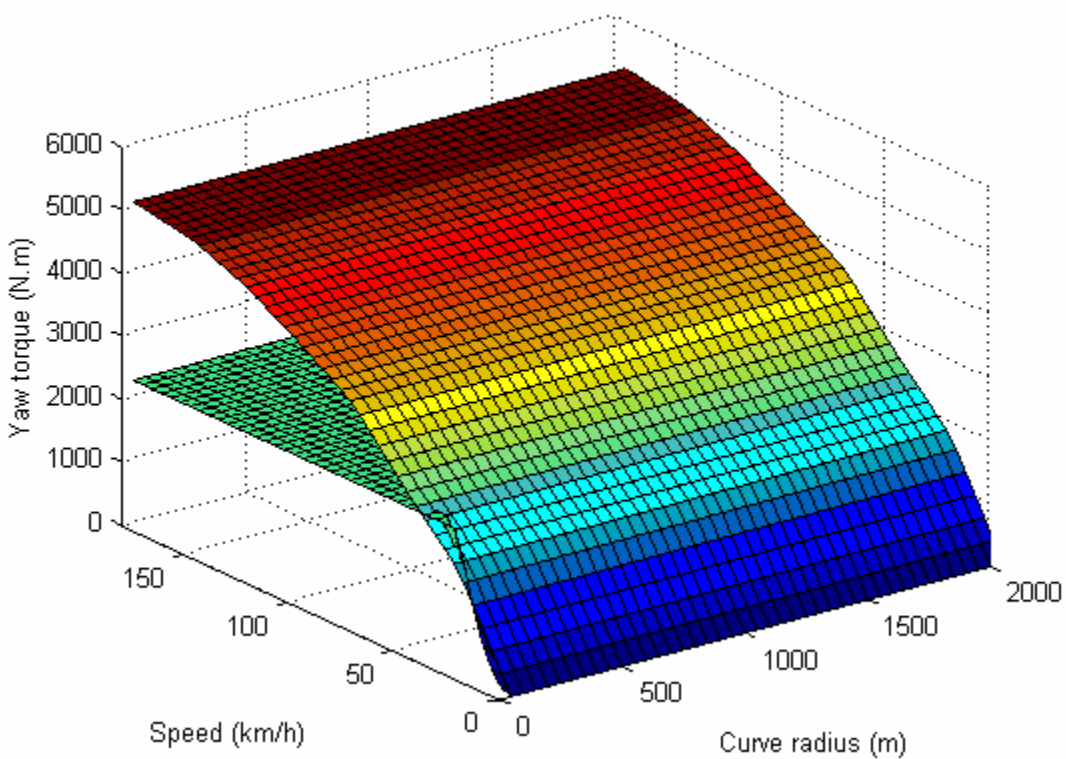


Fig. 166: Yaw torque and compensating torque, constrained critical speed

Fig. 166 shows the compensating torque generated by an eddy-current brake with a constrained critical speed (2000rpm) and the same peak torque as the conceptual brake. The compensating torque is greater than the yaw torque on the entire speed-radius range

except at very low speed and low radius. This is a region where the eddy-current brake produces only a low torque and where the lateral acceleration is large due to the low radius. The compensating torque is insufficient below 40km/h and below a 100m cornering radius. While the speed is low and the damages are limited in case of an accident, it is still desirable to provide the dynamic stability control system enough compensating torque to ensure the complete safety of the vehicle and its occupants. A 35% increase of the peak torque yields enough torque to allow compensating for yaw (see Fig. 167). There is however limited dynamic range at low speed to steer the vehicle back on the trajectory intended by the driver.

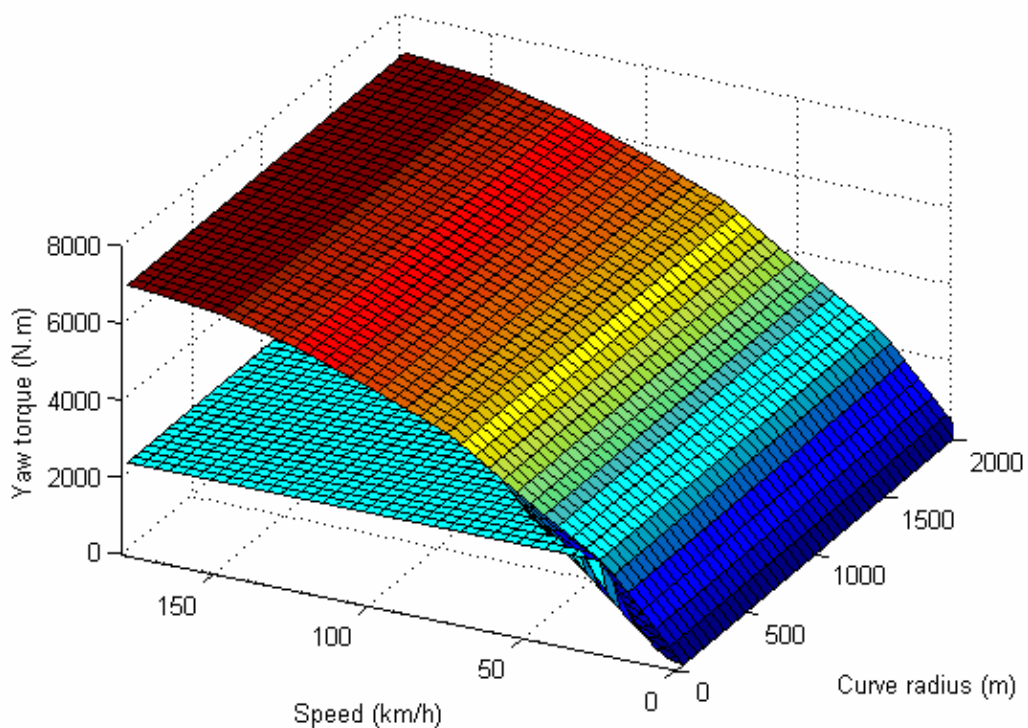


Fig. 167: Constrained critical speed and increased peak braking torque

The torque required to correct a deviation from the intended trajectory depends on the reaction time of the dynamic stability control system. If the control system is slow, then it will require a large force to bring the vehicle back on trajectory in a minimum time. On the contrary, if the system is fast, the control system compensates for yaw torque very quickly so the deviation from the intended trajectory is minimal. The vehicle can thus be steered back on trajectory with a minimal amount of force. The reaction time of the system depends on three factors: reaction time of control electronics, dynamics of the actuator, and dynamics of the braking torque in response to an excitation flux response. It is reasonable to assume that the control electronics will react in a period of time much shorter than the time constants of the actuator and brake. Control electronics can thus be assumed to be totally transparent. The actuator can be designed to react as fast as eddy-current braking. The reaction time of the dynamic stability control system thus ranges from 5ms to 20ms in the worst case scenario.

The deviation from the trajectory can be estimated easily. The vehicle hits the zero-adherence surface at time 0. The yaw torque steps up at that time as the front axle loses adherence completely:

$$T_{yaw}(t) = \frac{M}{2} \frac{V^2}{R} \frac{L}{2} u(t) \quad (142)$$

V is the speed of the vehicle, R is the cornering radius and L is the wheelbase of the vehicle. The rotational acceleration of the vehicle around the yaw axis is derived from the yaw torque expression:

$$\frac{d^2\theta_{yaw}(t)}{dt^2} = \frac{T_{yaw}(t)}{J} \quad (143)$$

J is the moment of inertia of the vehicle about the yaw axis. The yaw velocity and the yaw angle are obtained by integration:

$$\frac{d\theta_{yaw}(t)}{dt} = \int \frac{T_{yaw}(t)}{J} \cdot dt \quad (144)$$

$$\theta_{yaw}(t) = \int \int \frac{T_{yaw}(t)}{J} \cdot dt \quad (145)$$

The yaw velocity evolves linearly with time and the yaw angle evolves like the square value of time. This stresses the need for a fast reaction from either driver or control system.

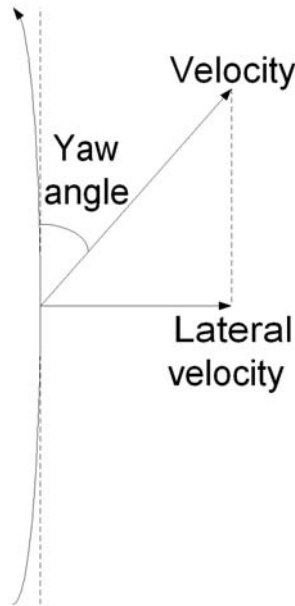


Fig. 168: Lateral velocity

Fig. 168 shows how the lateral velocity of the vehicle is computed from the yaw angle and vehicle velocity:

$$V_{lateral}(t) = V \cdot \sin(\theta_{yaw}(t)) \quad (146)$$

The lateral deviation from the trajectory is finally computed by integration:

$$\Delta L = \int_0^{T_{\max}} V_{lateral}(t) \cdot dt \quad (147)$$

A simulation is run for a vehicle having the parameters listed in TABLE 12 and the dimensions listed in TABLE 22.

TABLE 22
Chassis dimensions

PARAMETER	VALUE
Track width	1.6m
Wheel base	3m
Wheel radius	0.3m
Inertia momentum about yaw axis	1851 kg.m ²

Fig. 169 shows a plot of the lateral deviation from trajectory 1 second after the front axle has hit the zero-adherence surface. The deviation is very significant above 20km/h, and reaches values up to 10 meters at 180km/h. Such a deviation means a serious, deadly accident. The plot illustrates the extreme difficulty for a human driver to compensate for such an event and the need for a dynamic stability control system that can react much faster.

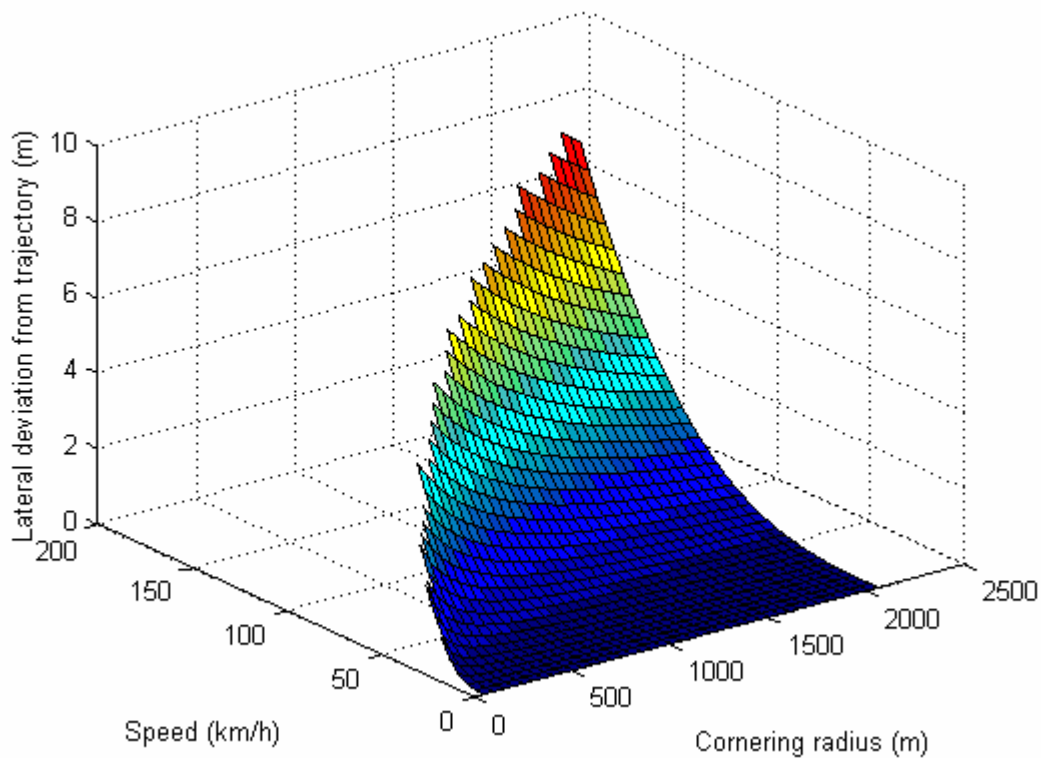


Fig. 169: Lateral deviation from trajectory after 1s

Fig. 170 shows the lateral deviation from trajectory after 67 milliseconds, which is the maximum reaction time of the actuator. The period of time is so small that the yaw angle has no time to widen significantly. The lateral velocity and lateral deviation are negligible at this point (less than 3 millimeters at 180km/h). If the dynamic stability control system did nothing but compensate for the yaw torque in 67 milliseconds, the deviation would imperceptible to the occupants and would not need to be compensated for. This greatly simplifies the dynamic stability control system that basically takes the

form of a yaw acceleration control loop. It also eliminates the need for a large excess of torque from the brake on top of the yaw torque to be compensated.

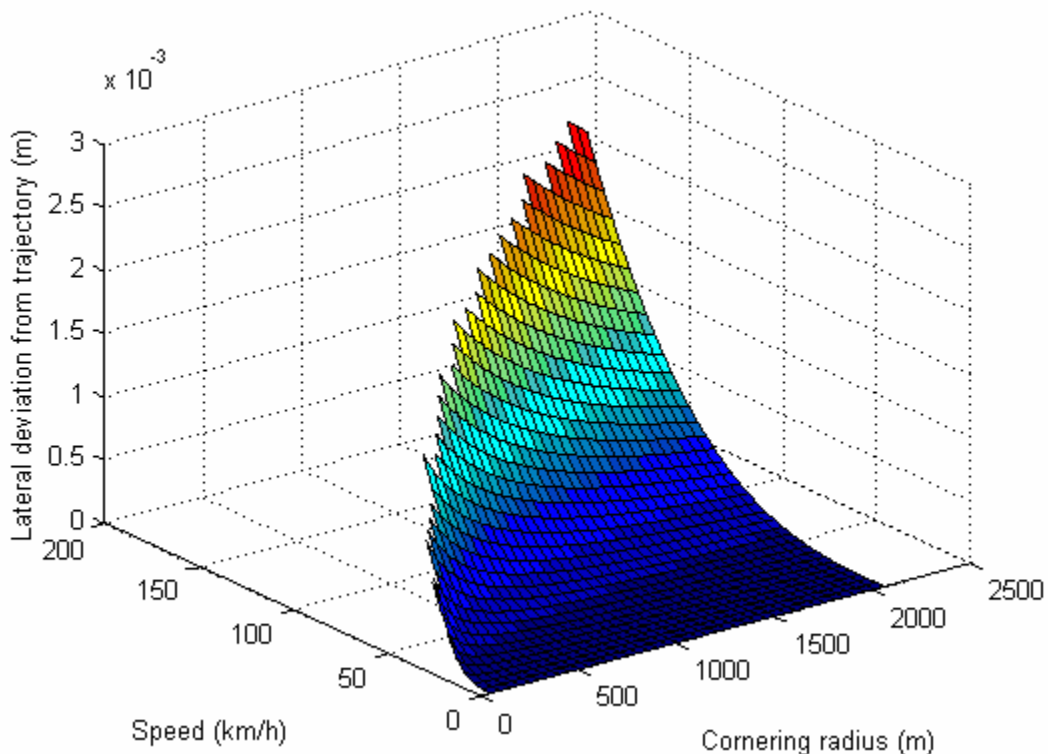


Fig. 170: Lateral deviation from trajectory after 67ms

It should be noted that the situation studied is an extreme situation and that studying it only provides an order of magnitude for the torques and time intervals involved. At any rate, a vehicle placing its front wheels on a zero-adherence surface at any speed would shortly after have all its wheels on that surface, and would irremediably run off of the

road. This illustrates one of the limitations of dynamic stability control: it cannot overcome the laws of physics.

3 – Integrated braking of heavy duty road vehicles

A potential application of the integrated brake is the replacement of electromagnetic retarders and other retarding mechanisms on heavy duty road vehicles such as commercial trucks and buses. In many countries, retarders are required by law on these vehicles to prevent from a catastrophe in case of a total failure of the friction brakes. The retarder acts as a secondary brake that can be engaged by the driver as needed.

3.1 – The integrated braking of commercial trucks and trailers

An electromagnetic retarder is installed on the driveshaft of the truck because the gear reduction in the differential (approximately 1:2.61, [52]) multiplies the braking torque approximately by the same ratio, which improves retarding performance greatly. The driveshaft spins at most at the speed of the engine unless there is an overdrive in the gearbox. Most commercial truck engines have a redline at up to 2,000rpm.

3.1.1 – Braking system architecture

TABLE 23
Renault Magnum commercial truck parameters

PARAMETER	VALUE
Vehicle mass	80,000 kg
Rolling resistance coefficient	0.015
Aerodynamic drag coefficient	1
Air density	1.25 kg.m ⁻³
Vehicle body frontal area	7.5 m ²
Wheel radius	0.45 m
Tire adhesion coefficient	0.8

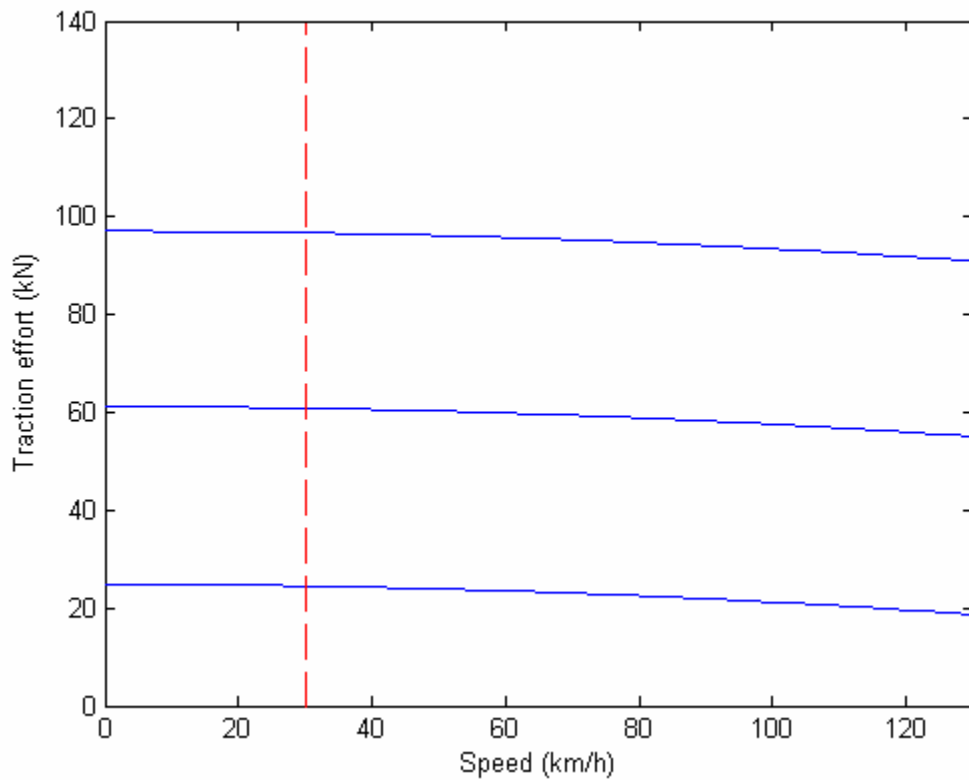


Fig. 171: Braking effort – speed vs. grade

Fig. 171 shows the braking effort – speed curves for an 80,000kg commercial truck comprising a tractor and a fully-loaded trailer [52] for various grades. TABLE 23 gives the parameters of the tractor and trailer ensemble. The design criterion for retarding mechanisms is the ability to hold the fully loaded vehicle at a constant speed in a given grade. European regulations require the retarder of a bus to maintain the vehicle at a maximum speed of 30km/h in a 14% grade. If the same criterion is used for a commercial truck, a braking effort of 96.71kN is required at the wheel. Given a wheel radius of 45cm and a final differential ratio of 1:2.61, the retarder has to provide a braking torque of 16,674N.m at a speed of 460rpm. This large figure needs to be related to the 3,300N.m that the largest TELMA retarder can provide [3]. Obviously, the TELMA is not designed to handle such heavy vehicles, but rather smaller trucks with a maximum gross mass of no more than 16,000kg.

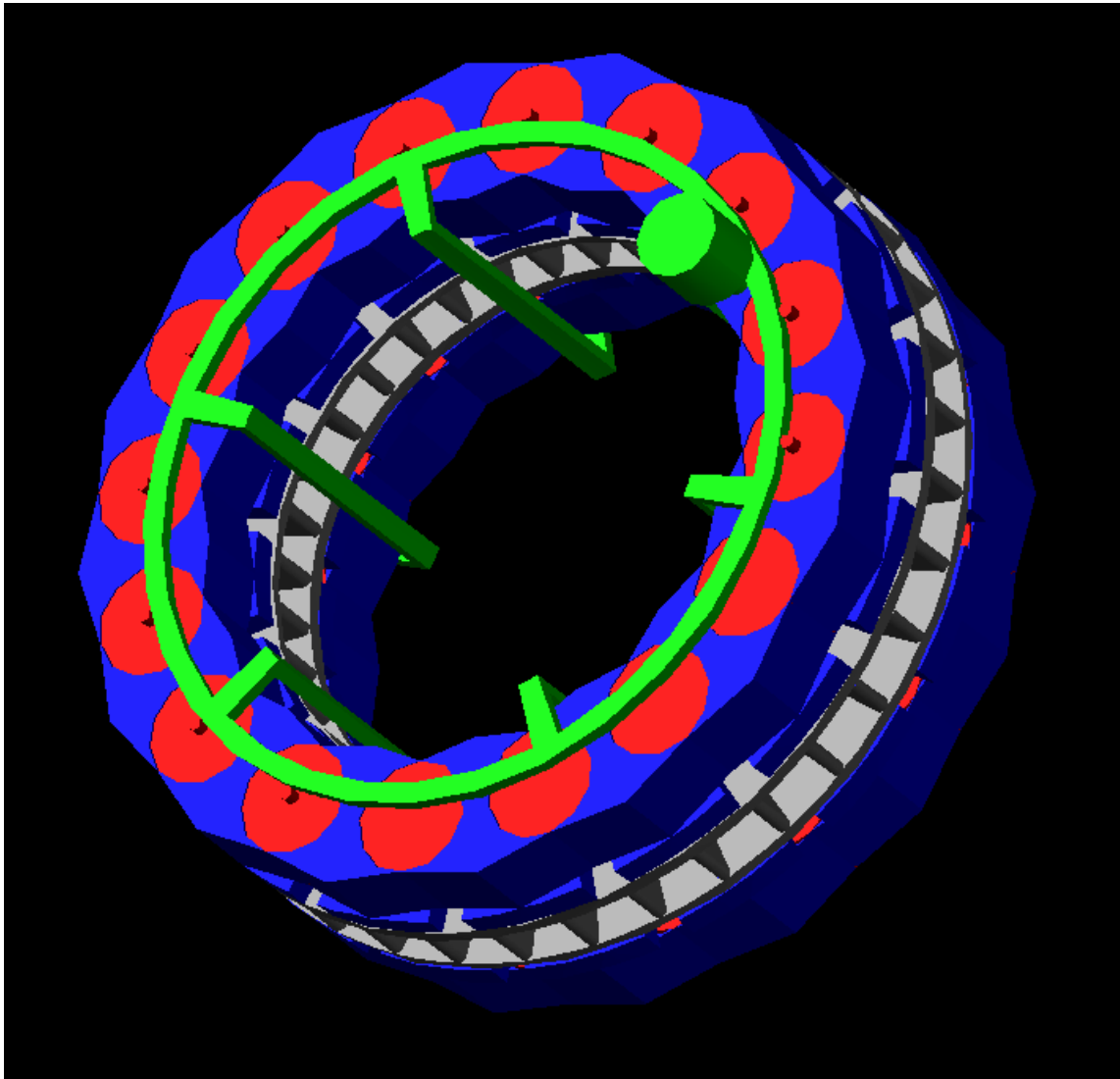


Fig. 172: Retarder design

A retarder can be built to handle such considerable braking effort on the base of the conceptual design given above for an automobile. The rotor is fully saturated and no appreciable increase in flux density can be achieved by using stronger magnets. The diameter of the rotor can be increased but only marginally due to space limitations in the chassis. The largest diameter of the TELMA retarders is 475mm, compared with 390mm

for the conceptual design. The peak torque may thus be increased by 48% through an increase of the diameter. The number of poles can also be increased to cover the whole circumference of the rotor (Fig. 172). The total number of poles would be 16 per side. With a diameter and pole number increase, the peak braking torque rises up to 2,306 N.m at 515rpm, which is close to the figures claimed by TELMA [3]. Adjustments to the pole pitches, airgap width and disc thickness are required to bring the critical speed to the 460rpm, which the driveshaft speed corresponding to a vehicle speed of 30km/h. The only way to increase the peak torque is to increase the number of rotors, which is equivalent to using several brakes. A total of 8 rotors would be required to exceed the required 16,674N.m of braking torque.

The heat dissipated by the brake would be 803kW, which is a lot of heat to be dissipated within the chassis of a vehicle. The temperature rise is probably more than some components can handle. Furthermore, an 8-rotor retarder would be a bulky and awkward machine to install in a chassis (Fig. 173). A better alternative would be to install a single rotor brake on each of the 6 wheels of the tractor and one twin-rotor brake on the driveshaft (Fig. 173). This would distribute the heat dissipation and would make the manufacturing and installation much easier.

An even better alternative would be to install single rotor brakes on all 4 rear wheels of the tractor and on all wheels (typically 4) of the trailer. This configuration (Fig. 173) distributes the braking torque between the trailer and the tractor, allows for a lighter directional axle, and extends the benefits of eddy-current braking (ABS, dynamic stability) to the trailer. This also relieves the owner of the tractor from the responsibility of equipping his vehicle for the maximum it may rarely handle.

The main advantage of having eddy-current brakes on the trailer is response time. Indeed, conventional pneumatic brakes are fairly slow since the braking command can only travel as fast as the speed of sound (340m/s in air). A 20 meter long trailer would induce a 59 millisecond delay on top of the minimum 100 millisecond response time of the braking system. An eddy-current brake guarantees a 67 millisecond response time regardless of the length of the trailer.

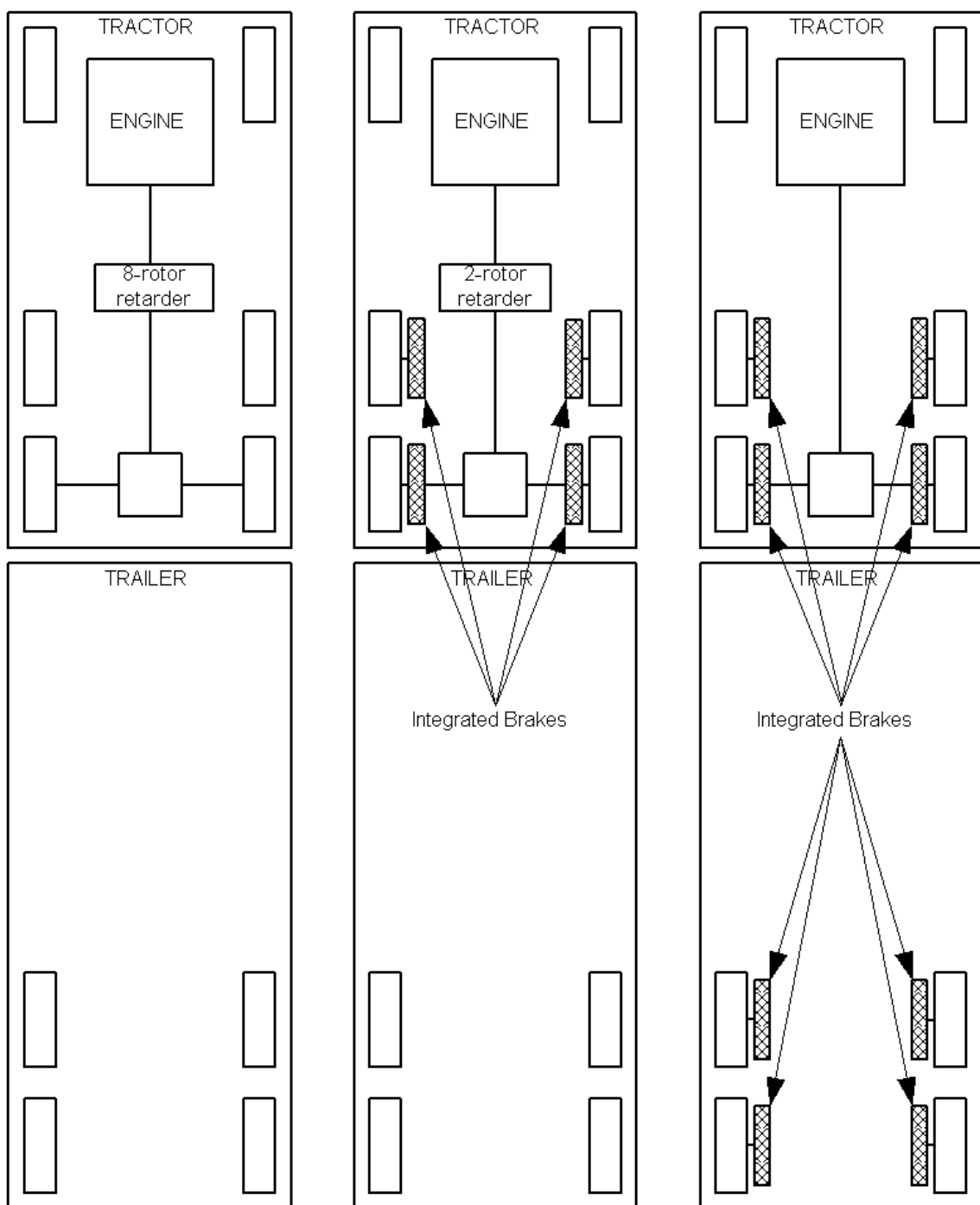


Fig. 173: Braking system configurations for a commercial truck

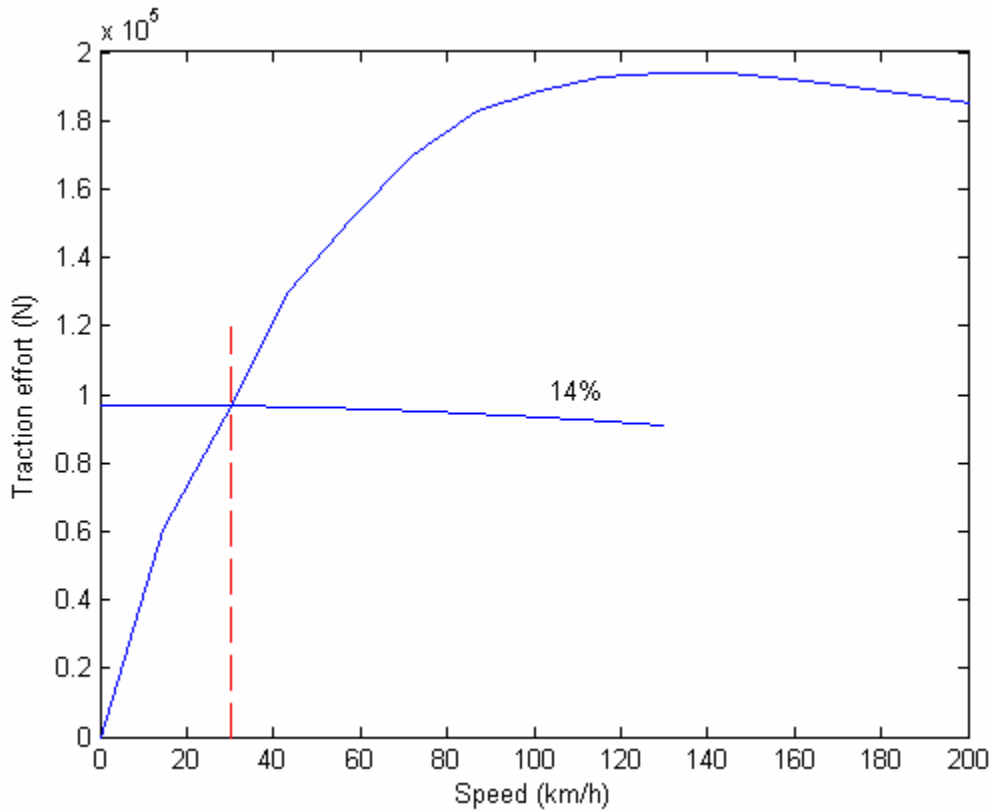


Fig. 174: Design of a constrained-speed retarder for a commercial truck

It is important to note that the above calculations assumed a non-constrained critical speed. In the event that critical speed is constrained, then the size of the brakes will rise considerably because their braking torque at 460rpm will be much lower than at 2000rpm. A brake for an 80,000kg heavy commercial truck application would become infeasible. The brake would have to be used in combination with friction brakes, or limited to lighter commercial trucks. Fig. 174 shows how the force-speed curve of a constrained critical speed retarder would be matched with the braking effort of the truck.

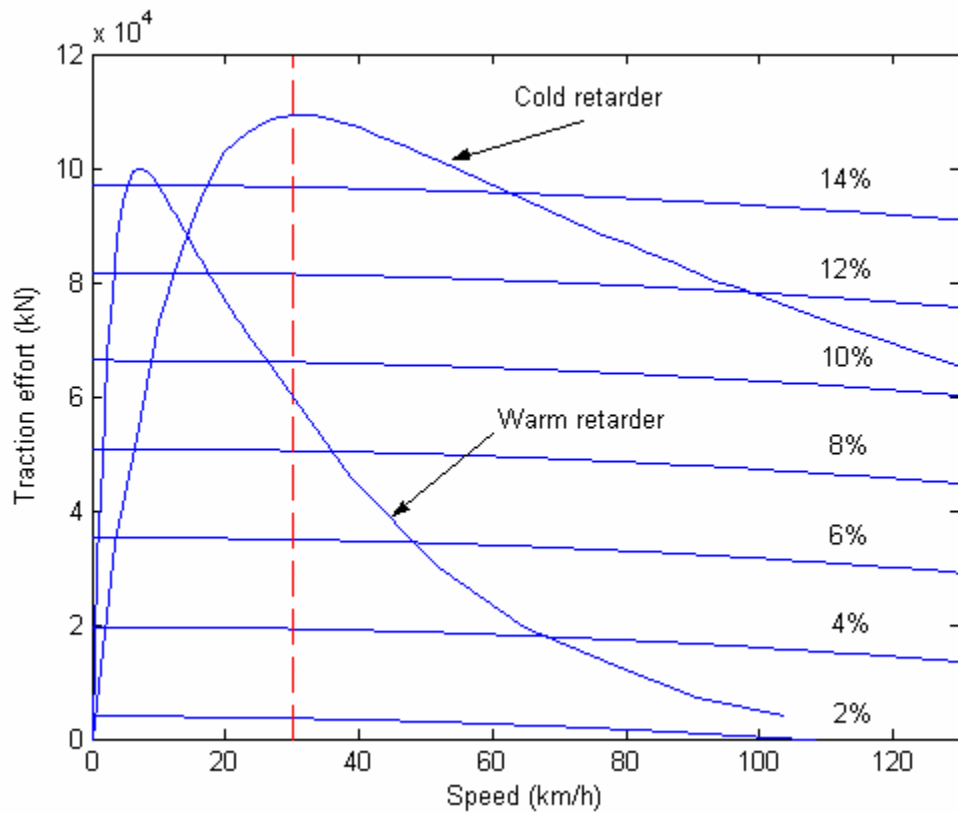


Fig. 175: Braking effort curves vs. braking force – speed curves

Temperature impacts the ability of the retarder to hold the truck in a grade. Fig. 175 shows the braking effort vs. speed curves plot against the torque-speed curves for a total of 8 brakes at 20°C and 200°C. The over-designed braking system provides some room to compensate for temperature drift by controls. It is helpful that the peak torque is not affected as much by temperature as critical speed. A properly over-designed brake will be capable of holding a vehicle in a 14% grade, although it will be at increasingly lower speed. It should be noted that because it is over-designed for torque, the retarder will not hold the vehicle at 30km/h in a 14% grade but it will hold it at about 18km/h. If the

target speed of 30 km/h must be maintained for the operation, the retarder will have to be redesigned with a different critical speed (Fig. 176).

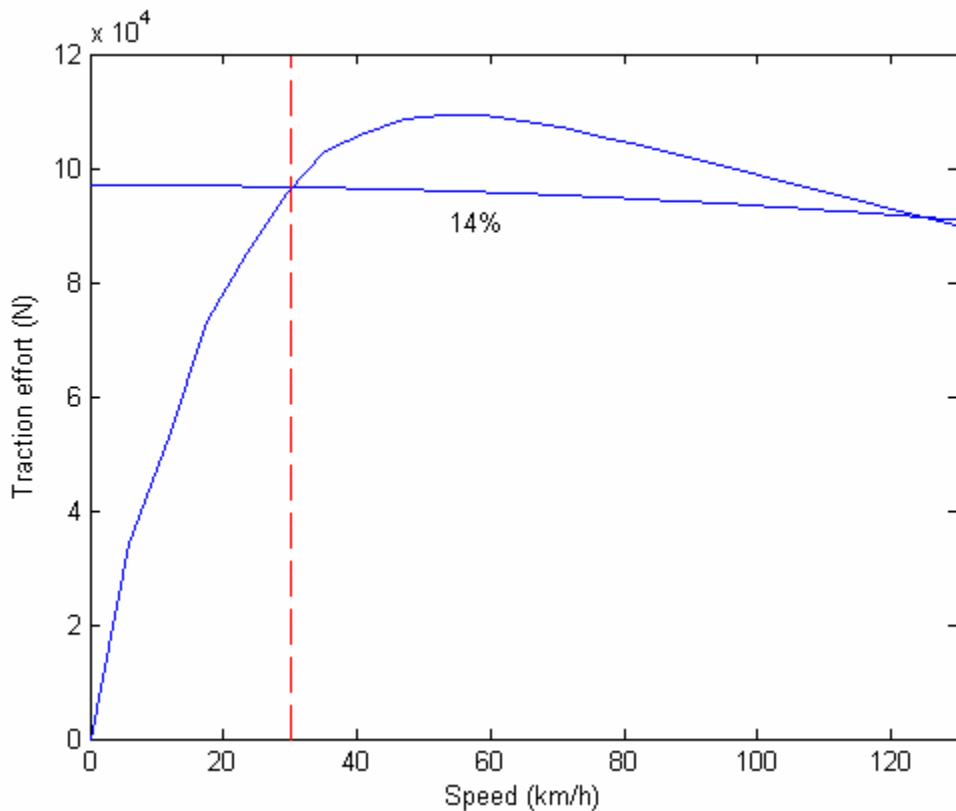


Fig. 176: Matching retarder and vehicle braking effort

3.1.2 – Dynamic stability control of commercial trucks

The dynamic stability control of the tractor alone is of interest if this later is not hooked up to a trailer. The problem is thus similar to the problem in automobiles, with the added complexity of a third axle. However, the dynamic stability control of the tractor-trailer

ensemble is of greater practical significance because of the dangers and costs associated with a loss of control of such a large ensemble. Analyzing the dynamic stability of a two-body vehicle is far more complex than analyzing that of a single body vehicle like an automobile. However, some general consideration can be inferred without delving into excessive calculations:

- If all the trailer wheels are on a low-adherence surface, there is only a limited range for the tractor's brakes to bring it back on the intended trajectory. Indeed, the angle between the tractor's centerline and the trailer's centerline must be such that the resulting torque acts against the disturbance.
- If only part of the trailer's wheels are on a low-adherence surface, then the dynamic stability control has more room to generate a compensating torque that opposes the yaw torque.
- The brakes on the trailer can be used to steer the tractor back on the intended trajectory.
- The momentum of inertia of the trailer around the yaw axis is many times larger than that of an automobile, primarily because it evolves like the square dimension of the vehicle. A greater force is thus required to get the trailer off trajectory, which minimizes the impact of a disturbance. However, a greater force must be exerted by the brakes to control the vehicle. The dimensions of the trailer reduce the effectiveness of the brakes in controlling the yaw motion. Indeed, the arm lever of the disturbance is the whole length of the trailer, while

the arm lever of the compensating force is only the half-width of the trailer. The compensating force is thus at a disadvantage (Fig.177).

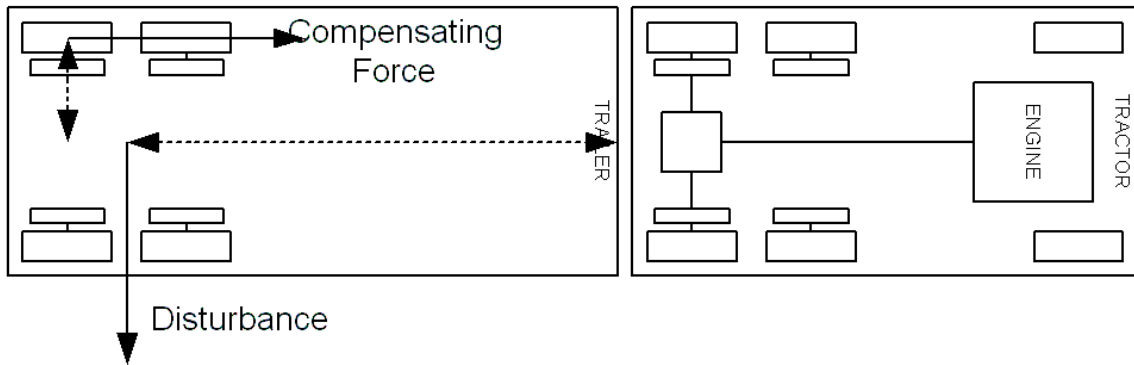


Fig. 177: Dynamic stability balance of forces for a trailer

3.1.3 – Anti-lock control of commercial trucks

Commercial trucks have much larger and heavier wheels than personal automobiles. The significantly greater momentum of inertia of the wheels prevents the build up of a significant difference between the wheel and the road speed. The momentum of inertia of a truck wheel can be reasonably estimated around 3 to 4 times greater than an automobile's wheel. Therefore, an anti-lock control system using eddy-current brakes on a commercial truck does not need as fast of a reaction time as on an automobile. With a 67ms brake reaction time, a truck will have a more effective anti-lock brake system than an automobile.

3.1.4 – The integrated brake as a backup brake

Eddy-current brakes provide some degree of protection against a complete failure of the vehicle's braking system. This is particularly interesting for commercial trucks, which are far heavier than automobiles and may carry hazardous materials. Protection would be provided by a return mechanism (spring) that would bring all or part of the magnets in aligned position in case of failure of the actuator or of the control system. The drawback of a return mechanism is that it would be acting against the actuator, which would increase the power consumption and rating of this later.

There is some merit to using a return mechanism only on part of the magnets. This configuration would provide some retarding torque to the vehicle without exceeding the adhesive limit of dry or wet surfaces. Indeed, locked trailer wheels would be just as catastrophic as a total loss of braking torque. Furthermore, if one brake fails while the others keep working normally, the driver may drive a while before realizing the problem and the brake would heat up very quickly, leading to potential damage of the tire and brake components.

3.2 – Integrated braking of urban buses

Urban buses follow a drive cycle composed of many decelerations and accelerations. They would thus benefit greatly from the use of eddy-current braking, which would

significantly reduce the duty on their friction brakes. Traditionally, the primary design criterion for the retarder of an urban bus is the ability of the eddy-current braking component to hold the bus at 30km/h in a 14% grade. Fig. 178 shows the braking force – speed curves for an Irisbus Agora 18m urban bus [53]. The parameters of the vehicle are given in TABLE 24.

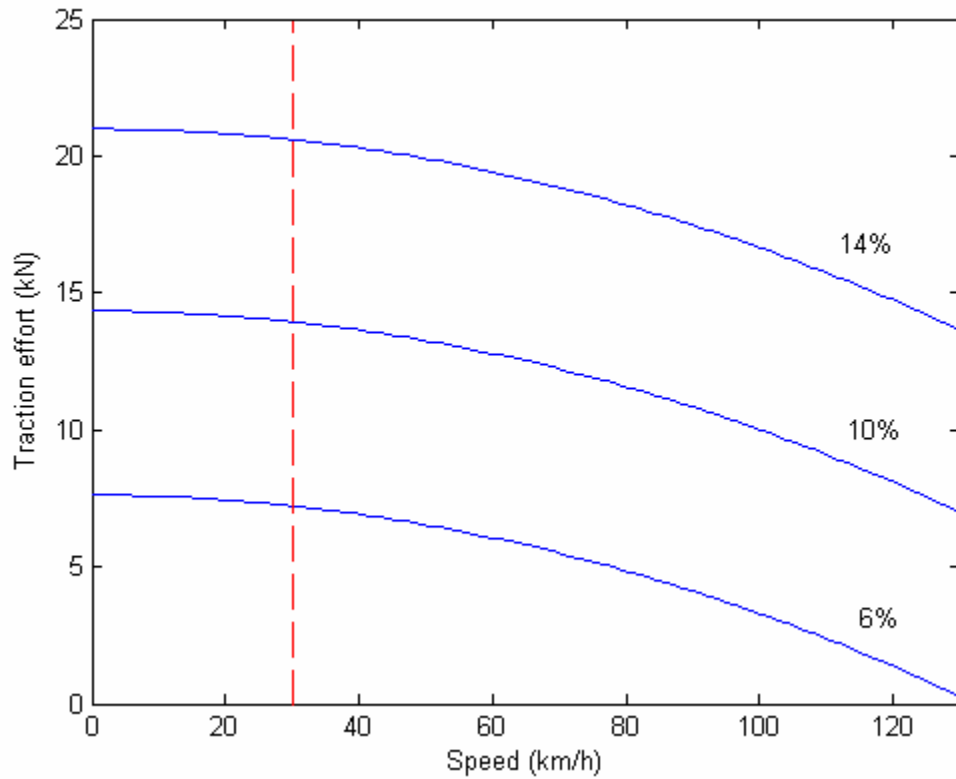


Fig. 178: Irisbus Agora 18m braking force – speed curves

TABLE 24
Irisbus Agora 18m parameters

PARAMETER	VALUE
Vehicle mass	17,300 kg
Rolling resistance coefficient	0.015
Aerodynamic drag coefficient	1.2
Air density	1.25 kg.m ⁻³
Vehicle body frontal area	7.5 m ²
Wheel radius	0.45 m
Tire adhesion coefficient	0.8

The total braking force that the braking system must provide at 30km/h is 20.6kN. Given the diameter of the wheels, this translates into a braking torque of 9,270N.m. Since urban buses use slow-revving diesel engines like commercial trucks do, it is reasonable to estimate that their final differential uses the same ratio commercial trucks do. The torque to be supplied by a retarder on the driveshaft would thus be 3,552N.m at a speed of 460rpm.

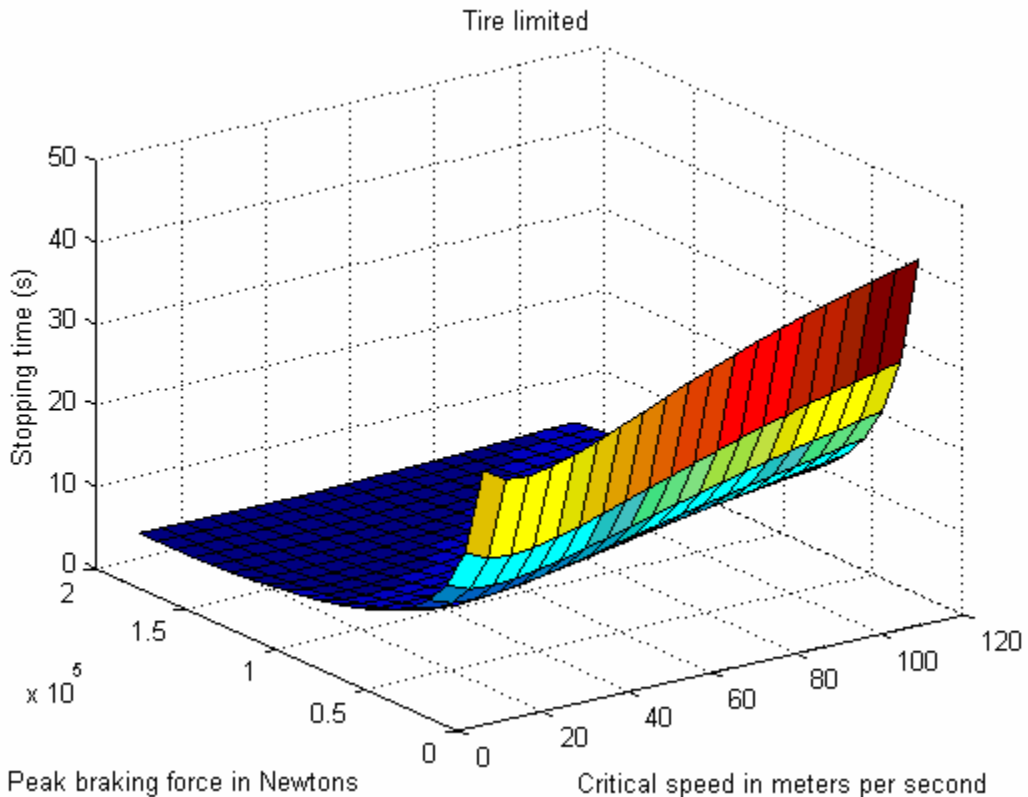


Fig. 179: Stopping time vs. critical speed and peak force, initial speed = 130km/h

On the other hand, if the brakes were distributed on each of the 6 wheels of the vehicle, each brake would have to supply only 1,545N.m. The brake would be designed by scaling up the conceptual design for an automobile. If the integrated brake is to be used, then it is desirable to calculate the optimal peak torque and critical speed, and verify that they are compatible with the retardation requirement. Fig. 179 shows the stopping time for the Irisbus Agora vs. critical speed and peak force for a deceleration from 130km/h. The graph shows an optimum critical speed at 21.25m/s (76.5km/h) and an optimum peak force 140kN. The critical speed is comparable to the requirements of retardation

(460rpm), while the peak force greatly exceeds them. Therefore a brake designed for primary braking will be sufficiently powerful to take care of holding the vehicle at 30km/h in a 14% grade.

The optimum braking force results in a braking torque rating of 10,500N.m for each of the 6 brakes. Given the dimensions of the wheel, a single rotor brake can produce a maximum of 2,306N.m if the circumference is entirely covered with poles. Such an arrangement would not leave any room for friction brakes. The rating of the wheel brakes can be reduced somewhat by using a retarder on the transmission shaft. The new rating is then 8,955N.m per brake, which is still far greater than can be reasonably achieved.

It is useful to realize however, that urban buses rarely exceed 60km/h because of their very “peaky” drive cycle. Therefore, the eddy-current brake can be designed based on a maximum speed of 60km/h, which put the requirements for higher speed braking on the friction brakes. Fig. 180 shows the new optimization graph.

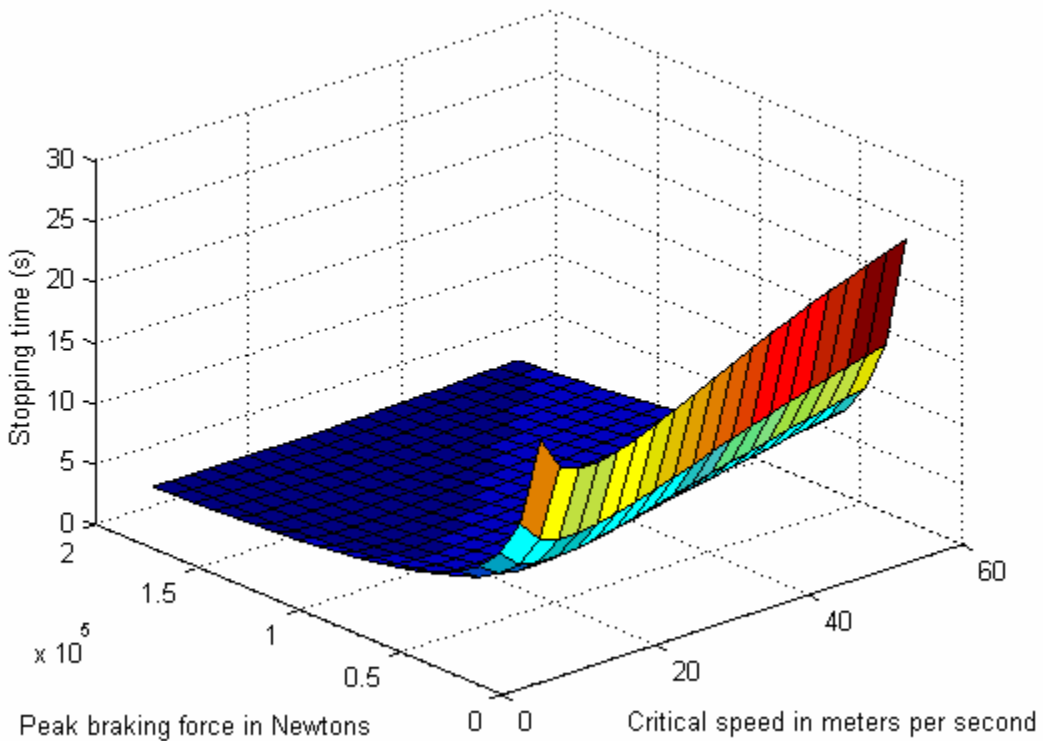


Fig. 180: Stopping time vs. critical speed and peak force, initial speed = 60km/h

The new optimum critical speed is 12.5m/s (45km/h) and the optimum peak force is 140kN. The peak force rating hasn't changed because only the maximum speed changed. It seems thus unrealistic for an eddy-current brake to provide primary emergency braking for an urban bus. Therefore, the eddy-current brake should be limited to retardation and perhaps braking during normal situations.

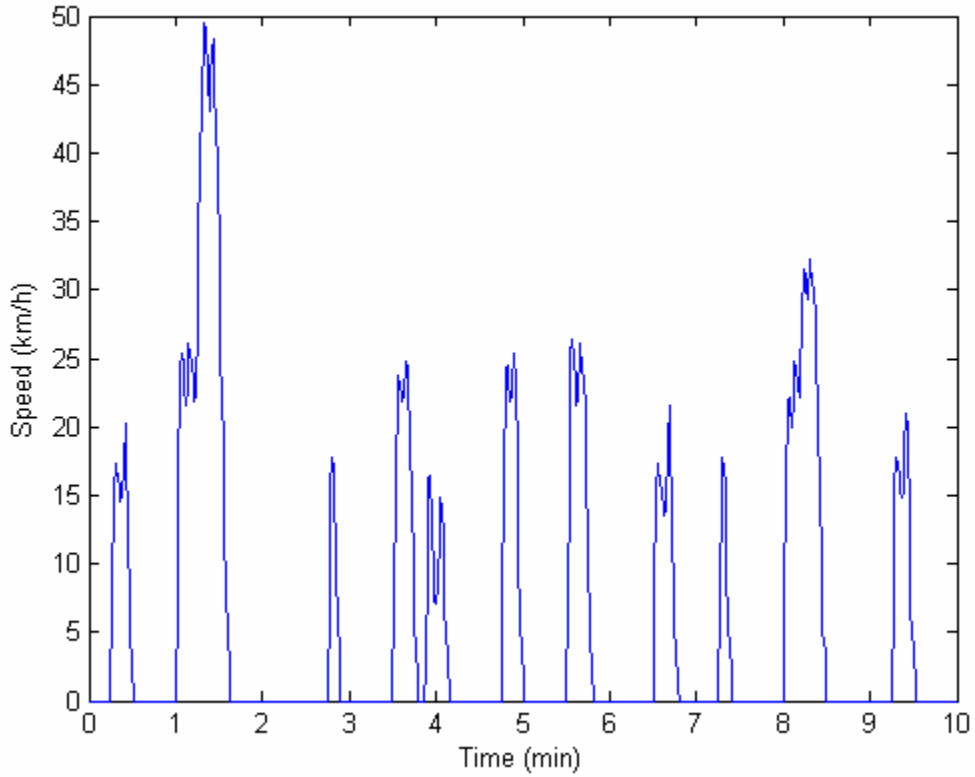


Fig. 181: New York Bus drive cycle speed profile

The Irisbus Agora 18m has been simulated along the New York bus drive cycle provided in Advisor (Fig. 181). Fig. 182 shows the braking points along the drive cycle (red asterisks) compared to several eddy-current brake total force-speed curves. The critical speed is 30km/h, and each curve corresponds to a different peak force:

- 20.6kN: This peak force corresponds to a single retarder with a peak torque 3,552N.m installed on the transmission shaft or 6 brakes rated at 1545N.m on each of the wheels.

- 30.8kN: This peak force corresponds to 6 brakes rated at 2,306N.m, the maximum feasible torque achievable given the dimensions of the wheels.
- 51.4kN: This peak force corresponds to 6 brakes rated at 2,306N.m plus a 3,552N.m retarder on the transmission shaft.
- 140kN: This peak force corresponds to the optimum peak force required for emergency braking.

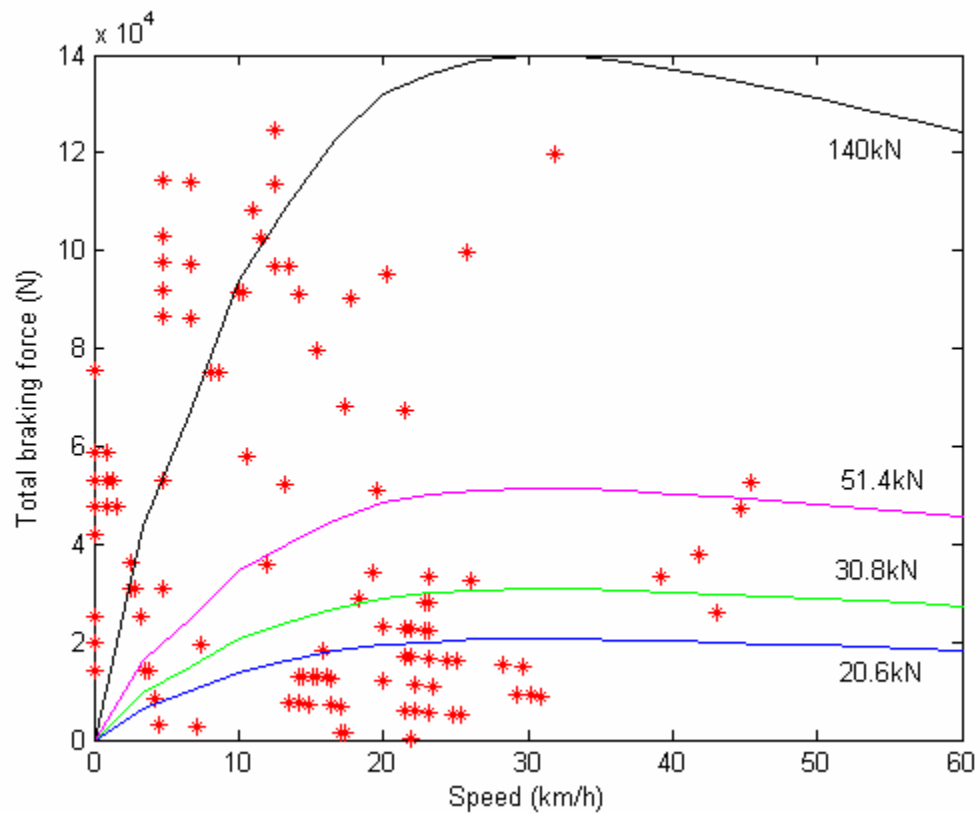


Fig. 182: New York Bus braking points vs. eddy-current brake curves

All curves are for cold brakes. The 140kN curve is not a practical curve and is included only to demonstrate how demanding the New York bus drive cycle is. No curve includes all of the braking points, which means that the friction component will have to be used often. Even with the most powerful practical braking system (51.4kN), the friction brake is called upon about half the time. It is interesting to note that there are many points above the eddy-current force-speed curve at low speed, which demonstrates how harsh the drive cycle is. TABLE 25 summarizes the kinetic energy dissipation for the total, eddy-current and friction braking systems.

TABLE 25
Kinetic energy dissipation summary

Peak force	Total dissipation	Eddy-current dissipation	Friction dissipation
20.6kN	61.7 MJ	25.0 MJ	36.7 MJ
30.8kN	61.7 MJ	32.1 MJ	29.6 MJ
51.4kN	61.7 MJ	41.3 MJ	20.4 MJ

The kinetic energy dissipation by the friction braking system can be reduced at most by 67% with the 51.4kN curve and at least by 40% with the 20.6kN curve. In either case, these are significant savings, but they may not justify the installation of such a large number of retarders and integrated brakes.

The difficulty in designing eddy-current brakes powerful enough for an urban bus make it impossible to consider them in case their critical speed is constrained and two different from the optimum requirements.

Anti-lock braking control brings the same benefits for urban buses and commercial trucks. Since both types of vehicles have roughly the same tires, they both benefit from the large momentum of inertia, which makes the wheel slower to build a speed difference with the road. A brake with a fast reaction time will allow minimizing considerably the average speed difference by making the tire catch up with the road quickly.

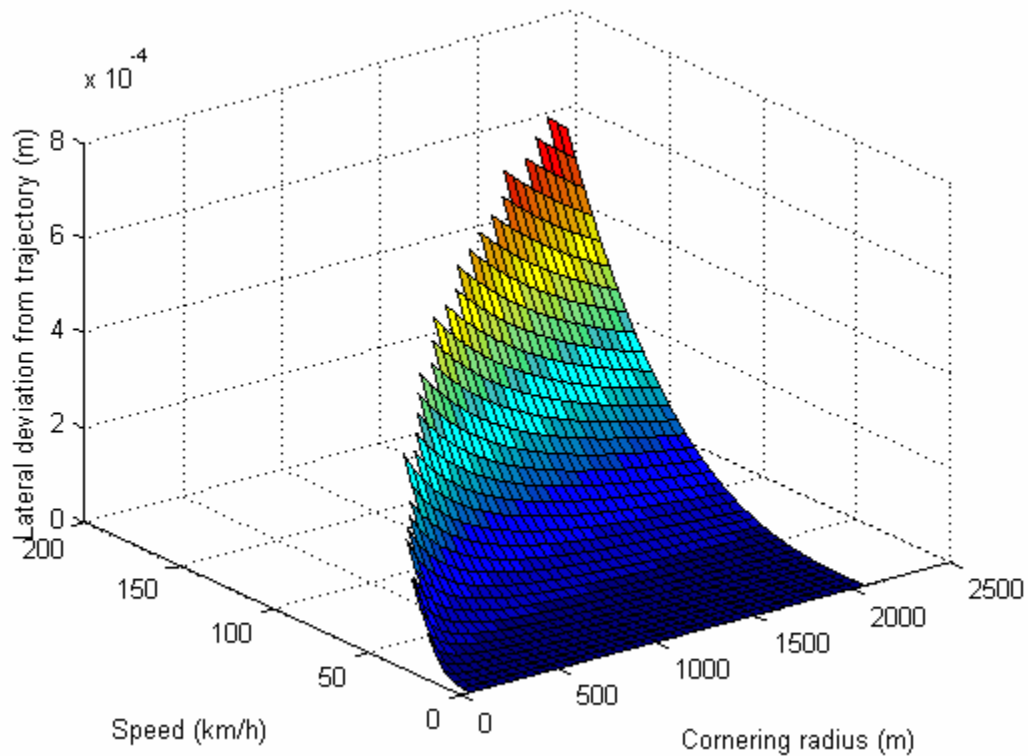


Fig. 183: Lateral deviation for the Irisbus Agora 18m after 67ms

Dynamic stability control on urban buses suffers from the same problem it does for commercial trucks. The lever arm for the disturbing force is much greater than the lever arm for the compensating force. However, since the inertia of the vehicle is much larger and its cornering speeds is much lower than an automobile's, the dynamic stability control system has more time to compensate the yaw torque before the deviation becomes dangerously large (Fig. 183). The twin body structure of some urban buses makes the design of a dynamic stability control system more challenging because the reaction of the trailer complicates the dynamics of the whole vehicle.

Traction control is available on the driven axle of the bus. There are therefore two brakes that can compensate the engine torque. A 2306 N.m brake can counter up to 86kW at 30km/h or 460rpm at the wheel. The Agora 18m bus can be drive by an engine up to 600hp (450kW). The torque margin of the eddy-current brakes is thus limited and the traction control will require some intervention of the fuel flow controller. However, the torques available are large enough for a limited slip differential application of traction control.

4 – Integrated braking of rail vehicles

4.1 – Integrated braking of light rail vehicles

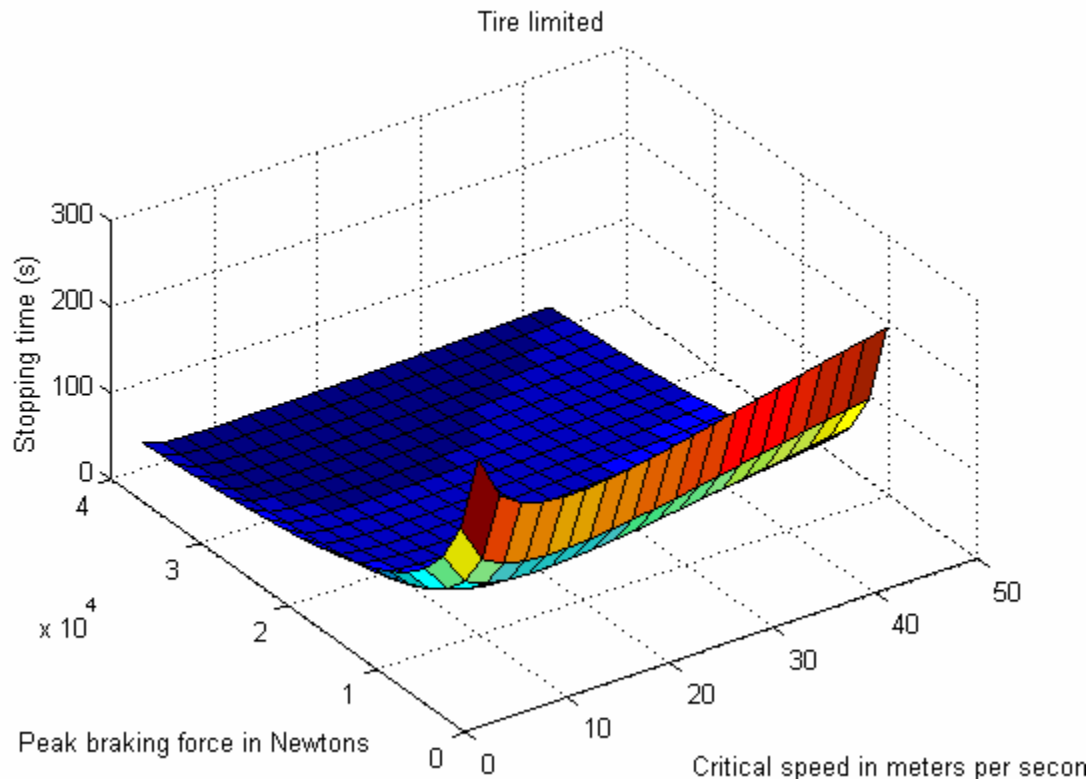


Fig. 184: Stopping time vs. critical speed and peak force

Light rail refers to tramway and subway rail vehicles. The primary advantage of an eddy-current brake would thus be the ability to limit the wear of the friction component.

Fig. 184 shows the optimization plot for an eddy-current brake for an Alstom tramway

operated by the city of Grenoble, France [54]. The optimum critical speed is 11.4m/s (41km/h or 520rpm for a 420mm wheel) and the optimum peak force is 36,000N.

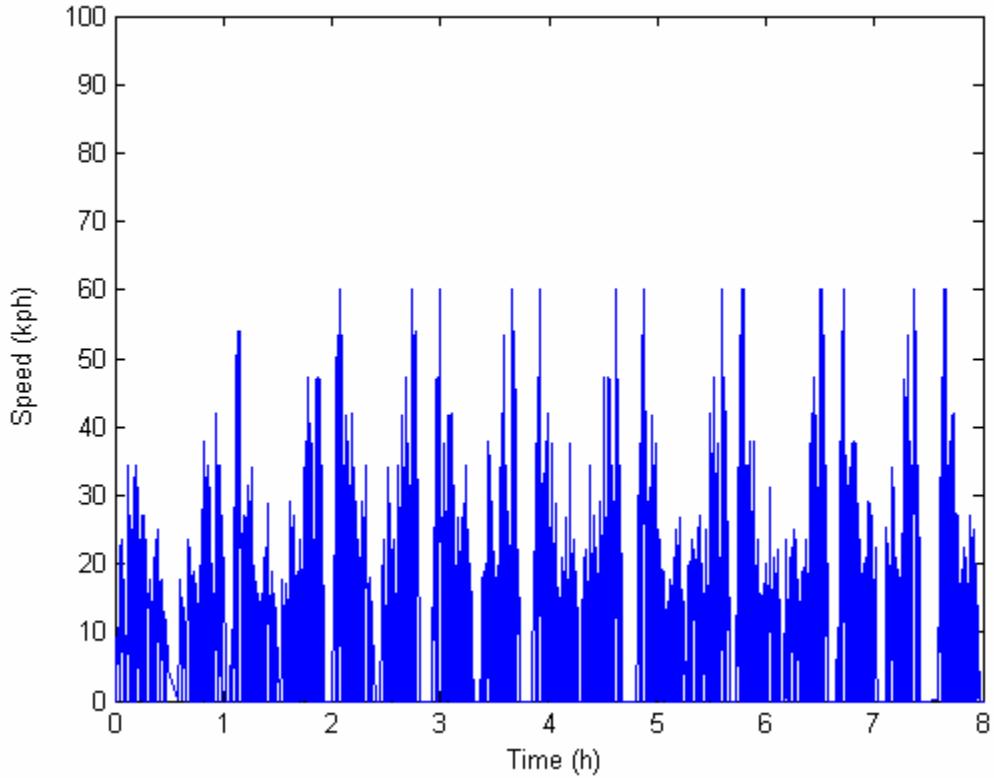


Fig. 185: 8-hour tramway drive cycle

Tramways have a regenerative braking capability, which is always available at all times except in case of an overhead line failure. Indeed, there is always another tramway under the line that can absorb the braking energy regenerated. A simulation was run with real-life drive cycles (Fig. 185 and Fig. 186) [54].

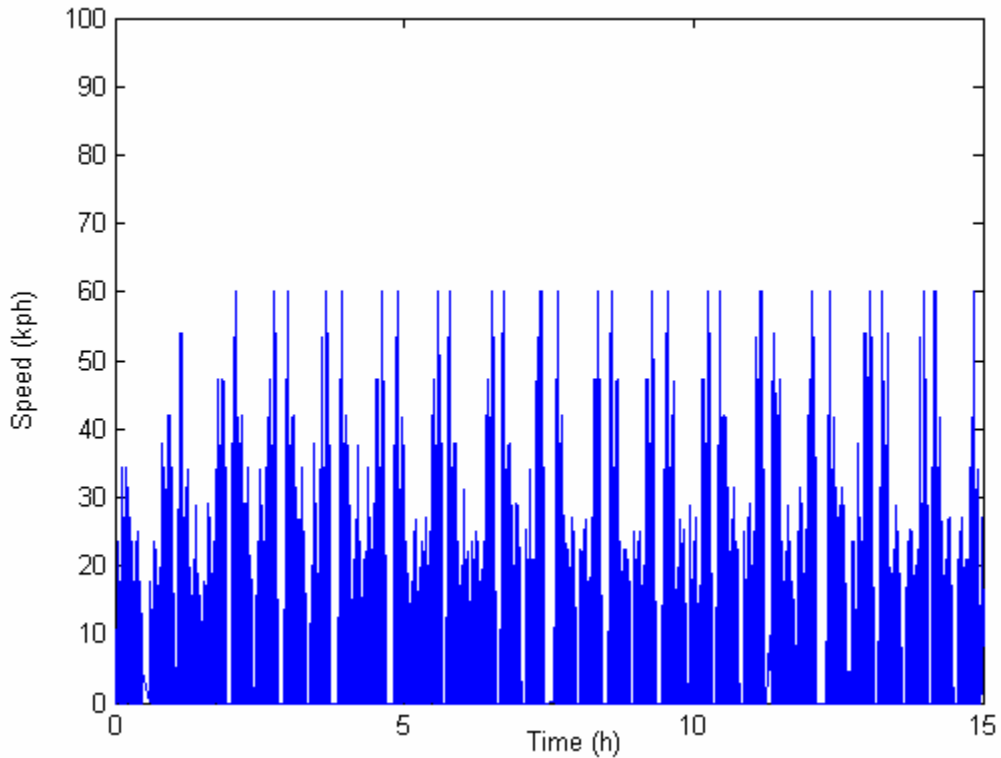


Fig. 186: 15-hour tramway drive cycle

Fig. 187 shows that if regenerative braking is available, then it is capable of braking the vehicle along the entire drive cycle. The upper line represents the maximum regenerative braking force defined by the 750kW traction motor. Therefore, the eddy-current braking system will only be used in case of an overhead line failure. The advantages of eddy-current braking over friction are not significant enough to justify the additional cost and complexity.

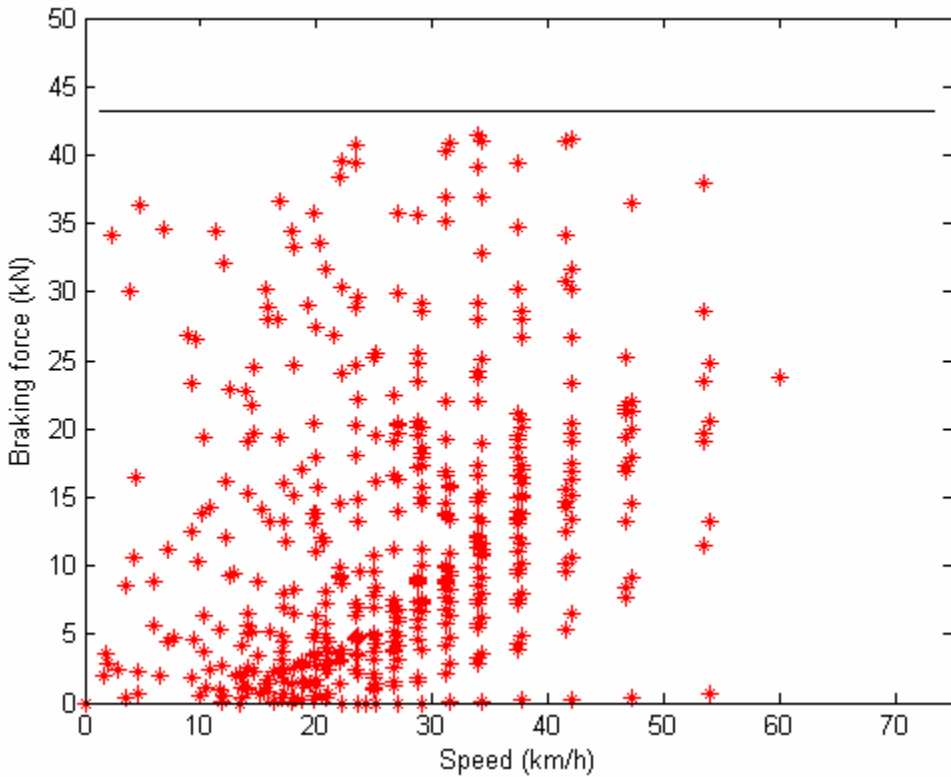


Fig. 187: Braking points, tramway

4.2 – Integrated braking of high-speed trains

The German company Knorr-Bremse developed linear eddy-current brakes for passenger rail applications [55]. These brakes use the steel rail as the secondary in which the eddy-currents develop. The system is simple and effective but its application to high-speed trains has been prevented by the high temperatures reached by the rails.

A rotary eddy-current brake installed on the wheels would provide the same benefits without overheating the rail. The heating of each disc would be reasonable if each wheel of the train receives a brake. Fig. 188 shows the stopping time for a 400 metric ton TGV at 300km/h [56].

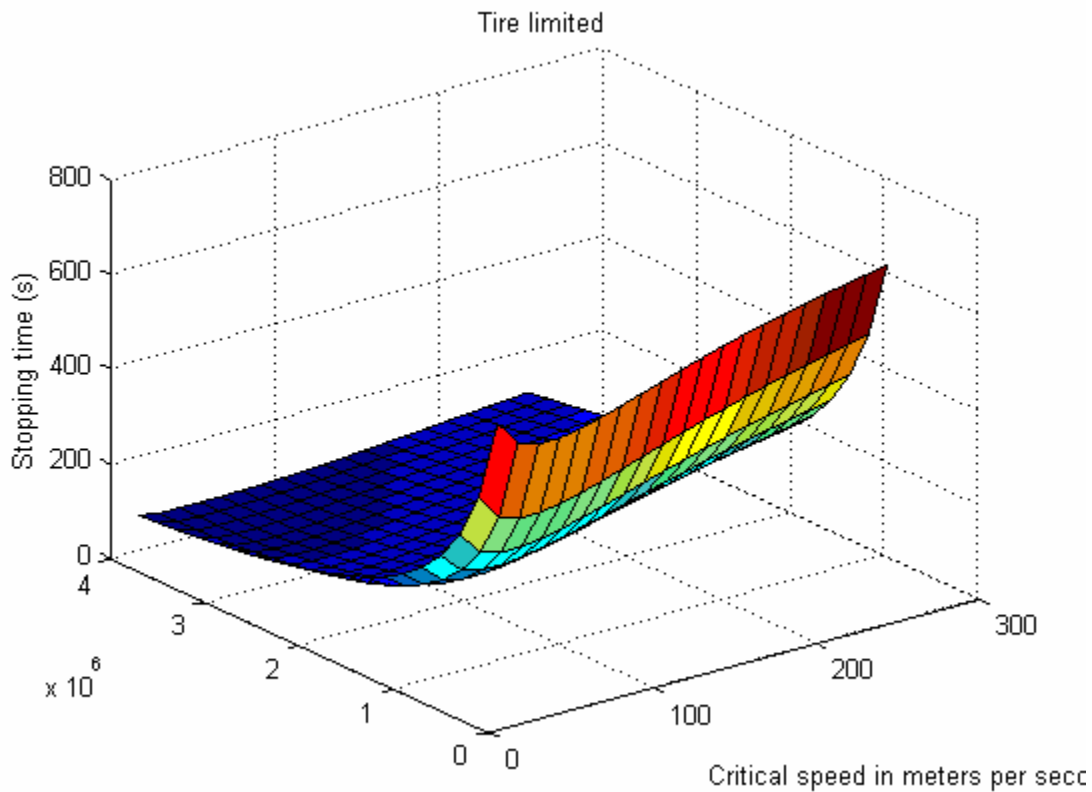


Fig. 188: Stopping time for TGV vs. critical speed and peak force

The optimum peak braking force is 340kN, and the optimum critical is 42.5m/s (153km/h or 1933rpm with a 420mm diameter wheel). The corresponding total torque is 143kN.m with the standard 420mm-diameter wheel. With a maximum 2,306N.m per

brake, a total of 62 brakes is required. The total number of wheels on a TGV (“Reseau” version) is 48. The limitation can be circumvented by using twin-rotor brakes on some axles. Provided an optimum peak force and critical speed, the eddy-current brake dissipates 91% of the kinetic energy of the train in a deceleration from 300km/h.

4.3 – Integrated braking of freight trains

Eddy-current braking is interesting for freight trains because it allows controlling the torque of each wheel individually. The pneumatic friction braking system of today's trains does not allow for individual wheel control. This is often cited as a problem by the engineers who operate the locomotives particularly when the train goes downhill. Furthermore, the eddy-current brake does not require compressed air. Consequently, the train can be driven without having to wait until the braking system is under pressure.

The pneumatic actuation of conventional rail friction brakes has an additional disadvantage: the pressure wave in response to the engineer's command can only travel as fast as the speed of sound (340m/s at sea level pressure and 20°C). Therefore, the response time depends on the distance of a car to the locomotive. Freight trains tend to be very long, some over a kilometer. Between the time the engineer open the circuit to command braking and the time the last car starts to brake, there can be a delay of several seconds. The cars at the end of the train are then pushing the cars up front, thus increasing the instability of the train and the risk of derailing, especially in downhill

driving. Information in an eddy-current based braking system travels at the speed of light, therefore resulting in a negligible time lag between the front and the back of the train.

Since the friction brakes on freight trains has shoes rubbing on the rolling band of the wheel instead of a disc, the eddy-current brake can have magnets covering the entire circumference of the disc, thereby increasing the amount of torque available.

Eddy-current braking would also allow holding the freight car at a safe speed down a given grade.

Because of its huge mass, a freight train has a very long time constant. Therefore, the brakes don't need to have a fast response to be effective. This reduces the size of their actuator and its power consumption.

Finally, if the power fails, the magnets can be designed to fall back into the aligned position by a spring-loaded return mechanism. This mechanism would be less intrusive to the actuation because this later must respond to less stringent requirements than for an automobile.

Anti-lock braking becomes easy to integrate, something which is hard to do in pneumatic braking systems because of their fail safe architecture that requires the system to brake upon decreasing pressure rather than increasing pressure.

5 – Integrated braking of other vehicles

Other vehicle may benefit from eddy-current brakes:

- Dump trucks in mining operations: used as a retarder, the eddy-current brake can save friction brakes when the truck is going downhill. A 290,000-kg dump truck ([57]) would need a maximum total braking force of 558kN in a 20% grade at zero speed. With a wheel radius of 1.5 meter, the total torque rating is 372kN.m. The individual torque is 93kN.m. Since the wheels of a dump trucks are much larger than those of a commercial truck, more torque can be achieved with a single rotor, and more rotors can be mounted inside the hub.
- Garbage trucks: with frequent accelerations and decelerations, a garbage truck would benefit significantly from the installation of eddy-current brake, which would greatly reduce the wear of the friction component. Because the speed of a garbage truck on duty is low, the brake should be mounted on the driveshaft and possibly mounted with a reduction gear in order to provide significant torque at the wheel.
- Motorcycles are good candidates for eddy-current retardation because of their high-revving engine. Indeed, speeds in excess of 10,000rpm are not uncommon

in powerful sport motorcycles [58,59]. If an eddy-current retarder was installed on the shaft of the engine, the gear reduction required to adapt the speed of the engine for the wheel would multiply the braking torque consequently. This allows designing a fairly small retarder, yet achieve good deceleration performance. The cooling of the retarder would benefit from the fact that engine is mounted in the open, rather than under a hood.

- Bicycles: the metal rim of the wheels could be used as the rotor for the brake, while the magnets on the stator are actuated mechanically by the rider. Large torques can be achieved with only a few magnets because of the large radius of the wheel rim. The main purpose of the eddy-current retarder would be to alleviate the stress on the very soft pads used on bicycles in downhill riding.

6 – Electric motor emergency braking with an eddy-current brake

Eddy-braking can be used for the soft-braking of electric motors in case of power failure in safety critical applications such as elevators and cranes. The eddy-current would be mounted on the shaft of the electric motor for simplicity of construction and to benefit from the gear reduction to increase the braking torque on the load. The magnets would be relay-actuated and spring-loaded so that when the power turns off, the magnets fall back into the aligned position, thus inducing a braking torque.

The design of the brake is based on the following specifications:

- Maximum load that the motor is lifting
- Maximum safe speed for a descending load
- Gear ratio

TABLE 26
Crane parameters

PARAMETER	VALUE
Crane lifting height	40m
Maximum mass lifted	10,000kg
Maximum speed	0.5m/s
Winch diameter	0.7m
Motor rated speed	3,000rpm
Winch gear ratio	220:1

TABLE 26 shows the parameters of a crane used for a case study. The motor is rated for 49kW at 3,000rpm, which corresponds to a rated torque of 156N.m. A reasonable assumption is that the eddy-current brake should hold the maximum load (10,000kg) at most at the maximum lifting speed (0.5m/s). Fig. 186 shows the match between the torque-speed curve of an eddy-current brake and the load from a winch.

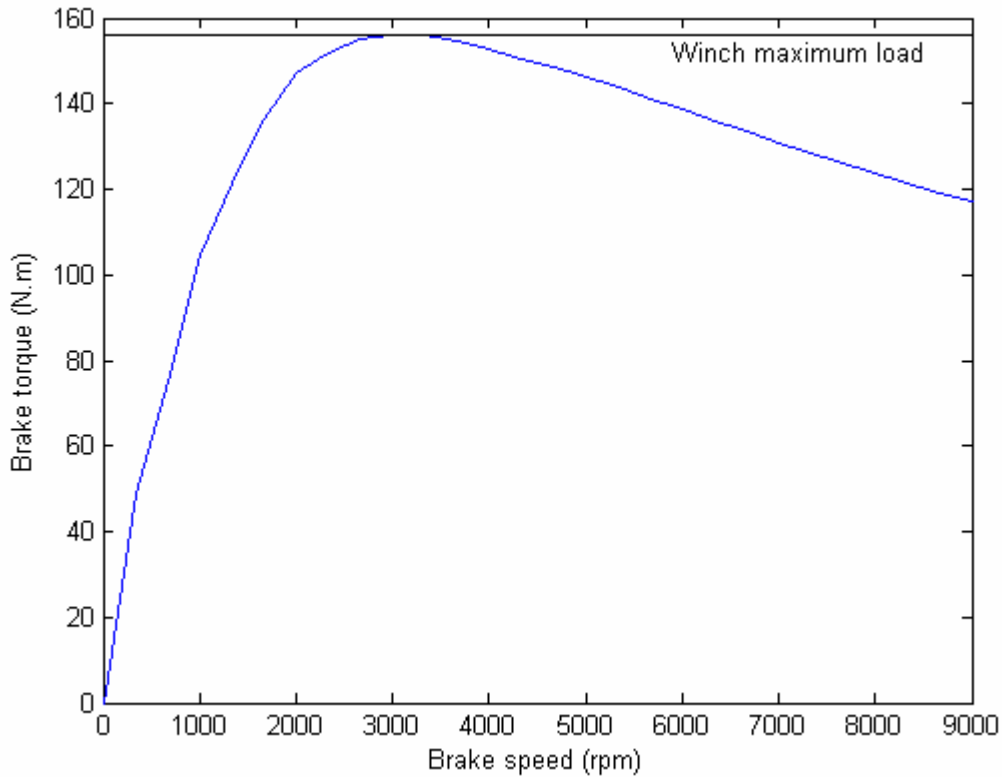


Fig. 189: Eddy-current braking of a winch

It is interesting to note that the torque rating is far lower than for an automobile. This results in a very compact brake. If the conceptual design for automobiles is taken as a reference, only 5 magnets are needed to accomplish the task. The cost of the brake is thus very low compared to an automotive brake. Fig. 190 shows the speed of a 10,000kg load after a motor failure at $t=0$ s. The motor is braked by an eddy-current brake with a peak torque corresponding to a braking force of 10,000kg on the load.

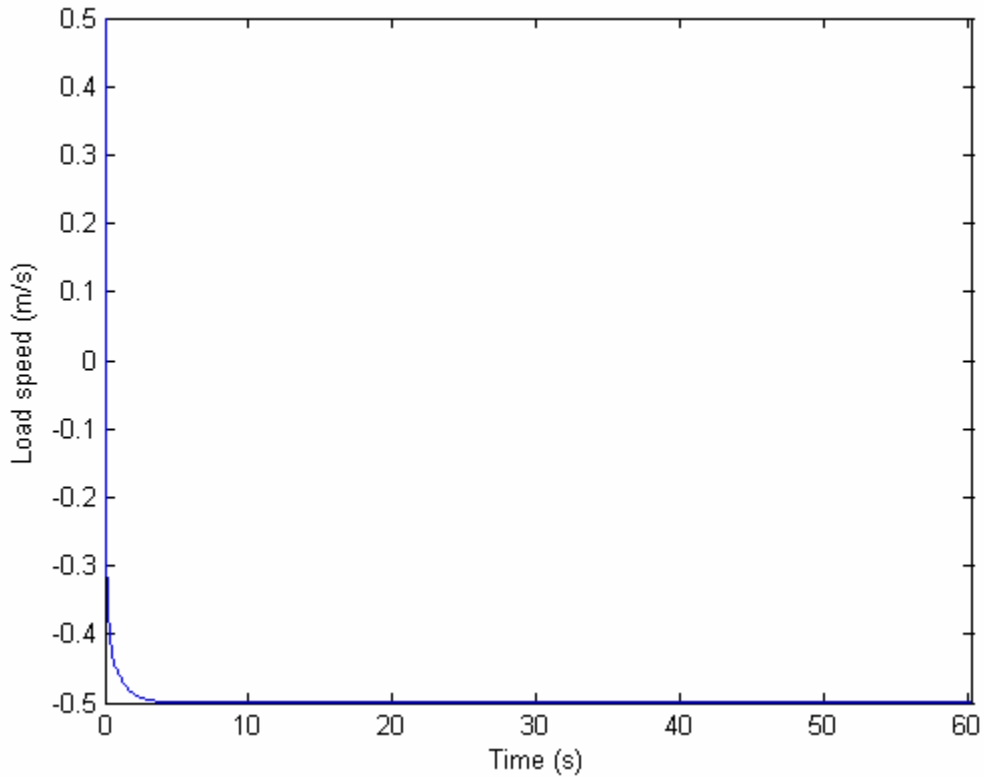


Fig. 190: Load speed after motor failure at t=0s

The speed quickly reverses from an upward speed of 0.5m/s to a downward speed because the motor torque disappears. The speed settles at negative value of 0.5m/s, which is the speed at which the eddy-current brake produces a braking force equal to the weight of the load. The load continues descending at that speed until it reaches the ground. Note that the time constant of the winch is much larger than the 20ms maximum reaction time of the brake. Fig. 191 shows the operating points of the eddy-current brake, which demonstrates that the brake spends most of its time operating around critical speed and peak torque.

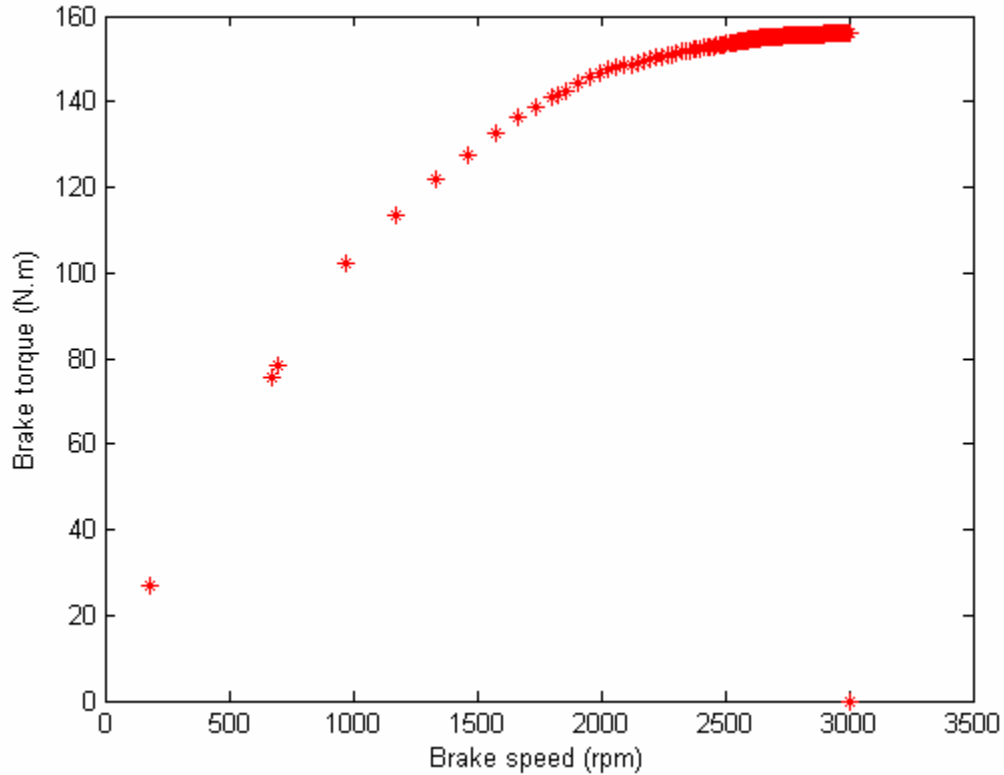


Fig. 191: Brake operating points

One of the events leading to a power outage is overload. In that case, the lifted load exceeds the maximum design load, which means that the brake will have to operate at a higher braking torque. A safety margin should thus be included in the design of the brake. The design peak torque should be several times greater than the maximum design load for the motor. A valid rule would be to match the maximum load that the crane can hold without collapsing. This load is usually equal to the maximum lifted loads times a safety coefficient between 2 and 5. The peak torque of the eddy-current brake should thus be equal to that load, at a maximum speed corresponding to a load speed of

0.5m/s. Furthermore, the brake heats up considerably during the operation, which changes its characteristics to a slightly lower peak torque and to a much lower critical speed. The brake must thus be over-designed with a peak torque higher than the motor's rated torque, such that in the worst case scenario (heaviest and highest load, highest ambient temperature), the final peak torque and critical speed permit braking the load at no more than 0.5m/s.

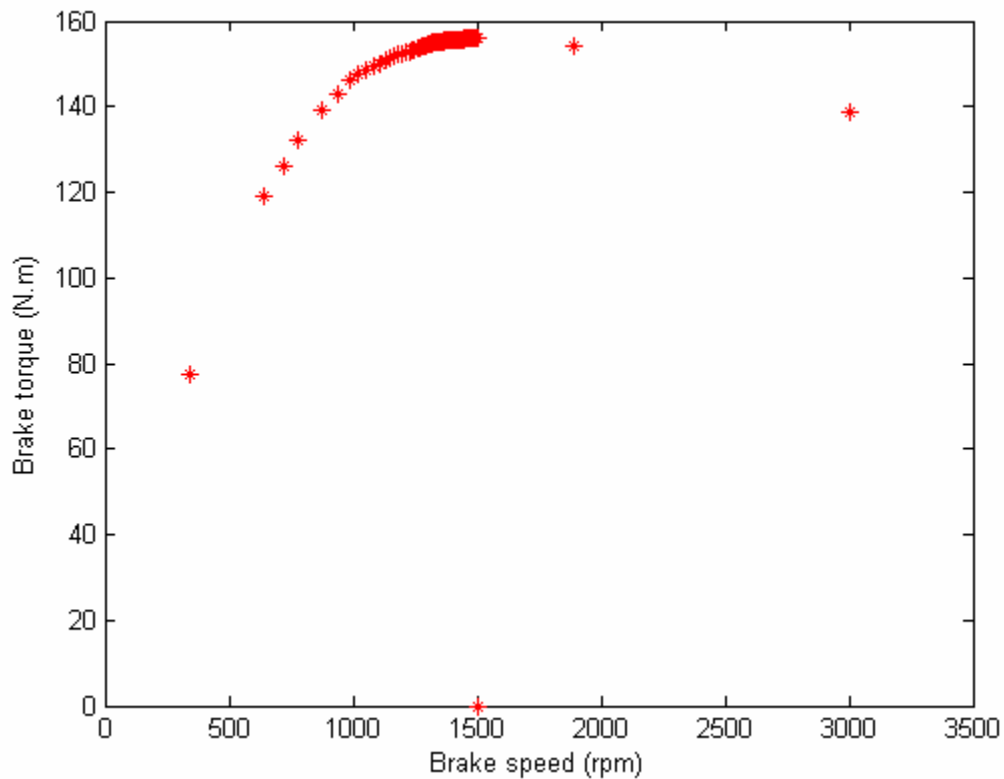


Fig. 192: Brake operating points for initial speed superior to critical speed

It is important to note that the choice of critical speed is influenced only by the desired descent speed in case of a motor failure. It matters little if the deceleration starts at a speed well beyond critical speed. The winch will just take slightly longer to settle to a steady state than if the deceleration started at critical speed. A brake with a constrained critical speed is thus useful, provided that the critical speed is below initial speed or only a few times greater. Fig. 192 shows the operating points of a brake designed with a critical speed of 1,500rpm and a deceleration starting at 3,000rpm.

7 – Trepan kinetic energy control by eddy-current braking

Eddy-current brakes are currently used on oil drilling platforms to descend the trepan down the borehole at a moderate speed so it doesn't break upon hitting the rock at the bottom [60]. The brakes currently used have electromagnets, which consume a significant amount of current and are obviously sensitive to power system failures. The conceptual permanent magnet brake can provide the same amount of torque with the added benefits of low power consumption and immunity against power failures.

CHAPTER VI

SUMMARY AND CONCLUSIONS

1 – Summary

Road, rail and air vehicles all rely mainly or solely on mechanical friction brakes. These brakes are composed of two functional parts: a cast-iron rotor (disc or drum) and pads pressed against the rotor to generate the braking force by friction. The pressure is applied by a hydraulic or pneumatic circuit. Friction braking is dissipative: the vehicle's kinetic energy is dissipated as heat on the disc, which heats up to several hundred Celsius degrees. Despite its tremendous advantages in compactness and effectiveness, friction braking suffers from severe limitations:

- Loss of braking force with increasing temperature (fading phenomenon)
- Warping of discs
- Wear of pads and rotors
- Complexity and fuel consumption of power assistance
- Slow response time due to power assistance, especially in trucks, buses and trains
- Complexity of controlling each wheel's braking independently
- Necessity of complex and costly anti-lock controls
- Risk of hydraulic fluid leak
- Risk of brake fluid contamination by water and subsequent loss of braking power
- Challenging integration with anti-lock, traction, and dynamic stability controls

The concept of integrated contactless magnetic brake was invented to remedy to these problems. The integrated brake combines a conventional friction brake with a magnetic brake. This novel concept has many advantages over friction brakes:

- Reduced wear
- Reduced sensitivity to fading
- Reduced fuel consumption of power assistance
- Faster control dynamics
- Easier integration with anti-lock, traction, and dynamic stability controls
- Easy individual wheel braking control
- Electric actuation, no fluid

The magnetic brake consists of a number of stationary magnets facing the friction brake's rotor across an airgap. When the disc spins, eddy-currents are induced in the disc and the interaction of these currents with the magnetic field creates the braking force. The braking force is directly controlled by the intensity of the magnetic field.

Eddy-current brakes are currently used as electromagnetic retarders for the secondary and downhill braking of commercial trucks, buses, and light rail vehicles. A single brake is mounted in the transmission aft of the differential gear underneath the chassis. The brake is energized by electromagnets connected to the battery and controlled manually by the driver. Electromagnetic retarders provide a large braking torque without contact between the magnets and the rotor thereby alleviating the duty on the main braking

system. They however suffer shortcomings such as heavy weight, excessive power consumption of the electromagnets, and vulnerability to power failure.

The concept analyzed in the present work solves these problems by using compact rare-earth permanent magnets that provide a strong magnetic field and a novel magnetic circuit structure that allows controlling the field easily by electrical means.

Analytical and three-dimensional finite element analyses have explained the fundamental physics and the impact of each design parameter on the performance of eddy-current braking. This investigation has yielded significant scientific contributions:

- The impact of electrical conductivity on the torque-speed curve has been found to be more significant than was previously thought. In addition to increasing the critical speed as was initially thought, it decreases the peak torque as well. An explanation for the phenomenon has been proposed and presented.
- The impact of magnetic the relative permeability on the performance was found to be secondarily significant.
- On the other hand, the saturation magnetization of the rotor material was found to be of prime importance. A high saturation magnetization allows a high flux density throughout the disc, which increases tremendously the braking torque achievable.
- For a given saturation magnetization the braking torque can be maximized by designing the magnetic circuit so that the maximum average flux density in the

poles exceeds the saturation magnetization of the rotor material. The brake thus operates with a low incremental relative permeability so a given eddy-current density results in a low reaction flux density. The average flux density remains high despite high eddy-current densities. The performance is maintained for a broader speed range.

The braking torque generated was found suitable for automotive applications. The power requirements for the actuation of the integrated brake are minimal, and the response time is on a par with the fastest friction brakes. An experiment was run to validate the results of the three-dimensional finite element analysis. While the peak torque was correct within approximately 25%, the experimental critical speed was several times the value obtained by numerical simulations. Several reasons for such wide discrepancy have been proposed and analyzed. Although it does not validate the exact shape of the torque-speed curve, the experiment nonetheless proves that the braking torque falls within range of the target value.

Following this result, the application of the integrated brake to vehicles was analyzed. The brake offers significant design and operational advantages over conventional friction brakes.

In conventional, electric, fuel cell, and hybrid automobiles, eddy-current braking allows traveling the entire FTP 75 Urban and Highway drive cycles without using friction brakes at all. In mountain drive cycles, the friction brakes are required only in rare

occasions, while the eddy-current brake handles most of the braking. Despite the rarity of their use, friction brakes need to be conserved for harsher drive cycles and for emergency braking. Temperature was shown to change significantly the torque-speed characteristics of the brake.

The integrated brake was found to provide significant advantages for interfacing with anti-lock, traction, and dynamic stability controls. The fast reaction time is the most important characteristic of the brake in these applications. If the reaction time is fast enough, the required size of the eddy-current brake is minimized. The interfacing of the brake actuators with the control electronics is straightforward because the actuators are electric motors. Performance is also provided by the fact that each wheel can easily be controlled independently.

The application of the integrated brake in commercial trucks and buses is less advantageous due to the large torques required. Retardation, traction control, and dynamic stability are the most fitting applications of eddy-current braking to these vehicles.

The application to rail vehicles has been investigated. While tramways have little use for such a brake because of their low-speed drive cycle, high-speed trains and freight trains can benefit tremendously from this technology. The reduction in the use of friction braking is the most significant advantage in high-speed trains. For freight trains, the

ability to brake each car independently is a significant advantage over conventional pneumatically actuated friction brakes. The fast reaction time is an advantage for long trains where the propagation time of the signal in pneumatic lines is counted in seconds. Both provide greater stability in downhill curves. The magnets can be designed to fall back into a braking position in case of power failure. The eddy-current brake thus provides the same level of safety as the conventional pneumatic actuation system.

Finally, the use of eddy-current braking for cranes and elevators was investigated and found to provide significant safety while necessitating smaller brakes than vehicular applications.

2 – Conclusions

The partial success of the experiments requires a separate work of validation of finite element results. A complete instrumentation is required to:

- measure the precise magnitude and orientation of each magnet's magnetization
- measure the temperature of the disc
- measure the flux density in the airgap

Access to these measurements will allow troubleshooting the experiment more easily for discrepancies with the finite element simulations. A broad variety of rotors should be tested, including nonmagnetic rotors (copper, aluminum) and ferromagnetic rotors of

various thicknesses. These would allow pointing at the parameter(s) causing the discrepancies.

The test bed should be reworked to reduce the friction torques to negligible values. Thrust bearings and custom designed washers should be used to maintain the airgap without recourse to a sheet of Teflon. Eliminating the Teflon will allow cooling the surface of the disc. Better cooling should be provided on the surface of the disc. Rather than letting the disc bathe in water, this later should be circulated by a pump from a large tank (plenum). Letting the brake in air will reduce the fluid friction and eliminate the associated uncertainty.

An accurate thermal model is required that would model the conductive, convective, and radiant heat transfer in the brake. The modeling of the gradients inside the brake may also be necessary for accurate performance prediction, especially in heavy duty applications where the brake heats up significantly and fast response is required. The results of this analysis should tell how important these gradients are and whether they should be taken into account in integration analyses.

Finally, the analysis of the application of the integrated brake in automobiles and other vehicles should be pushed furthermore by using complete dynamic models of the vehicles and actual driving situations. This will give a precise understanding of the

dynamic operation of the integrated brake in anti-lock, traction, and dynamic stability control applications and allow for a complete design of the integrated brake controller.

Means of estimating the braking force generated by each component of the brake need to be investigated as this information is crucial to designing a controller that actuates the brake to take full advantage of its abilities. Accurate knowledge or estimation of the state of the brake is important for steady state operation (at the time scale of the deceleration), but is vital for dynamic operation (anti-lock, traction, and dynamic stability control).

REFERENCES

- [1] R. Limpert, *Brake Design and Safety*. Warrendale, PA: Society of Automotive Engineers, 1999.
- [2] Robert Bosch GmbH, *Bosch Automotive Handbook*. Warrendale, PA: Society of Automotive Engineers, 2004.
- [3] Telma. (2004, December). Nos Produits. [Online]. Available: www.telma.com.
- [4] H. Sakamoto, "Design of permanent magnet type compact ECB retarder," *Society of Automotive Engineers #973228*, pp. 19-25, 1997.
- [5] H.P.R. Frederikse, "Properties of magnetic materials," in *CRC Handbook of Physics and Chemistry*. New York: CRC Press, 1996.
- [6] H.D. Wiederick, N. Gauthier, D.A. Campbell, and P. Rochon, "Magnetic braking: Simple theory and experiment," *American Journal of Physics*, vol. 55, no. 6, pp. 500-503, 1987.
- [7] M.A. Heald, "Magnetic braking: Improved theory," *American Journal of Physics*, vol. 56, no. 6, pp. 521-522, 1988.
- [8] L.H. Cadwell, "Magnetic damping: Analysis of an eddy current brake using an airtrack," *American Journal of Physics*, vol. 64, no. 7, pp. 917-923, 1996.
- [9] E.R. Laithwaite, *Induction Machines for Special Purposes*. London: Newnes, 1966.
- [10] J.H. Wouterse, "Critical torque and speed of eddy current brake with widely separated soft iron poles," in *IEE Proceedings-B*, vol. 138, no. 4, pp. 153-158, 1991.
- [11] L. Barnes, J. Hardin, C.A. Gross, and D. Wasson, "An eddy current braking system," in *Proc. IEEE Conference on Control Applications*. Vancouver, Canada, 1993, pp. 58-62.
- [12] E. Simeu, "Application of NARMAX modeling to eddy current brake process," in *Proc. IEEE Conference on Control Applications*. Albany, NY, 1995, pp. 444-449.

- [13] S.M. Jang, S.H. Lee, and S.S. Jeong, "Characteristic analysis of eddy-current brake system using the linear Hallbach array," *IEEE Trans. Magn.*, vol. 38, no. 5, pp. 2994-2996, 2002.
- [14] P.J. Wang and S.J. Chiueh, "Analysis of eddy-current brakes for high speed railway," *IEEE Trans. Magn.*, vol. 34, no. 4, pp. 1237-1239, 1998.
- [15] S.M. Jang, S.H. Lee, and S.S. Jeong, "The application of linear Hallbach array to eddy current rail brake system," *IEEE Trans. Magn.*, vol. 37, no. 4, pp. 3405-3408, 2001.
- [16] H.K. Collan, and J. Vinnurva, "Rapid optimization of a magnetic induction brake," *IEEE Trans. Magn.*, vol. 32, no. 4, pp. 3040-3044, 1996.
- [17] K. Lee and K. Park, "Modeling eddy currents with boundary conditions by using Coulomb's law and the method of images," *IEEE Trans. Magn.*, vol. 38, no. 2, pp. 1333-1340, 2002.
- [18] J. Lammeraner and M. Štafl, *Eddy Currents*. Cleveland: CRC Press, 1966.
- [19] A. Lesobre, A.H. Ben Ahmed, and D. Drecq, "An analytical dynamic model of eddy-current brakes," in *Proc. IEEE International Electric Motor Drive Conference*. Cambridge, MA: 2001, pp. 122-125.
- [20] W.L. Lorimer, "Correlation of experimental data and three-dimensional finite element modeling of a spinning magnet array," *IEEE Trans. Magn.*, vol. 30, no. 5, pp. 3004-3007, 1994.
- [21] D. Schieber, *Electromagnetic Induction Phenomena*. New York: Springer-Verlag, 1986.
- [22] J. Bigeon, *Contribution a la Modélisation de Structures Electromagnétiques a Courants de Foucault*. Grenoble, France : Institut National Polytechnique de Grenoble, 1983.
- [23] J. Bigeon and J.C. Sabonnadiere, "Analysis of an electromagnetic brake," *IEEE Journal of Electric Machines and Power Systems*, vol. 10, pp. 285-297, 1985.
- [24] K.J. Binns and P.J. Lawrenson, *Analysis and Computation of Electric and Magnetic Field Problems*. New York: Pergamon Press, 1973.
- [25] A. Wallace, "Performance prediction and test of adjustable, permanent-magnet, load transmission systems," in *Proc. IEEE IAS Annual Meeting*. Chicago, IL, 2001, vol. 3, pp. 1648-1655.

- [26] A.C. Smith, S. Williamson, A. Benhama, L. Counter, and J.M. Papadopoulos, “Magnetic drive couplings,” in *Proc. IEEE 9th International Conference on Electrical Machines and Drives*. Seattle, WA, 1999, pp. 232-236.
- [27] B. Daqiang, W. Xiangheng, and L. Decheng, “Magnetic analysis and design method for solid rotor induction motors based on directly coupled field-circuit,” in *Proc. IEEE PIEMC*. Beijing, China, 2000, vol. 3, pp. 1323 – 1327.
- [28] L.T. Ergene and S.J. Salon, “One-slot AC steady-state model of a canned-solid rotor induction motor,” *IEEE Trans. Magn.*, vol. 40, no. 4, pp.1892 – 1896, 2004.
- [29] R. Ibtiouen, R. Kechroud, O. Touhami, and S. Mekhtoub, “Complex finite element analysis of a solid rotor induction motor,” in *Proc. IEEE International Electric Motor Drive Conference*. Madison, WI, 2003, vol. 3, pp. 1606 – 1610.
- [30] C.N. Obiozor and M.N.O. Sadiku, “Finite element analysis of a solid rotor induction motor under stator winding defects,” in *Proc. IEEE Southeastcon*. Williamsburg, VA, 1991, vol. 1, pp. 449 – 453.
- [31] M. Sarma, “Current-density distribution in solid-rotor induction motor,” *IEEE Trans. Magn.*, vol. 15 , no. 6 , pp. 1473 – 1475, 1979.
- [32] M. Hecquet, P. Brochet, L.S. Jin, and P. Delsalle, “A linear eddy current braking system defined by finite element method,” *IEEE Trans. Magn.*, vol. 35, no. 3, pp.1841-1844, 1999.
- [33] M. Hofmann, Th. Werle, R. Pfeiffer, and A. Binder, “2D and 3D numerical field computation of eddy-current brakes for traction,” *IEEE Trans. Magn.*, vol. 36, no. 4, pp. 1758-1763, 2000.
- [34] A.B. Dietrich, I. E. Chabu, J. R. Cardoso, “Eddy-current brake analysis using analytical and FEM calculations – PART I: Theory,” in *Proc. IEEE International Electric Motor Drive Conference*. Cambridge, MA, 2001, pp. 454-457.
- [35] A.B. Dietrich, I. E. Chabu, and J. R. Cardoso, “Eddy-current brake analysis using analytical and FEM calculations – PART II: Application,” in *Proc. IEEE International Electric Motor Drive Conference*. Cambridge, MA, 2001, pp. 458-461.
- [36] J. Bigeon, “Finite element analysis of an electromagnetic brake,” *IEEE Trans. Magn.*, vol. 19, no. 6, pp. 2632-2634, 1983.

- [37] O. Bardon, *Etude et Mise au Point d'un Nouveau Type de Rotor pour Ralentisseurs Electromagnétiques*. Lyon, France : Institut National des Sciences Appliquées, 1996.
- [38] D. Albertz, S. Dappen, and G. Henneberger, “Calculation of the 3D non-linear eddy-current field in moving conductors and its applications to braking systems,” *IEEE Trans. Magn.*, vol. 32, no. 3, pp. 768-771, 1996.
- [39] M. Fujita, “3-dimensional electromagnetic analysis and design of an eddy-current rail brake system,” *IEEE Trans. Magn.*, vol. 34, no. 5, pp. 3458-3551, 1998.
- [40] N. Takahashi, “Optimization of permanent magnet type of retarder using 3-D finite element method and direct search method,” *IEEE Trans. Magn.*, vol. 34, no. 5, pp. 2996-2999, 1998.
- [41] K. Muramatsu, “3-D eddy current analysis in moving conductor of permanent magnet type of retarder using moving coordinate system,” *IEEE Trans. Energy Conversion*, vol. 14, no.4, pp. 1312-1317, 1999.
- [42] K. Muramatsu, “Comparison of coordinate systems for eddy current analysis in moving conductors,” *IEEE Trans. Magn.*, vol. 28, no. 2, pp. 1186–1189, 1992.
- [43] N. Labbe, *Modélisation du Couplage Magnétothermique Appliqué aux Ralentisseurs Electromagnétiques*. Grenoble, France : Institut National Polytechnique de Grenoble, 1996.
- [44] Cedrat, (2005, March), Flux ® One step ahead. [Online]. Available: www.cedrat.com.
- [45] W. Betteridge, *Cobalt and Its Alloys*. Chichester, West Sussex: Horwood, 1984.
- [46] R.M. Bozorth, *Ferromagnetism*. Piscataway, NJ: IEEE Press, 1993.
- [47] W.K.A. Baran, “Influence of different magnetic field profiles on eddy-current braking,” *IEEE Trans. Magn.*, vol. 6, no. 2, pp. 260-263, 1970.
- [48] T.D. Gillespie, *Fundamentals of Vehicle Dynamics*. Warrendale, PA: Society of Automotive Engineers International, 1992.
- [49] Danaher Motion. (2005, March). Danaher Motion > Motors > brushless DC – Product overview. [Online]. Available: <http://www.thomsonindustries.com/>.

- [50] M. Ehsani, Y. Gao, S. E. Gay, and A. Emadi, *Modern Electric, Hybrid Electric, and Fuel Cell Vehicles: Fundamentals, Theory, and Design*. Boca Raton, FL: CRC Press, 2004.
- [51] A.D. Sarkar, *Friction and Wear*. London: Academic Press, 1980.
- [52] Renault Trucks. (2005, March). Nouveau Renault Magnum. [Online]. Available: <http://www.renault-trucks.com/home.html>.
- [53] Irisbus Iveco. (2005, March). Cityclass 18m. [Online]. Available: www.irisbus.com.
- [54] S.E. Gay and M. Ehsani, "Design of a fuel cell hybrid tramway," in *Proc. IEEE 2002 Fall Vehicular Technology Conference*. Vancouver, BC, Canada, 2002, pp. 995-997.
- [55] Knorr-Bremse AG. (2005, March). Braking systems. [Online]. Available: <http://www.knorr-bremse.com/>.
- [56] Alstom Transport. (2005, March). Passenger trains. [Online], Available: <http://www.transport.alstom.com/>.
- [57] Komatsu Ltd. (2005, March). Construction and mining equipment. [Online]. Available: <http://www.komatsu.com/>.
- [58] Kawasaki Motor Co. (2005, March). Motorcycles. [Online]. Available: <http://www.kawasaki.com>.
- [59] American Suzuki Motor Co. (2005, March). Motorcycles. [Online]. Available: <http://www.suzukicycles.com/>.
- [60] M. DeLuca, (2003, June). Stellar Newbuild delivers extra deck space. OilOnline.com, [Online]. Available: http://www.oilonline.com/news/features/oe/20030.Stellar_10877.asp.

APPENDIX A

HEAT TRANSFER MODEL OF THE EDDY-CURRENT BRAKE

The model must take into account the influence of temperature because this latter considerably influences electrical and magnetic parameters. The dependence of conductivity on temperature has been taken into account by the means of look-up tables with values taken from [5] (see Fig. 193).

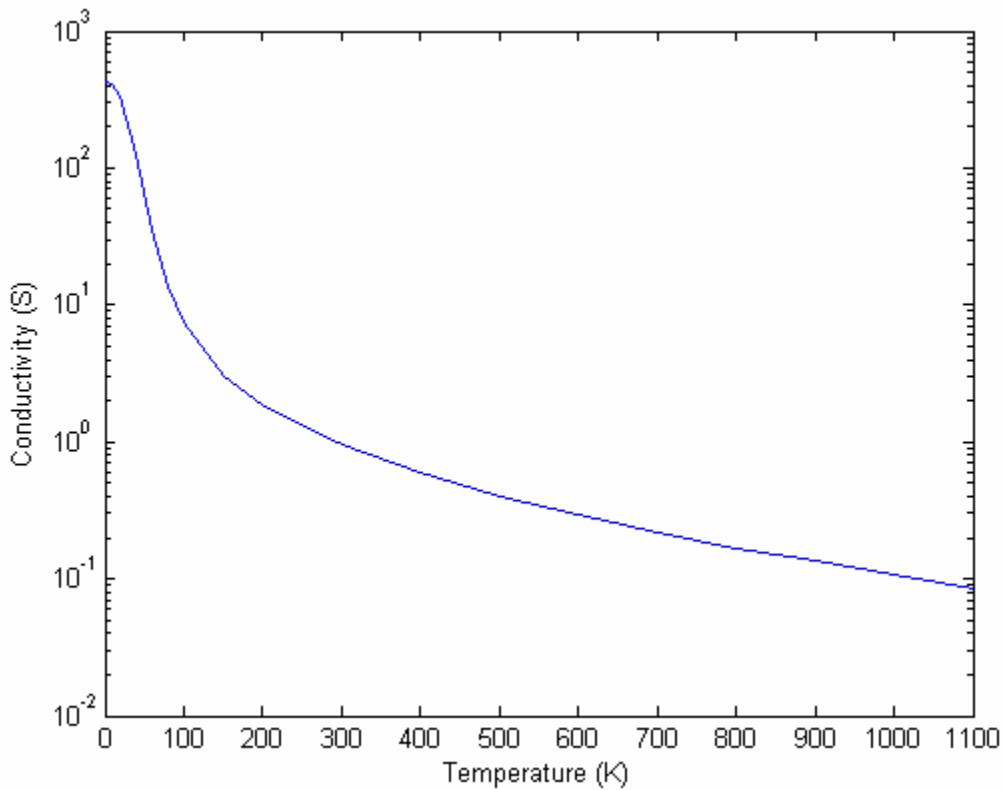


Fig. 193: Impact of temperature on electrical conductivity

Temperature has a limited influence on the relative permeability of a material [5,43] but has a major influence on its saturation magnetization. A look-up table is also used, based

on the Weiss theory [43]. Fig. 194 shows the normalized saturation magnetization versus temperature. Simulations use the saturation magnetization at 0°C instead of 0°K because the former is more often used than the latter.

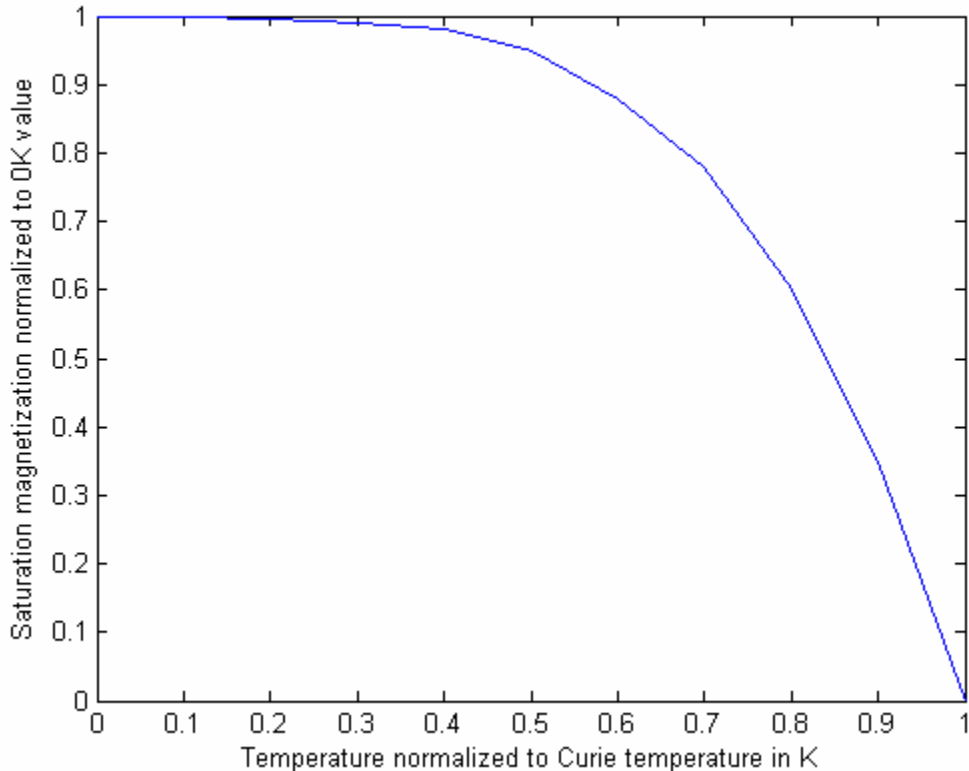


Fig. 194: Normalized saturation magnetization vs. temperature

Once computed, the conductivity and saturation magnetization are used in another set of look-up tables to derive the new peak torque and critical speed, based on results from finite element analysis.

The thermal model assumes a uniform temperature distribution, a uniform heat source distribution, and takes into account only the dominant heat transfer mode, which is forced

convection. Although there is a significant amount of radiant heat transfer, it is much more difficult to estimate than the forced convection. The thermal model consists of the following equations:

$$(Q_{\text{eddy_current_braking}} - Q_{\text{forced_convection}}) = m_{\text{disc}} \cdot C_{p_{\text{disc}}} \frac{d\theta_{\text{brake}}}{dt} \quad (148)$$

$$Q_{\text{forced_convection}} = h \cdot \frac{A_{\text{disc}}}{2} (\theta_{\text{brake}} - \theta_{\text{air}}) \quad (149)$$

$$h = \frac{V_{\text{car}}}{2\pi R_{\text{wheel}} 360} \sqrt[3]{V_{\text{air}}} \cdot \sqrt{P_{\text{air}} \theta_{\text{air}}} \cdot 0.2446 \quad (150)$$

The speed of the airflow is approximated to the speed of the vehicle. The effective area exposed to forced convection is taken as half the total area of the discs inner surface including the cooling fins. Sea level pressure and room temperature are assumed for the air. All variables are expressed in SI units.

VITA

Sébastien Emmanuel Gay
c/o Prof. M. Ehsani
Department of Electrical Engineering
Texas A&M University
College Station TX 77843-3128

Sébastien E. Gay received two undergraduate diplomas in mechanical engineering and electrical engineering from the Université Joseph Fourier, Grenoble, France in 1996 and 1997 respectively. He received his “Diplome d’Ingénieur” in electrical engineering from the “Ecole Nationale Supérieure d’Ingénieurs Electriciens” de Grenoble in 2000. He received his Master of Science in electrical engineering from Texas A&M University in 2001.

Sébastien E. Gay is the author of 14 conference publications, 3 journal publication, and 3 invention disclosures. He is the co-author of “Modern Electric, Hybrid Electric, and Fuel Cell Vehicles: Fundamentals, Theory, and Design” and contributed one chapter to the book “DSP Control of Electromechanical Motion Devices” by H. Toliyat. In 2003, Sébastien E. Gay received the “Spirit of Innovation Award” for 2000th Disclosure from the Texas A&M Technology Licensing Office. He has been a guest speaker to the “XIV Congresso Internacional de Ingenieria Mecanica” in Monterrey, Mexico in 2001.